ISOPRENE SECONDARY ORGANIC AEROSOL IN A GLOBAL CHEMISTRY CLIMATE MODEL

DISSERTATION

zur
Erlangung des Doktorgrades (Dr. rer. nat.)

der
Mathematisch-Naturwissenschaftlichen Fakultät

der
Rheinischen Friedrich-Wilhelms-Universität Bonn

vorgelegt von
SCARLET STADTLER

aus
Mexiko Stadt

Bonn
April 2018

Angefertigt mit Genehmigung der Mathematisch-Naturwissenschaftlichen Fakultät der Rheinischen Friedrich-Wilhelms-Universität Bonn

1. Gutachter:	PD. Dr. Martin G. Schultz
2. Gutachter:	Prof. Dr. Andreas Bott
Tag der Promotion:	12.07.2018
Erscheinungsjahr:	2018

Für Eduard und Arnold.

Veröffentlichte Teile der Dissertation

Bei der vorliegenden Dissertation handelt es sich um eine Monographie, dennoch wurde der Kernteil der Dissertation zur Veröffentlichung eingereicht und angenommen (Stand 24.07.2018). Dabei ist der publizierte Teil wie folgt in dieser Dissertation wiederzufinden:

1. Kapitel 1 - geringe Übereinstimmung
2. Kapitel 2 - nur in Dissertation
3. Kapitel 3 - weitgehende Übereinstimmung (besonders Unterkapitel 3.3, 3.5.1, 3.6)
4. Kapitel 4 - weitgehende Übereinstimmung (besonders Unterkapitel 4.1.2, 4.1.3, 4.2)
5. Kapitel 5 - Übereinstimmungen nur in Unterkapiteln 5.5 und 5.6.
6. Kapitel 6 - geringe Übereinstimmung

Die entsprechende Publikation ist zu finden als:

Stadtler, S., Kühn, T., Schröder, S., Taraborrelli, D., Schultz, M. G., and Kokkola, H.: Isoprene derived secondary organic aerosol in a global aerosol chemistry climate model, Geosci. Model Dev. Discuss., https://doi.org/10.5194/gmd-2017-244, in review, 2017.

Zusammenfassung

Atmosphärisches Aerosol wechselwirkt direkt und indirekt mit dem Klimasystem, indem es die Strahlungsbilanz modifiziert. Bis zu 90% des organischen Aerosols wird durch oxidierte Kohlenwasserstoffe gebildet. Diese oxidierten Kohlenwasserstoffe können entweder über Nukleation neue Partikel bilden, auf bereits existierenden Aerosolen kondensieren, oder mit deren Oberflächen chemisch reagieren. Über diese Prozesse gebildete Aerosole werden sekundäres organisches Aerosol genannt (SOA). Die globale Modellierung der SOA ist herausfordernd, weil es tausende von einzelnen, unterschiedlichen, organischen Molekülen in der Atmosphäre gibt. Dennoch ist das Verständnis von SOA essenziell für die Abschätzung dessen Einflusses auf das Klimasystem, sodass globale Modelle mittels verschiedenen Ansätzen versuchen SOA zu simulieren. Üblicherweise werden die SOA Bildungsprozesse aus der Gasphase grob parametrisiert, ohne dabei spezifische Vorlufersubstanzen zu betrachten, aufgrund von limitierter Rechenkapazität. Im Rahmen des globalen Chemieklimamodells ECHAM-HAMMOZ wurde für diese Studie eine neue explizite Kopplung zwischen dem Aerosolmodul HAM-SALSA und dem Chemiemodul MOZ entwickelt, um die Bildung von sekundären organischen Aerosol zu simulieren. Dabei liegt der Fokus auf Aerosolvorläuferstoffen, die bei der Isoprenoxidation produziert werden. Die Isoprenoxidation in dem Chemiemodul MOZ ist formuliert als semi-explizites Schema, welches 147 Oxidationsreaktionen von Isopren und seinen Abbauprodukten beinhaltet. Das Schema ist eingebettet in ein detaillierten atmosphärischen Mechanismus, der aus 779 Reaktionen besteht. Während der Oxidation von Isopren und dessen Oxidationsprodukten entstehen Komponenten, die sich durch eine geringe Volatilität auszeichnen. Diese Komponenten werden explizit von HAM-SALSA in das bereits existierende Aerosol partitioniert. Außerdem wurden auch Isoprenepoxidiol (IEPOX) und Glyoxal, welches ebenfalls durch Isoprenoxidation gebildet wird, als SOA Quellen implementiert. Diese beiden Stoffe reagieren mit der wässrigen Außenschicht der Aerosole und die gebildeten Produkte bleiben im Aerosol. Mit dieser Kopplung wird jeder einzelne SOA-Vorläuferstoff im Sinne von Kondensation, Evaporation und Oberflächenreaktion im Modell verfolgt. Der beschriebene Ansatz erlaubt es, dass die SOA Zusammensetzung und dessen Abhängigkeit von der atmosphärischen Chemie, des Aerosol-pH-Werts, der Wahl der Sättigungskonzentration und Evaporationsenthalpie untersucht wird. Isoprendihydroxidihydroperoxid (ISOP(OOH)2) und IEPOX wurden als bedeutendste Vorlufer fr die Isopren-SOA Bildung (iSOA) identifiziert. Weitere Untersuchungen von IEPOX zeigten, dass in verschmutzten Regionen die Verstärkung der Oberflächenreaktion durch saures Aerosol in direkter Konkurrenz zur Unterdrückung der IEPOX-Bildung durch NO_x steht.

Die Kopplung zwischen semi-expliziter Isoprenoxidation und expliziter Berechnung der Aerosolbildung simuliert eine globale, jährliche iSOA Ausbeute von 15 % relativ zum insgesamt emittierten Isopren. In dem simulierten Jahr 2012 werden 445.1 Tg (392.1 TgC) Isopren emittiert und eine iSOA-Quelle von 138.5 Tg (56.7 TgC) berechnet. IEPOX trug 42.4 Tg (21.0 TgC) bei und ISOP(OOH)2 78.0 Tg (27.9 TgC). Die Hauptsenke ist die Aerosolnassdeposition, welche 133.6 Tg (54.7 TgC) iSOA entfernt. Eine globale Belastung von 1.4 Tg (0.6 TgC) iSOA wurde im Jahr 2012 ermittelt. Bei dem Vergleich zwischen beobachteten organischen Aerosol und dem modellierten iSOA ergibt sich eine gute Übereinstimmung in isoprendominierten Regionen.

Abstract

Atmospheric aerosol influences the climate system, modifying atmospheric radiation directly and indirectly. Up to 90% to the total organic aerosol is formed through the oxidation of hydrocarbons and subsequent nucleation, condensation or chemical uptake onto pre-existing aerosols, defined as secondary organic aerosol (SOA). Due to thousands of individual compounds involved in SOA formation, modeling SOA related processes on a global scale is challenging. Understanding the formation of SOA is crucial to estimate its impact on the climate system, thus global models try to simulate SOA formation with different approaches. Usually, a detailed chemistry and evolution of single compounds is disregarded, due to computational limitations. Within the framework of the global chemistry climate model ECHAM-HAMMOZ, a novel explicit coupling between the sectional aerosol model HAM-SALSA and the chemistry model MOZ was established to form isoprene derived secondary organic aerosol (iSOA). Isoprene oxidation in the chemistry model MOZ is described by a semi-explicit scheme consisting of 147 reactions, embedded in a detailed atmospheric chemical mechanism with a total of 779 reactions. Low and semi-volatile compounds produced during isoprene photo-oxidation are identified and explicitly partitioned by HAM-SALSA. Furthermore, reactive uptake of isoprene epoxidiols (IEPOX) and isoprene derived glyoxal were included as iSOA sources. With this method, every single precursor is tracked in terms of condensation, evaporation and reactive uptake in each aerosol size bin. This approach allows the investigation of iSOA composition and its dependence on chemical regimes, aerosol acidity, choice of saturation concentration and evaporation enthalpy of each single compound. Isoprene dihydroxy dihydroperoxide (ISOP(OOH)2) and IEPOX were identified as main contributors to iSOA formation. Further study of IEPOX reactive uptake on aerosols with different pH values showed the competition between IEPOX uptake enhancement by acidic aerosol and NO_x suppression of IEPOX formation in polluted areas. Moreover, new aerosol sinks were introduced as iSOA photolysis and thermal decomposition of ISOP(OOH)2.

This model framework, connecting semi-explicit isoprene oxidation with explicit treatment of aerosol tracers, leads to a global, annual isoprene SOA yield of 15 %, relative to the primary oxidation of isoprene by OH, NO_3 and O_3. In the modeled year 2012, 445.1 Tg (392.1 TgC) isoprene are emitted and an iSOA source of 138.5 Tg (56.7 TgC) is simulated. IEPOX contributes 42.4 Tg (21.0 TgC) and ISOP(OOH)2 78.0 Tg (27.9 TgC) to iSOA in ECHAM-HAMMOZ. The main sink process is particle wet deposition which removes 133.6 Tg (54.7 TgC). The iSOA burden reaches 1.4 Tg (0.6 TgC) . The model iSOA concentrations compare well to observed organic aerosol concentrations in regions where isoprene emissions are high.

Contents

1. Introduction

Atmospheric aerosols impact Earth's climate and human health [Fröhlich-Nowoisky et al., 2016, Lakey et al., 2016]. Climate impacts related to aerosols are classified as direct and indirect effects. Aerosols directly absorb and scatter solar radiation modifying the atmosphere's radiation budget (direct aerosol effect). Moreover, aerosols act as cloud condensation nuclei depending on their micro-physical properties. As a consequence, cloud formation and resulting cloud properties are altered by aerosols. The modified clouds also interact with the climate system (indirect aerosol effect) [IPCC, 2013]. Additionally to the climate, humans are directly influenced by aerosols. Aerosols also impact human health. Depending on the size of the particles, inhalation transports them deep into the lungs to the pulmonary alveoli. A positive correlation between particulate matter concentrations and human morbidity and mortality is observed [Samet et al., 2000]. Toxicity arises from direct action of particulate matter on the respiratory tissue, enhancing respiratory inflammations [Wilson and Suh, 1997, Morio et al., 2001]. Unfortunately, aerosol processes like aerosol-cloud interactions, aerosol formation and transformation in the atmosphere, are not fully understood. As a consequence, impacts on humans, climate and climate change cannot be assessed accurately [IPCC, 2013]. Research on atmospheric particles is still ongoing and motivates this thesis.

Aerosol size, number distributions and composition play a key role in particle interactions with the climate system and with human health. Atmospheric number concentrations of 10^1–$10^2\,\mathrm{cm}^{-3}$ are found in remote areas, areas influenced by anthropogenic pollution reach higher values between 10^5–$10^6\,\mathrm{cm}^{-3}$. Also particle sizes vary within orders of magnitude. Typical values range from 10^0–$10^5\,\mathrm{nm}$ [Seinfeld and Pandis, 2012]. More variable than the aerosol size (diameter), is the aerosol shape. Wet aerosols contain water smoothing their surface or dissolving aerosol components leading to a spherical shape. In contrast, dry aerosols can have any shape, they might be porous and their surface area cannot be described easily [Pöschl, 2005]. Aerosol sizes and shapes vary greatly due to their origin and atmospheric transformation, two factors also controlling aerosol composition. Particles of different compositions are emitted directly into the atmosphere (called primary aerosols). These are usually large $> 10^{-1}\,\mu\mathrm{m}$ and emitted by forest fires, mineral dust re-suspension, (volcanic) ash, sea spray, pollens and spores. In contrast to primary aerosols, secondary aerosols are air-borne particles formed by gas-phase precursors. Two processes lead to secondary aerosol formation. First, new particle formation by clustering of gas-phase molecules, called nucleation, yields in particles smaller than $10^{-1}\,\mu\mathrm{m}$. Second, gas-phase precursors can condense on pre-existing particles [Tomasi et al., 2017] or react on particle surfaces. Tropospheric chemistry is affected by aerosols acting as substrates [Dentener and Crutzen, 1993]. After emission or air-borne formation, aerosols are transported through the atmosphere, where they are transformed chemically or undergo cloud-formation until they are removed. Removal processes are dry deposition, gravitational sedimentation and wet deposition [Seinfeld and Pandis, 2012].

The variety of atmospheric aerosols leads to different impacts on climate processes. A large fraction of 20 to 90 % of sub-micron particles consists of organic material [Murphy et al., 2006, Zhang et al., 2007, Jimenez et al., 2009], called organic aerosol (OA). OA is observed in mid

latitudes [Putaud et al., 2004], tropical forests [Roberts et al., 2001] and the middle troposphere [Huebert et al., 2004]. OA is mainly formed in the atmosphere by oxidized hydrocarbons [Hallquist et al., 2009] and other precursor gases. Fine organic particles are formed via nucleation of gas-phase compounds involving sulfate and organic gases. Additionally, organic gases can also condense on pre-existing aerosols of any composition and size. In contrast, large organic particles originate from biogenic material like pollen and organic debris. Directly emitted OA is classified as primary organic aerosol (POA) and airborne particles are called secondary organic aerosol (SOA) [Seinfeld and Pandis, 2012]. Depending on source, OA exists in several phase-states; it can be liquid, aqueous or in an amorphous solid or semi-solid state [Shiraiwa et al., 2011]. The phase-state of OA can change while it is transported by atmospheric motion. During the atmospheric residence time, OA is constantly transformed. Multiphase chemistry takes place on the particle surface and bulk phase, changing the OA composition and also gas-phase compounds. The longer the atmospheric residence time, the more constituents are found in the particles. In the particle-phase they can react further, a process called "aerosol aging" [Kroll and Seinfeld, 2008].

Airborne formation of secondary organic aerosol depends on precursor gases' physico-chemical properties, pre-existing aerosol composition and air temperature [Donahue et al., 2011]. SOA precursor gases are generally not directly emitted into the atmosphere, but are formed in several oxidation steps involving different radicals [Kanakidou et al., 2000]. After oxidation, SOA precursors are multifunctional molecules. Multifunctional molecules include several oxygen atoms, which make them heavier compared to hydrocarbons without functional groups. Further, the functional groups lead to a higher water-solubility of the precursors. Both, high molecular weight and multifunctionality, lead to low volatile precursors which form highly oxidized SOA [Saxena and Hildemann, 1996, Donahue et al., 2012]. SOA interacts directly with solar radiation [Chung and Seinfeld, 2002] and is observed to act as cloud condensation nuclei [Lambe et al., 2011, Engelhart et al., 2011]. In polluted regions, it plays a crucial role in photochemical smog episodes [Kleeman et al., 2007], harming human health [Yang and Omaye, 2009]. This highlights the importance of SOA formation for direct and indirect climate forcing and motivates the process to be considered in climate models. At the same time, the SOA formation process is still poorly understood. Therefore, SOA formation is currently investigated from different perspectives in theoretical studies, experiments and ambient measurements [Fuzzi et al., 2015]. Especially the global SOA budget is not well constrained and the source strength is estimated roughly between 140 - 910 $\mathrm{TgC\,a^{-1}}$ [Tsigaridis and Kanakidou, 2003, Goldstein and Galbally, 2007, Hallquist et al., 2009].

Modeling of secondary organic aerosol formation is challenging, because first, a large variety of organic molecules can be found in the atmosphere. Second, these molecules can be SOA precursors under certain atmospheric and micro-physical conditions [Donahue et al., 2011]. SOA formation efficiency varies depending on conditions as atmospheric temperature, humidity, photo-chemistry, pre-existing aerosol, aerosol surface area and aerosol acidity.

Different methods were developed to describe SOA formation in atmospheric models with different levels of complexity [Farina et al., 2010]. At first, global models assumed an instantaneous SOA formation applying a constant fractional yield of non-volatile organic compounds forming SOA [Liousse et al., 1996]. Later, the two-product-model by Odum et al. [1996] was developed based on the partitioning theory of Pankow [1994], which describes SOA as an pseudo-ideal solution of multiple organic compounds of two different volatilities. Odum et al. [1996] also applied SOA yields, but as a function of suspended organic aerosol mass. Recently, Donahue et al. [2006, 2011, 2012] developed the volatility basis set describing several compounds accord-

ing to their volatility classes. To classify the volatility of the compounds, the saturation vapor pressure in the gas-phase and the organic and inorganic mixture in the particle-phase are taken into account. The yield, two-product and volatility basis set methods focus on SOA formation using no or very simplified chemical processing of emitted organic gases. The simple chemical parametrizations save computational time otherwise needed to solve a complex chemical system capable of explicitly forming SOA precursors. In contrast to these methods, a different approach was taken by Lin et al. [2012] considering individual compounds to SOA formation which were identified by experimental studies. Therefore, Lin et al. [2012] simulated explicit chemistry for SOA precursor formation from peroxides, organic nitrates, glyoxal and isoprene epoxide. Although many SOA formation schemes were developed, global models tend to underestimate SOA formation and atmospheric concentration [Tsigaridis et al., 2014], in spite of the fact that global models usually only include deposition loss of SOA and lack in additional loss processes like in-particle fragmentation [Hodzic et al., 2016].

In order to improve the knowledge about SOA formation, solve the underestimation problem and get insight of anthropogenic impacts on SOA, a novel explicit treatment of SOA formation is developed in this thesis. To accomplish this, the sectional aerosol model HAM-SALSA [Kokkola et al., 2018] is coupled to the chemistry model MOZ [Schultz et al., 2017] within the state-of-the-art global climate model ECHAM [Stevens et al., 2013]. SOA is formed from individual compounds following atmospheric oxidation according to ambient conditions. These conditions e.g., temperature, atmospheric oxidants, humidity, aerosols and clouds, impact atmospheric chemistry and SOA formation. Moreover, features in aerosol evolution related to individual chemical processes are not captured if species are lumped together in excessive large groups. The detailed formation scheme following individual compounds allows for process understanding of SOA formation on a global scale. Here, the focus lies on isoprene derived secondary organic aerosol (iSOA) formation. Isoprene is the most emitted volatile organic compound after methane [Guenther et al., 2012]. The isoprene emission strength is estimated to be between 500 and 750 $\mathrm{Tg\,a^{-1}}$, which has a huge potential for SOA formation [Surratt et al., 2006]. This study aims to model iSOA on a global scale using an updated isoprene oxidation mechanism, saturation vapor pressure and evaporation enthalpy estimated for each compound, reactive uptake for isoprene products undergoing heterogeneous reactions and new SOA sinks.

This thesis is organized as follows: chapter 2 introduces the theoretical concepts of volatile organic compounds and their oxidation to form SOA precursors, SOA formation, SOA loss processes at the state of knowledge provided by current research. Chapter 3 describes the model ECHAM-HAMMOZ and its extensions made for SOA formation and sink processes developed and used in this study. Chapter 4 presents results obtained by ECHAM-HAMMOZ with the new SOA formation coupling. The results are discussed in chapter 5, including tests demonstrating which features in aerosol evolution are resolved, but also the model limitations. Finally, chapter 6 summarizes the main findings and concludes. Parts of this thesis, i.e section 3.5 and parts of chapters 4 and 5 have been previously published in Stadtler et al. [2017].

2. Secondary organic aerosol

Natural secondary organic aerosols are formed in the atmosphere as a result of the mass transfer of gas-phase compounds to the particle-phase. These compounds have to have either sufficiently low saturation vapor pressures or undergo reactive uptake via multi-phase chemistry into the particle-phase. Therefore, there are two separate steps in SOA production: (i) production of SOA precursors in the gas-phase, and (ii) partitioning and uptake of the precursor gases into the particle-phase [Tomasi et al., 2017]. These two steps are explained in sections 2.1 and 2.2. To close the SOA life cycle, loss processes are discussed in section 2.3. Since this study focuses on isoprene secondary organic aerosol, isoprene chemistry and isoprene products leading to iSOA are presented in detail in section 2.4.

2.1. Secondary organic aerosol precursors

Thousands of organic compounds from different sources and with various sizes and physico-chemical characteristics are emitted into the atmosphere. This section gives an overview of volatile organic compounds (VOC) and their transformation to SOA precursors.

2.1.1. Volatile organic compounds

Processes associated with life, like growth, preservation and decay of plants, animals and microbes are sources for organic compounds in the atmosphere. Usually, organic compounds are produced in living creatures and some also leave the organism as metabolic waste products or hormones for signaling or defense. Furthermore, combustion of organic material, like biomass burning and fossil fuel consumption also emit organic compounds into the atmosphere [Goldstein and Galbally, 2007, Gkatzelis et al., 2017]. The majority of organic compounds is released by biological processes in a variety of plant types. Looking at the organic compounds themselves it can be differentiated between biogenic volatile organic compounds (BVOC) and anthropogenic volatile organic compounds (AVOC). BVOC emissions refer to emissions by plants and other organisms, while AVOC are mainly released from usage of solvents and traffic. Moreover, BVOC emissions are one order of magnitude larger than AVOC emissions. In Table 2.1, emission strengths of different compounds and compound classes can be found. Showing all individual compounds is impossible, because there are thousands of organic compounds in the atmosphere, some of which are not detectable by state-of-the-art measurement instruments [Goldstein and Galbally, 2007]. In total around 1089 Tg BVOC [Guenther et al., 2012] and around 130 Tg AVOC [Lamarque et al., 2010] are estimated to be emitted annually. Table 2.1 shows that around 50 % of BVOC emissions are estimated to be isoprene emissions. Both estimates, of BVOC and AVOC emissions are highly uncertain. The individual BVOC emissions hold an uncertainty of factors 2 to 3 [Guenther et al., 2012]. These are estimated usually by models based on flux measurements of BVOC emissions in different vegetation types, like tropical forests, deciduous forests and grassland. Based on this, model parametrizations including plant physiology, nutrient availability, leaf age and location within the canopy and weather conditions are

formulated to estimate global BVOC emissions [Guenther et al., 2006]. AVOC emissions are estimated following several steps, involving knowledge of source emissions and emission factors. Emission factors indicate how much of a species is emitted for a specific mass of fuel burned in a specific technological process. These factors are partially unknown or not proved by tests. Thus, AVOC emissions are uncertain, especially in regions where the reported source emissions are not reliable [Lamarque et al., 2010].

Figure 2.1 sketches the estimated global budget for all volatile organic compounds. Goldstein and Galbally [2007] assume an annual total VOC emission strength of 1300 TgC a^{-1}. Once the VOCs are in the atmosphere, they are either oxidized by atmospheric chemistry or removed by dry and wet deposition. If not lost due to deposition, VOCs are either oxidized until they are transformed into CO and CO_2 or they form SOA. Thus, VOCs can act as precursor gases for SOA formation. According to this budget, between 40 and 70 % of carbon emitted as VOCs forms SOA. Subsequently, VOCs are lost via dry and wet deposition of SOA or they are released back into gas-phase as oxidized CO or CO_2. The budget shows that carbon emitted as VOCs transforms and is lost to the atmosphere via several pathways.

Table 2.1.: Global VOC emissions in Tg a^{-1}. BTX: benzene, toluene, xylene. Anthropogenic VOC from Piccot et al. [1992] and biogenic VOC from Guenther et al. [2012]

Compound	Emission in Tg a^{-1}
Paraffins	50.3
Olefins	38.3
Aromatics BTX	14.0
Formaldehyde	1.0
Other VOC	5.9
Total	109.5
Isoprene	535
α-Pinene	66.1
t-β-Ocimene	19.4
β-Pinene	18.9
Limonene	11.4
Sabinene	9.0
Myrcene	8.7
3-Carene	7.1
Other Monoterpenes	21.7
α-Farnesene	7.1
β-Caryophyllene	7.4
Other Sesquiterpenes	14.5
232-MBO	2.2
Methanol	99.6
Acetone	43.7
Bidirectional VOC	53.8
Stress VOC	47.7
Other VOC	32.8
CO	81.6
Total VOC and CO	1089

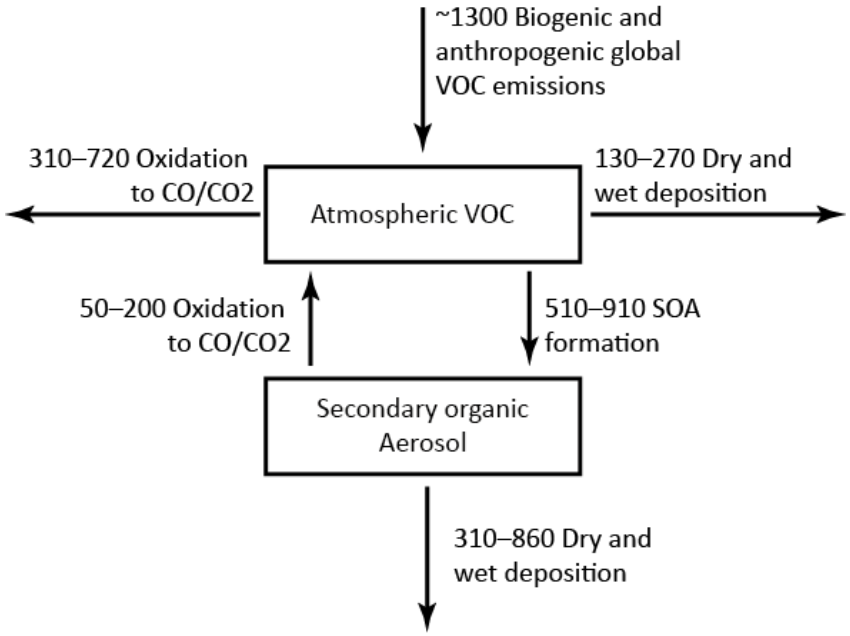

Figure 2.1.: Mass-balance-based estimation of the global VOC budget in $TgC\,a^{-1}$ adapted from Goldstein and Galbally [2007]. Arrows indicate best estimates of fluxes. Three possible pathways lead to removal of total emitted VOCs: Oxidation to CO and CO_2, dry or wet deposition, and SOA formation. The SOA is removed by oxidation and dry or wet deposition.

2.1.2. Oxidation of volatile organic compounds

In figure 2.1, the arrow indicating the flux between VOC and SOA gives a oversimplified impression of SOA formation. As the name indicates, "volatile" organic compounds are gas-phase compounds which do not easily condense to the liquid- or solid-phase. First, a transformation reducing volatility has to happen. This is achieved by atmospheric chemistry. Atmospheric chemistry is driven by solar radiation, it can be compared to a flame converting hydrocarbons to CO_2, but at a very slow rate since its temperature is much lower than in a flame. Decomposing a large hydrocarbon in the atmosphere takes several oxidation steps [Seinfeld and Pandis, 2012].

As an example, a schematic view of biogenic VOC oxidation is shown in figure 2.2. The two arrows between biogenic VOC and the alkyl radical $R^\bullet$ indicate initial reaction with the hydroxyl radical (OH), nitrate radical (NO_3) or ozone (O_3). OH abstracts an H-atom from the hydrocarbon, while O_3 and NO_3 add to carbon double bonds. Both types of reactions lead to an alkyl radical $R^\bullet$. Radicals are very reactive species and a large fraction of atmospheric air is made of oxygen molecules (O_2). Thus, $R^\bullet$ will most probably react quickly with O_2 leading to peroxy radicals $RO_2^\bullet$. Peroxy radicals can follow different reaction pathways, depending on radical concentrations in the atmosphere: 1) reaction with HO_2 and formation of hydroperoxides (ROOH), 2) reaction with NO_2 and formation of peroxynitrates ($ROONO_2$), 3) reaction with another $RO_2^\bullet$ and formation of cabonyl compounds or alcohols or an alkoxy radical $RO^\bullet$, 4) reaction with NO and formation of alkyl nitrates ($RONO_2$) or an alkoxy radical $RO^\bullet$ [Atkinson and Arey, 2003]. The products resulting from VOC oxidization are largely determined by sub-

sequent reactions of alkoxy radicals. In tropospheric conditions $RO^{\bullet}$, undergoes unimolecular decomposition, isomerization or reaction with O_2 [Seinfeld and Pandis, 2012].

Larger molecules with several carbon and hydrogen atoms iterate several times through the oxidation process with different radicals and several reaction types. As already seen in figure 2.2, reaction products include more oxygen and sometimes nitrate functional groups. These functional groups lead to heavier molecules. Hydrocarbons without any functional group are hydrophobic. By adding functional groups as hydroxyl (R-OH), carbonyl (R-C=O-R', where R' can be H), nitrite (R-ONO) and nitrate (R-ONO_2) groups, reaction products become comparably more water soluble than the initially emitted VOC. To conclude, several oxidation steps lead to functionalization of VOC, if they do not decompose, they become heavier and more water soluble [Clayden et al., 2001].

The volatility of a molecule is correlated to the carbon number, and oxidation state. This means, larger molecules with high carbon atom numbers are less volatile than smaller molecules with just few carbon atoms. Further, given the same number of carbon atoms, the molecules with more functional groups are less volatile than the ones with less or without any functional groups. In the context of atmospheric oxidation this means that VOCs which are oxidized several times lose their volatility and become sticky [Donahue et al., 2011]. A measure of the amount of oxygen in a VOC is the O:C ratio. This ratio describes the fraction of oxygen atoms to carbon atoms in a given VOC. Thus, the more oxidation steps were taken by one molecule, the higher its the O:C ratio becomes, assuming no fragmentation.

Figure 2.3 shows the relations between carbon number, O:C ratio and volatility. The formal introduction of the variable C^0 follows in the next section 2.2.1, here it is only important to know, that it represents volatility. The lower the value of $\log_{10}(C^0)$, the less volatile the

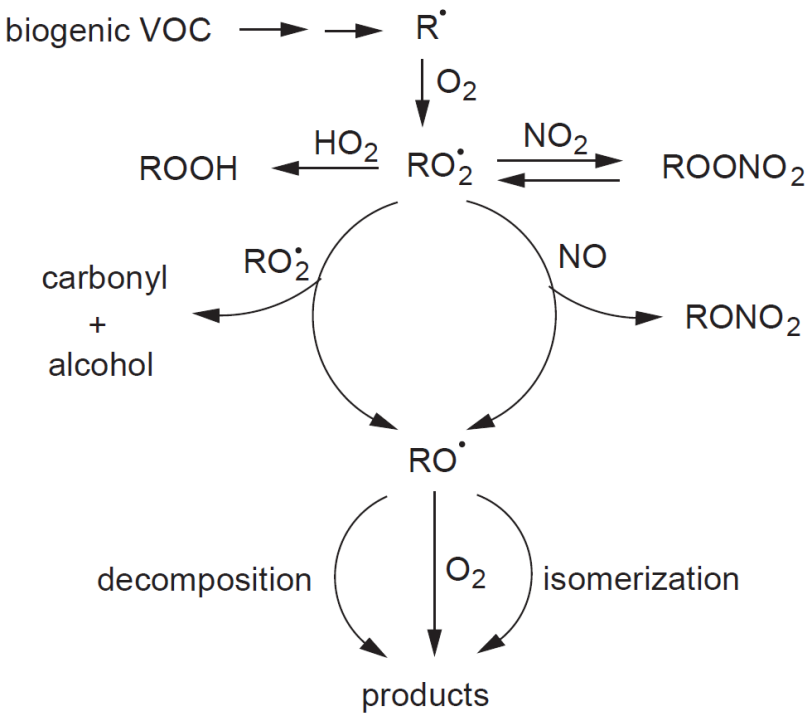

Figure 2.2.: VOC reaction mechanism scheme from Atkinson and Arey [2003].

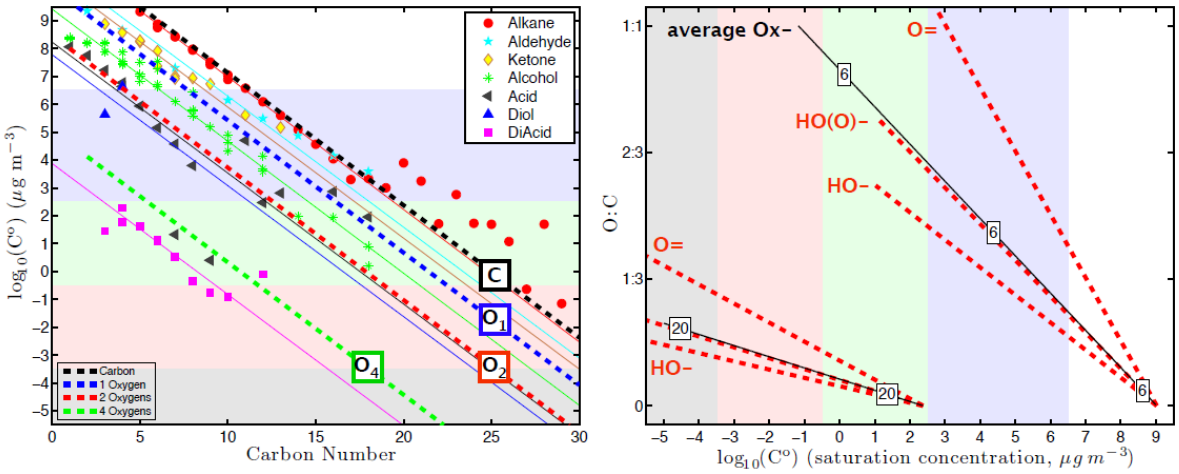

Figure 2.3.: Relation of volatility to carbon number (left, a) and O:C ratio (right, b) [Donahue et al., 2011]. Plot a) shows classes of organic compounds with the same oxygen functionality but a range of carbon numbers. The slopes show the effect of increasing carbon number, while the offset shows the impact of functionalization. Plot b) shows the effect of different functional groups on volatility with increasing O:C ratio. Two hydrocarbons, one with a C6 and a second with a C20 backbone are sown. The different slopes indicate the impact of different functional groups (carbonyl (=O), hydroxyl (-OH), acid (-(O)OH)).

compound. In figure 2.3 a), the relation between volatility and carbon number of several groups of substances is shown. The larger the carbon number of a molecule, the less volatile it is compared to molecules of lower carbon numbers within the same group of substances. Figure 2.3 a) also shows that compounds containing functional groups are less volatile than the ones with less or without functional groups. For example, alkanes with 19 carbon atoms are more volatile ($\log_{10}(C^0) = 2$) than alcohols with the same carbon atom number ($\log_{10}(C^0) = 0.5$). Figure 2.3 b) shows the relationship between O:C ratio and volatility as well as the impact of different functional groups. This time, only hydrocarbons with either 6 or 20 carbon atoms are shown. Basically, addition on any functional group to the C6 or C20 hydrocarbon leads to a decrease in volatility. There are functional groups which are more polar than others. Figure 2.3 b) shows, for example, that the addition of a highly polar hydroxyl group (HO-) leads to a steeper decrease in volatility in hydrocarbons of both sizes, compared to the addition of a cabonyl group (=O). Moreover, it can be seen that each addition of an oxygen atom increases the O:C ratio towards one. Here, unity is quickly reached by the smaller C6 molecule after an oxygen atom was added for each carbon atom, while the C20 molecule has the potential to become less volatile, because it can undergo oxidation longer [Donahue et al., 2011].

O:C ratios are usually measured in the particle-phase, but the concept holds true for any hydrocarbon. Measurements of O:C ratios help to determine the residence time of the hydrocarbons in the atmosphere, since they are oxidized at a certain speed by the mechanism discussed before. Therefore, the O:C ratio is used to distinguish between primary organic aerosol and secondary organic aerosol, since primary organic aerosol has a lower O:C ratio than secondary. This is the result of SOA formation by oxygenated VOC with higher O:C ratios than organics found in freshly emitted POA. O:C ratio measurement interpretations are limited,

since POA is also oxidized with residence time in the atmosphere and subsequently mixes with SOA. Distinguishing "aged" OA is challenging, because in-particle and gas-phase chemistry, both alter O:C ratios [Aiken et al., 2008].

2.2. Secondary organic aerosol formation

Secondary aerosol formation can take place via several gas to particle conversion processes. SOA can be composed of organic matter or a mixture of organic and inorganic matter. Nucleation forms particles with diameters less than 0.01 µm directly from gas-phase precursors [Tomasi et al., 2017], which is a process which can gain relevance in pristine regions with extremely low pre-existing aerosol concentrations. Nevertheless, on a global scale it is assumed to be of minor importance and will not be discussed here. Partitioning and reactive uptake into pre-existing particles leading to particle growth and changes in their physico-chemical properties are described in sections 2.2.1 and 2.2.2.

2.2.1. Partitioning

Partitioning describes the equilibrium state of condensation and evaporation between organic gases and airborne particles. Gas-to-particle partitioning is related to two physical processes: adsorption [Pankow, 1987] and absorption [Pankow, 1994]. While adsorption characterizes uptake of gas-phase molecules by the particle surface, absorption describes the uptake into the bulk-phase. In the atmosphere, both mechanisms can lead to the uptake of the molecule in the gas-phase, also a combination of both is possible. The following formulation of this process, using a partitioning coefficient, does not assume anything about the underlying physical processes [Pandis and Seinfeld, 2006].

The condensed mass fraction ξ_i of a compound i in the condensed phase is given by (2.1), where the total organic aerosol concentration c_{oa} and the effective saturation concentration C_i^* are required:

$$\xi_i = \left(1 + \frac{C_i^*}{c_{oa}}\right)^{-1} \tag{2.1}$$

All concentrations are usually expressed in $\mu g\,m^{-3}$ units. In equation (2.1), C_i^* expresses empirically the volatility of compound i and therefore determines the amount of c_{oa}. When $C_i^* = c_{oa}$, then $\xi_i = 0.5$, which means that 50 % of the compound i are in the particle-phase [Donahue et al., 2012]. The effective saturation concentration C_i^*, used in this equation, includes the corrections for organic mixtures and curvature effects. It is based on the saturation vapor pressure $p_i^0(T)$ of compound i which can be described by the Clausius-Clapeyron equation (2.2), assuming an ideal gas:

$$p_i^0(T) = \frac{\Delta H p_i^0}{RT} dT \tag{2.2}$$

which can be integrated around a reference Temperature T^{ref}, usually 300 K, leading to an exponential equation:

$$p_i^0(T) = p_i^0(T^{ref}) \exp\left(\frac{\Delta H}{R}\left(\frac{1}{T^{ref}} - \frac{1}{T}\right)\right) \tag{2.3}$$

Where ΔH is the enthalpy of phase transition (vaporization or sublimation, often referred as evaporation enthalpy) in kJ mol^{-1}, R the ideal gas constant 8.314 J mol^{-1} K^{-1} and the

temperature T is given in K. To link the saturation vapor pressure to a mixture of organic and inorganic compounds as usually found in atmospheric particles, the modified Raoult's law equation (2.4) is used:

$$p_i^{eq}(T) = \gamma_i x_i p_i^0(T) \tag{2.4}$$

Equation (2.4) describes equilibrium vapor pressure p_i^{eq} over a non-ideal mixture. The activity coefficient γ_i accounts for the deviations from an ideal behavior of the mixture caused by molecular interactions in the condensed phase and depends on the mixture composition and temperature. For an ideal solution with respect to i, γ_i would be equal to 1. Further, x_i is the mole fraction of i in the mixture.

Another effect of atmospheric particles influencing the saturation vapor pressure is the Kelvin effect. A curved surface alters the mechanical equilibrium between the molecules at a surface. Comparing the equilibrium vapor pressure p_i^{eq} of a flat surface to a curved one $\tilde{p}_i^{eq}$, $\tilde{p}_i^{eq}$ over a curved surface is higher than p_i^{eq} over a flat one. The Kelvin effect leads to stronger growth of larger particles, because their curved surface is flatter than the one of small particles. To correct the equilibrium vapor pressure for this effect, the Kelvin equation (2.5) is used:

$$\tilde{p}_i^{eq}(T, D_p) = p_i^{eq}(T) \exp\left(\frac{4\sigma\nu_i}{RTD_p}\right) \tag{2.5}$$

where ν_i is the molar volume of compound i, σ is the surface tension of the condensed phase surface, and D_p the diameter. Atmospheric relevance is gained for diameters D_p smaller than ~ 20 nm [Bilde et al., 2015].

Finally, correcting the saturation vapor pressure for curvature and non-ideal mixture effects, the effective saturation concentration can be calculated as follows:

$$C_i^* = \tilde{p}_i^{eq}(T, D_p)\frac{M_i}{RT} \tag{2.6}$$

where M_i is the molar mass in g mol^{-1} of the compound i. In this study, the saturation concentration is derived from the chemical structure of organic molecules, therefore another notation including the saturation mass concentration C_i^0 over the flat, ideal condensed phase is useful:

$$C_i^0 = p_i^0 \frac{M_i}{RT} \tag{2.7}$$

which can be substituted into (2.6)

$$C_i^* = \gamma_i x_i C_i^0 \exp\left(\frac{4\sigma\nu_i}{RTD_p}\right). \tag{2.8}$$

C_i^* is a descriptive variable for partitioning, because it can be evaluated for each particle individually. If the gas-phase concentration of i c_i is higher than C_i^*, condensation occurs, otherwise evaporation:

$$C_i^* < c_g \quad \text{Condensation}$$
$$C_i^* > c_g \quad \text{Evaporation}$$

Alternatively, partitioning can be described as a partitioning coefficient $K_{p,i}$ embedded in the SOA yield formulation. The partitioning coefficient $K_{p,i}$ is usually used in experimental studies [Hohaus et al., 2015] describing the SOA formation potential Y ("SOA yield") as:

$$Y = \frac{\Delta M_0}{\Delta HC} \tag{2.9}$$

where ΔM_0 is the organic aerosol mass produced and ΔHC the hydrocarbon mass that reacted, both given in $\mu g\,m^{-3}$.

$$Y = \sum_i Y_i = \Delta M_0 \sum_i \left(\frac{\alpha_i K_{p,i}}{1 + K_{p,i} \Delta M_0} \right) \tag{2.10}$$

The SOA yield depends on the pre-existing aerosol mass, stochiometric coefficients α_i and the partitioning coefficient $K_{p,i}$, which is related to the saturation concentration

$$K_{p,i} = \frac{1}{C_i^*} \tag{2.11}$$

[Hoffmann et al., 1997, Bilde et al., 2015], but will not be further discussed, because this study uses the saturation concentration formulation. The interested reader is referred to Bian and Bowman [2002].

The saturation concentration C^0 (index i omitted) can be used to characterize the volatility of a certain atmospheric organic gas. In section 2.1.1, volatile organic compounds were introduced, which are the precursors of the compounds partitioning into the particle-phase. During atmospheric oxidation, and therefore addition of functional groups, the former volatile organic compounds are transformed into less volatile compounds (section 2.1.2). Their volatility can be quantified by C^0, see Table 2.2. To indicate that the compounds are less volatile, prefixes are defined to classify the xVOC (x = I, S, L, EL). The reader should note that volatility depends on ambient conditions and properties of pre-existing aerosol. Therefore, classification of even individual compounds into the xVOC classes is not trivial and compounds can change the volatility class if ambient conditions change.

The lower C^0 of a certain compound, the more of it will be found in the particle-phase. Not only gas-phase chemistry can transform volatility, but also subsequent in-particle- or aqueous-phase reactions like oligomerization [Kanakidou et al., 2005, Hallquist et al., 2009, Donahue et al., 2012, Lin et al., 2012].

Table 2.2.: Definitions of organic compounds with varying volatility according to Donahue et al. [2012].

	Phase state under ambient conditions	Saturation concentration in $\mu g\,m^{-3}$			
VOC	Volatile Organic Compounds	$3 \cdot 10^6$	$<$	C^0	
	See section 2.1.1.	6.5	$<$	$\log_{10}(C^0)$	
IVOC	Intermediate Volatility Organic Compounds	$3 \cdot 10^2$	$<$	C^0	$< 3 \cdot 10^6$
	Almost exclusively in the gas-phase.	2.5	$<$	$\log_{10}(C^0)$	< 6.5
SVOC	Semi-volatile Organic Compound	$3 \cdot 10^{-1}$	$<$	C^0	$< 3 \cdot 10^2$
	Often have sizable	-0.5	$<$	$\log_{10}(C^0)$	< 2.5
	mass fractions in particle and gas-phase.				
LVOC	Low Volatility Organic Compounds	$3 \cdot 10^{-4}$	$<$	C^0	$< 3 \cdot 10^{-1}$
	Predominantly in particle-phase.	-3.5	$<$	$\log_{10}(C^0)$	< -0.5
ELVOC	Extremely Low Volatility Organic Compounds			C^0	$< 3 \cdot 10^{-4}$
	Almost entirely in particle-phase.			$\log_{10}(C^0)$	< -3.5

2.2.2. Reactive uptake

Reactive uptake of a trace gas by a particle leads to changes in gas-phase and particle-phase composition [Pöschl, 2005]. Here, heterogeneous reactions, i.e. chemical reactions proceeding on the particle surface, are considered. This reactive uptake depends on gas-phase diffusion of the tracer to the particle surface and is parametrized as pseudo first order loss equation (2.12) [Dentener and Crutzen, 1993, Tie et al., 2001, 2003, Alexander et al., 2009, Macintyre and Evans, 2010, Stadtler et al., 2018]:

$$\frac{d[X]_g}{dt} = -k_X[X]_g, \tag{2.12}$$

where $[X]_g$ is the tracer concentration in $\mathrm{mol\,cm^{-3}}$ and k_X the reaction rate coefficient in $\mathrm{s^{-1}}$. Gas-phase loss is proportional to the heterogeneous reaction rate coefficient k_X and the tracer concentration itself. The reaction rate coefficient k_X describes the gas-phase diffusion to the gas-particle interface and mass transport into the particle and is formulated following Schwartz [1986] as:

$$k_X = \left(\frac{r}{D_g} + \frac{4}{\bar{v}_X \gamma_X}\right)^{-1} S_a, \tag{2.13}$$

with D_g describing gas-phase diffusion, $\bar{v}_X$ as the mean molecular speed according to Maxwell-Boltzmann, the reactive uptake coefficient/reaction probability γ_X and particle related properties as particle radius r and particle surface area density S_a. For small reaction probabilities γ_X, this equation simplifies to

$$k_X = \frac{1}{4}\bar{v}_X \gamma_X S_a. \tag{2.14}$$

Therefore, the reactive uptake for small reaction probabilities is proportional to the uptake coefficient γ_X and the particle surface area density S_a. Both of these parameters are not easily estimated. The uptake coefficient depends on relative humidity, particle composition (e.g. pH value) and temperature [Evans and Jacob, 2005], and describes the mass transport from gas to particle-phase, normalized by the number of collisions per time unit. The surface area is calculated using the particle distribution and assuming spherical particles, which is a good approximation for aqueous particles, but not for solid ones (Seinfeld and Pandis [1998], see section 1).

The net reaction probability γ_X can be measurend in laboratory experiments [Wahner et al., 1998, Kleffmann et al., 1998, Thornton et al., 2003, Liggio et al., 2005b, Gross et al., 2009, Cole-Filipiak et al., 2010]. In the case of reactive uptake this net probability describes diffusion in the gas-phase, adsorption, desorption and reaction on the surface [Davidovits et al., 2006]. These processes are formulated as resistances. The trace gas X has to pass these resistances to enter into the particle-phase, see figure 2.4.

First, diffusion is formulated by a collision normalized transport coefficient Γ_{diff}, which is described by the empirical formula [Fuks and Sutugin, 1970]:

$$\frac{1}{\Gamma_{diff}} = \frac{0.75 + 0.283Kn}{Kn(1+Kn)} \tag{2.15}$$

$$Kn = \frac{\lambda}{r}, \tag{2.16}$$

where Kn is the Knudsen number defined over the mean molecular free path λ and the particle radius r. Second, the trace gas has to accommodate on the particle surface, which is described

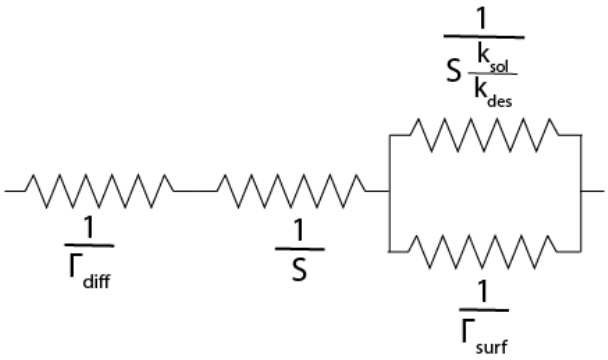

Figure 2.4.: Resistance diagram visualizing equation (2.18). Resistances describing processes on the aerosol surfaces are $\frac{1}{S}$, $\frac{1}{S\frac{k_{sol}}{k_{des}}}$ and $\frac{1}{\Gamma_{surf}}$, while $\frac{1}{\Gamma_{diff}}$ proceeds in the gas-phase.

by the mass accommodation coefficient α. Accommodation on a surface can be split into two parts, the thermal adsorption and solvation (2.17), which are also formulated as resistances

$$\frac{1}{\alpha} = \frac{1}{S} + \frac{1}{S\frac{k_{sol}}{k_{des}}}. \tag{2.17}$$

The fraction of collisions resulting on thermal accommodation is described by the adsorption coefficient S which is around 1 for a gas-liquid interface at room temperature. Accomodation depends on competing adsorption and desorption and solvation into the liquid itself. In the second part of (2.17) k_{sol} describes the rate coefficient of solvation and k_{des} the one of desorption. Finally, when trace gas X is adsorbed onto the surface, but not yet solved in the particle-phase, the reaction takes place on the surface. Using the resistance formalism, surface reaction resistance Γ_{surf} is proportional to the reaction rate between X and surface molecule. Thus, net uptake coefficient can be formulated as:

$$\frac{1}{\gamma_X} = \frac{1}{\Gamma_{diff}} + \frac{1}{S} + \frac{1}{\frac{1}{S\frac{k_{sol}}{k_{des}}} + \frac{1}{\Gamma_{surf}}} \tag{2.18}$$

Equation (2.18) is visualized in figure 2.4. The net uptake coefficient γ_X is measured in laboratory experiments and used in models to parametrize reactive uptake. In this study, reactive uptake of eight compounds is included, where two organic compounds contribute to SOA formation.

2.3. Secondary organic aerosol sinks

SOA can be lost via the particle-phase and gas-phase. The main loss process proceeds via the particle-phase, therefore this section describes wet and dry deposition focusing on the particle-phase. Furthermore, in-particle loss of organic compounds is explained.

2.3.1. Deposition

The removal of particles from the atmosphere through adsorption or absorption on solid and liquid surfaces is called deposition. There are two main classes of deposition, dry deposition and wet deposition. SOA is removed via both processes.

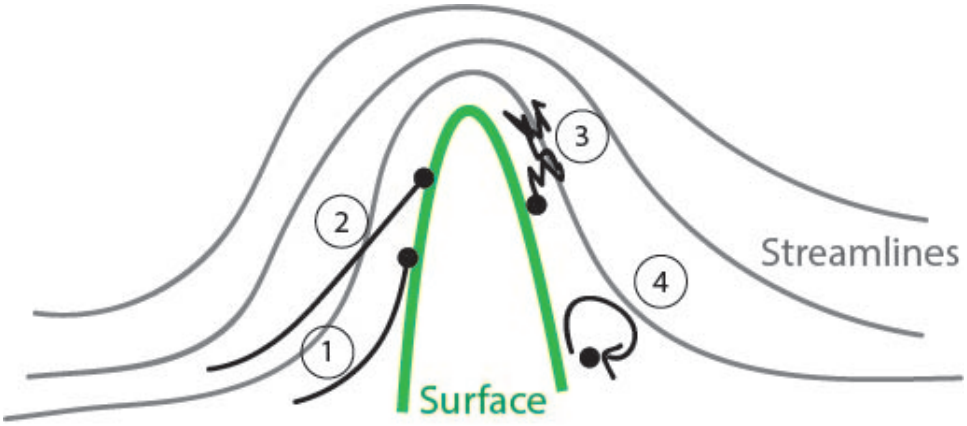

Figure 2.5.: Sketch of aerosol dry deposition on a surface caused by (1) interception, (2) impaction, (3) diffusion (Brownian motion) and (4) turbulent eddies.

Dry deposition

Particles are removed via dry deposition, if collision with a surface leads to removal of the particle from the air. The surface can be solid or liquid. It is also defined as dry deposition if particles are captured by collision by a wet surface. Therefore, the removal depends on chemical and solubility characteristics of the particle and on the roughness/nature of the surface or terrain which takes up the particle. Several micro-physical processes can lead to collision of the particle with a surface: (i) gravitational sedimentation, (ii) interception, (iii) impaction, (iv) Brownian motion (diffusion of aerosols due to random motion caused by collision with gas molecules), (v) turbulent eddies, (vi) processes based on gradients in temperature (thermophoresis), electromagnetic-fields (electrophoresis), turbulence (turbophoresis) and concentrations (diffusiophoresis). Figure 2.5 visualizes interception, impaction, diffusion and turbulent eddies leading to a collision between aerosols and a solid obstacle. Dry deposition is most efficient for large particles ($> 1\,\mu m$), which are removed quickly via sedimentation and impaction, and for very small particles ($< 0.1\,\mu m$) via Brownian diffusion. Particles of sizes between $0.1\,\mu m$ and $1\,\mu m$ are not removed efficiently by dry deposition. Their size range was named accordingly as "accumulation mode" [Pandis and Seinfeld, 2006, Tomasi et al., 2017].

Wet deposition

In contrast to dry deposition, where particles collide with liquid or solid surfaces, wet deposition describes the removal of particles scavenged exclusively by hydrometeors. Three sub-processes are involved; the aerosol has to be brought to condensed water, it must be scavenged by the hydrometeor and finally the hydrometeor has to reach Earth's surface. The total wet deposition is the sum of in-cloud ("rainout") and below-cloud ("washout") particle removal. The in-cloud scavenging describes the removal of aerosols which are either collected by cloud droplets or act as cloud condensation nuclei (CCN) or ice condensation nuclei (ICN) and then precipitate. Subsequently, the precipitation, in form of liquid rain drops or solid graupel, hail or snow, collides with aerosols which are in the air below the cloud. Several processes lead to the collection (see figure 2.5) of aerosols by the falling hydrometeors, which is mainly dependent on the hydrometeor size distribution. Depending on what kind of hydrometeor scavenges the aerosol

particles, different terms are used: precipitation scavenging, cloud interception (cloud colliding with mountain), fog deposition and snow deposition [Pandis and Seinfeld, 2006]. An overview of the connection between gases, aerosols and hydrometeors can be found in figure 2.6. Figure 2.6 shows that the uptake of particles and gases is reversible. A gas or particle can undergo uptake by cloud droplets or droplet formation several times until being removed. Nevertheless, figure 2.6 also illustrates the high complexity of wet deposition which leads to several uncertainties in the mathematical formulation. Omitted by figure 2.6 is the fact, that not only liquid hydrometeors remove aerosols, but also frozen hydrometeors like snow, hail or ice clouds. The whole spectrum of shapes and characteristics of frozen hydrometeors is complex and also introduces uncertainties in the mathematical formulation [Pandis and Seinfeld, 2006, Tomasi et al., 2017].

While nucleation scavenging, formation of cloud droplets out of aerosols acting as CCN, is very efficient, interstitial aerosol collection is slow. Particles with diameters $> 0.5\,\mu m$ usually become cloud droplets in a typical cloud. During a precipitation event, particles between the Earths surface and cloud base are collected via diffusion (small particles with diameters $< 0.1\,\mu m$) and inertial collection (particle diameters of a few µm), called below-cloud scavenging. A falling drop is approximately shaped like a cylinder. Its volume can be calculated as a function of the falling drop diameter a_f and the falling velocity u_f of the rain drop, $\frac{\pi}{4} a_f^2 u_f(a_f)$. Moreover, the aerosol particle diameter a and particle velocity $u(a)$ have to be included into the volume within which particles can be collected, leading to a collection volume depended of both, particle

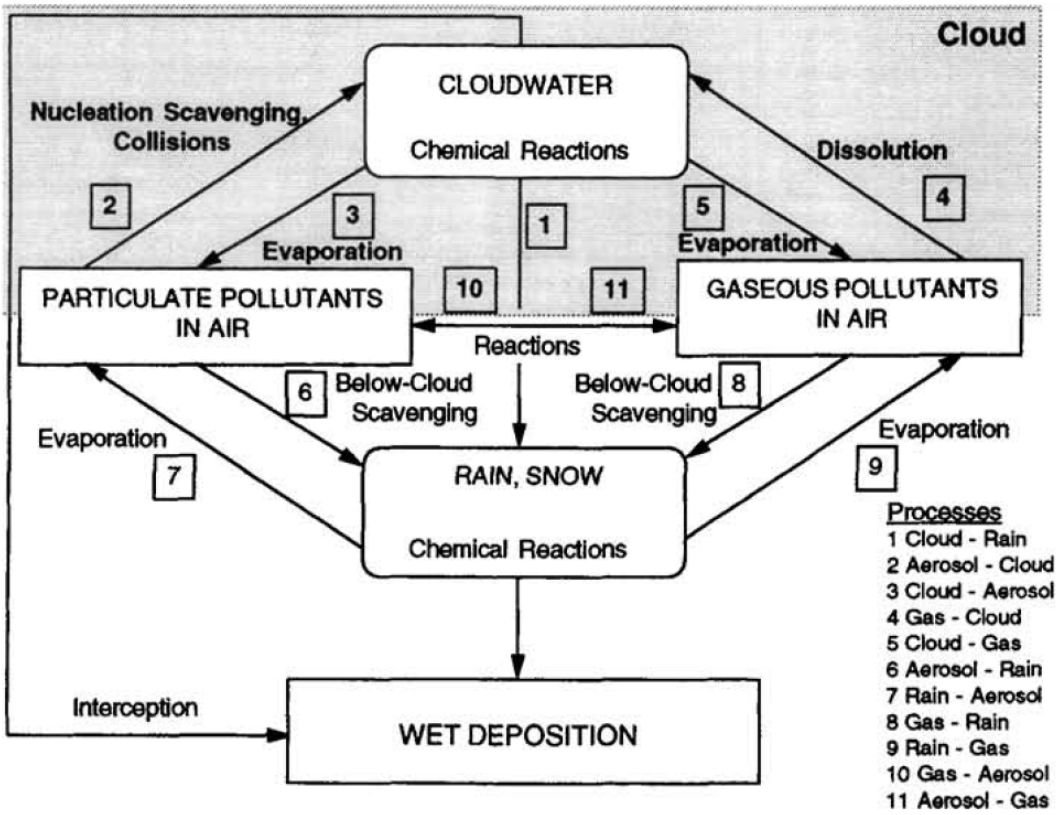

Figure 2.6.: Conceptual framework of wet deposition process from Pandis and Seinfeld [2006].

and raindrop diameter, $\frac{\pi}{4}(a_f + a)^2(u_f(a_f) - u(a))$. Falling raindrops perturb the streamlines of aerosols particles heading for a collision, thus not all particles are collected [Tomasi et al., 2017]. Therefore, a collision efficiency $E(a, a_f)$ is defined as a correction factor. $E(a, a_f)$ could theoretically be predicted solving the Navier-Stokes equation for a general raindrop-aerosol, which is impracticable. Therefore, semi-empirical correlations are used, exploiting that the collision efficiency is usually $\ll 1$ [Pandis and Seinfeld, 2006]. Finally, a below-scavenging rate can be defined as:

$$\frac{dM}{dt} = -\Lambda(a, a_f)M(a) \tag{2.19}$$

where $M(a)$ is the mass concentration size distribution of the aerosols and $\Lambda(a, a_f)$ the scavenging coefficient depending on the particle diameter a and raindrop diameter a_f as in equation (2.20).

$$\Lambda(a, a_f) = \int_0^\infty \left(\frac{\pi}{4}\right) a_f^2 u_f(a_f) E_{col}(a, a_f) N(a_f) da_f \tag{2.20}$$

Equation (2.20) includes the falling raindrop size distribution $N(a_f)$, which is connected to the rainfall rate R equation (2.21), which can be measured. The evaluation of the rainfall rate to obtain the falling raindrop size distribution is challenging since it varies in space and time even during a single precipitation event.

$$R = \int_0^\infty \left(\frac{\pi}{6}\right) a_f^3 u_f(a_f) N(a_f) da_f \tag{2.21}$$

Assuming the same diameter a_f for all raindrops, the scavenging coefficient just depends on particle diameter. Figure 2.7 shows the scavenging coefficient for monodispersed aerosols collected by monodispersed raindrops with diameter of 0.2 and 2 mm assuming a rainfall intensitiy of $1\,\mathrm{mm\,h^{-1}}$. Thus, a mean scanning coefficient can be defined:

$$\Lambda_m(a) = \frac{\int_0^\infty \Lambda(a) a^3 n(a) da}{\int_0^\infty a^3 n(a) da} \tag{2.22}$$

where $n(a)$ is the aerosol number distribution. Using the mean scavenging coefficient $\Lambda_m(a)$ in equation (2.19) leads to an equation hiding a high complexity in one parameter, the scavenging coefficient [Tomasi et al., 2017]. Scavenging coefficients vary within orders of magnitude depending on raindrop and particle distributions which makes it a highly uncertain parameter and one has to be aware of its physical meaning and limitations [Pandis and Seinfeld, 2006]. Neither raindrop nor aerosol size distributions are easily measurable [Peters et al., 1993, Brandes et al., 2002, Tokay et al., 2001, Cao and Zhang, 2009].

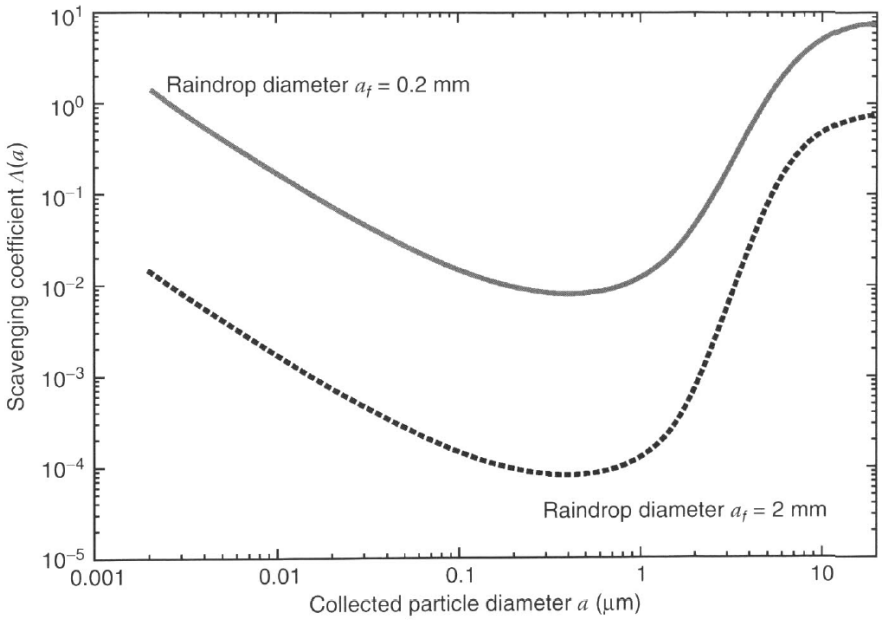

Figure 2.7.: Scavenging coefficient as a function of aerosol diameter. Particles and raindrops have monodisperse distributions. Two raindrop diameters are shown, 0.2 mm and 2 mm. A rainfall intensity of 1 mm h^{-1} is assumed. Graph taken from Tomasi et al. [2017].

2.3.2. In-particle fragmentation

In-particle fragmentation is defined as the decay of organic molecules via energy uptake. In the atmosphere, two types of energy can lead to molecule fragmentation: thermal energy and ultra violet radiation energy (photolysis). Breaking the chemical bonds of organic molecules leads to smaller fragments of these molecules and formation of radicals in the particle-phase [Henry and Donahue, 2012]. These radicals attack other molecules in the particle, which can either again lead to fragmentation or to functionalization [Kroll et al., 2009].

Recently, in-particle photolysis of highly oxidized organic compounds was identified as potential SOA sink [Kroll et al., 2009]. Photolysis leads to smaller molecules that are more volatile and evaporate, reducing the SOA mass [Kroll et al., 2009]. More functionalized organic compounds are more photo-labile and more susceptible to fragmentation via reaction with the OH radical [Kroll et al., 2009, Henry and Donahue, 2012, Malecha and Nizkorodov, 2016]. Especially peroxides and carbonyls undergo in-particle photolysis [Henry and Donahue, 2012, Epstein et al., 2014] and a decrease in oligomers was found in aqueous particles [Bateman et al., 2011]. Products from photolysis are organic acids, reducing the pH value of the particle and altering its physico-chemical properties [Bateman et al., 2011]. Another particle property is its oxidation state, described by the ratio of carbon atoms to oxygen atoms in the organic-phase (O:C ratio), and measured by aerosol mass spectrometry [Canagaratna et al., 2015]. Photolysis increases the O:C ratio monotonically, even if SOA mass is reduced which means that in-particle photolysis leads to loss of carbon in the particle [Kroll et al., 2009, Ervens et al., 2011]. In-particle photolysis depends on the physico-chemical properties of the individual particle determined by its composition and phase-state. Lignell et al. [2014] found that photolysis of 2,4-dinitrophenol

depends on the viscosity of the surrounding dry organic material enhancing 2,4-dinitrophenol photolysis. Dry organic aerosol is an amorph state, which might also inhibit photolysis. This has been observed for stratospheric particles [Lignell et al., 2014]. The photolysis rate of wet aerosol depends on relative humidity. With increasing relative humidity, also photolysis is enhanced [Wong et al., 2014]. Nevertheless, these single laboratory studies do not unify to a solid theory yet and the in-particle loss, transformation or even formation is still poorly constrained [Daumit et al., 2015]. In terms of atmospheric relevance, the photolysis lifetimes of organic particles are estimated to be between some hours and days [Bateman et al., 2011, Epstein et al., 2014, Wong et al., 2014]. Therefore, in-particle fragmentation via photolysis is a SOA sink which is usually ignored by global models [Hodzic et al., 2015].

2.4. Isoprene as a SOA precursor

The scientific exploration of SOA formation and SOA precursors neglected isoprene as a SOA precursor for several years. It was assumed that there is no SOA from isoprene, because isoprene itself and its first generation products are too volatile to partition into the particle-phase. Nevertheless, isoprene chemistry is highly complex and still not fully understood. Claeys et al. [2004] were the first ones pointing to isoprene as a relevant precursor under pristine conditions. Several experimetal studies followed (see following paragraphs) to explain isoprene oxidation and formation of iSOA precursors. Thus, in the present study the focus lies on isoprene SOA (iSOA) formation. The following section describes the current knowledge about the isoprene oxidation mechanism and oxidation products relevant for iSOA formation.

2.4.1. Isoprene oxidation

Isoprene (2-methyl-1,3-butadien) is a colorless, easily inflammable liquid, which forms an explosive mixture with air in standard conditions. Its melting point lies at -146° C and its boiling point at 34° C. At 20° C it has a density of $0.68\,\mathrm{g\,cm^{-3}}$. Isoprene is poorly soluble in water [Stoffdatenbank, 2006]. As described in Section 2.1.1, isoprene is the non-methane VOC with the largest emission source strength in the atmosphere [Jenkin et al., 2015] and is therefore considered the most important biogenic hydrocarbon [Seinfeld and Pandis, 2012]. Isoprene is susceptible to oxidation by O_3 and NO_3 because of its double bonds, as well as to reaction with OH radicals. Combining the rate constants of these reactions with typical tropospheric concentrations, atmospheric lifetimes for isoprene related to the different radicals are calculated, see Table 2.3. Table 2.3 shows that during day time isoprene oxidation proceeds almost entirely via addition of the OH radical, because of its high reaction rate constant, while the nitrate radical gains importance during night time [Seinfeld and Pandis, 2012]. The reaction rate constant of isoprene oxidation by ozone is orders of magnitude lower than reaction rate constant of isoprene oxidation by OH or NO_3, but atmospheric ozone concentration is much higher leading to some isoprene oxidation by ozone on a smaller scale.

Table 2.3.: Isoprene lifetimes for the reactions with the main oxidants. Lifetimes were calculated using average concentrations [molec cm^{-3}] and reaction rates [cm^3 s^{-1}molec^{-1}] at 300 K as follows: $k_{OH}(300\,K) = 9.92 \cdot 10^{-11}$ and [OH] = $2.0 \cdot 10^6$ daytime average, $k_{O_3}(300\,K) = 1.27 \cdot 10^{-17}$ and [O_3] =$7.0 \cdot 10^{11}$, $k_{NO_3}(300\,K) = 6.94 \cdot 10^{-13}$ and [NO_3] = $2.5 \cdot 10^8$ from Atkinson and Arey [2003].

Atmospheric lifetimes		
OH	NO_3	O_3
1.4 h	1.6 h	1.3 days

Isoprene oxidation pathways and products are studied theoretically and experimentally via kinetics [Gutbrod et al., 1997, Zhang et al., 2002, Eddingsaas et al., 2010], in chamber experiments [Karl et al., 2004, 2006, Surratt et al., 2007, Liu et al., 2016], which are then applied to field measurements [Tan et al., 2001, Martinez et al., 2003, Ren et al., 2008, Murphy et al., 2012] to formulate reaction chains. Jenkin et al. [2015] describe the current isoprene oxidation including 1926 reactions of 602 isoprene derived species in the Master Chemical Mechanism (MCM).

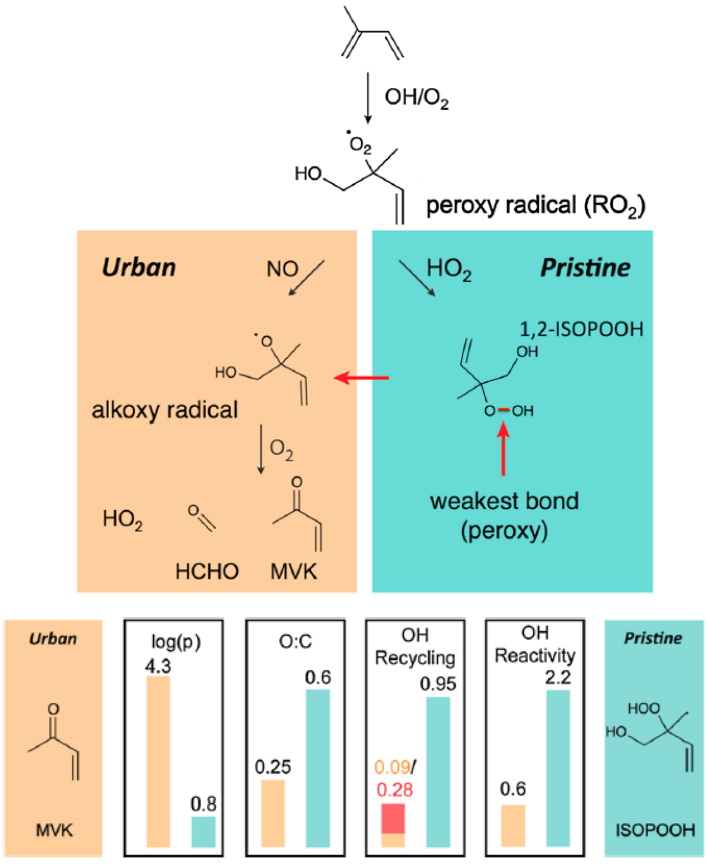

Figure 2.8.: Proposed mechanisms by Rivera-Rios et al. [2014] for high-NO_x conditions (light-brown) and pristine low-NO_x conditions (blue). The lower sketch summarized chemical and physical properties of both systems with the same color coding.

This mechanism is still under construction, because state-of-the-art measurement techniques do not allow the identification of each molecule and its molecular structure [Hallquist et al., 2009, Stark et al., 2017]. Especially the differences of the isoprene oxidation pathways under urban and pristine conditions currently attracts scientific attention, because the products show major differences in their chemical and physical properties [Rivera-Rios et al., 2014]. The main differences found by Rivera-Rios et al. [2014] are shown in figure 2.8, where it can be seen that urban conditions lead to alkoxy radical formation, while pristine conditions lead to isoprene hydroxy hydroperoxides (ISOPOOH). Both intermediates react further; in urban conditions the alkoxy radical forms formaldehyde (HCHO) and methyl vinyl ketone (MVK), while in pristine environments ISOPOOH forms isoprene epoxides (IEPOX) and highly oxidized molecules (sections 2.4.3 and 2.4.4). Isoprene products from the pristine environment are more oxidized (higher O:C ratio) and less volatile (low $\log(p)$). Therefore, isoprene secondary organic aerosol formation is favored in pristine environments and it is claimed that NO_x (= NO + NO_2) suppresses iSOA formation [Surratt et al., 2006, D'Ambro et al., 2017a], because oxidation products are smaller and more volatile. In both cases iSOA is formed, but the iSOA composition differs. An overview over isoprene oxidation products capable of iSOA formation is given in figure 2.9. The present study focuses on several isoprene products important for iSOA formation, the following paragraphs present these compounds and their formation.

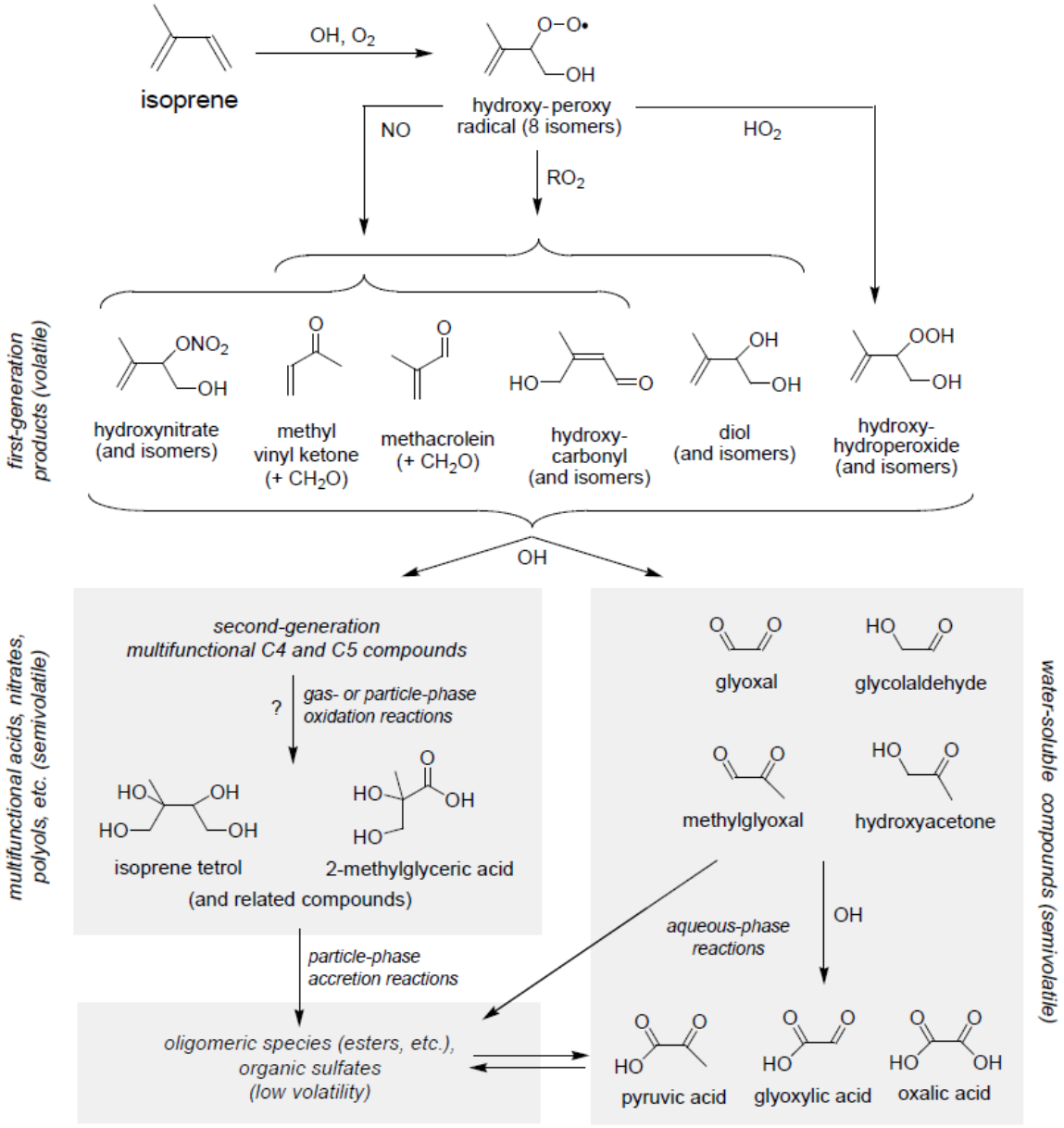

Figure 2.9.: Oxidation pathways of isoprene leading to SOA formation from Carlton et al. [2009].

2.4.2. Isoprene derived glyoxal

Glyoxal (Ethanedial) is a yellow liquid which evaporates to a green gas in standard conditions. Its melting point lies at 15° C and its boiling point at 51° C. At 15° C it has a density of $1.14\,\mathrm{g\,cm^{-3}}$ [Kohlpaintner et al., 2000]. The small α-dicarbonyl [Pandis and Seinfeld, 2006] glyoxal is emitted directly into the atmosphere, because it is a precursor for several industrial processes and it is emitted by the transportation sector [Stavrakou et al., 2009]. Moreover, it is produced in the atmosphere by oxidation of a variety of hydrocarbons. From the total glyoxal sources, which are estimated to be around $45\,\mathrm{Tg\,a^{-1}}$ [Fu et al., 2008], the main source is attributed to isoprene. How much of glyoxal is derived from isoprene varies by region between 28 % to 74 % [Fu et al., 2008, Washenfelder et al., 2011, Knote et al., 2014]. Finally, glyoxal is also transformed chemically and lost due to deposition, leading to a lifetime in the range of hours [Ervens and Volkamer, 2010], Fu et al. [2008] report a value of 2.9 h.

In figure 2.9 glyoxal formation from isoprene oxidation is sketched. Glyoxal is a as a second and third generation product [Yu et al., 1995, Washenfelder et al., 2011]. Isoprene products leading to glyoxal formation are methacrolein, hydroxy methacrolein, 4-hydroxy-2-methyl-2-butenal, methacrolein, 4-hydroxy-3-methyl-2-butenal and methyl vinyl ketone [Zimmermann and Poppe, 1996].

The small α-dicarbonyl glyoxal is highly soluble and volatile, therefore classical condensation on pre-existing particles is inefficient, but SOA formation can proceed via the aqueous-phase [Lim et al., 2005]. In clouds, glyoxal easily dissolves and forms oxalic acid, which stays in the cloud droplet after evaporation, thus leading to SOA formation [Lim et al., 2005]. The yield for the transformation of glyoxal to oxalic acid was measured between 1 and 2 % [Carlton et al., 2007]. Other SOA formation pathways are reversible and irreversible uptake onto aqueous particles [Fu et al., 2008]. Glyoxal dissolves in the aqueous-phase and undergoes oligomerization forming monomers, dimers and organosulfates [Liggio et al., 2005a,b]. This process is likely acid catalyzed [Liggio et al., 2005a,b, Fu et al., 2008, Knote et al., 2014], depends on ultra violet radiation [Washenfelder et al., 2011] and on particle salt concentration [Knote et al., 2014]. Once oxalic acid, monomers, oligomers or organosulfates are formed, they are not released back into the gas-phase, which means that overall evaporation is small, characterizing glyoxal as SOA precursor.

In summary, glyoxal is a volatile molecule which can form SOA undergoing in-particle processing.

2.4.3. Isoprene epoxides

There are three isomeric structures of isoprene epoxides found in the atmosphere, IEPOXA (2-(2-oxiranyl)-1,2-propanediol), IEPOXB (2-methyloxirane-2,3-dimethanol) and IEPOXC (1-(2-methyl-2-oxiranyl)-1,2-ethanediol). In atmospheric chemistry, usually all isoprene epoxides are addressed as IEPOX, although it is mainly IEPOXB. IEPOXB (also β-IEPOX), is the most abundant one, contributing 95 % to total IEPOX [Jenkin et al., 2015]. It is a colorless oil with a density of $1.3\,\mathrm{g\,cm^{-3}}$, a boiling point at $(243.9° \pm 10.0)°$ C [ChemSpider, accessed 01.03.2018] and a volatility which characterizes it as not condensing quickly under atmospheric conditions. IEPOX is not directly emitted into the atmosphere, but formed during isoprene oxidation. Figure 2.9 shows the initial steps for IEPOX formation. The OH initiated isoprene oxidation reaction leads to eight different hydroxy-peroxy radicals, which also react with HO_2 leading to hydroxy hydroperoxide (ISOPOOH) formation. Further oxidation of ISOPOOH

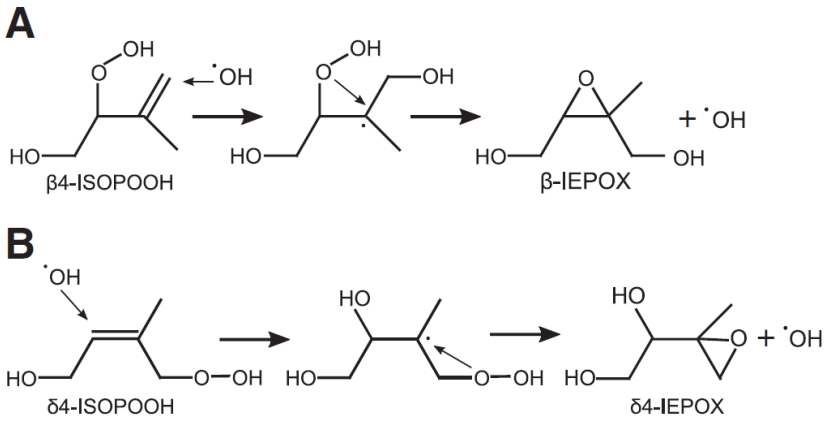

Figure 2.10.: IEPOX formation [Paulot et al., 2009].

with OH leads to unknown products described as "second-generation multifunctional C4 and C5 compounds" by Carlton et al. [2009]. Later in 2009 Paulot et al. [2009] found a mechanism to form IEPOX in the gas-phase, shown in figure 2.10. ISOPOOH is oxidized by OH and undergoes isomerization to form the characteristic ring approximating an equilateral triangle. 70 % of isoprene is oxidized to ISOPOOH in pristine environments and 75 % of ISOPOOH is oxidized to IEPOX [Eddingsaas et al., 2010]. The global total IEPOX source strength is estimated to be $(95 \pm 45)\,\mathrm{TgC\,a^{-1}}$ [Paulot et al., 2009]. In figure 2.1 an annual SOA source between 510 and $910\,\mathrm{TgC\,a^{-1}}$ is estimated. If a yield of 20 % [Lin et al., 2013] of IEPOX forming SOA is used, $(19 \pm 9)\,\mathrm{TgC\,a^{-1}}$ up to 5 % of total SOA could originate from IEPOX.

Figure 2.9 was created based on ambient measurements showing isoprene tetrol in the particle-phase. This was interpreted as evidence of iSOA formation before IEPOX formation was explained later in 2009. Claeys et al. [2004] observed particle-phase 2-methylthreitol and 2-methylerythritol in the Amazonian rain forest and further field and laboratory measurements confirm these observations [Eddingsaas et al., 2010, Budisulistiorini et al., 2015, Hu et al., 2015, Sá et al., 2017]. The missing step between gas-phase IEPOX and particle-phase isoprene tetrol formation is not fully closed yet. A first explanation is given by Eddingsaas et al. [2010], who propose an acid catalyzed ring opening reaction in the aqueous-phase (see figure 2.11 A-1 and A-2 mechanisms). Based on this hypothesis, further studies investigated the dependence of IEPOX-SOA formation and observed reactive uptake coefficients on aerosol pH [Pye et al., 2013, Gaston et al., 2014, Riedel et al., 2015]. Xu et al. [2015] claim that statistical analysis of ambient measurements does not support pH value dependence, but a dependence on sulfate aerosol. Indeed, laboratory studies usually use sulfate aerosols as acidic seeds, so this question is not answered yet. The possible mechanisms are shown in figure 2.11, it can also be seen that IEPOX might be an explanation for organosulfates.

To summarize, IEPOX is too volatile to partition into the particle-phase, but products from IEPOX oxidation (isoprene tetrols, oligomeric structures) have been found in the particle-phase. It is unclear which mechanism leads to isoprene tetrol formation, it might be depending on aerosol pH or aerosol sulfate content. Further study is needed to explore the IEPOX-SOA formation process.

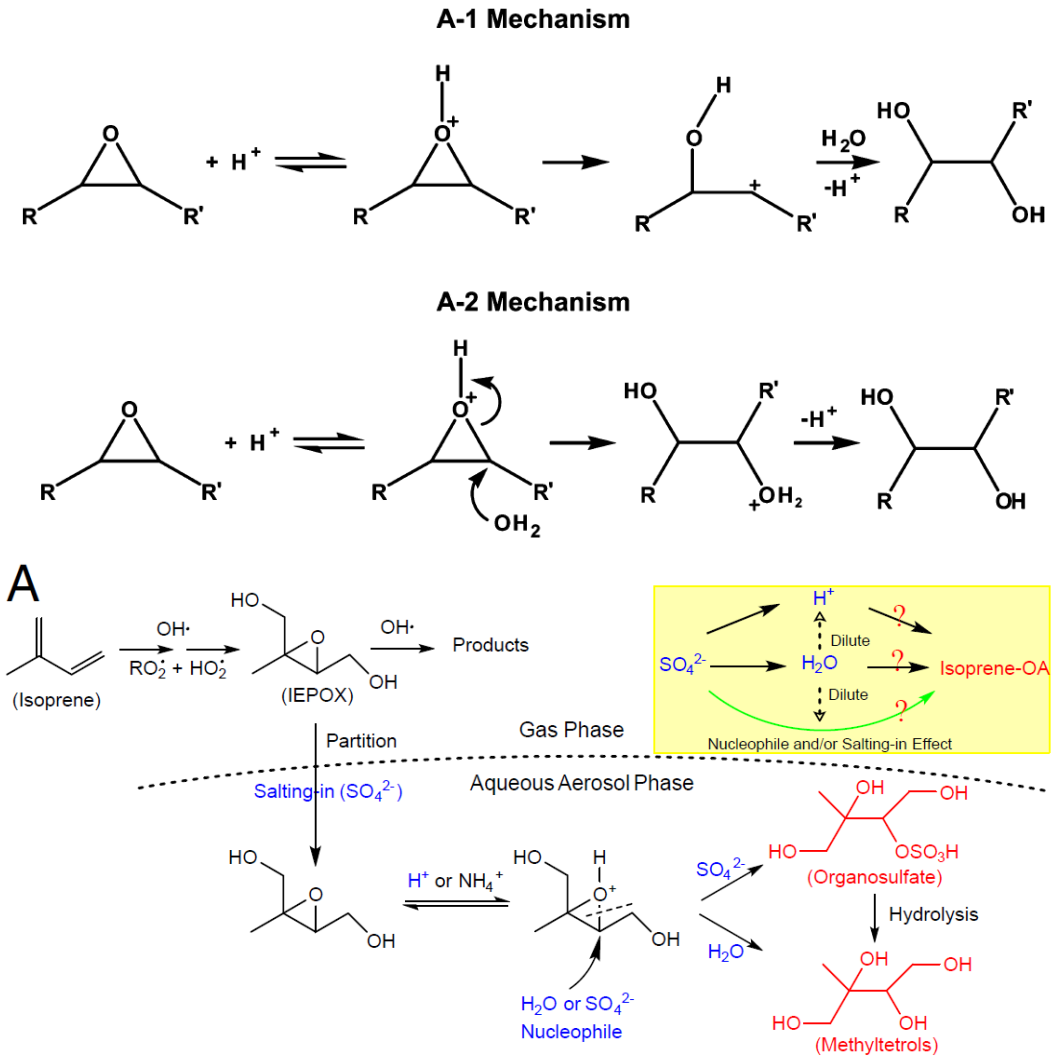

Figure 2.11.: Possible isoprene tetrol formation pathways. On the top the two acid catalyzed mechanisms A-1 and A-2 are shown proposed by Eddingsaas et al. [2010]. On the bottom the competing mechanism A based on field observations by Xu et al. [2015] is shown.

2.4.4. Isoprene dihydroxy dihydroperoxide

Recent experimental studies explored a non-IEPOX-SOA formation pathway via production of a highly oxidized molecule called dihydroxy dihydroperoxide ISOP(OOH)2. Like IEPOX, ISOP(OOH)2 is formed from ISOPOOH oxidation, see figure 2.12 [Riva et al., 2016, Liu et al., 2016, Berndt et al., 2016, D'Ambro et al., 2017a]. D'Ambro et al. [2017a] identified in an experimental study ISOP(OOH)2 as a major isoprene SOA component, which is formed in pristine conditions, where NO_x concentrations are low and ISOPOOH is mainly oxidized by HO_x (= OH + HO_2) [Liu et al., 2016, Berndt et al., 2016]. Chemical formation of ISOPOOH and subsequent oxidation to ISOP(OOH)2 require oxidation by OH and HO_2. Liu et al. [2016]

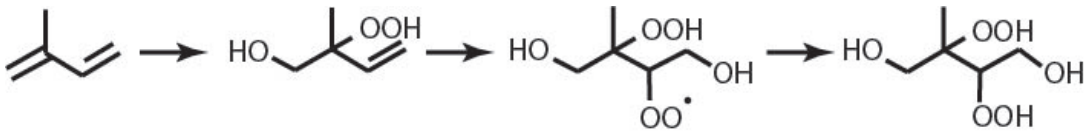

Figure 2.12.: Sketch ISOP(OOH)2 formation based on Scheme 1 in D'Ambro et al. [2017a].

report a SOA mass yield from ISOP(OOH)2 of 15 % on neutral aerosol, which drops to 3 % when high NO_x was mixed into the system. Further, ISOP(OOH)2 formation efficiency was observed to be dependent on relative humidity in experiments, using aerosol seeds. A lower relative humidity resulted in more ISOP(OOH)2 with less IEPOX formation [Riva et al., 2016]. Berndt et al. [2016] estimated the atmospheric relevance of ISOP(OOH)2 using isoprene emissions and ISOP(OOH)2 chemical formation rate. They estimate an annual ISOP(OOH)2 source strength of 16 to 35 GgC. From the multifunctional structure of ISOP(OOH)2, it is expected that it is highly soluble in water, thus it is removed by deposition. Further, D'Ambro et al. [2017a] observed in-particle decay of ISOP(OOH)2 with a half-life of 4 h. This is also observed for other hydoperoxides from monoterpenes [Krapf et al., 2016].

In summary, ISOP(OOH)2 was recently identified and found in the particle-phase. ISOP(OOH)2 has a sufficiently low volatility to efficiently partition into the particle-phase, where it decomposes.

3. Model system ECHAM-HAMMOZ

In order to simulate secondary organic aerosol formation with an explicit approach, the aerosol chemistry climate model system ECHAM-HAMMOZ was updated. The base version ECHAM6.3-HAM2.3MOZ1.0 is used [Schultz et al., 2017]. This model framework consists of three coupled models, the sixth generation, general circulation model ECHAM6 [Stevens et al., 2013], the Hamburg Aerosol Model HAM and the chemistry model MOZ [Stein et al., 2012]. HAM aerosol micro-physics can be calculated with two different modules, either the modal approach M7 [Vignati et al., 2004] or with the Sectional Aerosol module for Large Scale Applications SALSA [Kokkola et al., 2008, Bergman et al., 2012, Kokkola et al., 2018]. The coupling for SOA formation was developed for the sectional approach SALSA using an extended chemical mechanism in MOZ. A detailed description of the HAMMOZ model system can be found in Schultz et al. [2017]. Please note that Schultz et al. [2017] use the HAM configuration with M7 and a slightly smaller chemical mechanism. Additional to the normal HAMMOZ model system, SALSA is extended [Kühn et al., in preparation] to partition organic trace gases simulated by MOZ between the gas and aerosol-phases and organic reactive uptake is implemented [Stadtler et al., 2017]. Emissions of volatile organic compounds needed here, are provided by the plant emission model MEGAN (Model of Emissions of Gases and Aerosols from Nature) [Guenther et al., 2006, Henrot et al., 2017]. Model description and results were already published in Stadtler et al. [2017].

3.1. ECHAM6

The general circulation model (GCM) ECHAM6, subversion 3, in its sixth generation has been developed by the Max Planck Institute for Meteorology in Hamburg, Germany and is based on the European Center for Medium Range Weather Forecasts (ECMWF) model [Roeckner et al., 1996, Stevens et al., 2013]. ECHAM uses a spectral dynamical core consisting of the primitive equations, which are solved via spherical harmonics for vorticity, divergence temperature and surface pressure. An associated Gaussian grid is used to determine adiabatic processes such as convection, turbulence, diffusion and gravity waves. For the vertical discretization, a hybrid sigma-pressure, terrain following coordinate system is applied [Phillips, 1957, Giorgetta et al., 2006, Manzini et al., 2006].

Transport of trace components like water vapor, cloud liquid water and cloud ice is performed with the flux-form semi-Lagrangian scheme on the regular Gaussian grid [Eliasen et al., 1970, Machenhauer and Rasmussen, 1972, Lin and Rood, 1996]. For turbulent mixing the total flow is separated into the mean-flow and the unresolved turbulent eddies. This results in turbulent kinetic energy for momentum exchange between the atmosphere and the surface [Brinkop and Roeckner, 1995]. Moist convection and convective transport are parameterized according to Tiedtke [1989] with modifications by Nordeng [1994] and Möbis and Stevens [2012]. To derive stratiform clouds diagnostically, a relative humidity threshold [Sundqvist et al., 1989] is used. In contrast to stratiform clouds, cloud water and cloud ice are treated prognostically [Lohmann and Roeckner, 1996]. Cloud droplet number concentration is calculated explicitly

as a function of aerosol activation when ECHAM is coupled to HAMMOZ [Lohmann et al., 2007, Lohmann and Hoose, 2009]. The rapid and accurate radiative transfer model (RRTM-G) [Iacono et al., 2008] is used for radiative transfer calculations, using every two hour updated optical properties. The RRTM-short wave is based on 14 spectral bands and RRTM-long wave has 16 spectral bands [Giorgetta et al., 2012]. Instead of using climatological fields of these optical properties, ECHAM-HAMMOZ uses the prognostic tracer concentrations of gases and aerosols for scattering and absorption [Schultz et al., 2017]. The parameterization of the surface albedo follows Brovkin et al. [2013] and cloud scattering is calculated according to Mie theory. To account for three-dimensional effects, a maximum-random cloud overlap and an inhomogeneity parameter are used. JSBACH is the land vegetation model coupled to ECHAM, which uses 12 plant functional types and two types of bare surface to model surface processes [Reick et al., 2013]. Soil temperatures and hydrology are modeled in an updated five-layer scheme [Stevens et al., 2013, Hagemann and Stacke, 2015].

3.2. HAM

The Hamburg Aerosol Model (HAM) [Stier et al., 2005] is a component of the global climate model ECHAM and designed to investigate aerosol-climate interactions. HAM is driven by meteorological conditions provided by ECHAM. These conditions include humidity, pressure, temperature and wind, convective and turbulent transport. HAM provides feedback to ECHAM by modifying cloud micro-physics and radiative transfer. This two-moment scheme [Lohmann et al., 2007] provides links between the simulated aerosol population and the number concentrations of cloud droplet and ice crystal via aerosol activation and ice nucleation parameterizations. Prognostic variables are cloud droplet number concentration (CDNC) and ice crystal number concentration (ICNC) [Lohmann and Hoose, 2009]. Radiative properties of aerosols are computed dynamically in the model, considering both the longwave and shortwave effects of aerosols [Stier et al., 2007]. HAM predicts the evolution of five different types of atmospheric particles: sulfate (SU), black carbon (BC), particulate organic matter (OC), sea salt (SS) and mineral dust (DU). The aerosol composition and size distribution can be simulated with two different schemes, M7 and SALSA, but HAM hosts both models in a way that treatment of emissions and deposition are harmonized. Emissions of dust and sea salt are calculated interactively as function of the 10 m wind speed [Monahan et al., 1986, Tegen et al., 2002]. Also biogenic marine emissions of dimethyl sulfide (DMS), a precursor of sulfate aerosol, are calculated online [Nightingale et al., 2000, Kettle and Andreae, 2000]. Emissions of terrestrial DMS, sulfur dioxide, particulate sulfate, black carbon and organic matter are prescribed [Dentener et al., 2006]. If MOZ is not coupled, climatological monthly mean mixing ratios of oxidants (O_3, OH, H_2O_2, NO_2, and NO_3) are used in HAM to calculate sulfur chemistry for sulfate aerosol formation [Feichter et al., 1996]. Deposition in HAM covers dry deposition, wet deposition and sedimentation. These are parameterized as functions of particle size, composition and mixing state, as well as the meteorological conditions. Dry deposition is computed as the product of tracer concentration, deposition velocity and air density, calculated for each of the surface types considered in ECHAM [Ganzeveld et al., 1998]. Sedimentation of a single particle is described by the Stokes theory [Seinfeld and Pandis, 1998]. Wet deposition in HAM consists of in-cloud and below-cloud scavenging as described in section 2.3.1. In ECHAM-HAMMOZ, especially wet depsosition is a major removal process for SOA. Thus, it is described more detailed in the following paragraphs.

Table 3.1.: Parameter R_i for cloud scavenging of SALSA aerosol bins [Bergman et al., 2012]. A visualization of the sub-ranges and corresponding aerosol types is shown in figure 3.1.

Sub-range	Stratiform liquid	Stratiform mixed	Stratifrom ice	Convective mixed
1a1	0.10	0.10	0.10	0.20
1a2 - 1a3	0.25	0.40	0.10	0.60
2a1 - 2a4	0.85	0.75	0.10	0.99
2b1 - 2b4	0.20	0.10	0.10	0.20
2a5 - 2a7	0.99	0.75	0.10	0.99
2b5 - 2b7	0.40	0.40	0.10	0.40

Wet deposition in HAM distinguishes scavenging by stratiform and convective clouds. The partitioning between the air and cloud water is prescribed by a cloud-type, size- and composition-dependent scavenging parameter R_i. R_i describes the fraction of the tracer embedded in the cloud water/ice and can be found in table 3.1. The change in tracer mixing ratio c_i by stratiform cloud scavenging is calculated as:

$$\frac{\overline{\Delta c_i}}{\Delta t} = \frac{R_i c_i f^{cl}}{c_{wat}} \left(\frac{Q^{liq}}{f^{liq}} + \frac{Q^{ice}}{f^{ice}} \right) \tag{3.1}$$

where c_{wat} is the total cloud water mixing ratio, f^{cl} is the cloud fraction, f^{liq} and f^{ice} are the liquid and ice fraction of the cloud water and Q^{liq} and Q^{ice} are the sum of conversion rates of cloud liquid water and ice to precipitation via accretion, aggregation and auto-conversion.

To calculate the convective scavenging, convective tracer fluxes have to be adjusted by wet deposition. In a convective updraft, tracer mixing ratio in the liquid c_i^{liq} or ice c_i^{ice} phase is proportional to the corresponding f^{liq} and f^{ice} liquid and ice fraction of the cloud water. Therefore, the change in the updraft can be calculated as:

$$\Delta c_i = \Delta c_i^{liq} + \Delta c_i^{ice} = c_i^{liq} R_i E^{liq} + c_i^{ice} R_i E^{ice} \tag{3.2}$$

where E^{liq} and E^{ice} are the fractions of updraft liquid water and ice water, which are converted into precipitation during one time step. The local Δc_i can be used to calculate the mean deposition flux $\overline{F_i^{dep}}$ as in equation (3.3), which is needed to compute the tracer tendency.

$$\overline{F_i^{dep}} = \Delta c_i \overline{F^{up}} \tag{3.3}$$

$\overline{F^{up}}$ is the mean updraft mass flux for the grid box. Since a non-negligible fraction of precipitation does not reach the ground, but re-evaporates, an integrated deposition flux $\overline{F_i^{dep}}^{int}$ is needed which is proportional to the re-evaporation. Therefore, f^{evap} describes the evaporating fraction of precipitation in equation (3.4).

$$\overline{F_i^{dep}}^{int} = \overline{F_i^{dep}} f^{evap} \tag{3.4}$$

Finally, the tracer tendency is computed as:

$$\frac{\overline{\Delta c_i}}{\Delta t} = \overline{F_i^{dep}} \frac{g}{\Delta p} \tag{3.5}$$

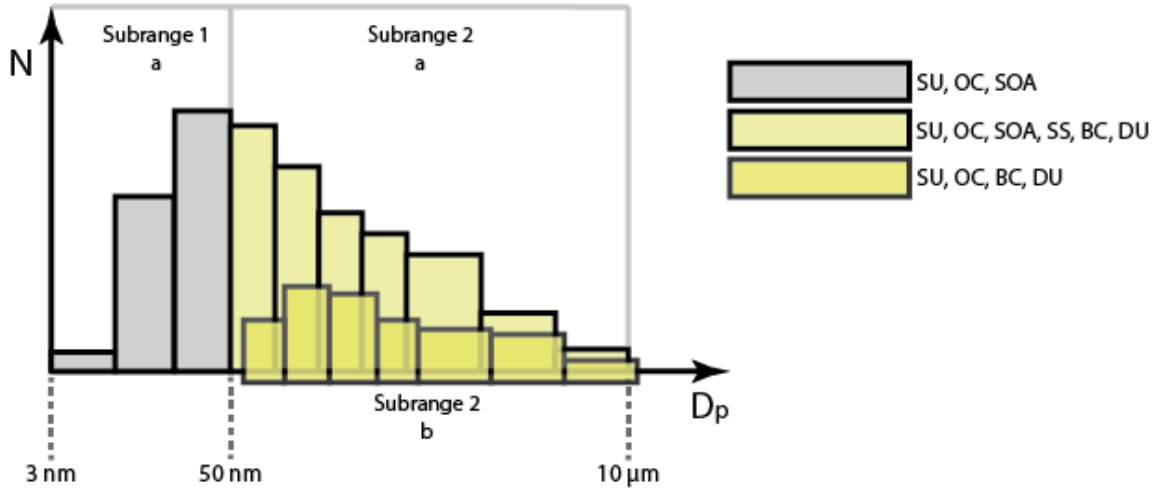

Figure 3.1.: Schematic of the number size distribution ($N(D_p)$) representation as a function of particle diameter D_p in SALSA2.0. Colors indicate the aerosol types included in the size class. Adapted from Kokkola et al. [2018].

In equation (3.5) g is the gravitational acceleration and Δp the layer thickness in pressure units.

Currently, SALSA uses a simplified parametrization for below-cloud scavenging, calculating the tracer tendency equation (3.6) of aerosol tracer i based on the tracer ambient mixing ratio c_i^{amb}, the fraction of the grid-box affected by precipitation f^{precip}, the rain (F^r) or snow (F^s) flux, and the corresponding size-dependent collection efficiencies R^r and R^s. The water and ice precipitation fluxes are calculated by ECHAM6 [Stier et al., 2005].

$$\overline{\frac{\Delta c_i}{\Delta t}} = c_i^{amb} f^{precip} (R_i^r F^r + R_i^s F^s) \tag{3.6}$$

In summary, HAM uses equations (3.1), (3.5) and (3.6) to calculate tracer tendencies altered by wet deposition.

3.3. SALSA

The aerosol micro-physical model SALSA is designed for application in different scales of aerosol modeling starting from 0-dimensional simulations of laboratory or chamber experiments [Kokkola et al., 2014], but also for 1-, 2-, 3-dimensional simulations [Tonttila et al., 2017]. This study uses SALSA2.0 as described in Kokkola et al. [2018]. In SALSA the aerosol size distribution is divided into 10 size bins using the volume ratio discretization [Jacobson, 2005]. The width of the size bins vary over two size ranges: subrange 1, for particles with diameters from 3 nm to 50 nm, subrange 2 from 50 nm to 10 µm. Figure 3.1 shows a visualization of the size bins and corresponding notation previously used in table 3.1. All size sections use the hybrid bin method [Young, 1974, Chen and Lamb, 1994]. The smallest bin is assumed to be internally mixed, while the other bin can also simulate internally and externally mixed aerosol populations. Aerosol bins are separated into insoluble and soluble aerosols with the possibility of insoluble aerosols becoming soluble via interaction with soluble particles or gases. Insoluble particles just occur in the larger size bins [Kokkola et al., 2018]. SALSA treats nucleation, condensation of H_2SO_4, coagulation, hydration and SOA formation [Bergman et al., 2012, Kokkola

et al., 2018]. The flexible formulation of SALSA allows extension to more aerosol types, such as SOA formation via the volatility basis set [Kühn et al., in preparation]. In Kühn et al. [in preparation], SALSA uses a so-called pseudo chemistry to obtain SOA precursors, which is a simplified, yield based chemistry parametrization. In the present study, no volatility basis set is used for the reference simulation, instead SOA precursors modeled by MOZ are explicitly partitioned by SALSA. Moreover, SALSA provides the surface area density for heterogeneous uptake of organic substances. The formulation of this coupling is described in detail in sections 3.5.2 and 3.5.3.

3.4. MOZ

Atmospheric chemistry in ECHAM-HAMMOZ is simulated by MOZ. MOZ solves the chemical equations using an implicit Euler backward solver. It calculates emissions, dry and wet deposition of gases. The basis of MOZ version 1.0 evolved from an extensive atmospheric chemical mechanism based on MOZART version 3.5 (Model for Ozone and Related chemical Tracers) [Stein et al., 2012], which merges the tropospheric version MOZART-4 [Emmons et al., 2010] with the stratospheric version MOZART-3 [Kinnison et al., 2007]. The combined chemical mechanism was further developed with a detailed representation of the oxidation of isoprene following the Mainz Isoprene Mechanism 2 [Taraborrelli et al., 2009, 2012, Nölscher et al., 2014, Lelieveld et al., 2016], with revised peroxy radical chemistry. This includes recently discovered 1,6 H-shift reactions [Peeters et al., 2009], the formation of isoprene epoxide IEPOX [Paulot et al., 2009] and the photolysis of HPALD [Wolfe et al., 2012]. Additionally, reaction products and rates were taken from the Master Chemical Mechanism version 3.3.1 [Jenkin et al., 2015, Schultz et al., 2017]. In Schultz et al. [2017], the Jülich Atmospheric Mechanism version 2, JAM2, is described and evaluated, but the present study uses version 3, JAM3. Differences to version 2 include self and cross reactions of isoprene products, added nitrates, initial reactions for monoterpenes and sesquiterepenes and production of low volatile, highly oxidized molecules. A summary of the differences can be found in appendix C (table S1 in supplementary material of Stadtler et al. [2017]). The complete JAM3 mechanism is given in appendix D. In total, JAM3 includes 254 gas species, 779 chemical reactions including 146 photolysis, 16 stratospheric heterogeneous and 8 tropospheric heterogeneous reactions. The semi-explicit isoprene oxidation with 147 reactions constitutes a major part of these reactions in JAM3. Eight tropospheric, heterogeneous reactions are considered in JAM3: 1) uptake of O_3 on dust forming HO_2, 2) HO_2 uptake on aqueous aerosol and cloud droplets, yielding H_2O_2, 3) uptake of NO_3 on wet aerosol, 4) uptake of NO_2 on wet aerosol, 5) HNO_3 uptake on sea salt and dust, 6) uptake of N_2O_5 7) IEPOX uptake on wet aerosol and 8) isoprene derived glyoxal uptake on wet aerosol. Details and discussion of the relevance of the inorganic heterogeneous reactions in ECHAM-HAMMOZ are given in [Stadtler et al., 2018]. Stratospheric heterogeneous reactions occur on four types of particles: 1) liquid binary sulfate; 2) supercooled ternary solution; 3) nitric acid tri-hydrate; and 4) water-ice [Kinnison et al., 2007].

Biogenic VOC emissions are simulated by the plant emission model MEGAN [Guenther et al., 2006, Henrot et al., 2017], while anthropogenic emissions are taken from the Atmospheric Chemistry Climate Model Inter-comparison Project [Lamarque et al., 2010]. Furthermore, oceanic VOC emissions from the POET project [Granier et al., 2005] are used. Natural lightning emissions are parametrized as a function of the average convective updraft velocity in one model column following Grewe et al. [2001] and described in Rast et al. [2014].

3.5. Explicit SOA formation scheme

The explicit SOA formation in ECHAM-HAMMOZ requires the coupling between MOZ and SALSA. MOZ chemistry forms SOA precursors from semi-explicit isoprene oxidation explained in the following section 3.5.1. These precursors are used in SALSA to form SOA in ten soluble size bins via partitioning and reactive uptake. The required model equations are explained in sections 3.5.2 and 3.5.3.

3.5.1. Isoprene oxidation mechanism

In order to identify SOA precursors produced via isoprene oxidation, first, each species in MOZ is assigned to the corresponding molecular structure. Species, which are not represented explicitly, are represented by groups of compounds with similar chemical properties (lumping). In these cases a group of isomers was assigned to one structure. With those molecular structures, the saturation vapor pressure $p^*(T)$ was estimated using the group contribution method by Nannoolal et al. [2008] and the boiling point method by Nannoolal et al. [2004] in the framework of the online open source facility UManSysProp [Topping et al., 2016]. Group contribution methods are approaches used to obtain formulas describing the dependence of the saturation vapor pressure $p^*(T)$ on corresponding sizes and functional groups of the individual molecules. Similar structures are assumed to have similar $p^*(T)$. Scanning all isoprene oxidation products in MOZ to sufficiently low volatile ones, SVOC and LVOC with p_0^* at 298.15 K lower than 0.01 Pa, leads to four iSOA precursors in ECHAM-HAMMOZ. The precursor structures are expressed as SMILES codes in Table 3.2 and as chemical structures in Figure 3.2. Table 3.2 gives the SMILES codes and resulting saturation vapor pressure p_0^* and evaporation enthalpy ΔH_{vap} at the reference temperature for all iSOA precursors. To get specific values for the evaporation enthalpy ΔH_{vap} of each molecule, the group contribution method output data was fitted to the Clausius-Clapeyron equation. p_0^* and ΔH_{vap} slightly differ for some of the isomers. The uncertainties in structure assignment of lumped species and the sensitivity to ΔH_{vap} are explored in Sections 5.5 and 5.6.

Isoprene oxidation leads to four iSOA precursors which partition: LNISOOH, LC578OOH, C59OOH and LISOPOOHOOH. Moreover, two precursors form iSOA via irreversible aerosol uptake: LIEPOX and isoprene derived glyoxal (IGLYOXAL). Figure 3.2 shows a simplified overview of the chemical pathways of isoprene oxidation and their products to form LIEPOX, IGLYOXAL, LNISOOH, LISOPOOHOOH, LC578OOH and C59OOH. Names starting with "L" indicate that this species is lumped. The compound IGLOYXAL was introduced to differentiate between isoprene derived glyoxal and glyoxal from other sources (emissions, atmospheric chemistry). For the whole chemical mechanism, including IGLYOXAL formation, the reader is referred to the model description of ECHAM-HAMMOZ in Schultz et al. [2017] and appendix D. In the following, a strongly simplified isoprene oxidation is described, only including the direct oxidation pathways leading to LIEPOX, LNISOOH, LISOPOOHOOH, LC578OOH and C59OOH. Chemical destruction and photolysis of these compounds are not explained in detail. Also, stochiometric coefficients and other products are omitted for the sake of simplicity. All compounds, stochiometric coefficients and rate coefficients can be found in the appendix D.

Semi and low volatile isoprene oxidation products are formed in MOZ via several reaction steps. Based on two initial reaction pathways from the oxidation of isoprene by OH and NO_3, three semi volatile and one low volatile compound are formed. The O_3 initiated reaction pathways are also included in MOZ, but do not lead to products considered low volatile enough

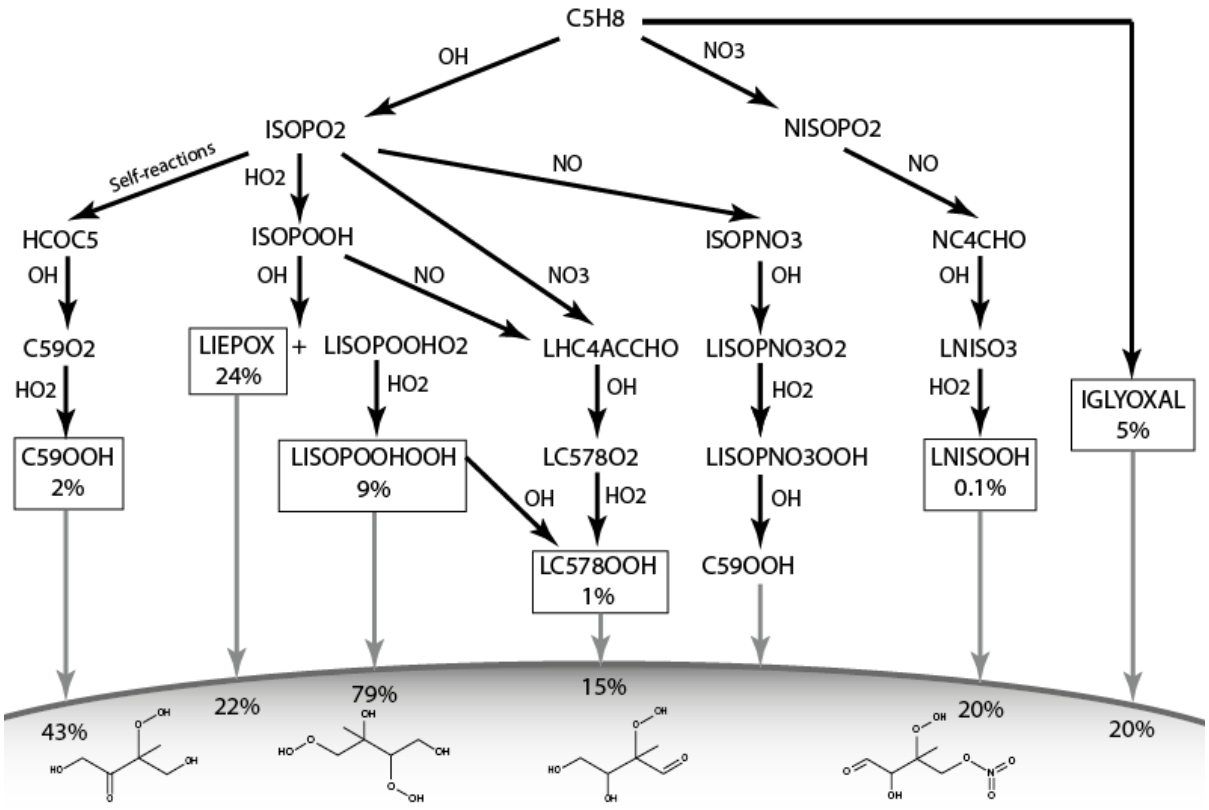

Figure 3.2.: Simplified overview of chemical pathways leading to isoprene derived compounds, able to either be taken up by reactions on the particle surface or partition into the aerosol-phase. Structures of partitioning molecules are relevant to estimate the saturation vapor pressure and evaporation enthalpy (table 3.2) and are therefore shown here. The percentages in the boxes indicate the reaction turnover of isoprene, leading to these products for the whole year 2012 over the globe. For IGLYOXAL, there are too many formation pathways and are not shown for simplicity (details can be found in appendix D). The solid horizontal curve represents the boundary to the particle-phase. Percentages found under the corresponding arrow express the individual iSOA yield of the compound for the whole year 2012 over the globe. Note that ISOPO2 here is used for simplicity, JAM3 includes three different ISOPO2 (LISOPACO2, ISOPBO2, ISOPDO2), same applies for ISOPOOH (Appendix D), not all isomers undergo the same reaction types.

Table 3.2.: Isoprene oxidation products in JAM3 forming iSOA, physical characteristics and molecular structure expressed as SMILES codes. Saturation vapor pressure at the reference temperature 298 K p_0^*, Henry's law coefficient H and evaporation enthalpy ΔH_{vap}. ΔH_{vap} and p_0^* are used in Clausius-Clapeyron equation for calculation of the saturation vapor pressure as a function of temperature in SALSA. Names of the compounds correspond to the ones in the Master Chemical Mechanism (MCM 3.2), except for LISOPOOHOOH, which is not in MCM 3.2. Names starting with "L" indicate that this species is lumped, SMILES codes of all isomers are shown, but just the ones marked with * are used.

Compound	SMILES code	p_0^*(298.15K) [Pa]	ΔH_{vap} $[\frac{kJ}{mol}]$	H $[\frac{mol}{atm}]$
LNISOOH	O=CC(O)C(C)(OO)CON(=O)=O*	$2.2 \cdot 10^{-4}$	122.7	$2.1 \cdot 10^{5}$
	CC(O)(CON(=O)=O)C(OO)C=O	$3.8 \cdot 10^{-4}$	120.0	
LISOPOOHOOH	OC(C)(COO)C(CO)OO*	$3.8 \cdot 10^{-7}$	155.3	$2.0 \cdot 10^{16}$
	CC(CO)(C(COO)O)OO	$1.9 \cdot 10^{-7}$	158.9	
LC578OOH	OCC(O)C(C)(OO)C=O*	$2.0 \cdot 10^{-4}$	123.2	$3.0 \cdot 10^{11}$
	O=CC(O)C(C)(CO)OO	$2.0 \cdot 10^{-4}$	123.2	
C59OOH	OCC(=O)C(C)(CO)OO*	$1.0 \cdot 10^{-4}$	125.0	$3.0 \cdot 10^{11}$

applying the threshold of p_0^* at 298.15 K lower than 0.01 Pa. The OH initiated pathway leads to three iSOA precursors called C59OOH, LC578OOH and LISOPOOHOOH in the JAM3 mechanism. First, OH attacks isoprene (C_5H_8) and forms three isoprene peroxy radical isomers, of which one is a lumped species (R1). For simplicity all isomers are referred as ISOPO2.

$$C_5H_8 + OH \longrightarrow ISOPO2 \tag{R1}$$

ISOPO2 isomers either decompose (R2) or undergo reactions with ambient radicals, but also self and cross reactions forming isoprene hydroperoxides (ISOPOOH) and isoprene nitrates (ISOPNO3) (R3).

$$ISOPO2 \longrightarrow HO_2 + \text{other products} \tag{R2}$$

$$ISOPO2 \longrightarrow ISOPOOH + ISOPNO3 + HO_2 + \text{other products} \tag{R3}$$

From the reactions of ISOPOOH with OH a hydroperoxide peroxy radical is formed, a lumped species called LISOPOOHO2, which can be oxidized by HO_2 to LISOPOOHOOH (R4) and (R5).

$$ISOPOOH + OH \longrightarrow LISOPOOHO2 + LIEPOX + OH \tag{R4}$$

Not included is the H-shift of LISOPOOHO2 that yields compounds that are two orders of magnitude more volatile than LISOPOOHOOH [D'Ambro et al., 2017b], so the chemical yield of LISOPOOHOOH in MOZ is expected to be an upper estimate.

$$\text{LISOPOOHO2} + \text{HO}_2 \longrightarrow \text{LISOPOOHOOH} \tag{R5}$$

LISOPOOHOOH can either react with OH back to LISOPOOHO2, be photolyzed and form, among other products, IGLYOXAL or be oxidized by OH to form LC578OOH (R6).

$$\text{LISOPOOHOOH} + \text{OH} \longrightarrow \text{LC578OOH} + \text{OH} \tag{R6}$$

LC587OOH is a lumped species representing two MCM species C57OOH and C58OOH. LC578OOH is also produced by the degradation of the species LHC4ACCHO (R7), which is a lumped species representing the MCM species HC4ACHO and HC4CCHO, followed by oxidation of LC578O2 (R8).

$$\text{LHC4ACCHO} + \text{OH} \longrightarrow \text{LC578O2} \tag{R7}$$

$$\text{LC578O2} + \text{HO}_2 \longrightarrow \text{LC578OOH} \tag{R8}$$

LHC4ACCHO is produced via reaction of ISOPO2 with NO_3 (R9) or via self reactions of ISOPO2 (R10).

$$\text{ISOPO2} + \text{NO}_3 \longrightarrow \text{LHC4ACCHO} \tag{R9}$$

LC578OOH can react with OH back to LC578O2, photolyze and undergo a 1,4-H-shift reaction, both recycling OH.

The third compound formed from the OH initiated oxidation of isoprene is C59OOH. Starting from ISOPO2, there are two possible oxidation ways for C59OOH formation; one where nitrogen oxide is not required (R11–R13) and a second one with organic nitrates as intermediates (R14–R17). The ISOPO2 isomers undergo self reactions (R11) and yield HCOC5 ($C_5H_8O_2$, same name as in MCM), which reacts with OH to form C59O2 (R12) and finally C59OOH (R13).

$$\begin{aligned}
\text{ISOPO2} + \text{ISOPO2} &\longrightarrow \text{LHC4ACCHO} + \text{HO}_2 && \text{(R10)}\\
\text{ISOPO2} + \text{ISOPO2} &\longrightarrow \text{HCOC5} + \text{HO}_2 && \text{(R11)}\\
\text{HCOC5} + \text{OH} &\longrightarrow \text{C59O2} && \text{(R12)}\\
\text{C59O2} + \text{HO}_2 &\longrightarrow \text{C59OOH} && \text{(R13)}
\end{aligned}$$

The nitrate pathway for C59OOH formation starts with the formation of ISOPNO3 (R14), continues with reactions consuming OH (R15) to form isoprene nitrate peroxy radicals

LISOPNO3O2, which represents several isomers.

$$\begin{aligned} \text{ISOPO2} + \text{NO} &\longrightarrow \text{ISOPNO3} && \text{(R14)} \\ \text{ISOPNO3} + \text{OH} &\longrightarrow \text{LISOPNO3O2} && \text{(R15)} \\ \text{LISOPNO3O2} + \text{HO}_2 &\longrightarrow \text{LISOPNO3OOH} && \text{(R16)} \\ \text{LISOPNO3OOH} + \text{OH} &\longrightarrow \text{C59OOH} + \text{OH} && \text{(R17)} \end{aligned}$$

Via formation and oxidation of a nitrate hydoxyperoxy radical LISOPNO3OOH (R16), finally C59OOH is formed (R17). This pathway requires, in contrast to the first one, the availability of NO. C59OOH can also react back to C59O2 or be lost via photolysis producing OH and other products.

For the formation of the fourth iSOA precursor, an isoprene derived nitrate LNISOOH, special atmospheric conditions are required; first, NO_x dominated conditions and second, a HO_2 dominated environment, because only the first two oxidation steps consume nitrogen species, then HO_x is needed. First, isoprene reacts with a NO_3 radical and forms a nitrate peroxy radical NIOSPO2 (R18), which reacts with NO (R19) or NO_3 (R20) and forms NC4CHO. NC4CHO in contrast, has to react with OH to form LNISO3 (R21), which then reacts with HO_2 and forms LINSOOH (R22).

$$\begin{aligned} \text{C}_5\text{H}_8 + \text{NO}_3 &\longrightarrow \text{NISOPO2} && \text{(R18)} \\ \text{NISOPO2} + \text{NO} &\longrightarrow \text{NC4CHO} + \text{HO}_2 + \text{NO}_2 && \text{(R19)} \\ \text{NISOPO2} + \text{NO}_3 &\longrightarrow \text{NC4CHO} + \text{HO}_2 + \text{NO}_2 && \text{(R20)} \\ \text{NC4CHO} + \text{OH} &\longrightarrow \text{LNISO3} && \text{(R21)} \\ \text{LNISO3} &\longrightarrow \text{LNISOOH} + \text{HO}_2 + \text{OH} && \text{(R22)} \end{aligned}$$

LNISOOH can be photolyzed or react back to LNISO3. Formation of LINSOOH is limited by the requirement of both radicals, NO and HO_2, thus this compound is only generated in very small amounts.

To cover multiphase chemical iSOA formation, reactive uptake on aerosols of IEPOX and IGLYOXAL are included. LIEPOX is formed along the pathway described for LISPOOHOOH in reaction (R4). ECHAM-HAMMOZ does not include in-particle or in-cloud aqueous-phase chemistry, therefore no assumptions of in-particle products of these heterogeneous reactions are made. Furthermore, no SOA formation via cloud droplets is included in ECHAM-HAMMOZ due to constraints in the aerosol cloud interaction formulation.

In figure 3.2, the simplified overview of the described chemical reactions can be found. Resulting reaction branching ratios from isoprene to the final compounds are shown for the whole year 2012 over the globe. The relevant chemical structures used for iSOA precursors undergoing partitioning are shown in the particle-phase. In the particle-phase, the fraction which ends up in the iSOA by partitioning compound and reactive uptake, is expressed as percentage of total iSOA precursor mass produced by atmospheric oxidation. For example, of the global annually emitted isoprene in ECHAM-HAMMOZ, 24% form gas-phase LIEPOX. Of the total global gas-phase LIEPOX, 22% form LIEPOX-SOA. Chemical branching and iSOA are not prescribed as figure 3.2 suggests. These vary in space and time and are thus regionally different.

3.5.2. Partitioning formulation

LNISOOH, LISOPOOHOOH, LC578OOH and C59OOH are partitioned explicitly by SALSA taking their saturation vapor pressure and evaporation enthalpy into account. To explicitly track each chemical species j in the aerosol size bin i, SALSA creates additional ten tracers per isoprene-derived iSOA precursor. The index j describes all chemical aerosol species (water, sulphate, organics, black carbon, dust, sea salt, iSOA species), while J only refers to iSOA precursors. As described in Section 2.2.1, the volatility of a compound can be described by its saturation concentration C^*, which is assumed to follow the Clausius-Clapeyron relation:

$$C_J^*(T) = C_0^* \frac{T}{T_0} \left(\frac{\Delta H_{vap}}{R} \left(\frac{1}{T_0} - \frac{1}{T} \right) \right), \tag{3.7}$$

where ΔH_{vap} can be found in Table 3.2 and $T_0 = 298.15\,K$. Furthermore, dilution effects are treated using Raoult's law of an ideal mixture:

$$\tilde{C}_J^*(T) = C_J^* \frac{c_{i,J}}{\sum\limits_j c_{i,j}}. \tag{3.8}$$

In equation (3.8), the saturation concentration is modified by the fraction between iSOA concentration in the particle phase $c_{i,J}$ and the sum of other compound concentrations $c_{i,j}$ in the same particle. Furthermore, the Kelvin-correction factor is needed and calculated as:

$$S_{i,J} = \exp\left(\frac{4\sigma_w v_J}{D_{p,i} k_B T} \right), \tag{3.9}$$

where σ_w is the surface tension of water, $D_{p,i}$ is the mean particle diameter in size bin i and v_J the molecular volume of species J. Using equation (3.8) and (3.9), iSOA precursors are partitioned between the gas- and particle-phase in each time step. The corresponding gas-phase concentrations are given as $c_{g,J}$. Updated gas-phase concentrations $c'_{g,J}$ are computed as

$$c'_{g,J} = \min\left(\frac{c_{g,J} + dt \sum\limits_i k_{m,i} \tilde{S}_i C_J^*}{1 + dt \sum\limits_i k_{m,i}}, c_{t,J} \right) \tag{3.10}$$

where $c_{g,J}$ are the previous gas-phase concentrations, $c_{t,J} = c_{g,J} + \sum\limits_i c_{i,J}$ is the total species concentration as a sum of gas-phase and particle-phase concentrations, dt is the time step length and $k_{m,i}$ is the mass-transfer coefficient from the gas- to the particle-phase. To calculate the updated particle concentrations, a two step process is used. In the first step, gas-phase concentration changes are reflected onto the particle-phase:

$$c'_{i,j} = \max\left(c_{i,j} + dt k_{m,i} (c'_{g,J} - \tilde{S}_i C_J^*), 0 \right). \tag{3.11}$$

Evaporation of iSOA could yield into a negative first argument, therefore the max-function is needed. Conversely, mass conservation of $c_{t,J}$ is not longer guaranteed. To fulfill the mass conservation constraint, in the second step the updated particle-phase concentrations are scaled:

$$c''_{i,j} = c'_{i,j} \frac{c_{t,J} - c'_{g,J}}{\sum\limits_i c_{i,J}} \tag{3.12}$$

The partitioning described above strongly depends on current particle size and composition, which change a lot during one time step. Thus, this process is calculated using 10 logarithmically equidistant sub-steps within one model time step [Kühn et al., in preparation].

3.5.3. Heterogeneous uptake

IGLYOXAL and LIEPOX undergo irreversible reactive uptake onto wet aerosol. In ECHAM-HAMMOZ, reactive uptake is formulated as described in section 2.2.2 using equation (2.13). The surface area density is calculated based on particle radii given by SALSA. Particles are assumed to be spherically, which is a good approximation, because only wet particles provide the reactive surface. Reactive uptake coefficients for IGLYOXAL and LIEPOX in equation (2.13) do not change in time or depend on aerosol composition in ECHAM-HAMMOZ reference case. If the aerosol is dry, no reactive uptake occurs.

As described in section 2.4.2, glyoxal is observed to produce a variety of compounds in the aqueous-phase, like oligomers or organosulfates. It was also observed that glyoxal can be released back in the gas phase [Volkamer et al., 2007, Ervens and Volkamer, 2010, Washenfelder et al., 2011, Li et al., 2013]. The simplification assuming irreversible uptake might thus overestimate its impact on iSOA. Following previous model studies [Fu et al., 2008, Lin et al., 2012] a reaction probability of $\gamma_{\text{glyoxal}} = 2.9 \cdot 10^{-3}$ [Liggio et al., 2005b] is used.

For IEPOX (see section 2.4.3) the irreversibility is a less critical assumption, because IEPOX forms 2-methyltetrol and organosulfates in the aqueous aerosol-phase, which stay in the aerosol-phase [Claeys et al., 2004, Eddingsaas et al., 2010, Lal et al., 2012, McNeill et al., 2012, Woo and McNeill, 2015]. However, ECHAM-HAMMOZ does not include explicit treatment of aqueous-phase reactions. The reaction probability of IEPOX varies with pH value [Lin et al., 2013, Pye et al., 2013, Gaston et al., 2014], which cannot be captured by ECHAM-HAMMOZ due to the lack of ammonium and nitrate in the aerosol-phase. Thus, ECHAM-HAMMOZ cannot simulate the aerosol pH value. For these reasons, the reaction probability of IEPOX $\gamma_{\text{IEPOX}} = 1 \cdot 10^{-3}$ [Gaston et al., 2014] is used, which is close to the value given by [Pye et al., 2013]. To explore the impact of the pH dependence, a sensitivity run with γ_{IEPOX} as a function of aerosol pH is analyzed. Additionally, no assumptions of in-particle products are made, in ECHAM-HAMMOZ LIEPOX is simply taken up irreversibly into aerosol phase without further transformation.

3.6. Formulation of additional loss processes

As described in chapter 1, global models usually include deposition as the only aerosol sink. Recently, other aerosol sinks as in-particle decay of hydroperoxides and in-particle photolysis were observed (see section 2.3.2). The following sections describe the formulation of additional aerosol loss processes in ECHAM-HAMMOZ, which were implemented and tested during this study.

3.6.1. In-particle decay of LISOPOOHOOH

Hydropreoxides from monoterpenes were observed to undergo in-particle thermal decay [Krapf et al., 2016] and furthermore, D'Ambro et al. [2017a] report a ISOP(OOH)2 in-particle decay with a half-life of 4 h, but did not point out fragmentation products (Sections 2.4.1 and 2.3.2).

To explore how such a decay could change atmospheric SOA concentrations, this additional SOA sink was introduced in ECHAM-HAMMOZ.

LISOPOOHOOH (= ISOP(OOH)2, name in ECHAM-HAMMOZ) can be transformed in the gas-phase into LC578OOH (R6), which is also an aerosol tracer, therefore it was chosen as product of LISOPOOHOOH decay. Since LC578OOH is more volatile than LISOPOOHOOH, it evaporates quickly and is lost via gas-phase reactions or deposition. This approximation fits in a sense, that aerosol mass is lost, but a decay of a C5 molecule would not lead to another C5 molecule in reality. Nevertheless, the decay takes place in the aerosol-phase, this means that SALSA is converting one tracer to the other. This decay is no formal chemical reaction treated by MOZ, which can produce any gas-phase tracer, but restricted to aerosol tracers. To keep the coupling between SALSA and MOZ simple, this parametrization was chosen.

The decay rate in equation (3.13) is given using the reported half-life of 4 h [D'Ambro et al., 2017a] for ISOP(OOH)2.

$$\frac{d[\text{LISOPOOHOOH}]}{dt} = -[\text{LISOPOOHOOH}]_0 \exp\left(-\frac{t}{\tau}\right) \tag{3.13}$$

In equation (3.13), $[\text{LISOPOOHOOH}]_0$ is the initial LISOPOOHOOH concentration, t the time and τ the mean lifetime which can be calculated using the half-life of 4 h.

3.6.2. SOA photolysis

As discussed in Section 2.3.2, SOA photolysis was observed in laboratory experiments, but is usually not implemented in global models due to general underestimation of SOA formation and poor understanding of in-particle photolysis of single molecules. Nevertheless, a first SOA-photolysis parametrization was developed and tested by Hodzic et al. [2015], this parametrization was implemented into ECHMAM-HAMMOZ. The SOA-photolysis parametrization is based on the measured SOA mass absorption coefficient and formulated as a first order loss process with an effective reaction coefficient rate J_{SOA}:

$$J_{SOA} = [AF] \times [MAC] \times [mc] \times [QY] \tag{3.14}$$

with AF describing the actinic flux in photons $\mathrm{m}^{-2}\,\mathrm{s}^{-1}$, the SOA mass absorption coefficient MAC in $\mathrm{m}^2\,\mathrm{g}^{-1}$, the mass of one carbon atom mc in g and the quantum yield QY. The quantum yield describes the probability of absorbed photons, leading to a bond cleavage and therefore SOA mass loss. It is assumed that each photon leads to the loss of one carbon atom, thus $QY = 1$. Equation (3.14) is scaled to NO_2 photolysis, because it is known in the model system:

$$J_{SOA} = J_{\mathrm{NO_2}} \times \frac{[AF]}{J_{\mathrm{NO_2}}} \times [MAC] \times [mc] \times [QY] \tag{3.15}$$

The UV actinic flux is estimated to be $2 \cdot 10^{20}$ photons $\mathrm{m}^{-2}\,\mathrm{s}^{-1}$ [Madronich, 1993] and the NO_2 photolysis in a range over 280–400 nm at 1 km latitude is $9.7 \cdot 10^{-3}\,\mathrm{s}^{-1}$. This combined with the mass of one carbon atom gives $[AF] \times J_{\mathrm{NO_2}}^{-1} \times [mc] = 0.4$ photons $\mathrm{g\,m}^{-2}$, which can be used in equation (3.15) to rewrite it:

$$J_{SOA} = 0.4 \times J_{\mathrm{NO_2}} \times [MAC] \times [QY] \tag{3.16}$$

For $[MAC]$, a lower limit for ambient aerosols of $0.1\,\mathrm{m}^2\,\mathrm{g}^{-1}$ and for $[QY]$ a conservative value of 0.01 are used. Hodzic et al. [2015] give a value of $J_{SOA} = 0.04\,\%\,J_{\mathrm{NO_2}}$ as their best estimate.

Malecha and Nizkorodov [2016] pointed out that this estimate made by Hodzic et al. [2015] might be too high, because of linking condensed-phase photolysis to gas-phase photolysis. Nevertheless, this simple parametrization is suitable for usage in ECHAM-HAMMOZ, because no detailed knowledge of the phase-state of aerosols is implemented, no in-particle chemistry and not all aerosol types are treated explicitly like SOA components. Dust and organic carbon consist of many species lumped together in two aerosol types. Therefore, $J_{SOA} = 0.04\,\% \, J_{\mathrm{NO_2}}$ can be seen as an upper limit. A ten times lower $J_{SOA} = 0.004\,\% \, J_{\mathrm{NO_2}}$ is tested as a sensitivity simulation.

3.7. Experimental setup

For the analysis of iSOA formation, evolution and loss in ECHAM-HAMMOZ, several simulations were performed. The reference simulation RefBase uses a spin-up time of 3 months and is run for the whole year 2012. For all simulations, the triangular truncation 63, with its associated Gaussian grid with an approximate resolution of to horizontal resolution of 1.875° × 1.875°, and 47 vertical layers, is used. The surface layer is around 50 m thick. The atmosphere spans up to 0.01 Pa. Several sensitivity simulations give additional information about the dependence of iSOA formation on parameters like saturation concentration, evaporation enthalpy, aerosol pH, particle photolysis and decomposition.

All sensitivity simulations, except RefM7JAM2 are performed starting from the conditions in RefBase depending on the time period calculated. For example, simulations performed for a three month time period (June, July, August) in 2012 start from RefBase conditions in end of May 2012. Descriptions and names of the simulations can be found in table 3.3.

Table 3.3.: Description of simulations performed.

Name	Time period mm-mm.yyyy	Description
RefBase	01-12.2012	Reference run, iSOA formation from all species including partitioning and reactive uptake.
RefVBS	06-08.2012	ECHAM-HAM simulation. VBS approach with pseudo chemistry only for isoprene.
noiSOA	01-12.2012	Simulation without iSOA formation.
ΔH30	01-12.2012	Same evaporation enthalpy $\Delta H_{vap} = 30 \frac{kJ}{mol}$ for all compounds.
γpH	06-08.2012	$\gamma_{IEPOX} = f(\text{pH})$.
EVA	01-12.2012	EVAPORATION [Compernolle et al., 2011] method instead of Nannoolal et al. [2008] for estimation of saturation vapor pressures.
J04PHOT	06-08.2012	With additional sink iSOA photolysis with $J_{\text{iSOA}} = 0.04\,\% \, J_{NO_2}$.
J004PHOT	06-08.2012	With additional sink iSOA photolysis with $J_{\text{iSOA}} = 0.004\,\% \, J_{NO_2}$.
DECAY	06-08.2012	With additional sink LISOPOOHOOH $\longrightarrow$ LC578OOH transformation.
SinkL	02-03.2012	With both additional sinks $J_{\text{iSOA}} = 0.004\,\% \, J_{NO_2}$ and LISOPOOHOOH $\longrightarrow$ LC578OOH transformation.
SinkS	02-03.2012	With both additional sinks $J_{\text{iSOA}} = 0.04\,\% \, J_{NO_2}$ and LISOPOOHOOH $\longrightarrow$ LC578OOH transformation.
RefM7JAM2	01-12.2012	Reference run presented in Schultz et al. [2017]. Instead of SALSA, M7 is used and instead of JAM3, JAM2 is used. The comparison to RefBase is shown in appendix A.

4. Results

The results chapter shows the evaluation of the reference run. On on hand, key variables and iSOA are analyzed and on the other hand iSOA concentrations are compared to other models and observations.

4.1. Evaluation of reference run RefBase

The reference run is evaluated globally with focus on especially iSOA rich regions. Before iSOA itself is discussed, the global aerosol surface area distribution is compared to observations. The aerosol surface area density is a key variable influencing iSOA formation, providing the needed surface area for partitioning and reactive uptake. Then, global iSOA distributions are shown as a global annual mean and as an average for the northern hemispheric summer. The global iSOA budget is compared to budgets of several global models, which contributed to the model inter-comparison AeroCom [Tsigaridis et al., 2014]. Regional results for an average month and results for two particular grid-boxes in three hourly resolution are shown, in order to compare different chemical regimes in different regions.

A comparison to some inorganic gas-phase species and radicals to the ten-year reference run evaluated in Schultz et al. [2017] is given in appendix A.

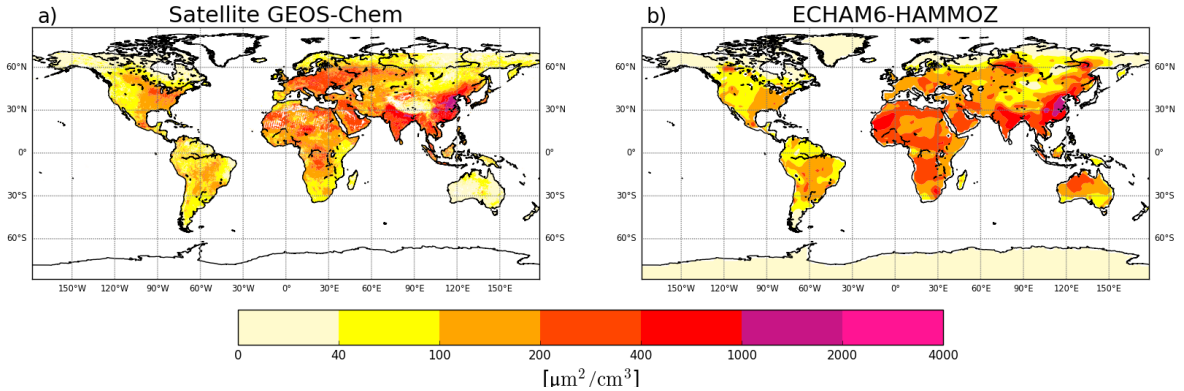

Figure 4.1.: Satellite estimated (left, a) and simulated surface area density by ECHAM-HAMMOZ (right, b) at ground level. The Satellite data is an average value for the time period 2010 - 2012, from van Donkelaar et al. [2015] and used in Stadtler et al. [2018] to evaluate a prior ECHAM-HAMMOZ version without SOA formation. The model data is for 2012 and the lowest model level in $\mu g\,m^{-3}$ for 2012.

4.1.1. Global aerosol distribution

The total surface area of all aerosol types, including iSOA, is calculated by HAMMOZ and compared to a satellite product by van Donkelaar et al. [2015]. Van Donkelaar et al. [2015] derive global surface $PM_{2.5}$ concentration estimates in the time period between 1998 and 2012, by using data from moderate resolution imaging spectroradiometers (MODIS). MODIS are used on board of the Terra and Aqua satellites. Both MODIS instruments measure aerosol optical depth on a near-daily, global coverage. Additionally, van Donkelaar et al. [2015] used the model GEOS-chem to retrieve the surface area. The measurements of the fourteen-year time period were used for the climatology shown in figure 4.1 a). The satellite data has a higher resolution of 10 km × 10 km compared to ECHAM-HAMMOZ. Nevertheless, patterns agree well between the two pictures.

In USA and Canada, the west-east gradient in particles is captured, although ECHAM-HAMMOZ simulates a slightly lower surface area density (SAD) than observed over Canada. For South America, Central and South Africa, where ECHAM-HAMMOZ without SOA formation could not capture the values of the satellite product (see figure 2 in Stadtler et al. [2018], Appendix figure B.4), patterns now agree well. On the eastern edge of the Andes, HAMMOZ-even overestimates SAD compared to the satellite, which also shows maxima in this area, but with a lower SAD. Overestimation of SAD can be found all over Africa. The Sahara in ECHAM-HAMMOZ is loaded with dust and in Central and South Africa strong iSOA formation lead to high values, still with patterns agreeing. Over Europe, a slight underestimation can be found. In this region, ECHAM-HAMMOZ does not form much iSOA. Low iSOA concentrations in Europe are caused by lower isoprene emissions than in other regions. In Europe, terpenes are found to contribute largely to SOA formation Gelencsér et al. [2007]. Especially over the middle east and Asia, even East Asia, satellite and model agree well in SAD. ECHAM-HAMMOZ overestimates SAD in North Australia.

In summary, ECHAM-HAMMOZ including iSOA formation agrees well with the satellite retrieved SAD, although some details are not resolved and ECHAM-HAMMOZ overestimates SAD especially in Africa and Australia. In particular, South American and Asian SAD values are captured well.

4.1.2. Global iSOA and precursor distributions

Figure 4.2 shows the annual mean surface concentrations for total iSOA (b) and its precursors (a) in the gas-phase. The precursors are formed, except for LNISOOH, during daytime and build up in a few hours after sunrise. Therefore, these compounds are found very close to isoprene source regions mostly in the tropics and southern hemisphere. Their highest mean values (figure 4.2 a), up to $3\,\mu g\,m^{-3}$, are simulated over the Amazon, the east flank of the Andes, Central Africa, North Australia, Indonesia and Southeast Asia. In the annual mean, the northern hemispheric summer contribution is visible as well, but peak values of over $2\,\mu g\,m^{-3}$ are only reached on Mexico's west coast and in the Southeastern US. In Europe and North Asia, where isoprene emissions are much lower, mean values up to $0.5\,\mu g\,m^{-3}$ of precursors are formed.

These low precursor concentrations correspond to the low iSOA concentrations (figure 4.2 b) over Europe and North Asia, compared to Southeastern US and Mexico's west coast, where up to $4.5\,\mu g\,m^{-3}$ iSOA is formed. The highest iSOA concentrations are found where high precursor concentrations meet pre-existing aerosol, like in Central Africa, where high biomass

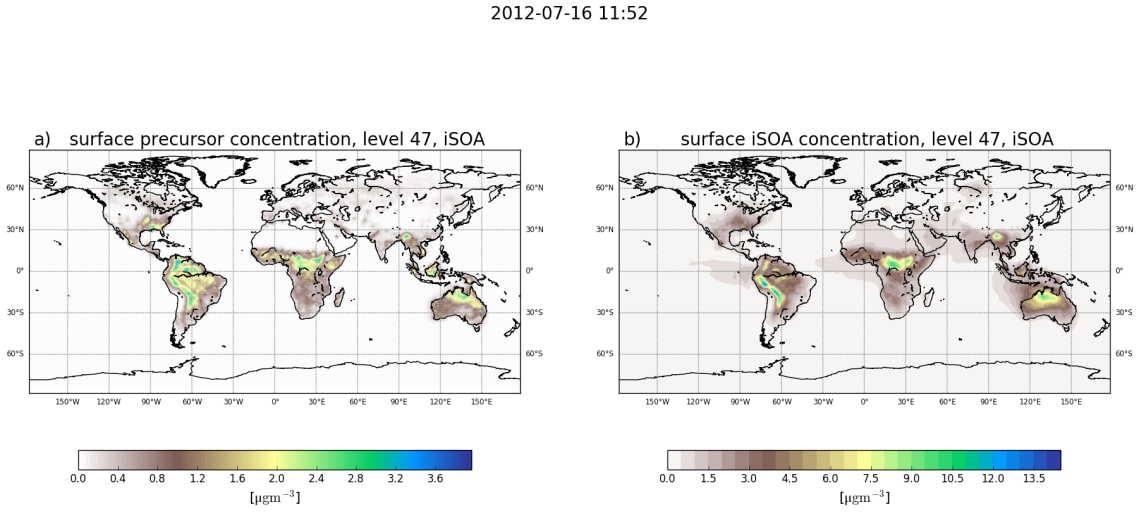

Figure 4.2.: Reference run annual average surface distribution of iSOA precursor gases a) and iSOA b) in $\mu g\,m^{-3}$ for 2012.

burning emissions lead to high aerosol loadings, or Southeast Asia, where anthropogenic aerosol pollution is high. In the latter ECHAM-HAMMOZ simulates values of up to $10\,\mu g\,m^{-3}$ of iSOA. In the northern part of Australia, higher gas-phase precursor loadings of around $2\,\mu g\,m^{-3}$ are found, leading to iSOA ground-level concentrations of up to $9\,\mu g\,m^{-3}$. The Amazon is a region of very high isoprene emissions and therefore high iSOA precursor concentrations, nevertheless the local maximum in iSOA of $13\,\mu g\,m^{-3}$ can be seen on the east side of the Andes. This pattern is caused by transport of pre-existing aerosol and iSOA, which in ECHAM-HAMMOZ tends to accumulate iSOA on the east side of the Andes. Also, relatively high iSOA precursor concentrations are visible in this region. There is a positive feedback between iSOA concentrations and iSOA formation. The more iSOA is formed, the larger the particles and the higher the surface area grows. A high surface area is especially beneficial for reactive uptake. Tests with ECHAM-HAMMOZ show that more iSOA formed by partitioning leads to more iSOA formed by reactive uptake. This is further discussed in section 5.6, where a reduction in SAD due to less partitioning leads to a reduced reactive uptake.

In figure 4.2 b), it can be seen, that iSOA has a longer lifetime than its gas-phase precursors. Prevailing wind directions are recognizable, clearly showing transport of iSOA over the oceans, for example in the South American and African outflow regions. Also, iSOA is transported from Australia to Indonesia where it meets more gas-phase precursors. The average iSOA lifetime was calculated to be around 4 days, so long-range transport is limited, before iSOA is lost mainly due to wet deposition (see section 4.1.3).

Farina et al. [2010] used a so-called unified chemistry-climate-aerosol model based on Goddard Institute for Space Studies General Circulation Model II and included SOA formation using the volatility basis set formulation. To produce the corresponding gas-phase precursors, chemical yields are defined. Isoprene reactions with OH and O_3 under high and low NO_x conditions lead to SVOC and IVOC in the VBS classes 1 and 10. This means, no chemical reactions are calculated instead, a certain fraction of isoprene mass is shifted to the VBS classes. Farina

et al. [2010] show a global annual surface distribution of iSOA for 1979–1980 (figure 6 in their manuscript, appendix figure B.1). Compared to the results of Farina et al. [2010], ECHAM-HAMMOZ simulates nearly one order of magnitude higher maximum iSOA concentrations. This can be explained by much higher reaction turnover from MOZ chemistry, leading to higher amounts of iSOA precursors compared to the amounts which are produced by the low chemical yields prescribed in Farina et al. [2010]. The global patterns agree in high iSOA values over Southeastern US, South America, Central Africa and North Australia.

Hodzic et al. [2016] used the GEOS-Chem global chemical transport model, including SOA formation as well, using the volatility basis set approach and prescribed chemical yields for SOA precursor formation. Compared to Farina et al. [2010], they include higher yields for isoprene derived precursors and also partition them into lower volatility classes. In figure 1, Hodzic et al. [2016] (Appendix figure B.2) show biogenic SOA for the lower 5 km on a global scale. Again, general patterns agree with the distribution in ECHAM-HAMMOZ. Nevertheless, Hodzic et al. [2016] simulated higher concentrations over Eurasia, which is not captured by ECHAM-HAMMOZ due to the lack in other BVOC (e.g. monoterpenes and sesquiterpenes) derived SOA. Total biogenic SOA concentrations of Hodzic et al. [2016] compare well with iSOA surface concentrations of ECHAM-HAMMOZ in their order of magnitude, which again underlines the higher overall yields resulting in ECHAM-HAMMOZ. High concentrations in ECHAM-HAMMOZ result from the highly oxidized compounds produced by MOZ chemistry, especially LISOPOOHOOH molar mass of $168.14\,\mathrm{g\,mol^{-1}}$ is very large. LISOPOOHOOH and LIEPOX contribute most to iSOA, followed by isoprene glyoxal. To further discuss this, iSOA composition concentrations for northern hemispheric summer (June, July, August) are shown in figure 4.3.

On the left column, figure 4.3 shows gas-phase precursor concentrations. First, LIEPOX (a) and LISOPOOHOOH (c) are shown, because they have greatest impact in the particle-phase, followed by IGLYOXAL (e). The other iSOA precursor SVOCs are shown together (g), because of their low concentrations in gas and particle-phase. On the right column corresponding mean values in the particle-phase are displayed.

From the gas-phase LIEPOX (a) distribution it can be seen that MOZ simulates concentrations of around $0.5\,\mathrm{\mu g\,m^{-3}}$ over isoprene rich areas. Peak values of $4.5\,\mathrm{\mu g\,m^{-3}}$ LIEPOX are found over Southeastern US, north Venezuela and north of Myanmar. Higher concentrations of LIEPOX are reached in the aerosol-phase (b), for example in South America, LIEPOX gas-phase concentration varies between 0.5 and $0.8\,\mathrm{\mu g\,m^{-3}}$, but LIEPOX-SOA concentrations higher than $7.0\,\mathrm{\mu g\,m^{-3}}$ are reached on the eastern edge of the Andes. Especially, the LIEPOX-SOA transport over the ocean and over Sahara can be seen. No assumption of in-particle products for LIEPOX was made, but usually 2-methyltetrols in the order of $\mathrm{ng\,m^{-3}}$ are measured in the particle-phase [Claeys et al., 2004, Kourtchev et al., 2005, Clements and Seinfeld, 2007]. Lopez-Hilfiker et al. [2016] report that 80 % of IEPOX forms dimers instead of 2-methyltetrols, which would increase the concentrations of IEPOX derived SOA in the ambient measurements. Accounting additionally for these 80 %, the mass concentrations would reach around $10–100\,\mathrm{ng\,m^{-3}}$, still a slight overestimation of simulated LIEPOX-SOA is indicated.

In contrast to LIEPOX, LISOPOOHOOH gas-phase concentrations (c) are very low and even with a scale focusing on low values, these cannot be captured on a scale fitting to the other compounds. For the gas-phase LISOPOOHOOH annual mean values lower than $0.1\,\mathrm{\mu g\,m^{-3}}$ are calculated on a global scale. This is a consequence of iSOA formation. On the LISOPOOHOOH-SOA plot (d) it can be seen that LISOPOOHOOH appears in quite large amounts in the particle-phase, because it is the lowest volatile isoprene derived compound in MOZ. Over large

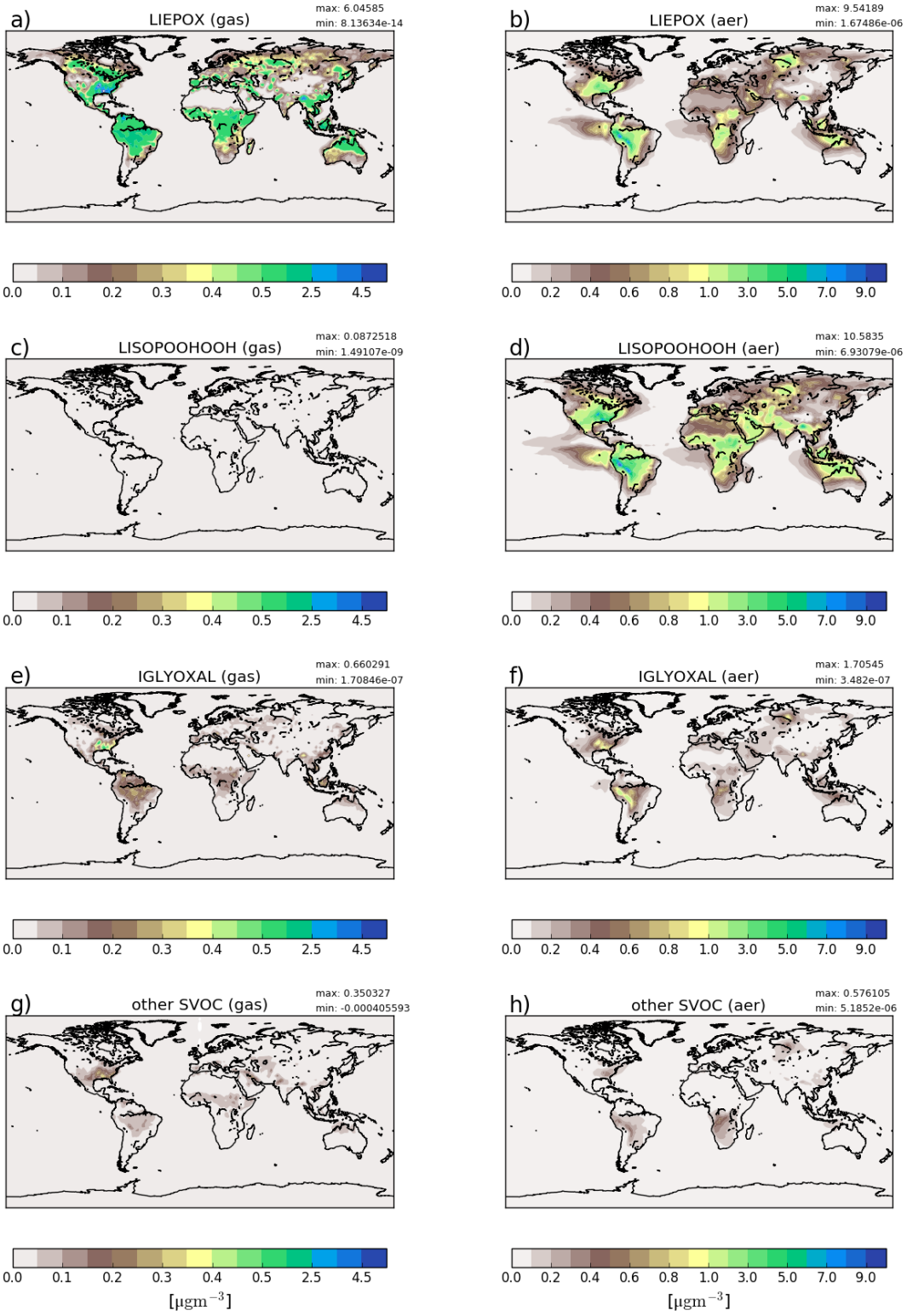

Figure 4.3.: Reference run average surface distribution of precursor gases (left, a), c), e), g)) and corresponding component concentration in the particle-phase (right, b), d), f), h)) in µg m^{-3} for June, July and August 2012. Since concentrations of other SVOC are quite low, they are shown together in plots g) and h). Different scales are used for precursors and iSOA to capture the concentration ranges accordingly. Note, that the concentration scales are not linear and emphasize low concentrations.

continental areas LISOPOOHOOH-SOA concentrations over 3.0 µg m^{-3} are simulated. Even more iSOA is formed by LISOPOOHOOH than by LIEPOX, especially over the Amazon (up to 9 µg m^{-3}), Central Africa (up to 6 µg m^{-3}) and the Middle East (up to 3.5 µg m^{-3}). Indeed, the sum of LIEPOX and LISOPOOHOOH makes up to 90 % of total iSOA mass in ECHAM-HAMMOZ.

Gas-phase IGLYOXAL (e) is found in the same regions as LIEPOX, but in lower concentrations varying between 0.1 and 0.5 µg m^{-3}. Peak values of 0.5 µg m^{-3} can be found over Southeastern US. IGLYOXAL shows similar local maxima as LIEPOX over the American continent, north of Myanmar and over Siberia. Similar patterns with comparably lower maxima of up to 1.0 µg m^{-3} in IGLYOXAL-SOA (f), than LIEPOX-SOA (b) can be identified. Reactive uptake of IGLYOXAL (20% of IGLOYXAL form iSOA) is nearly as efficient as LIEPOX uptake (22% of LIEPOX for iSOA, see table 4.1 particle formation yield), but not as important since less IGLOYXAL than LIEPOX is produced by isoprene oxidation and therefore concentrations are comparably low.

Figure 4.3 (g) and (h) show that the contribution of the other SVOC (= $\sum$ of LNSIOOH, LC578OOH, C59OOH) is minor; in the gas-phase, values between 0.05 and 0.3 µg m^{-3} are visible, while in the particle-phase maxima of 0.4 µg m^{-3} can be found in Myanmar, Central Africa and Southeastern US and the East edge of the Andes.

To summarize, figure 4.3 shows that concentrations of all compounds in the particle-phase reach higher values than in the gas-phase, but not within the same regions due to pre-existing aerosols, transport and longer lifetime of iSOA compared to iSOA precursors. Since all compounds are produced by isoprene, the global distribution of the individual gases does not differ a lot. In contrast to the annual mean, the Northern Australian maximum does not appear that prominently. Hence, the great impact of isoprene on SOA in Southeastern US is clearly visible. For Europe, even during summer, iSOA seems to play a minor role compared to the equatorial regions due to the minor role of isoprene in BVOC emissions [Steinbrecher et al., 2009].

4.1.3. Global iSOA budget

The global annual budget for isoprene derived secondary organic aerosol is shown in figure 4.4. For the evaluated simulation period of 2012 a total of 392.1 TgC isoprene were emitted, which is a bit lower than the range of estimated isoprene emissions 440 – 660 TgC [Guenther et al.,

Table 4.1.: Total annual chemical production of individual iSOA precursors 2012 and corresponding amount of iSOA formed. In parenthesis the corresponding yields are given, for the gas-phase how much of total isoprene was converted to the precursors and the yield of those precursors into iSOA for the global annual budget.

Specie	Gas-phase production in TgC (fraction of isoprene source)		Particle formation in TgC (individual yield in %)	
LIEPOX	94.0	(24 %)	21.0	(22 %)
IGLYOXAL	19.8	(5 %)	3.6	(20 %)
LISOPOOHOOH	35.1	(9 %)	27.9	(79 %)
C59OOH	6.5	(2 %)	2.8	(43 %)
LC578OOH	4.5	(1 %)	0.3	(15 %)
LNISOOH	0.5	(0.1 %)	0.1	(20 %)

2006, Henrot et al., 2017]. The oxidation of isoprene leads to production of 160.4 TgC of the six iSOA precursors identified in this study. Comparing it to the initially emitted amount, 41 % of isoprene is chemically transformed into iSOA precursors. 24 % of isoprene end up in IEPOX, 9 % in LISOPOOHOOH, 5 % in IGLYOXAL, 2 % in C59OOH, 1 % in LC578OOH and 0.1 % in LNISOOH (see table 4.1). For LIEPOX, 94.0 TgC are produced, which agrees well with the production of (95 ± 45) TgC IEPOX estimated by Paulot et al. [2009]. LISOPOOHOOH production is an order of magnitude higher than the estimation given by Berndt et al. [2016] of 15 – 35 GgC. The reasons for this discrepancy are discussed in section 5.9.1. Of the total iSOA precursors produced, about a third (56.7 TgC) form iSOA. Half of iSOA is formed by reactive uptake, where LIEPOX contributes 21.0 TgC and IGLYOXAL 3.6 TgC, corresponding to a reactive uptake yield of 22 % (LIEPOX) and 20 % (IGLYOXAL), respectively. The other half is mainly formed by LISOPOOHOOH (27.9 TgC) and C59OOH (2.8 TgC). These numbers describe the net amount of iSOA produced by partitioning. In terms of yields, LISPOOHOOH has an overall annual yield of 79 % and C59OOH one of 43 %. This results in an annual overall isoprene SOA yield of 15 % and in a global burden of 0.6 TgC, taking all compounds into account. An isoprene SOA yield of 15 % lies within the range of 1 % to 30 % as observed under different conditions by Surratt et al. [2010]. The conditions refer to high NO_x (1 %) and low NO_x (30 %). The isoprene SOA yield of 15 % is an annual global mean including many regions with lower NO_x levels. Sinks of the precursor gases are chemical loss including photolysis, dry and wet deposition. The main portion of precursors is destroyed chemically, the second most important sink is gas-phase wet deposition. Aerosols can be lost via three processes in ECHAM-HAMMOZ, via sedimentation, dry and wet deposition. Just 0.2 TgC of iSOA are removed by sedimentation, thus to keep a clear structure it is not included in figure 4.4. The main loss of iSOA is wet deposition removing 54.7 TgC of the total 56.7 TgC.

Table 4.2 shows the iSOA budget in Tg for comparison with the mean values of the AeroCom (Aerosol Comparisons between Observations and Models) models given in Tsigaridis et al. [2014]. As can be seen from Table 4.2, the iSOA production of ECHAM-HAMMOZ in the reference simulation exceeds the total SOA of the AeroCom models in the upper third quartile limit. Even if this comparison here seems to show a vast overestimation by ECHAM-HAMMOZ 56.7 TgC, iSOA do not reach the lower end of the top down estimated source strength ranging from $140 - 910\,\mathrm{TgC\,a^{-1}}$ [Goldstein and Galbally, 2007, Hallquist et al., 2009]. Therefore, according to these studies, the AeroCom models generally produce too little SOA, while our new approach might lead to more realistic SOA concentrations. Using the range of $140 - 910\,\mathrm{TgC\,a^{-1}}$ for total SOA and our iSOA production of $56.7\,\mathrm{TgC\,a^{-1}}$ would imply that isoprene contributes between 6 % and 40 % to total SOA. This does not seem unrealistic. SOA loss is stronger in ECHAM-HAMMOZ as well. Dry deposition and wet deposition are higher than the AeroCom mean value. These higher deposition values are partially explained by the high iSOA burden in ECHAM-HAMMOZ, but comparing the SOA lifetime range of AeroCom models to ECHAM-HAMMOZ, it is clear that ECHAM-HAMMOZ simulates a stronger deposition sink. The AeroCom mean SOA lifetime is 8.2 days, while ECHAM-HAMMOZ iSOA lifetime is 3.7 days. Another difference is ECHAM-HAMMOZ wet deposition. It is more than ten times higher than dry deposition, something that is not seen in the AeroCom models. First, this might point to a too low aerosol dry deposition in ECHAM-HAMMOZ. Second, high wet deposition might be caused by moisture and convection overestimation of ECHAM6 in the tropical regions where most of iSOA is formed. Finally, the iSOA burden in ECHAM-HAMMOZ is also higher than the mean of AeroCom models, despite the quick wet deposition loss.

As stated in Hodzic et al. [2016], global models are missing aerosol sinks, like in-particle fragmentation and particle photolysis and should therefore overestimate SOA formation. On the contrary, global models tend to underestimate SOA formation. The comparison of ECHAM-HAMMOZ iSOA to total SOA of other models shows that the criticized underestimation can be resolved with an explicit formulation of SOA precursors, since no SOA from aromatics or terpenes is considered in this study. Including semi-explicit chemistry and explicit partitioning leads to a high isoprene SOA yield in ECHAM-HAMMOZ, which motivated several sensitivity runs (section 5).

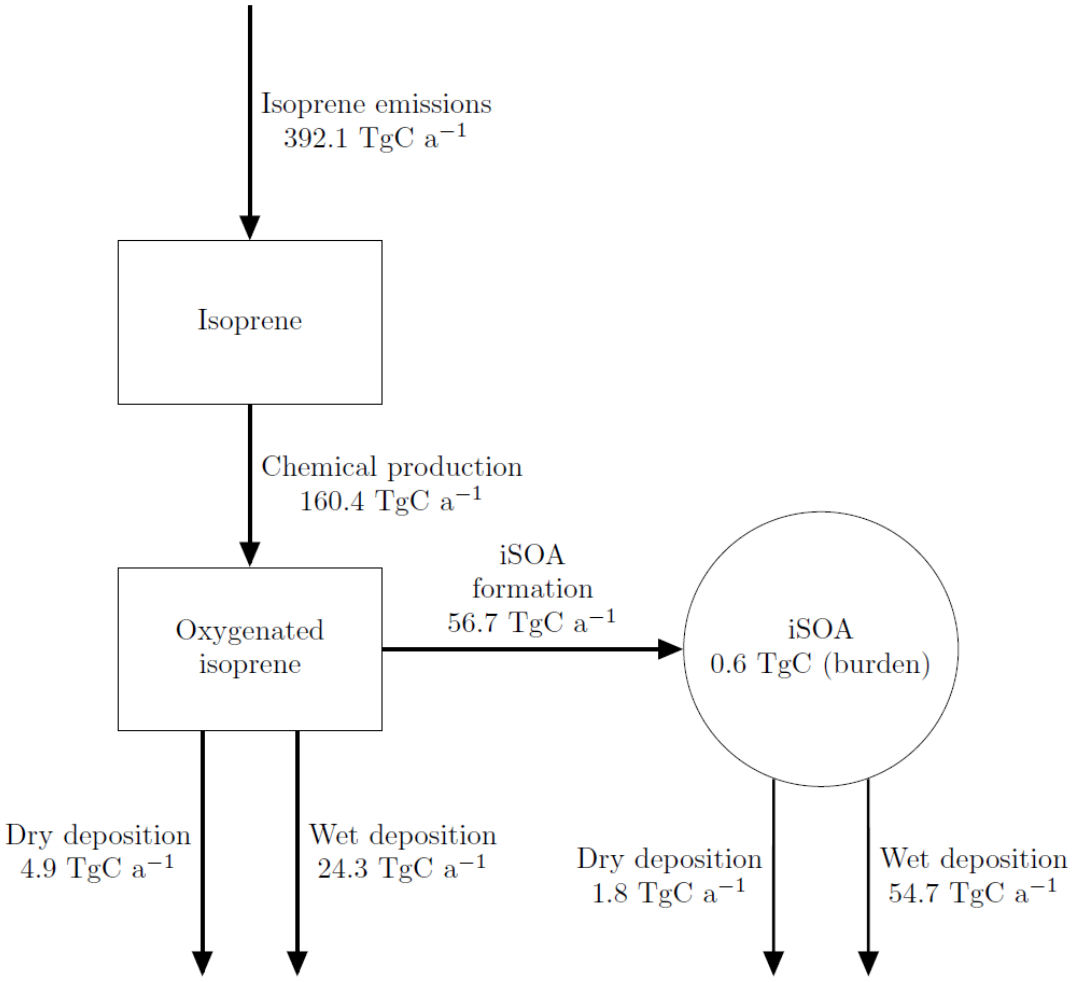

Figure 4.4.: Global budgets for isoprene derived secondary organic aerosol and its precursors (sources/sinks in TgC a^{-1} and burden in TgC) predicted by ECHAM-HAMMOZ reference simulation RefBase for 2012. For details about the individual compounds see table 4.1.

Table 4.2.: Comparison of the ECHAM-HAMMOZ iSOA budget to total SOA budget terms from AeroCom models mean value in OA budgets (Tsigaridis et al. [2014], personal communication).

	ECHAM-HAMMOZ	AeroCom mean	AeroCom range
Sources	138.5 $\mathrm{Tg\,a^{-1}}$	36.3 $\mathrm{Tg\,a^{-1}}$	12.7–120.8 $\mathrm{Tg\,a^{-1}}$
Dry deposition	4.4 $\mathrm{Tg\,a^{-1}}$	5.7 $\mathrm{Tg\,a^{-1}}$	1.4–14.5 $\mathrm{Tg\,a^{-1}}$
Wet deposition	133.6 $\mathrm{Tg\,a^{-1}}$	47.9 $\mathrm{Tg\,a^{-1}}$	12.4–113.1 $\mathrm{Tg\,a^{-1}}$
Burden	1.4 Tg	1.0 Tg	0.3–2.3 Tg
Lifetime	3.7 days	8.2 days	2.4–14.8 days

4.1.4. iSOA daily cycle

In section 4.1.2, the highest iSOA surface concentrations were simulated over tropical regions, where highest isoprene emissions are found. To get an impression of iSOA evolution in time, average days over three tropical regions are shown in figures 4.5, 4.6 and 4.7. Not only iSOA and its precursors are given, but also OH concentrations, surface temperature and SAD. OH concentrations are important, because most of iSOA precursors are produced via the OH initiated isoprene oxidation pathway and require more OH and HO_2 to be produced. Moreover, time is given in local time for the corresponding regions. OH concentrations and temperature indicate the local daily cycle with highest incoming solar radiation. SAD represents the total surface area density provided by iSOA and other pre-existing aerosol for iSOA formation. The month of July was chosen for the evaluation, because it lies in the time period evaluated in section 4.1.2 for the single iSOA components.

The region with highest iSOA concentrations is the Amazon basin (figure 4.5). The concentrations of iSOA do not vary much over the average day and stay around 5 $\mu\mathrm{g\,m^{-3}}$. More variability can be found in iSOA precursor gases. Isoprene is quickly oxidized by OH during daytime, because OH is produced by photolysis. Thus, isoprene concentrations are lowered by oxidation while iSOA precursors, which are produced by this oxidation, increase. Once OH starts rising, mainly LIEPOX and IGLYOXAL are found in the gas-phase. Therefore, a daily cycle of iSOA precursors which correlates to OH can be seen in the average day (∼8:00 AM – 8:00 PM). During night (∼9:00 PM – 7:00 AM), no OH is available and precursor gas production stops. Furthermore, isoprene concentration increases once OH concentration decreases around 21:00 UTC. The temperature and SAD are anti-correlated. SAD tends to be higher, when temperature is lower. A lower temperature and higher SAD favors iSOA formation, but only very few precursor gases are produced during the nighttime. Existing iSOA precursors continue partitioning/reactive uptake during night, but are also lost due to dry deposition. The anti-correlation between temperature and SAD indicates the collapse of the planetary boundary layer during night, which also favors deposition loss. Aerosols and gases decrease during the average night until the next day starts and produces fresh iSOA.

Similar patterns are found over the Kongo (figure 4.6) region and Indonesia (figure 4.7). In Indonesia, iSOA concentrations have nearly no variability, but precursors concentrations follow OH. Also, isoprene concentrations peak after OH is declined. Again, SAD and temperature are clearly anti-correlated. The Kongo shows the highest variability in iSOA concentrations of nearly 2 $\mu\mathrm{g\,m^{-3}}$ during the average day. The drop in iSOA occurs during dawn, before

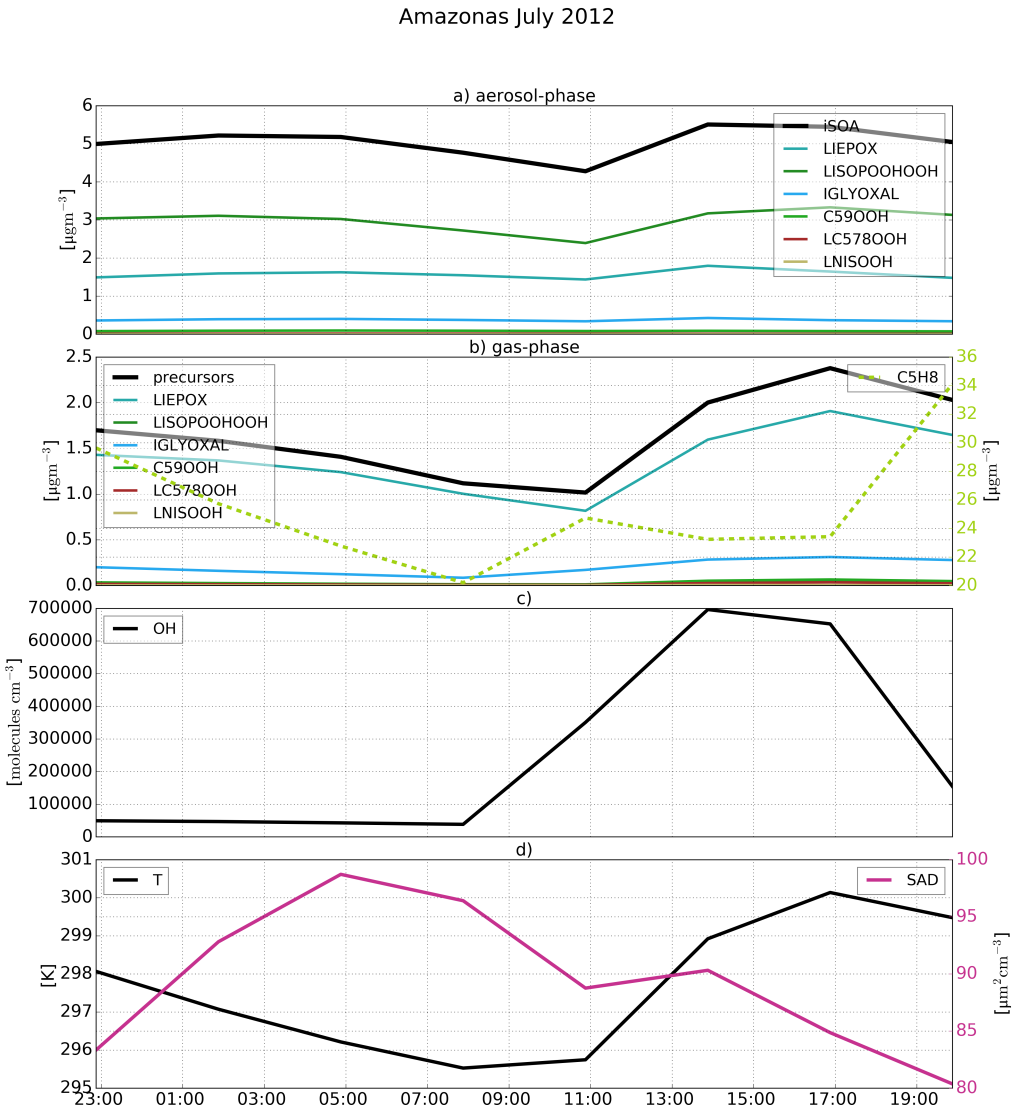

Figure 4.5.: An average day in the Amazon basin for iSOA, iSOA precursors, OH, temperature and SAD in July 2012. The Amazon basin, in this plot, is a field mean within the boundaries: 2.5°N 74°W, 2.5°N 53°W, 11°S 74°W, 11°S 53°W. The aerosol-phase plot (a) shows total iSOA in black and individual components in green/blue. The same colors are chosen to show gas-phase precursor concentrations in the plot (b). Moreover, gas-phase concentrations of isoprene itself are shown as well. Plot (c) shows OH concentration given in molecules cm^{-3}. Plot (d) gives temperature in K and SAD in $\mu\mathrm{m}^2\,\mathrm{cm}^{-3}$.

temperature starts rising and precursor gases are formed. This drop can also be found in Indonesia and the Amazon, but not as clear as over the Kongo.

A key difference between the three regions is the isoprene concentration and as a consequence iSOA levels. Over the Amazon isoprene concentrations are three times higher than over the Kongo and Indonesia. This is also visible in iSOA levels, which reach $5\,\mu g\,m^{-3}$ in the Amazon, while in Kongo concentrations up to $3.5\,\mu g\,m^{-3}$ and over Indonesia up to $1.2\,\mu g\,m^{-3}$ are simulated. The low values over Indonesia can be explained by the field mean also containing some regions of ocean, while the Amazon and Kongo regional means are completely over land. Another large difference between the regions is SAD. Lowest SAD is simulated over the Amazon, slightly higher values are reached over Indonesia, but the Kongo has high SAD values of up to $460\,\mu m^2\,cm^{-3}$. These values are caused by high biomass-burning emissions in July in

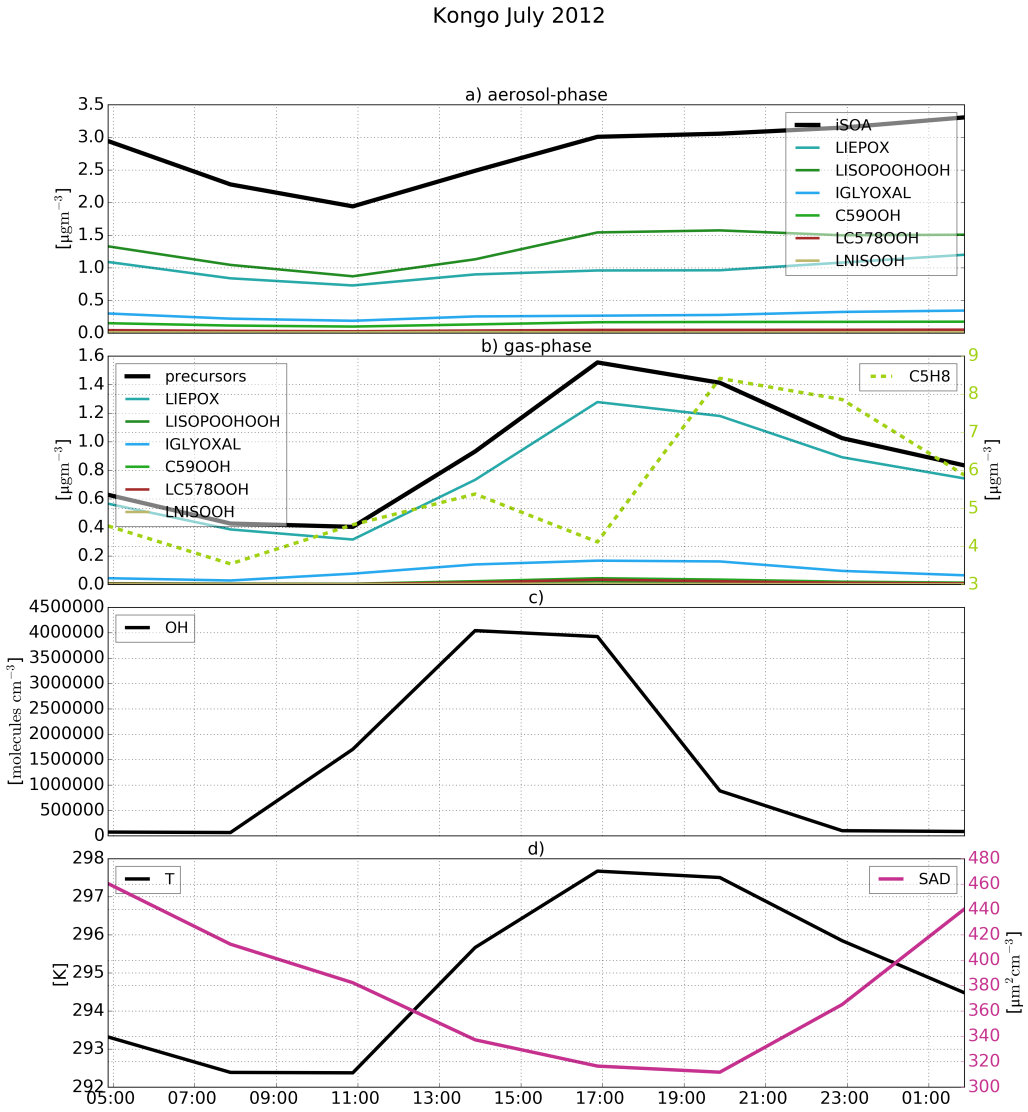

Figure 4.6.: Same as figure 4.5. The Kongo in this plot is a field mean within the boundaries: 8°N 15°E, 8°N 34°E, 10°S 15°E, 10°S 34°E.

the Kongo. The reader should note that variation is lost in exchange to representability. The mean values are accounted as more robust and thus shown here. Although the especially the Kongo region and the Amazon basin differ in terms of NO_x emissions (the radical chemistry is analyzed in the following section 4.1.5), the iSOA composition does not vary significantly. Figure 4.8 shows the average fractions of the three main contributors to iSOA. The largest fraction in all regions is taken by LISOPOOHOOH of up to 0.6, followed by LIEPOX of around 0.3. The IGLYOXAL is around 0.1 for all regions, thus these three fraction sum up to around one, explaining nearly all iSOA, with only small variations between the regions. The Kongo region has slightly more LIEPOX and IGLYOXAL in the particle-phase and less LISOPOOHOOH. This is explained by the biomass burning season, see section 4.1.5.

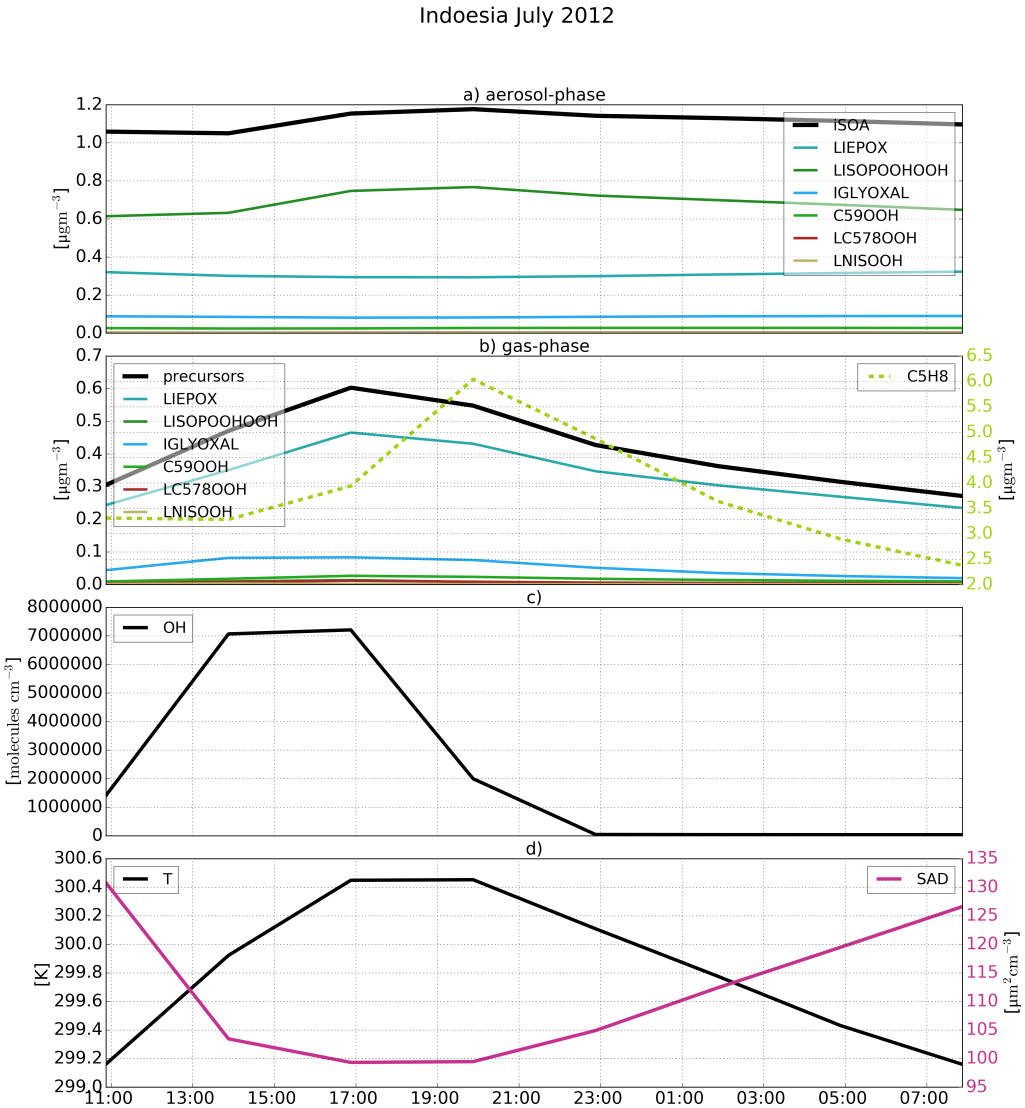

Figure 4.7.: Same as figure 4.5. Indonesia in this plot is a field mean within the boundaries: 9°N 94°E, 9°N 126°E, 9°S 94°E, 9°S 126°E.

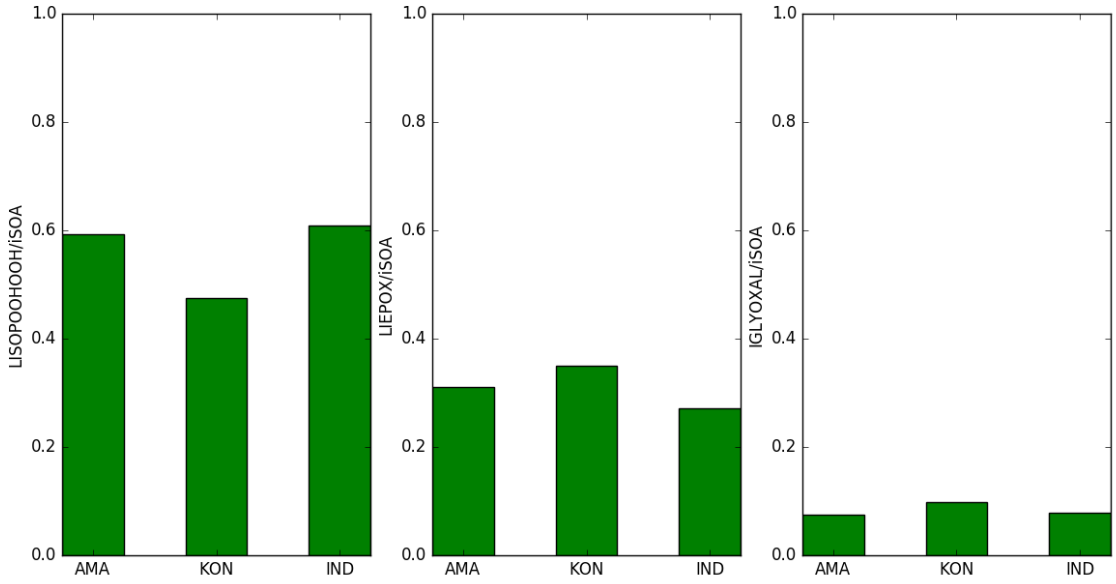

Figure 4.8.: Average fraction of the three most important iSOA compounds to total iSOA in the three regions defined in figures 4.5, 4.6 and 4.7 for the month of July 2012. Abbreviations: AMA = Amazon basin, KON = Kongo region, IND = Indonesia.

Nevertheless, not all model features and processes can be identified if only averages are evaluated. Therefore, the next section evaluates 3-hourly values in grid-boxes instead of regional averages.

4.1.5. iSOA formation in different chemical regimes

As described in section 2.4.1, isoprene oxidation products depend on radicals predominant in the ambient atmosphere, because different oxidation pathways lead to different products. These products differ in physico-chemical properties, thus some form iSOA and others do not. To explore the impact of different radical concentrations on iSOA formation, two grid-boxes are compared. One in the middle of the Amazon (6.1°S, 68.2°W) and a second including Sao Paulo (22.4°S, 46.4°W). In order to see a clearer isoprene product distribution, not the surface layer is shown, but a near surface layer at around 950 hPa. The grid-boxes were chosen in space and time according to radicals present. The Amazon is a pristine regions where NO values are low throughout the year, thus another grid-box had to be picked. For this reason, Sao Paulo was chosen during the biomass burning season.

To evaluate the impact of ambient radicals on isoprene oxidation in ECHAM-HAMMOZ, ISOPO2 chemical pathways are evaluated. Initial isoprene oxidation with OH lead to ISOPO2 production, which is the major pathway during daytime in ECHAM-HAMMOZ. ISOPO2 is important for production of C59OOH, LC578OOH, LIEPOX and LISOPOOHOOH, it can undergo several reactions: 1) self-reactions, 2) reaction with HO_2, 3) isomerization reactions, 4) reaction with NO. An overview over chemical pathways of ISOPO2, required oxidants and products is shown in figure 4.9. As can be seen, the pathways lead to 1) LC578OOH, C59OOH, 2) LIEPOX, LISOPOOHOOH, 3) HO_2 recycling and no iSOA precursors, 4) LC578OOH, C59OOH. Pathway 1) has a minor contribution since collision of two ISOPO2 is more unlikely than with

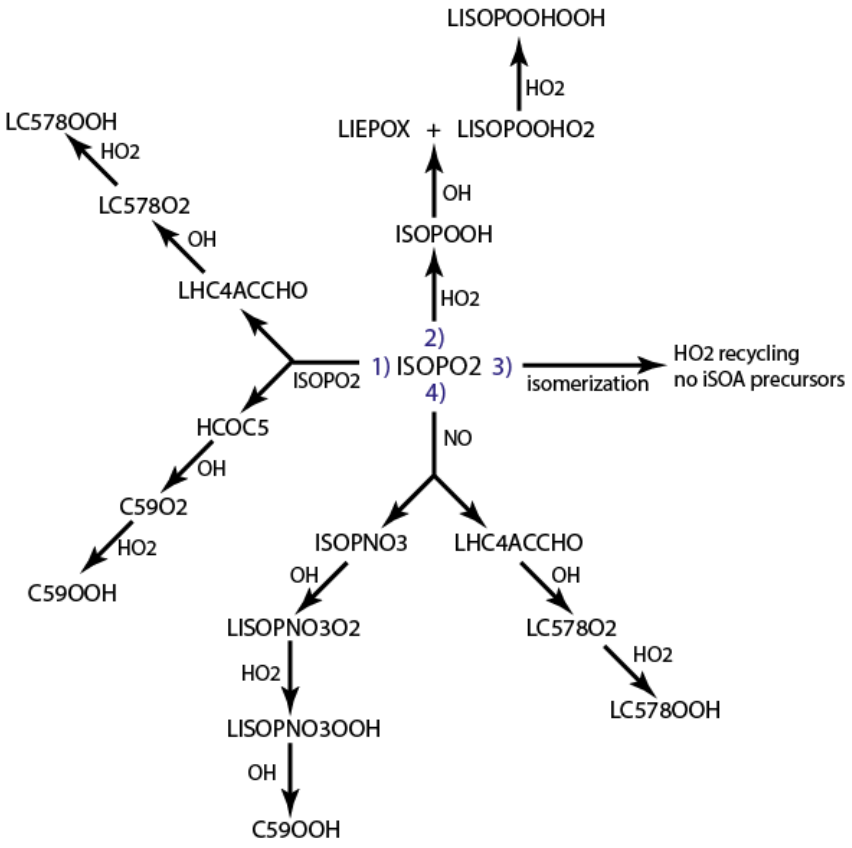

Figure 4.9.: Reaction pathways of ISOPO2 numbered according to the text. Here, intermediate compounds are depicted leading to iSOA precursor production. Pathway 1) is not further discussed, because of its minor contribution of 5–10%. The importance of 2), 3) and 4) is assessed in figures 4.10 and 4.11 for different regions. Production of the final iSOA precursor takes two to three oxidation steps.

other radicals or unimolecular isomerization. The radical mixing ratios control which reaction pathway is taken by ISOPO2. To assess the importance of each reaction, the ratio of a single pathway to the sum of the pathways 2), 3) and 4) is calculated. This is expressed using the reaction rate coefficients times the radical concentration $k_{m,X_i}[X_i]$, where m is the molecule which is oxidized by the radical X_i and $[X_i]$ is the concentration of X_i. For unimolecular reactions, like isomerization reactions, no concentration of X_i is needed. In this case here, the importance of ISOPO2 reactions is expressed by:

$$\frac{k_{\mathrm{ISOPO2},j}[\mathrm{X}_j]}{\sum_i k_{\mathrm{ISOPO2},i}[\mathrm{X}_i] + k_{\mathrm{ISOPO2},isomerization}}, \tag{4.1}$$

where j, i = NO, HO_2. Equation (4.1), without any radical concentration $[\mathrm{X}_j]$, is used to calculate the importance of the unimolecular, isomerization reaction:

$$\frac{k_{\mathrm{ISOPO2},isomerization}}{\sum_i k_{\mathrm{ISOPO2},i}[\mathrm{X}_i] + k_{\mathrm{ISOPO2},isomerization}} \tag{4.2}$$

Equations (4.1) and (4.2) give fractions between 0 and 1, describing which reaction pathway is the strongest and thus the dominant one. Not shown are self-reactions (pathway 1), which are a minor pathway between 5–10%. Following notation for the ratios of each pathway is used: equation (4.1) for NO is called w_{no}, for HO_2 w_{ho_2} and equation (4.2) w_{iso}.

Figure 4.10 and 4.11 a) show the relative production strength of one iSOA precursor to overall precursor production, b) shows NO and OH mixing ratios, c) predominant reaction pathways of ISOPO2 in terms of equations (4.1) and (4.2) and d) the ratio of iSOA to total aerosol including

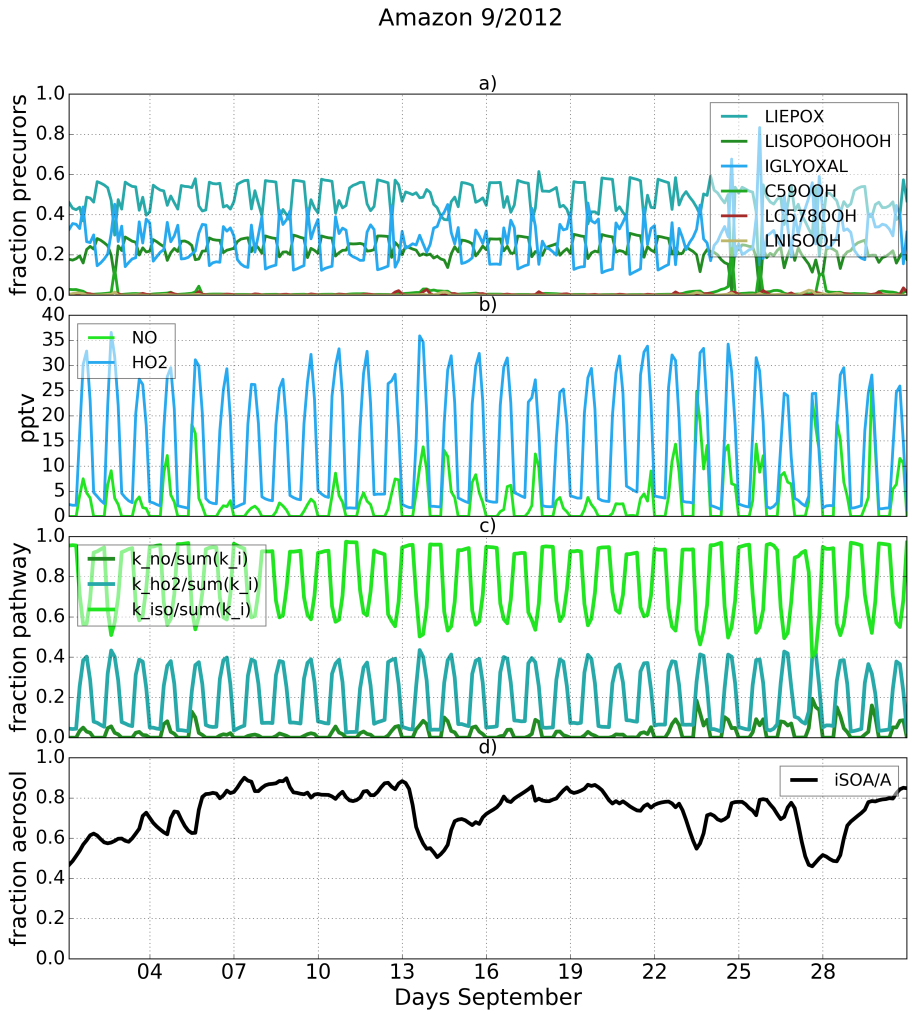

Figure 4.10.: Daily iSOA precursor production as fraction of total production of iSOA precursors from gas-phase chemistry ((mol mol s^{-1})(mol mol s^{-1})$^{-1}$) (a), radical mixing ratios of HO_2 and NO in volume mixing ratio pptv (b), ratio of reaction rate coefficients to total possible reactions excluding self-reactions (c), and ratio of iSOA to total aerosol (organic + inorganic). Grid-box including the Amazon (6.1°S, 68.2°W) in September 2012. The time resolution is 3 hourly, thus 8 values per day.

iSOA. Figure 4.10 b) shows that in the Amazon very low values of NO (maximum 25 pptv) are reached daily during September 2012. NO levels are always lower than HO_2, reaching 35 pptv. Accordingly, this also shows up in the fractions of their reaction rate coefficients (figure 4.10 c)). The overall dominant pathway is the isomerization pathway w_{iso} alternating between ~0.6 and ~0.95. During night, w_{iso} reaches ~0.95, because NO is not produced and HO_2 is only produced in small amounts, e.g via ISOPO2 isomerization and other H-shift reactions. During the day, w_{iso} is only slightly more dominant than w_{ho_2}. As expected from low NO mixing ratios, w_{no} is not dominant in the Amazon. This results in a chemical production of mainly LIEPOX, IGLYOXAL and LISPOOHOOH (figure 4.10 a), while LISPOOHOOH and LIEPOX production is relatively stronger during daytime and IGLYOXAL is produced during nighttime. The other three products usually contribute less than 1 % to total precursor production. Finally, figure 4.10 d) shows the fraction of iSOA to total aerosol, which is up to 90 % in the Amazon.

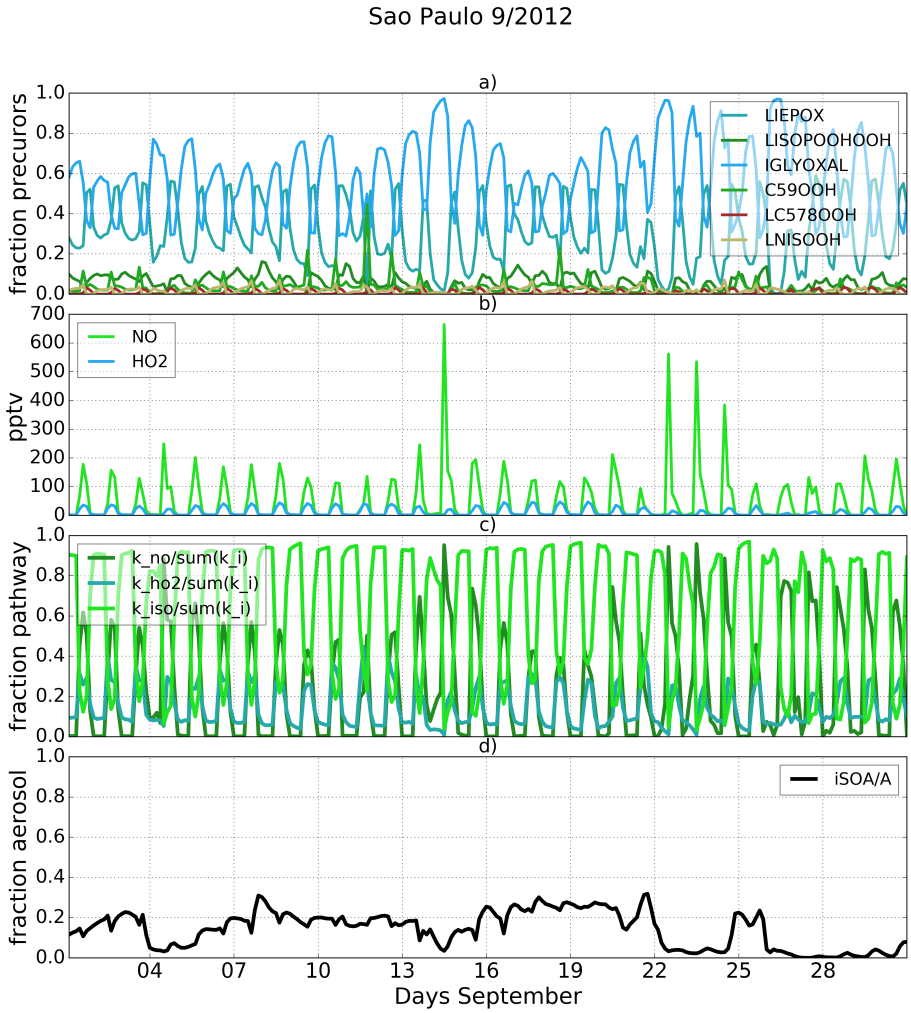

Figure 4.11.: Same as figure 4.10, but for grid-box including Sao Paulo (22.4°S, 46.4°W).

Figure 4.11 b) shows the reaction pathways for Sao Paulo highlighting the differences between both grid-boxes. NO mixing ratios are higher, usually of over 100 pptv each day, with peaks of over 400 pptv. These NO levels are needed for the reaction of ISOPO2 and NO to be competitive to the one with HO_2, as can be seen in figure 4.11 c). The ratio w_{no} reaches values between 0.5 and 0.9 during daytime showing that reaction of NO is dominant. Nevertheless, during night the same applies here, like in the Amazon, w_{iso} shows that isomerization is the dominant reaction followed by small contributions of $w_{ho_2} \cong 0.1$. The relative production of precursors in 4.11 a) differs significantly showing that mainly IGLYOXAL is produced during daytime, in contrast to nighttime IGYLOXAL production in the Amazon. On 15$^{\text{th}}$ of September, NO reaches mixing ratios of 700 pptv, thus mainly IGLYOXAL is produced. At the same time, LIEPOX production is suppressed nearly going to zero. Otherwise, it varies between 0.2 and 0.5. LC578OOH, LNISOOH and C59OOH production rates are higher than in the Amazon, but still these products make a minor contribution to iSOA. In the Sao Paulo grid-box, iSOA contributes up to 30 % of total aerosol. The reader should note that this aerosol can be transported there, thus compounds in the aerosol were not evaluated.

From the comparison of two grid-boxes with different ambient radical concentrations, it can be seen that JAM3 captures the influence of the predominant radical concentration on isoprene product distribution. According to literature (section 2.4.1), sufficiently high NO mixing ratios suppress iSOA formation [Surratt et al., 2006]. To completely suppress IEPOX and LISOPOOHOOH production, NO values of at least 400 pptv are needed (appendix B.6). NO_x suppression will be further discussed in section 5.4.

4.2. Comparison with observations

In order to evaluate how much of total organic aerosol (OA), including primary and secondary organic aerosol, is related to iSOA, iSOA concentrations and O:C ratios from ECHAM-HAMMOZ are compared to atmospheric Aerosol Mass Spectrometry (AMS) measurements from different field campaigns given in table 4.3. Measurements were selected from AMS global database [Zhang et al., last accessed on 22.09.2017] according to the availability of elemental ratios. Campaigns took place mainly either in Europe or North America and include six different countries. In Helsinki, Finland, winter and spring measurements are available.

Figure 4.12 a) shows the quartiles of the time series of the concentrations in the different locations, from left to right first the four European data sets and then the American ones. The European data sets display a diversity of local OA sources. For Helsinki, Carbone et al. [2014] report a variety of local sources for OA including biomass burning, traffic, coffee roaster and also SOA from long range transport. In Mace Head, two different OA types are measured depending on the advection of either marine air or continental air [Dall'Osto et al., 2009]. Saarikoski et al. [2012] identified a complex mixture of OA with local and regional sources, mainly from anthropogenic origin, in Po Valley. For Finland, Ireland and Italy, ECHAM-HAMMOZ reveals a minor contribution of iSOA to OA. This can be explained by the measurement time periods in winter or early spring. During these seasons, vegetation in Europe does not emit large isoprene amounts [Steinbrecher et al., 2009].

Looking at the concentrations measured in Houston Texas, USA, it can be seen that a great part of the variability is captured by iSOA, which is explained by high isoprene emissions found in Southeastern US. ECHAM-HAMMOZ median and percentiles are still lower than the observations since the observation includes total OA. The organic aerosol in Mexico City

Table 4.3.: Overview of ambient measurement locations, time periods, number of observation (n_o) and corresponding model (n_m) data points and references. For Helsinki, there are two time series, one during winter (W) and the second during spring (S).

Location	Observation period yyyy-mm-dd – yyyy-mm-dd	n_o	n_m	Reference
Helsinki, Finland	2009-01-08 – 2009-03-14 (W)	497	176	Carbone et al. [2014]
(60.2° N, 24.95° E)	2009-04-09 – 2009-05-08 (S)	13767	233	Timonen et al. [2010]
Mace Head, Ireland	2009-02-25 – 2009-03-26	4020	227	Dall'Osto et al. [2009]
(53.33° N, 9.99° W)				
Po Valley, Italy	2008-03-31 – 2008-04-20	454	171	Saarikoski et al. [2012]
(44.65° N, 11.62° E)				
Houston, USA	2000-08-15 – 2000-09-15	544	246	Zhang et al. [2007]
(29.8° N, 95.4° W)				
Mexico City, Mexico	2006-03-10 – 2006-03-30	2778	180	Aiken et al. [2009, 2010]
(19.48° N, 99.15° W)				
Manaus, Brazil	2008-02-06 – 2008-03-13	4565	282	Chen et al. [2009]
(2.58° S,60.2° W)				Pöschl et al. [2010]
				Martin et al. [2010]

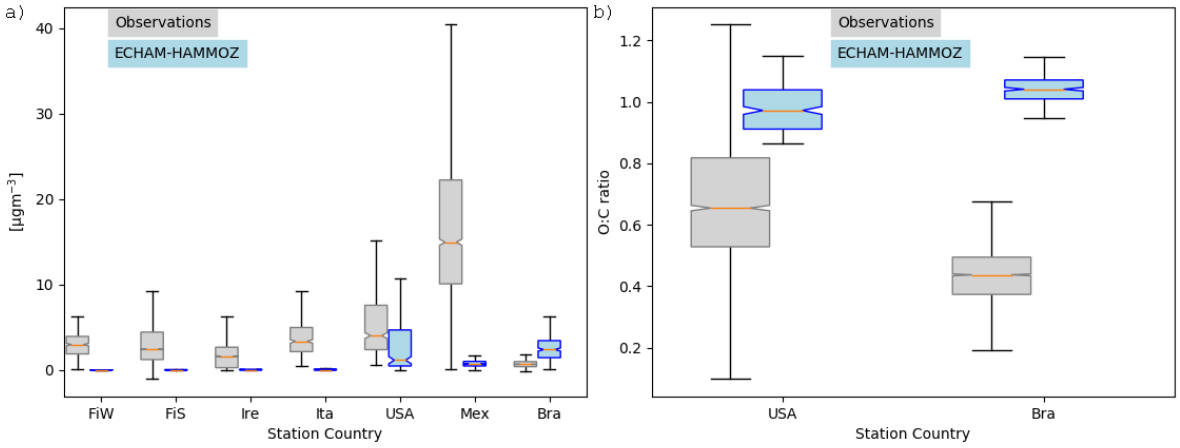

Figure 4.12.: Box plots showing the variability of concentrations measured and corresponding instantaneous values from ECHAM-HAMMOZ (left, a). Countries of measurement campaigns are given. First, European countries then American ones. The shortcuts refer to: FiW=Helsinki, Finland (Winter), FiS=Helsinki, Finland (Spring), Ire=Mace Head, Ireland, Ita=Po Valley, Italy, USA=Houston Texas, USA, Mex=Mexico City, Mexico, Bra=Manaus, Brazil. The model time resolution is three hours, whereas all observed values have a higher time resolution (see table 4.3 for the number of observed values). For Houston Texas, USA and Manaus, Brazil, the corresponding O:C ratios shown (right, b). These values are corrected by the factor 1.27 according to Canagaratna et al. [2015].

was measured at an urban super-site and covers such a big range of concentrations, which are dominated by anthropogenic emissions including biomass burning, nitrogen containing OA and primary hydrocarbon-like OA associated with traffic [Aiken et al., 2009]. According to the concentrations simulated by ECHAM-HAMMOZ, just a minor part of these can be explained by iSOA. Manaus, Brazil, is located in the Amazon Basin and is classified as a pristine environment close to pre-industrial conditions [Pöschl et al., 2010, Martin et al., 2010]. Therefore, the particles are nearly pure biogenic and Martin et al. [2010] report an upper limit of 5 % primary organic aerosol. These conditions are ideal to compare them to ECHAM-HAMMOZ, which only includes SOA from isoprene, because isoprene emissions are high in the Amazon Basin and should dominate the OA there. As can be seen in figure 4.12 a), ECHAM-HAMMOZ simulates overall higher iSOA concentrations than OA concentrations measured. Moreover, higher peak values are simulated and the median is higher than the upper 1.5 inter-quartile range whisker of observed concentrations.

For Houston Texas and Manaus, ECHAM-HAMMOZ relates a great part of the OA to iSOA, to further investigate this, O:C ratios are compared as well. Due to only isoprene based iSOA formation in ECHAM-HAMMOZ of different highly oxidized molecules with molecular O:C ratios between 0.6 and 1.4, the modeled O:C ratio is around 1 in both regions and has little variability, see figure 4.12 b).

The comparison of ECHAM-HAMMOZ with the concentration spectrum in Houston Texas shows that a great part of OA can be attributed to iSOA. This modeled subset covers upper values of the O:C ratio between 0.8 and 1.1, which still lie within the 75^{th} percentile and the upper 1.5×IQR whisker of the measured data. This is related to the fact of missing SVOC and IVOC usually having lower O:C ratios and the contribution of POA to OA, which is not included in this comparison, because no assumptions of POA O:C ratios are made.

In contrast, the OA measured in Manaus, located in the Amazon Basin, which consists of 95 % SOA does not show as high O:C ratios as iSOA modeled by ECHAM-HAMMOZ. The median of observed aerosol lies at 0.4, instead of 1. Certainly, part of it is explained by missing SVOC and IVOC in ECHAM-HAMMOZ, but might also be related to SOA from other organic molecules than isoprene. For Manaus, an overestimation of iSOA concentrations by the model might be related to mistakes in isoprene emissions, incompleteness of the chemical mechanism, missing sink processes and uncertainties in volatility. In terms of O:C ratio, modeled iSOA O:C ratios tange between 0.6 and 1.4. The simulated O:C values are covered by the ambient values in Houston Texas, but not in Manaus. This points to SVOC, IVOC and SOA from other sources than isoprene.

To summarize, isoprene emissions are not dominating OA in Europe, therefore the model shows iSOA having a small contribution to concentrations there. In contrast, American OA may consists to a large portion of iSOA, especially in USA and Brazil.

5. Discussion

In chapter 4, results of ECHAM-HAMMOZ novel SOA formation scheme were presented. These results show that ECHAM-HAMMOZ is capable of forming large amounts of iSOA, which improve the surface area density compared to satellite observations and explain a large portion of SOA in Southeastern US. Nevertheless, the iSOA budget comparison to AeroCom models' budgets as well as the comparison of ECHAM-HAMMOZ iSOA to OA measurements in the Amazon point to an overestimation in SOA formation by ECHAM-HAMMOZ. Particle iSOA concentrations seem quite high, taking into account that possible isoprene IVOC were excluded. Hodzic et al. [2016] claim that a stronger production and stronger removal processes can close the gap between atmospheric SOA observations and model studies. Currently, several SOA sinks are ignored by global models. These removal processes include fragmentation, aqueous-phase reactions and in-particle photolysis. As seen in section 4.1.3, iSOA production in ECHAM-HAMMOZ is stronger, resulting in high concentrations of iSOA. Including more aerosol sinks, following Hodzic et al. [2016], should reduce these rather high iSOA concentrations, without lowering the SOA production rate. To explore and finally explain why ECHAM-HAMMOZ forms too large amounts of iSOA motivated several sensitivity simulations. The additional information obtained by these tests, on one hand gives insights in atmospheric processes and on the other hand points to strengths and limitations of ECHAM-HAMMOZ in modeling the real atmosphere.

5.1. Impact of iSOA formation on atmospheric chemistry

This section intents to explore the impact of removal of iSOA precursors on the atmospheric chemistry in MOZ. Several oxidation steps are needed to produce the isoprene SVOC and LVOC, which are further oxidized or transformed (Section 3.5). Thus, they take part in atmospheric chemistry or are lost due to deposition. There is a connection among the iSOA precursors, as shown in figure 3.2 (reaction (R6)). LISOPOOHOOH reaction with particle OH leads to LC578OOH formation. Due to LISOPOOHOOH's rather low volatility in ECHAM-HAMMOZ, it is mainly found in the particle-phase (see figure 4.3 d). There is no in-particle chemistry in ECHAM-HAMMOZ, thus LISOPOOHOOH cannot react with OH to form LC578OOH in the given configuration of the model.

The chemical production terms of iSOA precursors resulting from global diagnostics over the whole year 2012 for RefBase and the simulation without iSOA formation "noiSOA" are shown in table 5.1. The reader should note, that iSOA formation impacts isoprene emissions. The biogenic emission module MEGAN calculates isoprene emissions depending on incoming solar radiation, among other atmospheric variables. Including iSOA formation leads to larger aerosols which interact with direct solar radiation and decrease the amount reaching the surface. Less direct radiation leads to lower isoprene emissions, in ECHAM-HAMMOZ this is a difference of 10 TgC between the model simulations including iSOA and neglecting it. Higher/lower isoprene emissions itself lead also to a higher/lower isoprene oxidation product production rates. To account for the different emissions, relative numbers are given in brackets. ECHAM-HAMMOZ

Table 5.1.: Isoprene emissions (in TgC) and chemical production of individual gas-phase iSOA precursors in the reference run and sensitivity run called "noiSOA" without SOA formation (see table 3.3 for the sensitivity run description). In the parenthesis, the resulting overall annual global yield is shown.

Emissions TgC		
Specie	RefBase	noiSOA
Isoprene	392.1	402.1

Chemical production TgC (yield %)				
Specie	RefBase		noiSOA	
LIEPOX	94.0	(24 %)	97.5	(24 %)
IGLYOXAL	19.9	(5 %)	21.4	(5 %)
LISOPOOHOOH	35.1	(9 %)	46.6	(12 %)
C59OOH	6.5	(2 %)	10.3	(3 %)
LC578OOH	4.5	(1 %)	23.7	(6 %)
LNISOOH	0.5	(0.1 %)	0.6	(0.1 %)

simulates an aerosol effect which is not unknown. The climate effect of lower incoming direct solar radiation due to interactions with aerosols is known as "global dimming" [Wild et al., 2005, Wild, 2009, 2016].

Table 5.1 shows that the highest relative and absolute change in chemical production comparing RefBase to noiSOA can be seen in LC578OOH as expected from reaction (R6). 19.2 TgC (5 %) more LC578OOH are produced when turning off iSOA formation. Except for LC578OOH, iSOA formation does not have major impacts on the atmospheric chemistry in MOZ. In addition to the iSOA precursors itself, oxidation capacity of the atmosphere in RefBase and noiSOA were compared. Species influencing global oxidation capacity are methane, methyl chloroform and the hydroxyl radical. Methane and methyl chloroform are long lived species which are degraded slowly by OH. Global models give these lifetimes to compare chemical mechanisms within each other. Methane, and methyl chloroform lifetime and global mean OH concentration in ECHAM-HAMMOZ do not differ significantly between the model runs RefBase and noiSOA. Therefore, oxidation capacity of the modeled atmosphere is not changed significantly by additional loss of hydrocarbons forming secondary organic aerosol.

5.2. Comparison to pseudo chemistry iSOA

Many global climate models exclude chemical calculations, because they quickly become computationally expensive when the number of species and reactions is increased. Nevertheless, to simulate the direct and indirect effects of clouds, SOA formation is needed. Therefore, state-of-the-art aerosol models include the volatility basis set (VBS) approach to resolve some complexity of SOA formation without including large chemical mechanisms or knowledge of individual species. The volatility basis set treats saturation vapor pressures in a uniform set of classes to distribute the organic material accordingly [Donahue et al., 2006, 2011, 2012]. As explained in section 3.3, ECHAM-HAM, coupled with SALSA in its base version, has a module to simulate SOA formation via the volatility basis set approach. To form the corresponding

gas-phase precursors, a pseudo chemistry prescribing yields to the different volatility classes is used. To compare the semi-explicit chemistry and explicit compound-wise partitioning to the pseudo chemistry and VBS system, an ECHAM-HAM run (RefVBS) was performed. RefVBS only includes isoprene emissions and no other VOC to form exclusively iSOA, as it is done in RefBase. From these isoprene emissions ECHAM-HAM produces gas-phase compounds which are lumped together in the VBS classes 0, 1 and 10. These VBS classes are defined as such, that, for example, VBS0 refers to compounds with a saturation concentration on a logarithmic scale of $\log_{10}(C^0) = 0$. VBS0 is the class with the lowest volatile compounds in RefVBS. More volatile compounds are grouped in VBS1 and intermediate volatile compounds are classified as VBS10. Therefore, intermediate volatile compounds of the class VBS10 are included in RefVBS, which lack in RefBase. Conversely, ECHAM-HAM does not include IEPOX and glyoxal SOA, thus these two compounds are not included in this comparison. If iSOA precursors in ECHAM-HAMMOZ were classified in terms of VBS, LNISOOH, C59OOH and LC578OOH would be in VBS1, while LISOPOOHOOH would be classified as VBS0 or would need a new class for negative values. Total iSOA formed by partitioning including IVOC and SVOC from ECHAM-HAM RefVBS is compared to iSOA from LISOPOOHOOH, LC578OOH, C59OOH and LNISOOH in ECHAM-HAMMOZ RefBase.

The formed precursors in the gas-phase from RefVBS and RefBase are shown in figure 5.1 (a) and (b) for comparison. From the higher gas-phase concentrations, it can be seen that the VBS system (b) also includes compounds with higher volatility. The emission pattern of MEGAN is only visible in RefVBS (b), because very low precursor concentrations in RefBase (a) mask isoprene emitting areas in this plot.

As can be seen in figure 5.1 c), iSOA concentrations in RefBase are overall higher and iSOA is transported horizontally over longer distances than iSOA formed by ECHAM-HAM RefVBS (d), although the precursor gas-phase concentrations in RefBase are lower (a) than in RefVBS (b). RefBase iSOA precursors quickly partition into the particle-phase and are therefore not found in the gas-phase in high concentrations. Local particle-phase maxima match in both models, the higher values in Southeastern US and in the Amazon are captured by both models. However, in Southeastern US RefBase simulates iSOA values around 5.0 $\mu g\,m^{-3}$ over a broader area with a maximum of 7.0 $\mu g\,m^{-3}$ on the coast, while RefVBS reaches 4.0 $\mu g\,m^{-3}$ in two local maxima. Similarly, over the Amazon and north of the Andes RefBase simulates iSOA up to 10.0 $\mu g\,m^{-3}$ while RefVBS calculates up to 3 $\mu g\,m^{-3}$. Both simulations also agree on local maxima in Central Africa and over North Australia, Myanmar and Indonesia. While the concentrations in Central Africa of around 3 $\mu g\,m^{-3}$ agree well, peak concentrations in North Australia, Myanmar and Indonesia differ by a factor of around 2.

Although RefVBS includes more volatile isoprene oxidation products as iSOA precursors, particle concentrations are higher in RefBase. This results from different chemical formation of precursor gases. Via the semi-explicit isoprene oxidation by MOZ SVOC and LVOC are formed in amounts large enough to make significant contributions to iSOA mass. In contrast, RefVBS pseudo chemistry forms more volatile compounds in volatility classes VBS1 and VBC10. Furthermore, LISOPOOHOOH formations is not taken into account in the ECHAM-HAM pseudo chemistry formulation. This explains comparably lower prescribed iSOA yields in RefVBS compared to the resulting yield in RefBase.

The comparison of ECHAM-HAMMOZ to ECHAM-HAM underlines once more the high iSOA formation rate in ECHAM-HAMMOZ and shows patterns in global transport and isoprene emissions, which are characteristic for ECHAM as well. In figure 5.1 b), isoprene emission patterns for the northern hemispheric summer show no maxima in Siberia and along the Andes.

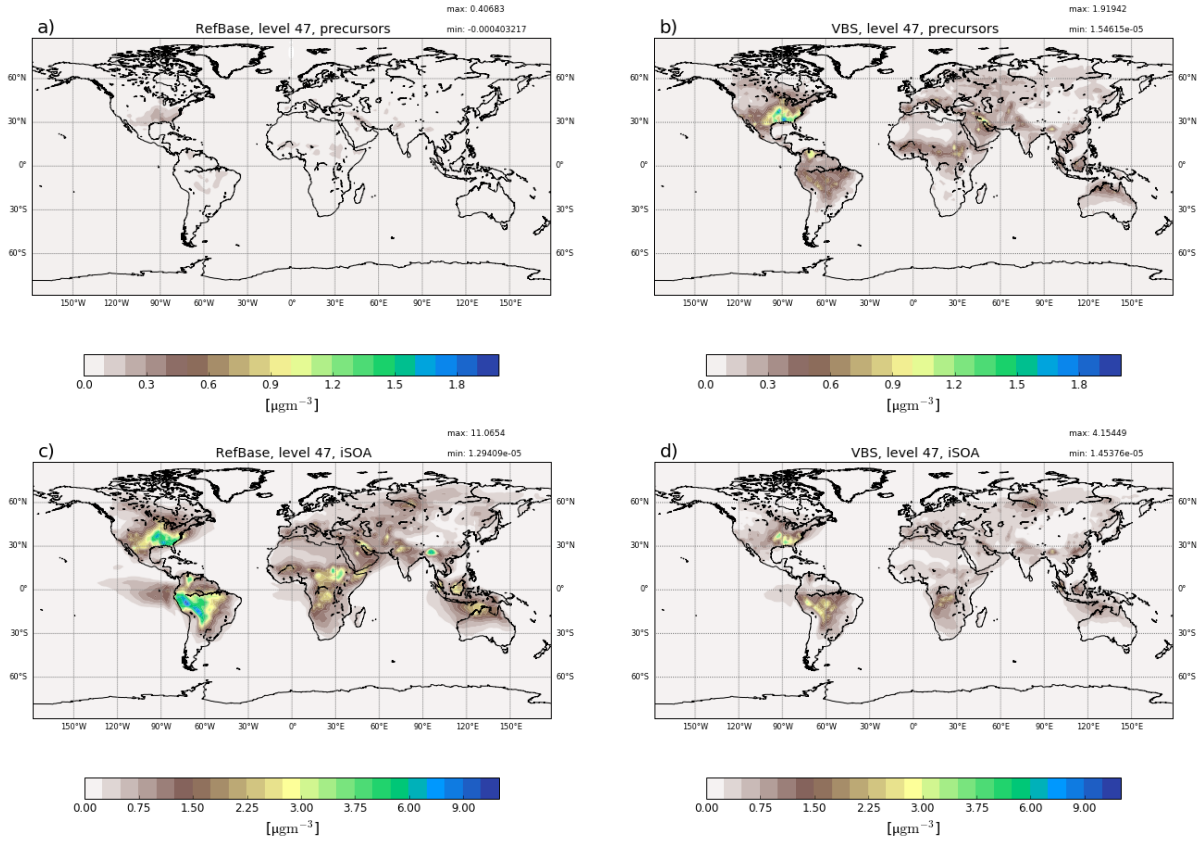

Figure 5.1.: Seasonal mean values of gas-phase precursors in RefBase a) and RefVBS b) and for iSOA in RefBase c) and RefVBS d) at the surface layer, for June, July and August 2012. For RefBase the precursors and iSOA consist of the four isoprene derived semi- and low volatile products described above, for RefVBS the sum of VBS classes 0, 1 and 10 is shown.

These maxima are found in RefBase and RefVBS and are caused by transport of air masses containing aerosols to these regions.

To summarize, the comparison between RefBase and RefVBS underlines the results found in comparison with other global model SOA budgets. The explicit treatment of chemistry and partitioning of individual compounds leads to much higher SOA concentrations, solving the underestimation problem. Moreover, this comparison helps to update the pseudo chemistry used in ECHAM-HAM, since the volatility of the isoprene products is too high or a larger fraction should be attributed to VBS0.

5.3. IEPOX sensitivity to aerosol pH

As discussed in section 2.4.3, several laboratory and field studies suggest that the aerosol pH value influences the reactive uptake of IEPOX. According to the mechanism described in section 2.4.3, IEPOX chemical reaction is catalyzed by hydrogen ions H^+, thus a lower aerosol pH enhances IEPOX uptake and higher pH values suppress IEPOX aerosol uptake.

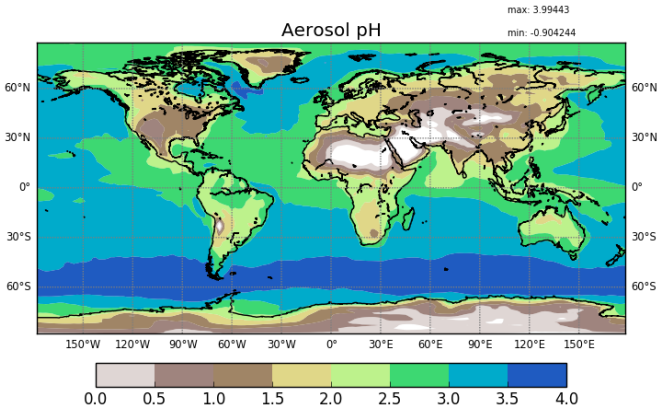

Figure 5.2.: Global particle pH calculated with AIM [Clegg et al., 1998] to be consistent with SALSA aerosol types and water content.

To see the impacts of aerosol pH on SOA formation, a model framework in ECHAM-HAMMOZ was developed. ECHAM-HAMMOZ does neither include ammonium and nitrate aerosol nor the calculation of particle-phase thermodynamics. Thus, particle pH values cannot be obtained from ECHAM-HAMMOZ itself. For this reason, aerosol pH was calculated offline using the AIM aerosol thermodynamics model [Clegg et al., 1998]. AIM is a phase equilibrium model for calculation of gas/liquid/solid partitioning in aerosol systems containing water, organic and inorganic components. To have some consistency, SALSA simulated annual mean mass of aerosol water and the mean mass of aerosol-phase inorganic compounds at the lowest model level were used as an input for AIM. This required two additional assumptions: (1) all aerosol is in liquid form, (2) all sulfate is in form of ammonium bisulfate. This second assumption for sulfate has to be done, because particle-phase ammonia is not modeled in the current configuration of ECHAM-HAMMOZ. Using these inputs, AIM provided the concentration of hydrogen ion H^+ as an output. The results of the AIM aerosol thermodynamics model is a global aerosol pH distribution, which is consistent to ECHAM-HAMMOZ aerosols (see figure 5.2). As can be seen from figure 5.2, atmospheric aerosols are rather acidic, with pH values between -1 and 4. This might not be completely accurate, especially the areas with high dust aerosol loadings seem too acidic and ammonia would buffer the sulfate acidity in regions, where sulfate and ammonia are present. Nevertheless, aerosol pH maps are not easily found in literature, for this reason creating an aerosol pH map with AIM is the best, possible way within the scope of this study. The aerosol pH distribution by AIM is used as input in the sensitivity simulation γpH, while the reference simulation RefBase uses a uniform value for the reactive uptake coefficient γ corresponding to a pH of around 2.5 for all aerosols. The simulation γpH was designed to to explore the impact of such a dependence. Therefore, based on reaction probability values given in Eddingsaas et al. [2010] and Gaston et al. [2014], a simple function for γ(pH) was formulated and implemented in ECHAM-HAMMOZ:

$$\gamma(\mathrm{pH}) = \begin{cases} 10^{-2}, & \mathrm{pH} < 2 \\ 0.1[\mathrm{H}^+] + 10^{-4}, & \mathrm{pH} \in [2,5] \\ 0, & \mathrm{pH} > 5 \end{cases}, \tag{5.1}$$

where $[H^+]$ is the concentration of hydrogen ions in the aerosol given in $\mathrm{mol\,l^{-1}}$. The reaction probability varies linearly between particles of pH values between 2 and 5. For acidic particles

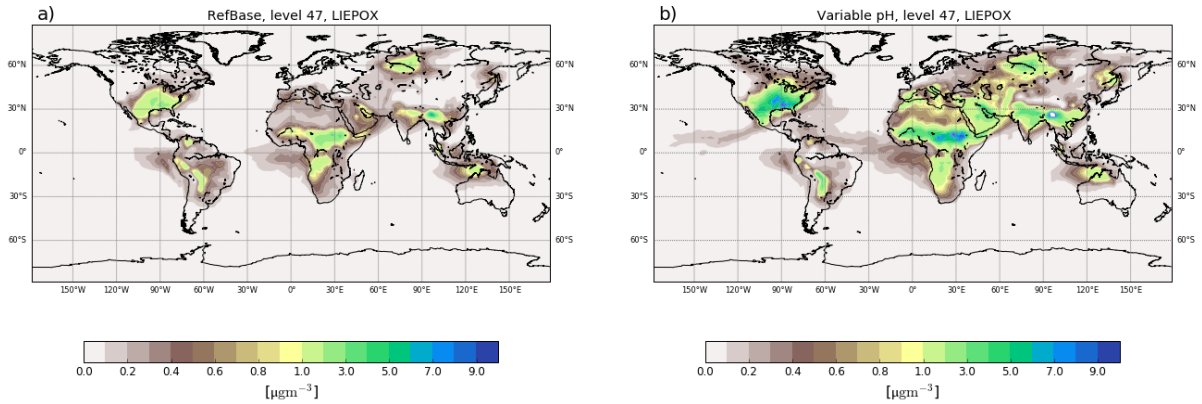

Figure 5.3.: Mean surface aerosol concentrations for LIEPOX derived iSOA with uniform pH value used in the reference run a) and with variable pH value calculated with AIM aerosol thermodynamics model in the sensitivity run γpH b) for the time period of June, July and August 2012. Note the non-linear scale formerly used in figure 4.3.

the upper limit of 10^{-2} is fixed. For particles which are not acidic enough (pH > 5) no reaction is assumed. The pH distribution (figure 5.2) is used as ECHAM-HAMMOZ input values. For the given pH values, this function results in nearly binary reaction probability values either enhancing or suppressing LIEPOX-SOA formation. The reader should note that the pH value of the surface aerosols is applied to each model layer. Nevertheless, the largest effect can be observed where high acidic aerosol concentrations and high gas-phase LIEPOX concentrations are present.

Figure 5.3 shows the resulting global surface distribution of γpH run (b) for northern hemispheric summer compared to RefBase (a). Enhancement of reactive uptake in γpH over land is clearly visible, especially over Southeastern US, maximum values are more than doubled. Further, more areas with $3 - 4\,\mu g\,m^{-3}$ over Africa, the Middle East and Eurasia can be found, where RefBase simulates values lower than $1\,\mu g\,m^{-3}$. In contrast, suppression of LIEPOX reactive uptake is observable over the Amazon, here γpH simulates up to $0.3\,\mu g\,m^{-3}$, while RefBase calculates $0.6\,\mu g\,m^{-3}$.

Total LIEPOX-aerosol produced during this time period increased by 58 % in γpH compared to RefBase. In RefBase an aerosol pH around 2.5 was assumed for all aerosols, also those which might be less acidic, like sea salt aerosol. In γpH most areas are covered by less acidic aerosol than assumed in RefBase, but LIEPOX is produced or transported to areas, where acidic aerosol can be found. This leads to the observed increase in iSOA formation.

As an alternative explanation for the pH value dependence, Xu et al. [2015] hypothesize that IEPOX uptake enhancement could be triggered by sulfate aerosol. Xu et al. [2015] argue that all experiments used sulfur seed aerosol to produce acidic seeds. Meanwhile, Xu et al. [2015] used ambient measurements in the Southeastern US and found no correlation between particle pH and isoprene organic aerosol. Instead, they found that sulfate-rich plumes lead to high values of IEPOX derived SOA. They conclude that the controlling parameter has to be sulfate, but admit that the mechanism has to be explored. Although sulfate aerosol is simulated in ECHAM-HAMMOZ, no sensitivity study was performed here due to lack of process understanding and possible reactive uptake parametrizations.

Results in section 4.1.5 showed that less LIEPOX and more IGLYOXAL is formed in regions with higher NO mixing ratios. The regions where high NO_x emissions are found correlate with sulfate emissions, thus with acidic aerosol. Therefore, suppression of iSOA precursor formation due to NO_x dominated chemistry competes with acidic enhancement of LIEPOX-SOA formation. Since nothing was changed in MOZ chemistry, γpH also shows that for the formulation in ECHAM-HAMMOZ, LIEPOX-SOA enhancement by acidic aerosol is stronger than NO_x suppression. This is further analyzed in the next section 5.4. Limits of ECHAM-HAMMOZ here are 1) the lack of ammonium aerosol leads to a biased aerosol pH to acidic values 2) the resolution of ECHAM-HAMMOZ does not allow for very high NO mixing ratios, because these are diluted into the around 200×200 km grid boxes. Although these limitations are given by ECHAM-HAMMOZ, the result of stronger acidic enhancement than NO_x suppression can explain why other global models produce less IEPOX-SOA. Usually its pH dependence is not included since the aerosol pH is unknown.

5.4. NO_x suppression vs. pH enhancement

As shown in section 4.1.5, NO_x suppression of iSOA precursor production is not clearly visible in mean values and thus 3-hourly output is used. In the following, NO_x suppression of precursor production is compared to the impact of pH enhancement of IEPOX uptake. The question to answer is whether NO_x suppression of IEPOX production is stronger than the enhanced IEPOX uptake or not. Therefore, two model runs are compared: RefBase and γpH. As seen from section 4.1.5, at least 400 pptv NO are required to completely suppress iSOA precursor production. Thus, a grid-box with high NO and isoprene mixing ratios in the Southeastern US is analyzed. The grid-box includes the city of Atlanta (33.6°N, 84.4°E).

Figure 5.4 and 5.5 a),b) and c) show precursor production in the surface layer per second, NO and HO_2 mixing ratios and the dominant reaction pathway as discussed in section 4.1.5. For both runs, these plots do not differ much but are shown to proof consistency between both runs. The reader should note that the Atlanta grid-box differs from the boxes including the Amazon or Sao Paulo (section 4.1.5). In these grid-boxes, daily maximum NO and daily maximum HO_2 are reached at the same time. In contrast, the Atlanta grid-box shows very high NO mixing ratios up to 1500 pptv (b), which suppress iSOA precursor production (a) and dominate the reaction pathway (c). Nevertheless, after NO peaks, HO_2 peaks with mixing ratios of up to 60 pptv, which is $10-50$ % higher than what is found in South America. During these high HO_2 periods during the day, iSOA precursors are produced.

Finally, Figure 5.4 and 5.5 d) give the fraction of LIEPOX to total iSOA, which differs due to uptake enhancement in this region in γpH. In RefBase, a more or less constant fraction of $30-40$ % of iSOA consist of LIEPOX, while around 60 % of iSOA is LIEPOX in γpH.

To summarize, NO_x suppression in ECHAM-HAMMOZ works for NO concentrations over 400 pptv, but in Southeastern US, NO and HO_2 do not compete with each other. Due to a shift in HO_2 maximum values, iSOA precursors are also produced in regions with high NO_x, just not at the same time of the day. Therefore, precursors are formed chemically and partition into or be taken up by pre-exisitng aerosol. Thus, overall pH enhanced uptake of LIEPOX leads to a larger fraction of LIEPOX in the particle-phase and is over-weighting NO_x suppression in ECHAM-HAMMOZ.

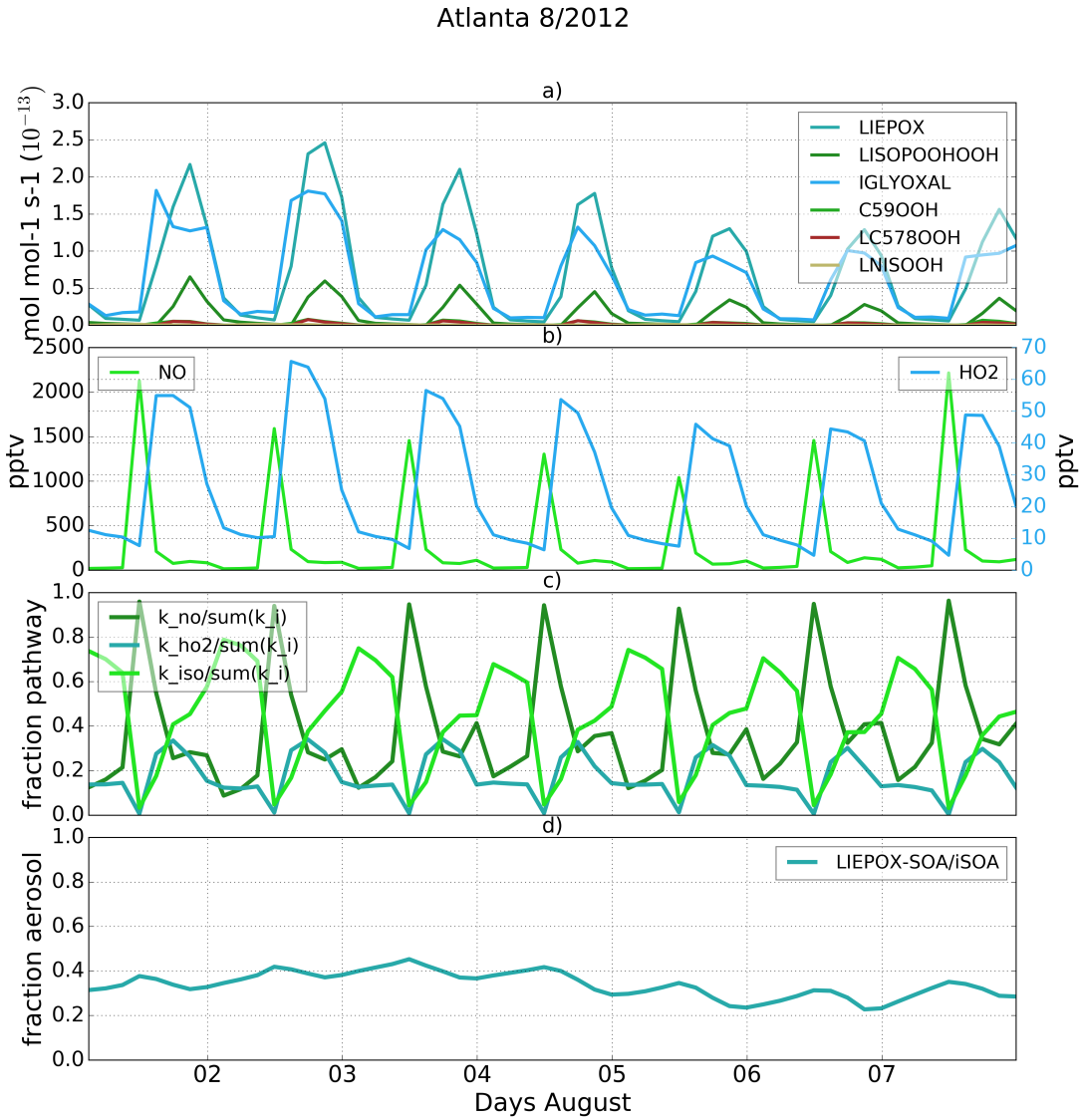

Figure 5.4.: Daily iSOA precursor production in mol $mol^{-1}s^{-1}\,10^{-13}$ (a), NO and HO_2 mixing ratios (b, please note the different y-axis for each species), dominant reaction pathways as defined in section 4.1.5 (c) and the fraction of LIEPOX in total iSOA for the grid-box in Southeastern US, including Atlanta (33.6°N, 84.4°E) in the reference run RefBase. Instead of showing the whole month, only the first week of August is shown, because then maximum values of NO and HO_2 are clearly visible. The other days of August show the same pattern.

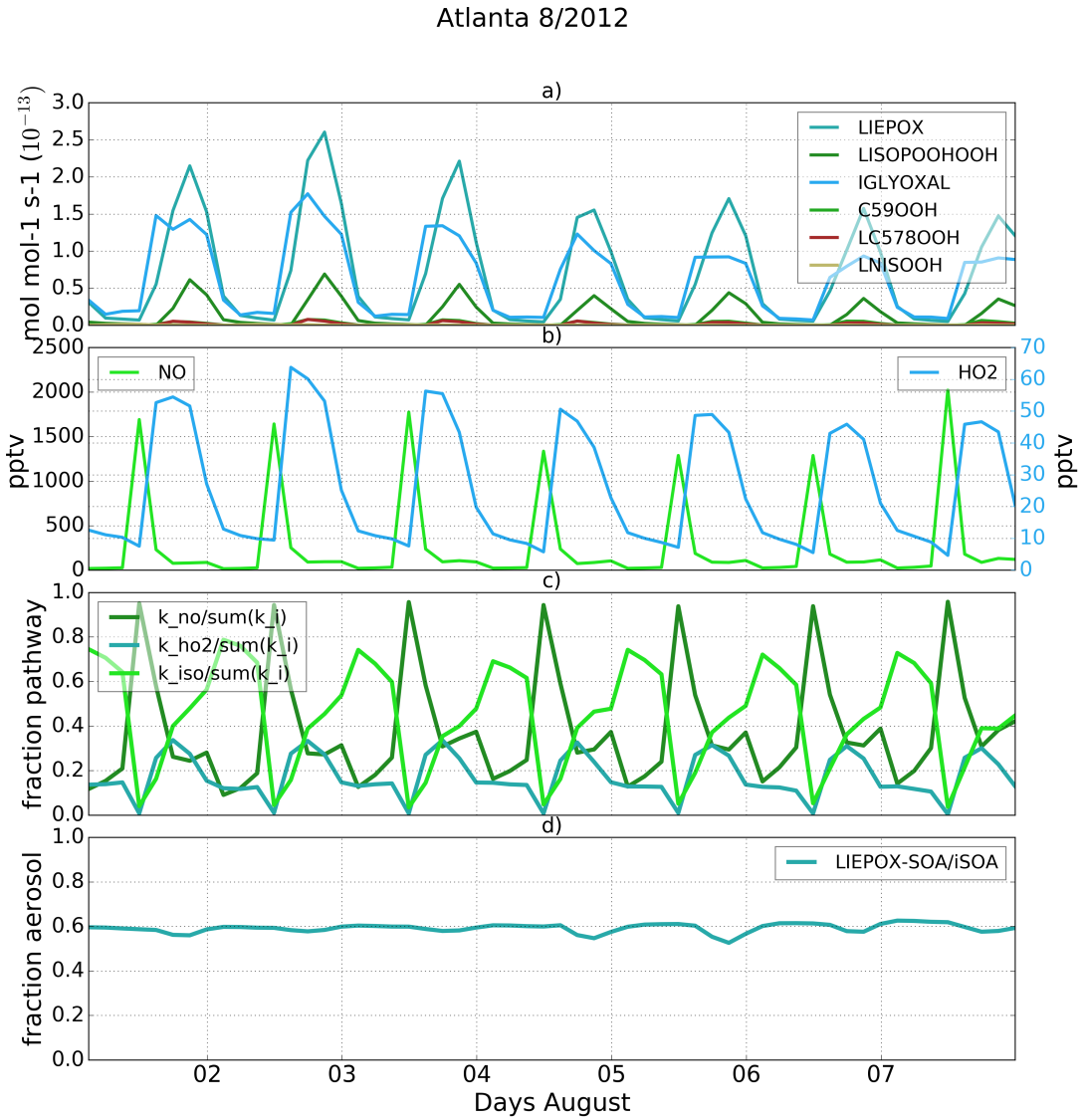

Figure 5.5.: Same as figure 5.4, but for the sensitivity run γpH.

5.5. Sensitivity to evaporation enthalpy

Tsigaridis and Kanakidou [2003] point out the sensitivity of SOA formation to the evaporation enthalpy ΔH_{vap}. Due to the lack of knowledge about ΔH_{vap} of the various different organic compounds, usually a fixed value or rather low value is used for all of them [Epstein et al., 2009]. Depending on the study, different estimations for ΔH_{vap} are made, ranging between 30 and 156 $\mathrm{kJ\,mol^{-1}}$ [Athanasopoulou et al., 2012]. Farina et al. [2010] also use the Clausius-Clapeyron equation to calculate saturation concentrations for a variety of organics, using for all of them $30\,\mathrm{kJ\,mol^{-1}}$. To explore the impact of this assumption and the impact of a lower evaporation enthalpy, the sensitivity run ΔH30 was designed to use ΔH_{vap} =30 $\mathrm{kJ\,mol^{-1}}$ but keeping the same reference saturation vapor pressure (see Table 3.2).

As an example, figure 5.6 shows the curves given by equation (2.2), using the ΔH_{vap} of the reference run and the sensitivity run ΔH30 for the compound C59OOH. Equation (2.2) changes its curve form drastically when lowering ΔH_{vap} from values around 150 $\mathrm{kJ\,mol^{-1}}$ to 30 $\mathrm{kJ\,mol^{-1}}$. For temperatures lower than the reference value of 298.15 K, the saturation vapor pressure of ΔH30 $p^*_{\Delta\mathrm{H30}}$ is higher compared to the reference p^*, but for temperatures higher 298.15 K the opposite is the case (see figure 5.6).

As a result, the impact of variable ΔH_{vap} on iSOA formation varies with temperature, therefore, also with region and height. The sensitivity simulation ΔH30 ran for the whole year 2012 with changed Clausius-Clapeyron equation curves according to figure 5.6. This means that compounds using $\Delta H_{vap} = 30\,\mathrm{kJ\,mol^{-1}}$ instead of their individual ΔH_{vap} are more volatile in regions where temperature is cooler than 298.15 K, while they are less volatile in warmer regions. On a global perspective, the atmosphere is cooler than 298.15 K on average, especially at higher altitudes. As a consequence, iSOA precursors are more volatile in ΔH30 than in RefBase. Nevertheless, global total iSOA production in ΔH30 for 2012 is just 1.8 TgC lower compared to RefBase. This is a reduction of 3% of the total iSOA produced in RefBase (see also Section 4.1.3). For surface temperatures higher than 298.15 K, $p^*_{\Delta\mathrm{H30}}$ is one order of magnitude smaller than the reference p^*, but gas-phase concentrations of iSOA precursors are sufficiently large. Thus, no significant impact on iSOA concentrations can be found. In agreement with the minor change in global iSOA production, surface concentration fields do not change much, thus they are not shown.

The assumption made by Farina et al. [2010], connected with the estimation of SVOC and LVOC p^*_0 in this study, therefore does not lead to significant changes in ECHAM-HAMMOZ model results. Lowest sensitivity to ΔH_{vap} can be found in the lowest volatile compound in MOZ, LISOPOOHOOH. In ECHAM-HAMMOZ, sensitivity to ΔH_{vap} increases with volatility of the compounds, therefore ΔH_{vap} should be crucial for additional consideration of IVOC. A ΔH_{vap} of $30\,\mathrm{kJ\,mol^{-1}}$ would fit for IVOCs.

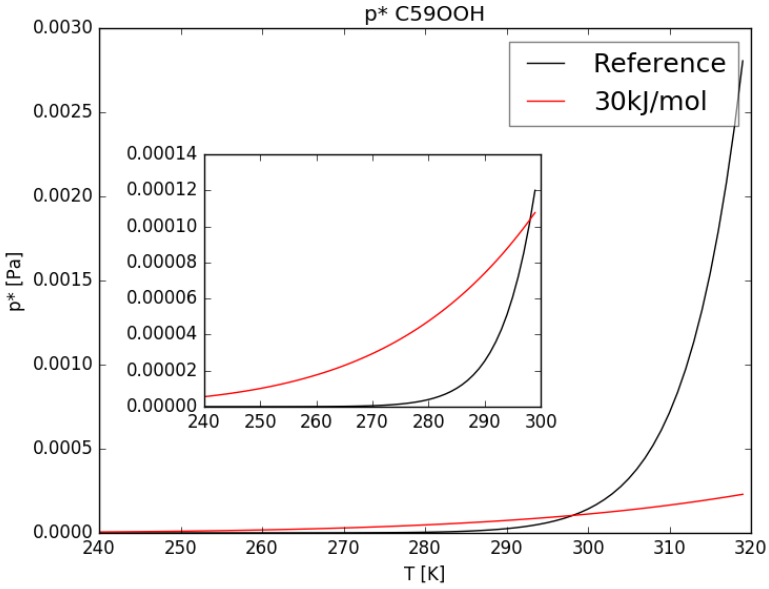

Figure 5.6.: Curves given by Clausius-Clapeyron equation (2.2) for C59OOH. The red curve is obtained by setting $\Delta H_{vap} = 30$ kJ mol^{-1}, the black one describes the parameters used in the reference run (see Table 3.2).

5.6. Uncertainty estimation saturation vapor pressure

As described in section 3.4, the group contribution method by Nannoolal et al. [2008] in combination with the boiling point method by Nannoolal et al. [2004] were used to obtain the saturation vapor pressure of originated isoprene products as a function of temperature. Group contribution methods estimate the contribution of functional groups on saturation vapor pressure. The Nannoolal et al. [2008] group contribution method is based on 68835 data points of 1663 components and only needs two inputs: the molecular structure and the normal boiling point. Nannoolal et al. [2008] focuses on the low-pressure compounds for low temperatures. Nannoolal et al. [2008] report a good performance against measurements. When its performance is compared to compounds outside the training set, results become worse [Barley and McFiggans, 2010, O'Meara et al., 2014]. Barley and McFiggans [2010] underline that databases are typically biased towards mono-functional groups and therefore, group contribution methods trained with these data perform well at volatile fluids, but not for low volatility compounds. O'Meara et al. [2014] arrive at similar conclusions. They tested seven saturation vapor pressure estimation methods and found that although Nannoolal et al. [2008] method results in the lowest mean bias error, the method shows poor accuracy for compounds with low volatility. This tendency holds true for the other tested methods, showing an increasing error with increasing number of hydrogen bonds. This systematic error results in a SOA formation overestimation.

A second group contribution method EVAPORATION was designed to include hydroperoxides' and peracids' molecuar structures [Compernolle et al., 2011]. EVAPORATON does not need a boiling point method as an input. It was also evaluated in the study of O'Meara et al. [2014], where they conclude that it gives good results for SOA formation.

Table 5.2.: Comparison logarithmic saturation concentrations $\log_{10}(C^0)$ at 300 K for iSOA precursors in this study calculated via the group contribution method used for the reference run [Nannoolal et al., 2008], EVAPORATION [Compernolle et al., 2011] and a simple group contribution method formulated by Donahue et al. [2012]. In brackets the $\log_{10}(C_0^*)$ for the isomers are shown.

	Nannoolal et al. [2008]	[Compernolle et al., 2011]	Donahue et al. [2012]
LNISOOH	1.2 (1.4)	2.2 (2.8)	1.3
LISOPOOHOOH	-1.6 (-1.9)	-0.2 (-0.9)	-0.7
LC578OOH	1.1 (1.1)	1.7 (1.7)	1.
C59OOH	0.8	1.4	1.

Furthermore, McFiggans et al. [2010] analyzed the dependence of SOA formation on the saturation vapor pressure of each compounds and state that SOA mass is highly sensitive to this parameter. Up to 30% overestimation can result from ignoring non-ideality of the organic mixture.

These studies already identified and emphasized several causes and consequences of the various group contribution methods for SOA formation. To evaluate the saturation vapor pressures of Nannoolal et al. [2008] used in this study, saturation concentrations are compared to two other group contribution methods. Thus, $\log_{10}(C_0^*)$ values are compared to the simple group method based on oxygen, carbon and nitrate atoms in the molecule described in Donahue et al. [2012] and the group contribution method EVAPORATION [Compernolle et al., 2011] (Table 5.2).

As can be seen from table 5.2, the $\log_{10}(C^0)$ values do not differ much between the simple group contribution method of Donahue et al. [2012] and the one by Nannoolal et al. [2008], except for the lowest volatility compound LISOPOOHOOH. For LISOPOOHOOH, Nannoolal et al. [2008] predict a much lower volatility than Donahue et al. [2012]. In contrast, all values given by the EVAPORATION method assign a higher volatility to all compounds. In terms of classification, this changes LNISOOH's volatility, reaching the threshold value to be called an IVOC. Especially the LNISOOH isomer with a $\log_{10}C^0$ of 2.8 has to be classified as an IVOC (see table 2.2). Moreover, LISOPOOHOOH would be classified as an SVOC, using EVAPORATION, rather than an LVOC, as when Nannoolal et al. [2008] is used.

In table 5.2, the $\log_{10}(C^0)$ values for the different isomers are also listed. Due to computational resource limits, no further sensitivity runs were performed assuming the other isomer. From the $\log_{10}(C_0^*)$ values and the values in table 3.2 it is clear that for LC578OOH, there is no difference caused by isomeric structures in volatility, for LNISOOH the other isomer is even slightly more volatile and for LISOPOOHOOH the opposite holds true, its second isomer is slightly less volatile. Since LNISOOH is only formed in very low concentrations, these deviations might not be visible in iSOA formation. Interestingly, EVAPORATION and Nannoolal et al. [2008] methods agree in the tendency of the isomers being higher or lower volatile compared to the one used in RefBase. The simple method by Donahue et al. [2012] cannot capture differences in isomeric structures, so the same value would be calculated and is omitted here.

The differences between EVAPORATION, Donahue et al. [2012] method and Nannoolal et al. [2008] method agree with the findings of the studies described above and indicate that LISOPOOHOOH-SOA formation might be too high in ECHAM-HAMMOZ. Based on the LISOPOOHOOH isomer having an even lower volatility, LISOPOOHOOH would not change

Table 5.3.: Percentage changes in total iSOA formation in 2012 for the sensitivity run EVA using EVAPORATION instead of Nannoolal et al. [2008] to estimate the saturation vapor pressure and the evaporation enthalpy of the isoprene derived SOA precursors.

Change in EVA compared to RefBase		
	%	TgC
LIEPOX	-5.2	-1.1
IGLYOXAL	-5.2	-0.2
LISOPOOHOOH	-16.7	-4.6
C59OOH	-36.3	-0.1
LC578OOH	-50.0	-0.3
LNISOOH	-90.0	-0.1
Total iSOA	-12.8	-7.3
Total iSOA burden	-16.7	-0.1

the main findings of this study, since it already dominates iSOA formation. The results of RefBase compared to the AeroCom models (4.1.3) and to observations showed that RefBase tends to overestimate iSOA formation. One reason could be the uncertainty in its volatility. To explore how sensitive ECHAM-HAMMOZ is to the saturation vapor pressure, a sensitivity simulation EVA using EVAPORATION was performed. The overall higher values for the saturation vapor pressure predicted by EVAPORATION reduce the iSOA amount formed in ECHAM-HAMMOZ.

Table 5.3 shows the percentage changes in iSOA produced by each compound using the higher volatility of the iSOA precursors predicted by EVAPORARION. Since iSOA formation has a positive feedback on itself, values for LIEPOX and IGLYOXAL are shown as well.

A reduction of 12.8 % in total iSOA production, which leads to a reduction in iSOA burden of 16.7 %, comparing EVA to RefBase, is shown in table 5.3. Highest relative changes can be found in production of SVOC C59OOH, LNISOOH and LC578OOH of up to 90 %. Nevertheless, these high relative changes are not driving the total reduction. Mainly LISOPOOHOOH is important here, followed by LIEPOX. LISOPOOHOOH's $\log_{10}(C_0^*)$ was increased by 88 % by usage of EVAPORATION, which leads to a 16.7 % reduced LISOPOOHOOH-SOA production. It should be noted that in EVA, most iSOA is produced by LISOPOOHOOH as well, a total of 23.2 TgC in 2012, followed by 20.4 TgC of LIEPOX. Therefore, the iSOA composition is still dominated by these two compounds. Thus, the main conclusions of this study, using the reference run RefBase, do not change although iSOA production is reduced when using the EVAPORATION method. This will be further discussed in section 5.8, where both runs are compared to aerosol observations.

5.7. Additional iSOA sinks

As described in section 3.6, additional iSOA loss processes were introduced in the model. This is motivated by the fact, that iSOA is formed in larger amounts in ECHAM-HAMMOZ compared to other models (see section 4.1.3). The typical underestimation of SOA is resolved and additional sink processes can be explored. The following sections discuss the impact of photolysis and thermal decay of one of the major iSOA components on surface concentrations and the global burden for the months June, July and August 2012. Only relative values of

concentrations can be discussed here, because the model diagnostics could not be implemented in time and a problem with the code occured when additional sinks are turned off.

5.7.1. iSOA photolysis

In-particle photolysis was recently identified as a SOA sink (see section 2.3.2). Hodzic et al. [2015] explored the impact of photolysis on SOA concentrations, but assumed quite high photolysis rates, which are criticized by Malecha and Nizkorodov [2016]. This motivated two sensitivity runs with different SOA photolysis rates. As described in section 3.6.2, the photolysis rate of SOA (J_{SOA}) is calculated using the photolysis rate of NO_2 ($J_{\mathrm{NO_2}}$). Thus, the lower estimate $J_{\mathrm{SOA}} = 0.04\,\% \, J_{\mathrm{NO_2}}$ presented in Hodzic et al. [2015] is used for the J04PHOT simulation. In addition, to take the criticism of Malecha and Nizkorodov [2016] into account, a second test was performed using a J_{SOA} one magnitude lower than the lower estimate of Hodzic et al. [2015] in J004PHOT. Malecha and Nizkorodov [2016] argue that in-particle photolysis might be much lower than gas-phase photolysis due to stabilization of molecules within the particle matrix.

Figure 5.7 shows the relative differences when SOA photolysis is tuned on. As can be seen from J04PHOT (figure 5.7 a), reductions in iSOA concentrations over land of 10 – 30 % are found over nearly all continents. Highest reductions of up to 96 % are reached over the oceans, but iSOA concentrations are very low in this regions, so these reductions are not very important and misleading. A similar effect is given in North Africa over the Sahara. In these regions iSOA is reduced by 65 %, but iSOA concentrations are very low anyway. Most important are the reductions over Southeastern US, South America, Central Africa and Indonesia. Southeastern US iSOA concentrations are reduced by up to 20 % like over the Amazon. At the edge of the Andes a iSOA reduction of 40 % occurs when photolysis with $j_{\mathrm{SOA}} = 0.04\,\% \, j_{\mathrm{NO_2}}$ is turned on. Central African and Indonesian iSOA is reduced by 10 – 30%.

Figure 5.7 (b) also shows relative differences to J004PHOT, caused by a photolysis rate of $J_{\mathrm{SOA}} = 0.004\,\% \, J_{\mathrm{NO_2}}$. Reductions of iSOA in J004PHOT are less strong throughout the globe and relevant reduction over land is about 5 %. Again, strongest impacts are found over the remote oceans with reductions of up to 50 %.

The reductions in iSOA vary strongly with region, but less over time. Figure 5.8 shows reductions in daily global burden. The blue and dashed blue curves show reductions by photolysis. Both runs start from conditions in end of May in RefBase. This is why all curves drop within the first week. After three weeks, around 2012-06-22, reduction in global iSOA burden stays nearly constant and a reduction of 10 % is achieved in J004PHOT, while 40 % less global iSOA burden is simulated in J04PHOT. One order of magnitude higher photolysis in J04PHOT leads to 30 % more reduction than in J004PHOT and not one order of magnitude more. Reductions in global iSOA burden fit well to reductions seen in figure 5.7 over land respectively, underlining the fact that very high values over the oceans do not contribute much.

Hodzic et al. [2015] report reductions of SOA by $J_{\mathrm{SOA}} = 0.04\,\% \, J_{\mathrm{NO_2}}$ of up to 40 % over land, except for the Sahara and Greenland. They also have highest reductions over the oceans between 50 and 90 % (figure 8 in their manuscript, Appendix figure B.3). Their results fit well to the values found here. In conclusion, as stated by Hodzic et al. [2015], particle photolysis could be a major SOA sink, if it would be strong enough. Nevertheless, if it is one order of magnitude lower, the impact is reduced to around 10 %. To further explore this, an approved value for SOA photolysis is needed, which is not easy to measure, taking into account all the different compounds which are in the particle-phase. As pointed out by Malecha and Nizkorodov [2016],

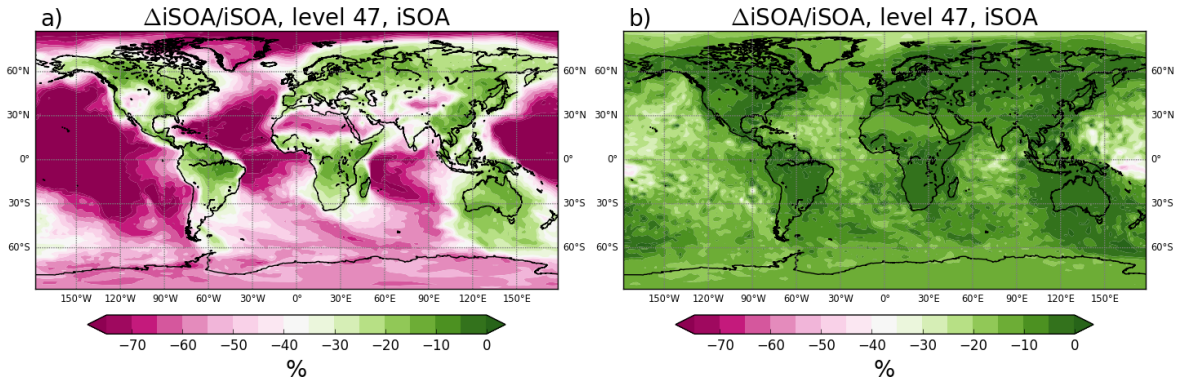

Figure 5.7.: Relative differences in surface iSOA concentration average for the months June, July and August 2012. The left plot shows results of J04PHOT and the right one for J004PHOT.

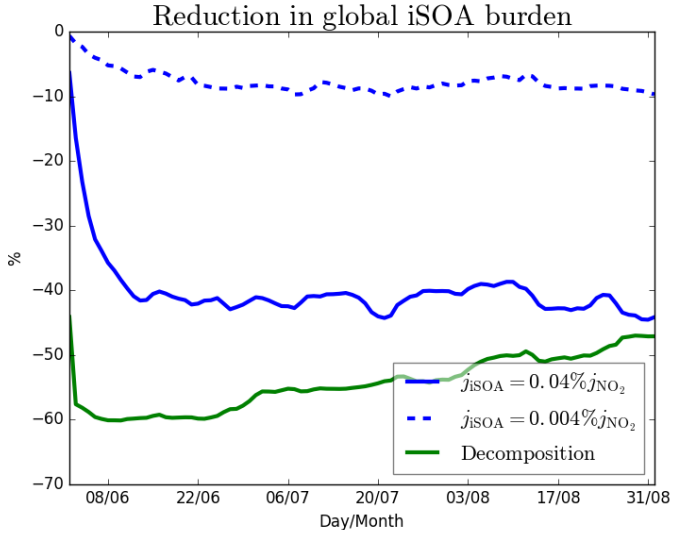

Figure 5.8.: Relative differences in daily global iSOA burden for the months June, July and August 2012. The global burden is calculated as a sum over the whole world. To get the relative contribution the difference to the reference without the additional sink is calculated and divided by the reference values.

the particle matrix could stabilize the single compounds which were photolysed individually. In contrast, compounds which do not photolyse can also take in the energy and transfer it to neighboring molecules which then photolyse. This processes are still under investigation and not fully understood yet.

5.7.2. LISOPOOHOOH in-particle decay

Recently, LISOPOOHOOH (ISOP(OOH)2) was identified in an experiment of iSOA formation under low NO_x conditions (see section 2.4.4). Moreover, in the same study it was observed to decompose thermally with a half-life of 4 h [D'Ambro et al., 2017a]. This decay was implemented in ECHAM-HAMMOZ as described in section 3.6.1. The decomposition product LC578OOH, which had been chosen for technical reasons (see section 3.3.1), is more volatile than LISOPOOHOOH and evaporates, thus reducing iSOA concentrations. Since LISOPOOHOOH is a major part of iSOA mass, its decay reduces iSOA efficiently.

The strong reduction of total iSOA burden during June, July and August can be seen in figure 5.8. The green line shows percentage reduction in daily global iSOA burden between 50 and 60 %. This fits well with the total contribution of LISOPOOHOOH to iSOA, which is also around 50 %. Additionally to the reduction caused by loss of LISOPOOHOOH and subsequent evaporation of LC578OOH, the lower total aerosol surface leads to less iSOA production. At the beginning of the simulation, which starts from RefBase with a high global LISOPOOHOOH burden reduction of 60 % is reached. Partitioning is an equilibrium process and, as can be seen, the reduction has a trend to become less strong with time. The model was perturbed by LISOPOOHOOH decay and has not reached an equilibrium. A longer simulation would be needed to see if an equilibrium would be reached or if LISOPOOHOOH seasonality would keep iSOA changing.

In comparison with photolysis, LISOPOOHOOH decay reduces global iSOA burden stronger, but the impact depends on the region. Regions with dominant LISOPOOHOOH-SOA lose more iSOA compared to photolysis iSOA loss. Particle photolysis destroys all iSOA compounds, only depending on available solar radiation. In figure 5.9, global reductions of over 40 % in iSOA burden can be found over nearly every continent. Greenish values now point to regions where LISOPOOHOOH relative contribution to iSOA is comparably lower, but still important. In Southwest Africa and East Asia, high NO_x levels make less favorable conditions for LISOPOOHOOH formation. This does not mean that LISOPOOHOOH is not formed at all, but in lower concentrations. In these regions, reductions in total iSOA surface concentration due to LISOPOOHOOH decomposition reaches between 20 and 30 %, which again mirrors LISOPOOHOOH fraction in iSOA.

To conclude, LISOPOOHOOH in-particle decay with a half-life of 4 h leads to an almost complete loss of LISPOOHOOH-SOA, although in the model LC578OOH is produced, which stays in the particle-phase iSOA under favorable conditions. Since LISOPOOHOOH is a major compound in iSOA, its decay is a crucial parameter for control of iSOA concentrations. The decay, with a half-life of 4 h, was observed within a laboratory study, using a constant temperature of 20° C. The atmosphere is, on global average, cooler than 20° C, especially in higher altitudes. Thus the in-particle decay used here might overestimate LISOPOOHOOH reductions. To formulate a better decay depending on temperature, knowledge of particle temperature itself would also be needed. Depending on the aerosol composition, the aerosol absorbs or scatters light efficiently. Organic carbon is sometimes also referred as brown carbon [Feng et al., 2013], because of its light color. Thus, it is accounted to the aerosol types which

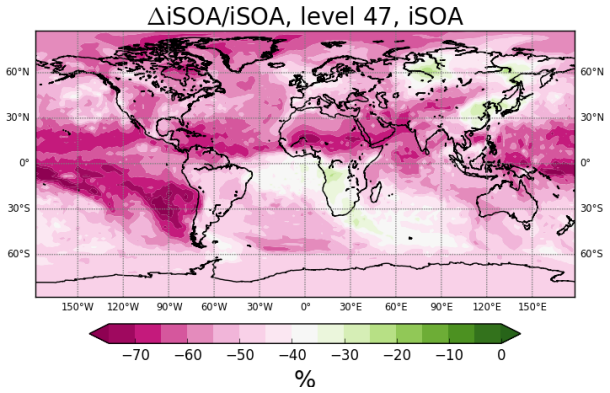

Figure 5.9.: Relative differences in surface iSOA concentration average for the months June, July and August 2012. As figure 5.7, but for LISOPOOHOOH decomposition simulation DECAY.

scatter solar radiation. Therefore, the assumption of the particle temperature equals to the atmospheric temperature would be sufficient and would probably lead only to very small deviations between air temperature and aerosol temperature. In addition, similar to the impacts of neighboring molecules in in-particle photolysis, other compounds in the particle could influence LISOPOOHOOH decay, for example, stabilizing it. This would further reduce the impact of LISOPOOHOOH decay on iSOA concentrations. These details in in-particle chemistry and physics go beyond the processes which can be captured by ECHAM-HAMMOZ and they are not fully understood yet.

5.8. Comparison to AMAZE measurement campaign

The comparison of RefBase to OA measurements in section 4.2 showed that iSOA is most important in Southeastern US and in the Amazon. In Southeastern US, it is a subset of other organics, but for the Amazon even higher values are simulated by ECHAM-HAMMOZ than observed. It is estimated that OA in the Amazon mainly consists of secondary OA (up to 95 %) and is dominated by isoprene. Thus, it is the ideal site to evaluate iSOA in ECHAM-HAMMOZ, although it is a point measurement compared to a grid-box. The overestimation of iSOA in RefBase motivated several sensitivity simulations discussed in the previous sections. Several aimed to explain reasons for this overestimation focusing on different parameters controlling the iSOA formation process or exploring missing processes. A caveat here is the lack in isoprene emission flux and isoprene concentration observation. One step ahead of process understanding is to assure if isoprene levels in ECHAM-HAMMOZ are accurate. Isoprene in ECHAM-HAMMOZ does not seem to be wrong, but discussing differences of some percent caused by different processes would require precise knowledge of the isoprene concentration error. Effects seen by altering parameters in iSOA formation could also arise from perturbations in isoprene emissions. To evaluate, which reduction in iSOA makes ECHAM-HAMMOZ comparable to the observations made in the AMAZE field campaign (see table 4.3), several runs were compared to the observation in figure 5.10.

Figure 5.10 shows that RefBase, EVA and ΔH30 overestimate concentrations by a factor of 3, assuming that all observed OA is SOA. This means that changing the evaporation enthalpy or the saturation vapor pressure according to state-of-the-art knowledge, does not resolve the overestimation problem. The two boxes representing the simulations SinkL and SinkS fit very well to observations, still slightly overestimating the median. SinkL and SinkS are not explicitly analyzed in the previous discussion. These two runs include both new SOA sinks, photolysis and LISOPOOHOOH decay, which are discussed in detail in section 5.7. The same conclusion applies here, taking into account that the indirect iSOA loss effect reduces iSOA further. The indirect iSOA loss effect is the feedback on iSOA formation: iSOA is lost quicker due to the additional sinks leaving less pre-existing aerosol for partitioning and reactive uptake. Therefore, not only iSOA concentrations are reduced, but also iSOA production is weaker.

To summarize, the iSOA overestimation in ECHAM-HAMMOZ leads to the exploration of previously ignored SOA sinks. Only including these new sinks brings SOA concentrations to levels comparable to observations (see figure 5.10 SinkL and SinkS). Changes in C^* (EVA) do not have impacts large enough the explain the overestimation by a too low volatility of all partitioning compounds. Please note that iSOA is compared to total OA. This which means that ECHAM-HAMMOZ simulates iSOA concentrations as high as total observed OA

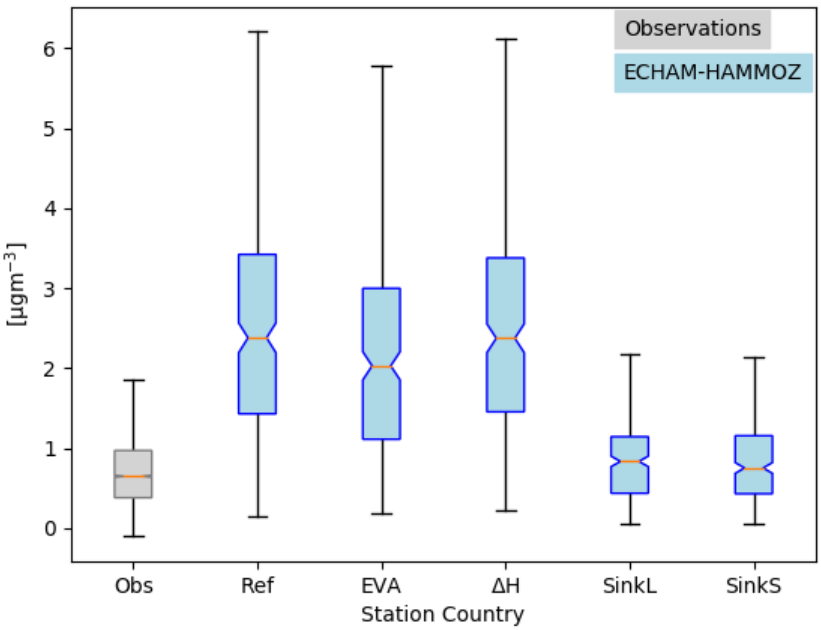

Figure 5.10.: Box plots showing the variability of concentrations measured and corresponding instantaneous values from ECHAM-HAMMOZ, like in figure 4.12. iSOA has the biggest impact on the Amazon region and showed an overall overestimation compared to observed OA. Thus, only these observations are compared some of the sensitivity simulations. The abbreviations in the plot describe: Obs = Observations, Ref = RefBase, EVA = EVA, ΔH = ΔH30, SinkL = SinkL, SinkS = SinkS, see section 3.7 for simulation descriptions.

concentrations, thus ECHAM-HAMMOZ clearly overestimates iSOA in the Amazon region. A combination of EVA and SinkS might lead to best results, but is not performed due to computational limits and no significant gain of knowledge at this point. Moreover, there are more parameters in ECHAM-HAMMOZ controlling iSOA concentrations, such as meteorology, aerosol and gas emissions, the chemical mechanism and deposition.

5.9. Closing remarks

The semi-explicit isoprene oxidation and explicit partitioning and reactive uptake of iSOA precursors, on one hand allows for a detailed process discussion, and on the other hand solves the typical underestimation of SOA formation by current global models. Details, as NO_x suppression, aerosol acidity enhancement, O:C ratio and novel aerosol sinks, can be explored with this new coupling in HAM and MOZ. Hodzic et al. [2016] claimed that a stronger production, faster removal and shorter lifetime might bring models closer to the real processes governing the global SOA budget in the ambient atmosphere. The SOA formation scheme here, which can easily be extended to other hydrocarbons than isoprene, for a given chemical mechanism, has a stronger SOA production and a faster removal compared to other models (section 4.1.3).

5.9.1. Gas-phase chemistry

The stronger production is achieved using individual compounds with sufficiently low volatility or reactive uptake on pre-existing aerosol. Therefore, SOA formation is strongly dependent on the chemical mechanism, which in JAM3 consists of 779 reactions. These reactions do not capture all atmospheric organic chemistry and all possible products which could lead to SOA production. The current version lacks a decent treatment of monoterpenes and sesquiterpenes. As discussed before, SOA formation depends on pre-existing aerosol. Thus, using more compounds than the ones used here for iSOA, would lead to a feedback and increase iSOA and total SOA formation.

Although an up-to-date isoprene oxidation mechanism is used to predict iSOA formation, isoprene chemistry is still not fully understood and there may be additional reactions occurring, which are not reflected in the current chemical mechanism. Indeed, ECHAM-HAMMOZ LISOPOOHOOH production is one order of magnitude higher than prior estimations (see section 4.1.3). LISPOOHOOH production might be too high due to missing intramolecular 1,6H-shift of LISOPOOHO2 which would lead to products with a saturation vapor pressure comparable to the one of LC578OOH. The LISOPOOHO2 isomerization reaction is quick compared to atmospheric oxidation, thus has the potential efficiently reduce LISOPOOHOOH formation. Moreover, LISOPOOHOOH in-particle, thermal decay efficiently reduces total iSOA, because LISOPOOHOOH is one of the major contributors to iSOA, as described in section 5.7.2.

Results of chemical regimes in section 4.1.5 show that JAM3 changes isoprene oxidation product distribution if sufficiently high values of NO ($> 400\,\text{pptv}$) are present in the grid-box. This change leads to the observed isoprene SOA suppression in NO_x dominated regimes. This feature vanishes in the time averaged values. In addition, the coarse resolution of around $200 \times 200\,\text{km}$ dilutes NO strongly, acting like a field average. Therefore, NO_x iSOA suppression might be underestimated in this study because of the model resolution.

Although Schultz et al. [2017] evaluated ECHAM-HAMMOZ, an evaluation focusing on the radical chemistry was not performed. Schultz et al. [2017] describe that the dynamical core of ECHAM-HAMMOZ generates too much OH in the free troposphere and the tropics, where

isoprene is oxidized and iSOA is formed as well. This leads to an imbalance in isoprene oxidation pathways. The budgets described in sections 4.1.3 and 5.1 represent the whole atmosphere, thus including the areas with spuriously high OH concentrations and quick hydrocarbon oxidation. Thus, the budgets might be biased towards HO_x dominated oxidation. This leads to high production rate of LIEPOX and LISOPOOHOOH, the main contributors to iSOA.

5.9.2. Particle formation

Particle formation itself is not well understood and still investigated in laboratory experiments. Particle formation in ECHAM-HAMMOZ assumes an equilibrium between the condensation and evaporation of SOA precursors for partitioning, which is a rather strong assumption (see section 2.2.1). As described in section 3.5.2, the model time-step is divided in sub-steps to achieve the equilibrium in time scales in agreement with current research. Nevertheless, in-particle processing is ignored. Compounds could undergo chemical reactions in the particle-phase quickly enough so that the equilibrium is never reached. Alternatively, the equilibrium is reached during nighttime, because in-particle chemistry is inactive, but not during daytime. Global models do not account for such cases.

ECHAM-HAMMOZ includes several aerosol types, but lacks in ammonium-nitrate aerosol. This is the reason why no aerosol ph values can be calculated using the current version of ECHAM-HAMMOZ. Aerosol pH values impact particle formation and in-particle chemistry. The impact of aerosol pH on aerosol formation on a global scale is not yet explored, especially with focus on SOA formation. SOA formation itself impacts aerosol pH, for example, organic acids are observed in the particle-phase.

Furthermore, as discussed in sections 5.5 and 5.6, the saturation concentrations function $C^*(T)$ is highly uncertain. Group contribution methods rely on many data points of compounds which are not very representative for atmospheric multifunctional hydrocarbons. It is widely known, but synthesis of atmospheric semi and low volatile compounds is challenging and therefore underrepresented. Further, the small number of experiments measuring $C^*(T)$ for atmospheric compounds usually use pure organic aerosol, which nucleated during the experiment. Therefore, the $C^*(T)$ on aqueous-aerosol as found in the atmosphere could deviate from these values. Moreover, water-solubility of the compounds might change partitioning and the equilibrium. More experiments under different conditions are needed to address these issues before improved parametrizations can be included in the models.

5.9.3. SOA loss processes

iSOA in ECHAM-HAMMOZ RefBase is mainly lost to aerosol wet deposition, followed by gas-phase wet deposition. This is a result of high solubility of gas-phase precursors and aerosols itself. Further, iSOA is mainly formed in tropical regions with deep convection, where scavenging parameters for iSOA aerosol bins are near to unity, efficiently removing iSOA. In HAM-SALSA all iSOA types are classified as soluble, which means they take part in cloud formation. Wet removal by cloud formation and collision with cloud droplets ("rainout", see section 2.3.1) might be the main removal process for iSOA. iSOA is mainly formed in the tropical regions where deep convection transports the particles to higher altitudes where they can form clouds. The current version of HAM-SALSA uses the wet deposition scheme described in section 3.2, but a new wet deposition scheme is currently under implementation. It is the scheme described in Croft et al. [2009], which is currently only available for M7. Croft et al. [2009] report local wet deposition

reductions of up to 20 % for organic carbon aerosol for some northern hemispheric regions, mainly over the ocean. Nevertheless, below cloud scavenging is not easily parametrized because it needs knowledge of particle and hydrometeor number and size distribution. Therefore, iSOA deposition remains uncertain, but it is a controlling parameter for SOA concentration. A stronger deposition would reduce the iSOA overestimation in ECHAM-HAMMOZ.

Additional loss processes were implemented and described in sections 5.7 and 5.8. As discussed, in-particle photolysis and thermal decay are processes happening in the aerosol-phase, which are still highly uncertain. In the aerosol-phase and in cloud droplets, in-particle chemistry occurs. In-particle oxidation can either lead to formation of larger, higher oxidized molecules or to fragmentation of aerosol compounds. These small fragments are more volatile and evaporate, leading to effective SOA loss. In-particle chemistry is beyond the realm of the current ECHAM-HAMMOZ model formulation. Moreover, limitations in aerosol cloud processing did not allow the implementation of in-cloud SOA formation. Once aerosol forms a cloud in ECHAM-HAMMOZ it is lost to the aerosol population, thus in-cloud SOA formation could not be implemented. This is not only an additional source, but also an additional sink. Reactive uptake of LIEPOX in cloud and rain droplets would lead to a quick loss, instead of iSOA formation. Since LIEPOX is also a major contributor to iSOA, this might be a potential strong, missing sink.

6. Conclusions

A novel explicit treatment of SOA formation was developed in this thesis to improve the knowledge about the SOA formation process, to tackle the usual problem of underestimation of SOA concentrations in global models and to explore anthropogenic impacts on SOA. A global model was used, because secondary organic aerosol is an important fraction of global, fine particulate matter, which influences human health and the climate system. Precise knowledge of particle amounts in the atmosphere helps to reduce human health issues, but also to investigate the impact of aerosol on climate via absorption, scattering and cloud formation.

Evaluation of SOA formation in ECHAM-HAMMOZ shows that large amounts of isoprene derived SOA are formed, especially in isoprene rich regions. These fit well to observations in the isoprene dominated Amazon region and show that the SOA production from isoprene alone surpasses total SOA production of global models compared in AeroCom. Both results show that ECHAM-HAMMOZ resolves the underestimation of SOA formation with a high model complexity. The high model complexity is needed in order to gain a deeper process understanding of several chemical processes influenced by meteorology and atmospheric conditions. Chemistry is calculated semi-explicitly and individual species are explicitly partitioned or taken up by reactive uptake onto pre-existing aerosol. This approach allows to evaluate the global O:C ratios as well, which to my knowledge has not been done yet by any global model.

Anthropogenic impacts on SOA formation addressed in this study are the NO_x suppression of iSOA observed in several experimental studies and the acidic enhancement of IEPOX uptake. NO_x emissions and acidic aerosol are found in similar regions, because both are emitted anthropogenically. Results of ECHAM-HAMMOZ show that acidic enhancement of IEPOX is stronger than NO_x suppression of IEPOX formation.

The process of SOA formation via partitioning to pre-existing aerosol depends on the molecular characteristic volatility. Thus, from all isoprene products four sufficiently low volatile and semi-volatile products were identified. Their volatility can be expressed using two key variables, saturation vapor pressure and enthalpy of vaporization. Results of sensitivity studies performed here using different values of saturation vapor pressure and enthalpy of vaporization according to literature and molecular structures showed that: 1) for these isoprene products, enthalpy of vaporization is not a controlling parameter and 2) saturation vapor pressure of these products varies strongly depending on which method was used to estimate it. The global SOA production is sensitive to this value. To conclude, precise knowledge of the saturation vapor pressure is more important than knowledge of enthalpy of vaporization. Nevertheless, not enough measurements of saturation vapor pressures of atmospherically relevant compounds are available. Characterization of atmospherically relevant hydrocarbons are needed to be able to further analyze SOA formation by model studies.

In order to explore all possible processes controlling SOA formation and the SOA burden, additional SOA sinks were explored in this study. Given the current understanding of SOA photolysis and knowledge of the compound ISOP(HOO)2, ECHAM-HAMMOZ results show that photolysis reduces global iSOA burden between 10 and 40 % and ISOP(HOO)2 decay reduces global iSOA burden around 50 %. To simulate iSOA concentrations comparable to

observations, the iSOA burden has to be either reduced by the combination both novel SOA sinks or less chemical LISOPOOHOOH production by alternative reaction pathways (isomerization reactions). Results here show that a reduced LISOPOOHOOH-SOA burden leads to best agreements of modeled iSOA and OA observed in the Amazon region.

The detailed processes which were explored with ECHAM-HAMMOZ also showed its limitations in its complexity. In-particle chemistry and a thermodynamic aerosol model including all aerosol types would improve the exploration of aerosol pH value and in-particle sinks. Currently missing secondary organic aerosol types are sesquiterpene-SOA, monoterpene-SOA, but also aromatic-SOA. Moreover, there is room for improvement of the chemical mechanism for a better HO_x recycling. A related problem to atmospheric chemistry is the model resolution. The coarse global resolution of around 200×200 km dilutes radicals and chemical species. This leads to lower concentrations of reactants. Thus atmospheric chemistry would proceed differently, if neighboring air masses were resolved. For example, one plume high in BVOC would mix with an urban plume rich in acidic aerosol and high NO_x concentrations. As discussed in this study, the chemistry in the BVOC plume differs from the one in the anthropogenic plume. Once they are mixed, again chemistry would change drastically, enhancing or suppressing SOA formation compared to the separated plumes. A high resolution regional model could adapt the explicit treatment of SOA formation presented in this study and solve this limitation. Otherwise, these dependencies have to be simulated with box models.

Although the current version of ECHAM-HAMMOZ only allowed to explore isoprene derived SOA, results show that iSOA could contribute between 6 % and 11 % to total estimated SOA ($510-910$ TgC a^{-1} [Goldstein and Galbally, 2007]). On a global average, an iSOA yield of 15 %, relative to global annual isoprene emissions, is calculated in ECHAM-HAMMOZ and an annual mean burden of 0.6 TgC. Further, the daily cycle of SOA formation can be resolved, which is important to understand when most SOA is formed and when it is lost. Most of iSOA precursors are formed during daytime, and particulate iSOA is deposited during nighttime. In ECHAM-HAMMOZ, precursor formation and in-particle destruction correlate with each other. The feedback of reduced pre-existing particle surface prevents SOA to be formed.

These results encourage to continue exploring SOA formation using both, a detailed atmospheric chemical mechanism and explicit SOA formation of individual compounds. With such model frameworks, processes can be investigated, understood and finally model complexity can be reduced again to meet computational capacities currently given. Furthermore, once SOA is predicted with sufficient accuracy, studies can focus on impacts on cloud formation, radiation modification and can predict impacts on human health. Not only the particle size is important here, but also the composition of these aerosols. Thus, knowledge of the individual particle composition is an advantage for these purposes.

Bibliography

A. Aiken, D. Salcedo, M. J. Cubison, J. Huffman, P. DeCarlo, I. M. Ulbrich, K. S. Docherty, D. Sueper, J. Kimmel, D. R. Worsnop, et al. Mexico city aerosol analysis during milagro using high resolution aerosol mass spectrometry at the urban supersite (t0)–part 1: Fine particle composition and organic source apportionment. *Atmospheric Chemistry and Physics*, 9(17): 6633–6653, 2009.

A. Aiken, B. d. Foy, C. Wiedinmyer, P. DeCarlo, I. M. Ulbrich, M. Wehrli, S. Szidat, A. Prevot, J. Noda, L. Wacker, et al. Mexico city aerosol analysis during milagro using high resolution aerosol mass spectrometry at the urban supersite (t0)–part 2: Analysis of the biomass burning contribution and the non-fossil carbon fraction. *Atmospheric chemistry and physics*, 10(12): 5315–5341, 2010.

A. C. Aiken, P. F. Decarlo, J. H. Kroll, D. R. Worsnop, J. A. Huffman, K. S. Docherty, I. M. Ulbrich, C. Mohr, J. R. Kimmel, D. Sueper, et al. O/c and om/oc ratios of primary, secondary, and ambient organic aerosols with high-resolution time-of-flight aerosol mass spectrometry. *Environmental Science & Technology*, 42(12):4478–4485, 2008.

B. Alexander, M. Hastings, D. Allman, J. Dachs, J. Thornton, and S. Kunasek. Quantifying atmospheric nitrate formation pathways based on a global model of the oxygen isotopic composition (δ 17 o) of atmospheric nitrate. *Atmospheric Chemistry and Physics*, 9(14): 5043–5056, 2009.

E. Athanasopoulou, H. Vogel, B. Vogel, A. Tsimpidi, S. N. Pandis, C. Knote, and C. Fountoukis. Modeling the meteorological and chemical effects of secondary organic aerosols during an eucaari campaign. *Atmospheric Chemistry and Physics*, 13:625, 2012.

R. Atkinson and J. Arey. Gas-phase tropospheric chemistry of biogenic volatile organic compounds: a review. *Atmospheric Environment*, 37:197–219, 2003.

M. Barley and G. McFiggans. The critical assessment of vapour pressure estimation methods for use in modelling the formation of atmospheric organic aerosol. *Atmospheric Chemistry and Physics*, 10(2):749–767, 2010.

A. P. Bateman, S. A. Nizkorodov, J. Laskin, and A. Laskin. Photolytic processing of secondary organic aerosols dissolved in cloud droplets. *Physical Chemistry Chemical Physics*, 13(26): 12199–12212, 2011.

T. Bergman, V.-M. Kerminen, H. Korhonen, K. Lehtinen, R. Makkonen, A. Arola, T. Mielonen, S. Romakkaniemi, M. Kulmala, and H. Kokkola. Evaluation of the sectional aerosol microphysics module salsa implementation in echam5-ham aerosol-climate model. *Geoscientific Model Development*, 5(3):845–868, 2012.

T. Berndt, H. Herrmann, M. Sipilä, and M. Kulmala. Highly oxidized second-generation products from the gas-phase reaction of oh radicals with isoprene. *J. Phys. Chem. A*, 120(51): 10150–10159, 2016.

F. Bian and F. M. Bowman. Theoretical method for lumping multicomponent secondary organic aerosol mixtures. *Environmental science & technology*, 36(11):2491–2497, 2002.

M. Bilde, K. Barsanti, M. Booth, C. D. Cappa, N. M. Donahue, E. U. Emanuelsson, G. McFiggans, U. K. Krieger, C. Marcolli, D. Topping, et al. Saturation vapor pressures and transition enthalpies of low-volatility organic molecules of atmospheric relevance: from dicarboxylic acids to complex mixtures. *Chemical reviews*, 115(10):4115–4156, 2015.

E. A. Brandes, G. Zhang, and J. Vivekanandan. Experiments in rainfall estimation with a polarimetric radar in a subtropical environment. *Journal of Applied Meteorology*, 41(6): 674–685, 2002.

S. Brinkop and E. Roeckner. Sensitivity of a general circulation model to parameterizations of cloud–turbulence interactions in the atmospheric boundary layer. *Tellus A*, 47(2):197–220, 1995.

V. Brovkin, L. Boysen, T. Raddatz, V. Gayler, A. Loew, and M. Claussen. Evaluation of vegetation cover and land-surface albedo in mpi-esm cmip5 simulations. *Journal of Advances in Modeling Earth Systems*, 5(1):48–57, 2013.

S. Budisulistiorini, X. Li, S. Bairai, J. Renfro, Y. Liu, Y. Liu, K. McKinney, S. Martin, V. McNeill, H. Pye, et al. Examining the effects of anthropogenic emissions on isoprene-derived secondary organic aerosol formation during the 2013 southern oxidant and aerosol study (soas) at the look rock, tennessee ground site. *Atmospheric Chemistry and Physics*, 15(15): 8871–8888, 2015.

M. Canagaratna, J. Jimenez, J. Kroll, Q. Chen, S. Kessler, P. Massoli, L. Hildebrandt Ruiz, E. Fortner, L. Williams, K. Wilson, et al. Elemental ratio measurements of organic compounds using aerosol mass spectrometry: characterization, improved calibration, and implications. *Atmospheric Chemistry and Physics*, 15(1):253–272, 2015.

Q. Cao and G. Zhang. Errors in estimating raindrop size distribution parameters employing disdrometer and simulated raindrop spectra. *Journal of Applied Meteorology and Climatology*, 48(2):406–425, 2009.

S. Carbone, M. Aurela, K. Saarnio, S. Saarikoski, H. Timonen, A. Frey, D. Sueper, I. M. Ulbrich, J. L. Jimenez, M. Kulmala, et al. Wintertime aerosol chemistry in sub-arctic urban air. *Aerosol Science and Technology*, 48(3):313–323, 2014.

A. Carlton, C. Wiedinmyer, and J. Kroll. A review of secondary organic aerosol (soa) formation from isoprene. *Atmospheric Chemistry and Physics*, 9(14):4987–5005, 2009.

A. G. Carlton, B. J. Turpin, K. E. Altieri, S. Seitzinger, A. Reff, H.-J. Lim, and B. Ervens. Atmospheric oxalic acid and soa production from glyoxal: Results of aqueous photooxidation experiments. *Atmospheric Environment*, 41(35):7588–7602, 2007.

ChemSpider. Csid:61032981, accessed 01.03.2018.

J.-P. Chen and D. Lamb. Simulation of cloud microphysical and chemical processes using a multicomponent framework. part i: Description of the microphysical model. *Journal of the Atmospheric Sciences*, 51(18):2613–2630, 1994. doi: https://doi.org/10.1175/15200469(1994)051⟨2613:SOCMAC⟩2.0.CO;2,http://dx.doi.org/10.1175/1520-0469(1994)051⟨2613:SOCMAC⟩2.0.CO;2.

Q. Chen, D. Farmer, J. Schneider, S. Zorn, C. Heald, T. Karl, A. Guenther, J. Allan, N. Robinson, H. Coe, et al. Mass spectral characterization of submicron biogenic organic particles in the amazon basin. *Geophysical Research Letters*, 36(20), 2009.

S. H. Chung and J. H. Seinfeld. Global distribution and climate forcing of carbonaceous aerosols. *Journal of Geophysical Research: Atmospheres*, 107(D19), 2002.

M. Claeys, B. Graham, G. Vas, W. Wang, R. Vermeylen, V. Pashynska, J. Cafmeyer, P. Guyon, M. O. Andreae, P. Artaxo, et al. Formation of secondary organic aerosols through photooxidation of isoprene. *Science*, 303(5661):1173–1176, 2004.

J. Clayden, N. Greeves, S. Warren, and P. Wothers. *Organic Chemistry*. Oxford University Press, 2001.

S. L. Clegg, P. Brimblecombe, and A. S. Wexler. Thermodynamic model of the system h+- nh4+- na+- so42– no3– cl– h2o at 298.15 k. *The Journal of Physical Chemistry A*, 102(12): 2155–2171, 1998. doi: DOI:10.1021/jp973043j.

A. L. Clements and J. H. Seinfeld. Detection and quantification of 2-methyltetrols in ambient aerosol in the southeastern united states. *Atmospheric Environment*, 41(9):1825–1830, 2007.

N. C. Cole-Filipiak, A. E. OConnor, and M. J. Elrod. Kinetics of the hydrolysis of atmospherically relevant isoprene-derived hydroxy epoxides. *Environmental science & technology*, 44 (17):6718–6723, 2010.

S. Compernolle, K. Ceulemans, and J. Müller. Evaporation: a new vapor pressure estimation method for organic molecules including non-additivity and intramolecular interactions. *Atmos. Chem. Phys. Discuss*, 11(13):229–13, 2011.

B. Croft, U. Lohmann, R. Martin, P. Stier, S. Wurzler, J. Feichter, R. Posselt, and S. Ferrachat. Aerosol size-dependent below-cloud scavenging by rain and snow in the echam5-ham. *Atmospheric Chemistry and Physics*, 9(14):4653–4675, 2009.

J. D. Crounse, F. Paulot, H. G. Kjaergaard, and P. O. Wennberg. Peroxy radical isomerization in the oxidation of isoprene. *Physical Chemistry Chemical Physics*, 13(30):13607–13613, 2011.

G. da Silva. Carboxylic acid catalyzed keto-enol tautomerizations in the gas phase. *Angewandte Chemie International Edition*, 49(41):7523–7525, 2010.

M. Dall'Osto, D. Ceburnis, G. Martucci, J. Bialek, R. Dupuy, S. Jennings, H. Berresheim, J. Wenger, J. Sodeau, R. Healy, et al. Aerosol properties associated with air masses arriving into the north east atlantic during the 2008 mace head eucaari intensive observing period: an overview. *Atmospheric Chemistry & Physics Discussions*, 9(6), 2009.

E. L. D'Ambro, B. H. Lee, J. Liu, J. E. Shilling, C. J. Gaston, F. D. Lopez-Hilfiker, S. Schobesberger, R. A. Zaveri, C. Mohr, A. Lutz, et al. Molecular composition and volatility of isoprene photochemical oxidation secondary organic aerosol under low-and high-no x conditions. *Atmospheric Chemistry and Physics*, 17(1):159–174, 2017a.

E. L. D'Ambro, K. H. Møller, F. D. Lopez-Hilfiker, S. Schobesberger, J. Liu, J. E. Shilling, B. H. Lee, H. G. Kjaergaard, and J. A. Thornton. Isomerization of second-generation isoprene peroxy radicals: Epoxide formation and implications for secondary organic aerosol yields. *Environmental Science & Technology*, 51(9):4978–4987, 2017b.

K. E. Daumit, A. J. Carrasquillo, R. A. Sugrue, and J. H. Kroll. Effects of condensed-phase oxidants on secondary organic aerosol formation. *The Journal of Physical Chemistry A*, 120 (9):1386–1394, 2015.

P. Davidovits, C. E. Kolb, L. R. Williams, J. T. Jayne, and D. R. Worsnop. Mass accommodation and chemical reactions at gas- liquid interfaces. *Chemical reviews*, 106(4):1323–1354, 2006.

F. Dentener, S. Kinne, T. Bond, O. Boucher, J. Cofala, S. Generoso, P. Ginoux, S. Gong, J. Hoelzemann, A. Ito, et al. Emissions of primary aerosol and precursor gases in the years 2000 and 1750 prescribed data-sets for aerocom. *Atmospheric Chemistry and Physics*, 6(12): 4321–4344, 2006.

F. J. Dentener and P. J. Crutzen. Reaction of n_2o_5 on tropospheric aerosols: Impact on the global distributions of no x, o_3, and oh. *Journal of Geophysical Research: Atmospheres (1984–2012)*, 98(D4):7149–7163, 1993.

N. Donahue, A. Robinson, C. Stanier, and S. Pandis. Coupled partitioning, dilution, and chemical aging of semivolatile organics. *Environmental Science & Technology*, 40(8):2635–2643, 2006.

N. M. Donahue, S. Epstein, S. N. Pandis, and A. L. Robinson. A two-dimensional volatility basis set: 1. organic-aerosol mixing thermodynamics. *Atmospheric Chemistry and Physics*, 11(7):3303–3318, 2011.

N. M. Donahue, J. Kroll, S. N. Pandis, and A. L. Robinson. A two-dimensional volatility basis set–part 2: Diagnostics of organic-aerosol evolution. *Atmospheric Chemistry and Physics*, 12 (2):615–634, 2012.

N. C. Eddingsaas, D. G. VanderVelde, and P. O. Wennberg. Kinetics and products of the acid-catalyzed ring-opening of atmospherically relevant butyl epoxy alcohols. *The Journal of Physical Chemistry A*, 114(31):8106–8113, 2010.

E. Eliasen, B. Machenhauer, and E. Rasmussen. *On a numerical method for integration of the hydrodynamical equations with a spectral representation of the horizontal fields*. Kobenhavns Universitet, Institut for Teoretisk Meteorologi, 1970.

L. Emmons, S. Walters, P. Hess, J.-F. Lamarque, G. Pfister, D. Fillmore, C. Granier, A. Guenther, D. Kinnison, T. Laepple, et al. Description and evaluation of the model for ozone and related chemical tracers, version 4 (mozart-4). *Geoscientific Model Development*, 3(1):43–67, 2010.

G. J. Engelhart, R. H. Moore, A. Nenes, and S. N. Pandis. Cloud condensation nuclei activity of isoprene secondary organic aerosol. *Journal of Geophysical Research: Atmospheres*, 116 (D2), 2011.

S. A. Epstein, I. Riipinen, and N. M. Donahue. A semiempirical correlation between enthalpy of vaporization and saturation concentration for organic aerosol. *Environmental science & technology*, 44(2):743–748, 2009.

S. A. Epstein, S. L. Blair, and S. A. Nizkorodov. Direct photolysis of α-pinene ozonolysis secondary organic aerosol: effect on particle mass and peroxide content. *Environmental science & technology*, 48(19):11251–11258, 2014.

B. Ervens and R. Volkamer. Glyoxal processing by aerosol multiphase chemistry: towards a kinetic modeling framework of secondary organic aerosol formation in aqueous particles. *Atmospheric Chemistry and Physics*, 10(17):8219–8244, 2010.

B. Ervens, B. Turpin, and R. Weber. Secondary organic aerosol formation in cloud droplets and aqueous particles (aqsoa): a review of laboratory, field and model studies. *Atmospheric Chemistry and Physics*, 11(21):11069–11102, 2011.

M. Evans and D. J. Jacob. Impact of new laboratory studies of n_2o_5 hydrolysis on global model budgets of tropospheric nitrogen oxides, ozone, and oh. *Geophysical Research Letters*, 32(9), 2005.

S. C. Farina, P. J. Adams, and S. N. Pandis. Modeling global secondary organic aerosol formation and processing with the volatility basis set: Implications for anthropogenic secondary organic aerosol. *Journal of Geophysical Research: Atmospheres*, 115(D9), 2010.

J. Feichter, E. Kjellström, H. Rodhe, F. Dentener, J. Lelieveldi, and G.-J. Roelofs. Simulation of the tropospheric sulfur cycle in a global climate model. *Atmospheric Environment*, 30 (10-11):1693–1707, 1996.

Y. Feng, V. Ramanathan, and V. Kotamarthi. Brown carbon: a significant atmospheric absorber of solar radiation? *Atmospheric Chemistry and Physics*, 13(17):8607–8621, 2013.

J. Fröhlich-Nowoisky, C. J. Kampf, B. Weber, J. A. Huffman, C. Pöhlker, M. O. Andreae, N. Lang-Yona, S. M. Burrows, S. S. Gunthe, W. Elbert, et al. Bioaerosols in the earth system: Climate, health, and ecosystem interactions. *Atmospheric Research*, 182:346–376, 2016.

T.-M. Fu, D. J. Jacob, F. Wittrock, J. P. Burrows, M. Vrekoussis, and D. K. Henze. Global budgets of atmospheric glyoxal and methylglyoxal, and implications for formation of secondary organic aerosols. *Journal of geophysical research: atmospheres*, 113(D15), 2008.

H. Fuchs, A. Hofzumahaus, F. Rohrer, B. Bohn, T. Brauers, H. Dorn, R. Häseler, F. Holland, M. Kaminski, X. Li, et al. Experimental evidence for efficient hydroxyl radical regeneration in isoprene oxidation. *Nature Geoscience*, 6(12):1023, 2013.

N. A. Fuks and A. G. Sutugin. Highly dispersed aerosols. 1970.

S. Fuzzi, U. Baltensperger, K. Carslaw, S. Decesari, H. Denier Van Der Gon, M. Facchini, D. Fowler, I. Koren, B. Langford, U. Lohmann, et al. Particulate matter, air quality and climate: lessons learned and future needs. *Atmospheric chemistry and physics*, 15(14):8217–8299, 2015.

L. Ganzeveld, J. Lelieveld, and G.-J. Roelofs. A dry deposition parameterization for sulfur oxides in a chemistry and general circulation model. *Journal of Geophysical Research: Atmospheres*, 103(D5):5679–5694, 1998.

C. J. Gaston, T. P. Riedel, Z. Zhang, A. Gold, J. D. Surratt, and J. A. Thornton. Reactive uptake of an isoprene-derived epoxydiol to submicron aerosol particles. *Environmental science & technology*, 48(19):11178–11186, 2014.

A. Gelencsér, B. May, D. Simpson, A. Sánchez-Ochoa, A. Kasper-Giebl, H. Puxbaum, A. Caseiro, C. Pio, and M. Legrand. Source apportionment of pm2.5 organic aerosol over europe: Primary/secondary, natural/anthropogenic, and fossil/biogenic origin. *Journal of Geophysical Research: Atmospheres*, 112(D23), 2007.

M. Giorgetta, E. Manzini, E. Roeckner, M. Esch, and L. Bengtsson. Climatology and forcing of the quasi-biennial oscillation in the maecham5 model. *Journal of Climate*, 19(16):3882–3901, 2006.

M. Giorgetta, E. Roeckner, T. Mauritsen, B. Stevens, J. Bader, T. Crueger, M. Esch, S. Rast, L. Kornblueh, H. Schmidt, S. Kinne, B. Mbis, and T. Krismer. The atmospheric general circulation model echam6 (model description). Technical report, Max-Planck Institute for Meteorology Hamburg, Germany., 2012.

G. I. Gkatzelis, R. Tillmann, T. Hohaus, M. Müller, P. Eichler, K.-M. Xu, P. Schlag, S. H. Schmitt, R. Wegener, M. Kaminski, et al. Comparison of three aerosol chemical characterization techniques utilizing ptr-tof-ms: A study on freshly formed 2 and aged biogenic soa. *Atmos. Meas. Tech. Discuss.*, 2017. doi: https://doi.org/10.5194/amt-2017-288.

A. H. Goldstein and I. E. Galbally. Known and unexplored organic constituents in the earth's atmosphere, 2007.

C. Granier, A. Guenther, J. Lamarque, A. Mieville, J. Muller, J. Olivier, J. Orlando, J. Peters, G. Petron, G. Tyndall, et al. Poet, a database of surface emissions of ozone precursors available online at: http://www. aero. jussieu. fr/projet/accent. *POET. php*, 2005.

V. Grewe, D. Brunner, M. Dameris, J. Grenfell, R. Hein, D. Shindell, and J. Staehelin. Origin and variability of upper tropospheric nitrogen oxides and ozone at northern mid-latitudes. *Atmospheric Environment*, 35(20):3421–3433, 2001.

C. Groß, T. Dillon, G. Schuster, J. Lelieveld, and J. Crowley. Direct kinetic study of oh and o3 formation in the reaction of ch3c (o) o2 with ho2. *The Journal of Physical Chemistry A*, 118(6):974–985, 2014.

S. Gross, R. Iannone, S. Xiao, and A. K. Bertram. Reactive uptake studies of no_3 and n_2o_5 on alkenoic acid, alkanoate, and polyalcohol substrates to probe nighttime aerosol chemistry. *Physical Chemistry Chemical Physics*, 11(36):7792–7803, 2009.

A. Guenther, T. Karl, P. Harley, C. Wiedinmyer, P. Palmer, and C. Geron. Estimates of global terrestrial isoprene emissions using megan (model of emissions of gases and aerosols from nature). *Atmospheric Chemistry and Physics Discussions*, 6(1):107–173, 2006.

A. Guenther, X. Jiang, C. Heald, T. Sakulyanontvittaya, T. Duhl, L. Emmons, and X. Wang. The model of emissions of gases and aerosols from nature version 2.1 (megan2. 1): an extended and updated framework for modeling biogenic emissions. 2012.

R. Gutbrod, E. Kraka, R. N. Schindler, and D. Cremer. Kinetic and theoretical investigation of the gas-phase ozonolysis of isoprene: Carbonyl oxides as an important source for oh radicals in the atmosphere. *Journal of the American Chemical Society*, 119(31):7330–7342, 1997.

S. Hagemann and T. Stacke. Impact of the soil hydrology scheme on simulated soil moisture memory. *Climate Dynamics*, 44(7-8):1731–1750, 2015.

M. Hallquist, J. Wenger, U. Baltensperger, Y. Rudich, D. Simpson, M. Claeys, J. Dommen, N. Donahue, C. George, A. Goldstein, et al. The formation, properties and impact of secondary organic aerosol: current and emerging issues. *Atmospheric Chemistry and Physics*, 9 (14):5155–5236, 2009.

A.-J. Henrot, T. Stanelle, S. Schröder, C. Siegenthaler, D. Taraborrelli, and M. G. Schultz. Implementation of the megan (v2. 1) biogenic emission model in the echam6-hammoz chemistry climate model. *Geoscientific Model Development*, 10(2):903, 2017.

K. M. Henry and N. M. Donahue. Photochemical aging of α-pinene secondary organic aerosol: effects of oh radical sources and photolysis. *The Journal of Physical Chemistry A*, 116(24): 5932–5940, 2012.

A. Hodzic, S. Madronich, P. Kasibhatla, G. Tyndall, B. Aumont, J. Jimenez, J. Lee-Taylor, and J. Orlando. Organic photolysis reactions in tropospheric aerosols: effect on secondary organic aerosol formation and lifetime. *Atmospheric Chemistry and Physics*, 15(16):9253–9269, 2015.

A. Hodzic, P. S. Kasibhatla, D. S. Jo, C. D. Cappa, J. L. Jimenez, S. Madronich, and R. J. Park. Rethinking the global secondary organic aerosol (soa) budget: stronger production, faster removal, shorter lifetime. *Atmospheric Chemistry and Physics*, 16(12):7917–7941, 2016.

T. Hoffmann, J. R. Odum, F. Bowman, D. Collins, D. Klockow, R. C. Flagan, and J. H. Seinfeld. Formation of organic aerosols from the oxidation of biogenic hydrocarbons. *Journal of Atmospheric Chemistry*, 26(2):189–222, 1997.

T. Hohaus, I. Gensch, J. Kimmel, D. R. Worsnop, and A. Kiendler-Scharr. Experimental determination of the partitioning coefficient of β-pinene oxidation products in soas. *Physical Chemistry Chemical Physics*, 17(22):14796–14804, 2015.

W. Hu, P. Campuzano-Jost, B. Palm, D. Day, A. Ortega, P. Hayes, J. Krechmer, Q. Chen, M. Kuwata, Y. Liu, et al. Characterization of a real-time tracer for isoprene epoxydiols-derived secondary organic aerosol (iepox-soa) from aerosol mass spectrometer measurements. *Atmospheric Chemistry and Physics*, 15(20):11807–11833, 2015.

B. Huebert, T. Bertram, J. Kline, S. Howell, D. Eatough, and B. Blomquist. Measurements of organic and elemental carbon in asian outflow during ace-asia from the nsf/ncar c-130. *Journal of Geophysical Research: Atmospheres*, 109(D19), 2004.

M. J. Iacono, J. S. Delamere, E. J. Mlawer, M. W. Shephard, S. A. Clough, and W. D. Collins. Radiative forcing by long-lived greenhouse gases: Calculations with the aer radiative transfer models. *Journal of Geophysical Research: Atmospheres*, 113(D13), 2008.

IPCC. *Annex I: Atlas of Global and Regional Climate Projections*, book section AI, pages 1311–1394. Cambridge University Press, Cambridge, United Kingdom and New York, NY, USA, 2013. ISBN ISBN 978-1-107-66182-0. doi: 10.1017/CBO9781107415324.029. URL `www.climatechange2013.org`.

M. Z. Jacobson. *Fundamentals of atmospheric modeling*. Cambridge university press, 2005.

M. Jenkin, S. Saunders, V. Wagner, and M. Pilling. Protocol for the development of the master chemical mechanism, mcm v3 (part b): tropospheric degradation of aromatic volatile organic compounds. *Atmospheric Chemistry and Physics*, 3(1):181–193, 2003.

M. Jenkin, J. Young, and A. Rickard. The mcm v3. 3.1 degradation scheme for isoprene. *Atmospheric Chemistry & Physics*, 15(20), 2015.

J. Jimenez, M. Canagaratna, N. Donahue, A. Prevot, Q. Zhang, J. H. Kroll, P. F. DeCarlo, J. D. Allan, H. Coe, N. Ng, et al. Evolution of organic aerosols in the atmosphere. *Science*, 326(5959):1525–1529, 2009.

Jülich Supercomputing Centre. JURECA: General-purpose supercomputer at Jülich Supercomputing Centre. *Journal of large-scale research facilities*, 2(A62), 2016. doi: 10.17815/jlsrf-2-121. URL `http://dx.doi.org/10.17815/jlsrf-2-121`.

M. Kanakidou, K. Tsigaridis, F. J. Dentener, and P. J. Crutzen. Human-activity-enhanced formation of organic aerosols by biogenic hydrocarbon oxidation. *Journal of Geophysical Research: Atmospheres*, 105(D7):9243–9354, 2000.

M. Kanakidou, J. Seinfeld, S. Pandis, I. Barnes, F. Dentener, M. Facchini, R. V. Dingenen, B. Ervens, A. Nenes, C. Nielsen, et al. Organic aerosol and global climate modelling: a review. *Atmospheric Chemistry and Physics*, 5(4):1053–1123, 2005.

M. Karl, T. Brauers, H.-P. Dorn, F. Holland, M. Komenda, D. Poppe, F. Rohrer, L. Rupp, A. Schaub, and A. Wahner. Kinetic study of the oh-isoprene and o3-isoprene reaction in the atmosphere simulation chamber, saphir. *Geophysical research letters*, 31(5), 2004.

M. Karl, H.-P. Dorn, F. Holland, R. Koppmann, D. Poppe, L. Rupp, A. Schaub, and A. Wahner. Product study of the reaction of oh radicals with isoprene in the atmosphere simulation chamber saphir. *Journal of atmospheric chemistry*, 55(2):167–187, 2006.

A. Kettle and M. Andreae. Flux of dimethylsulfide from the oceans: A comparison of updated data sets and flux models. *Journal of Geophysical Research: Atmospheres*, 105(D22):26793–26808, 2000.

D. Kinnison, G. Brasseur, S. Walters, R. Garcia, D. Marsh, F. Sassi, V. Harvey, C. Randall, L. Emmons, J. Lamarque, et al. Sensitivity of chemical tracers to meteorological parameters in the mozart-3 chemical transport model. *Journal of Geophysical Research: Atmospheres (1984–2012)*, 112(D20), 2007.

M. J. Kleeman, Q. Ying, J. Lu, M. J. Mysliwiec, R. J. Griffin, J. Chen, and S. Clegg. Source apportionment of secondary organic aerosol during a severe photochemical smog episode. *Atmospheric Environment*, 41(3):576–591, 2007.

J. Kleffmann, K. Becker, and P. Wiesen. Heterogeneous no_2 conversion processes on acid surfaces: possible atmospheric implications. *Atmospheric Environment*, 32(16):2721–2729, 1998.

C. Knote, A. Hodzic, J. Jimenez, R. Volkamer, J. Orlando, S. Baidar, J. Brioude, J. Fast, D. Gentner, A. Goldstein, et al. Simulation of semi-explicit mechanisms of soa formation from glyoxal in aerosol in a 3-d model. *Atmospheric Chemistry and Physics*, 14(12):6213–6239, 2014.

C. Kohlpaintner, M. Schulte, J. Falbe, P. Lappe, J. Weber, and G. D. Frey. *Aldehydes, Aliphatic*. Wiley-VCH Verlag GmbH & Co. KGaA, 2000. ISBN 9783527306732. doi: 10.1002/14356007.a01_321.pub3. URL `http://dx.doi.org/10.1002/14356007.a01_321.pub3`.

H. Kokkola, H. Korhonen, K. Lehtinen, R. Makkonen, A. Asmi, S. Järvenoja, T. Anttila, A.-I. Partanen, M. Kulmala, H. Järvinen, et al. Salsa–a sectional aerosol module for large scale applications. *Atmospheric Chemistry and Physics*, 8(9):2469–2483, 2008.

H. Kokkola, P. Yli-Pirilä, M. Vesterinen, H. Korhonen, H. Keskinen, S. Romakkaniemi, L. Hao, A. Kortelainen, J. Joutsensaari, D. Worsnop, et al. The role of low volatile organics on secondary organic aerosol formation. *Atmospheric Chemistry and Physics*, 14(3):1689–1700, 2014.

H. Kokkola, T. Kühn, A. Laakso, T. Bergman, K. Lehtinen, T. Mielonen, A. Arola, S. Stadtler, H. Korhonen, S. Ferrachat, U. Lohmann, D. Neubauer, I. Tegen, C. Siegenthaler-Le Drian, M. Schultz, I. Bey, P. Stier, N. Daskalakis, C. Heald, and S. Romakkaniemi. Salsa2.0: The sectional aerosol module of the aerosol-chemistry-climate model echam6.3.0-ham2.3-moz1.0. *Geoscientific Model Development Discussions*, 2018. doi: https://doi.org/10.5194/gmd-2018-47.

I. Kourtchev, T. Ruuskanen, W. Maenhaut, M. Kulmala, and M. Claeys. Observation of 2-methyltetrols and related photo-oxidation products of isoprene in boreal forest aerosols from hyytiälä, finland. *Atmospheric Chemistry and Physics*, 5(10):2761–2770, 2005.

M. Krapf, I. El Haddad, E. A. Bruns, U. Molteni, K. R. Daellenbach, A. S. Prévôt, U. Baltensperger, and J. Dommen. Labile peroxides in secondary organic aerosol. *Chem*, 1(4): 603–616, 2016.

J. H. Kroll and J. H. Seinfeld. Chemistry of secondary organic aerosol: Formation and evolution of low-volatility organics in the atmosphere. *Atmospheric Environment*, 42(16):3593–3624, 2008.

J. H. Kroll, J. D. Smith, D. L. Che, S. H. Kessler, D. R. Worsnop, and K. R. Wilson. Measurement of fragmentation and functionalization pathways in the heterogeneous oxidation of oxidized organic aerosol. *Physical Chemistry Chemical Physics*, 11(36):8005–8014, 2009.

T. Kühn, J. Merikanto, T. Mielonen, S. Stadtler, A. Hienola, H. Korhonen, S. Ferrachat, U. Lohmann, D. Neubauer, I. Tegen, C. Siegenthaler-Le Drian, S. Wahl, M. G. Schultz,

S. Rast, H. Schmidt, P. Stier, K. Lehtinen, and H. Kokkola. Salsa2.0 part2: Implementation of a volatility basis set to model formation of secondary organic aerosol. in preparation.

P. S. Lakey, T. Berkemeier, H. Tong, A. M. Arangio, K. Lucas, U. Pöschl, and M. Shiraiwa. Chemical exposure-response relationship between air pollutants and reactive oxygen species in the human respiratory tract. *Scientific reports*, 6:32916, 2016.

V. Lal, A. F. Khalizov, Y. Lin, M. D. Galvan, B. T. Connell, and R. Zhang. Heterogeneous reactions of epoxides in acidic media. *The Journal of Physical Chemistry A*, 116(24):6078–6090, 2012.

J.-F. Lamarque, T. C. Bond, V. Eyring, C. Granier, A. Heil, Z. Klimont, D. Lee, C. Liousse, A. Mieville, B. Owen, M. G. Schultz, D. Shindell, S. J. Smith, E. Stehfest, J. Van Aardenne, O. R. Cooper, M. Kainuma, N. Mahowald, J. R. McConnell, V. Naik, K. Riahi, and D. P. van Vuuren. Historical (18502000) gridded anthropogenic and biomass burning emissions of reactive gases and aerosols: methodology and application. *Atmospheric Chemistry and Physics*, 10(15):7017–7039, 2010. doi: 10.5194/acp-10-7017-2010. URL `https://www.atmos-chem-phys.net/10/7017/2010/`.

A. Lambe, T. Onasch, P. Massoli, D. Croasdale, J. Wright, A. Ahern, L. Williams, D. Worsnop, W. Brune, and P. Davidovits. Laboratory studies of the chemical composition and cloud condensation nuclei (ccn) activity of secondary organic aerosol (soa) and oxidized primary organic aerosol (opoa). *Atmospheric Chemistry and Physics*, 11(17):8913–8928, 2011.

J. Lelieveld, S. Gromov, A. Pozzer, and D. Taraborrelli. Global tropospheric hydroxyl distribution, budget and reactivity. *Atmos. Chem. Phys*, 16:12477–12493, 2016.

N. Li, T.-M. Fu, J. Cao, S. Lee, X.-F. Huang, L.-Y. He, K.-F. Ho, J. S. Fu, and Y.-F. Lam. Sources of secondary organic aerosols in the pearl river delta region in fall: Contributions from the aqueous reactive uptake of dicarbonyls. *Atmospheric environment*, 76:200–207, 2013.

J. Liggio, S.-M. Li, and R. McLaren. Heterogeneous reactions of glyoxal on particulate matter: Identification of acetals and sulfate esters. *Environmental science & technology*, 39(6):1532–1541, 2005a.

J. Liggio, S.-M. Li, and R. McLaren. Reactive uptake of glyoxal by particulate matter. *Journal of Geophysical Research: Atmospheres*, 110(D10), 2005b.

H. Lignell, M. L. Hinks, and S. A. Nizkorodov. Exploring matrix effects on photochemistry of organic aerosols. *Proceedings of the National Academy of Sciences*, 111(38):13780–13785, 2014.

H.-J. Lim, A. G. Carlton, and B. J. Turpin. Isoprene forms secondary organic aerosol through cloud processing: Model simulations. *Environmental science & technology*, 39(12):4441–4446, 2005.

G. Lin, J. Penner, S. Sillman, D. Taraborrelli, and J. Lelieveld. Global modeling of soa formation from dicarbonyls, epoxides, organic nitrates and peroxides. *Atmospheric Chemistry and Physics*, 12(10):4743–4774, 2012.

S.-J. Lin and R. B. Rood. Multidimensional flux-form semi-lagrangian transport schemes. *Monthly Weather Review*, 124(9):2046–2070, 1996.

Y.-H. Lin, E. Knipping, E. Edgerton, S. Shaw, and J. Surratt. Investigating the influences of so_2 and nh_3 levels on isoprene-derived secondary organic aerosol formation using conditional sampling approaches. *Atmospheric Chemistry and Physics*, 13(16):8457–8470, 2013.

C. Liousse, J. Penner, C. Chuang, J. Walton, H. Eddleman, and H. Cachier. A global three-dimensional model study of carbonaceous aerosols. *Journal of Geophysical Research: Atmospheres*, 101(D14):19411–19432, 1996.

J. Liu, E. L. DAmbro, B. H. Lee, F. D. Lopez-Hilfiker, R. A. Zaveri, J. C. Rivera-Rios, F. N. Keutsch, S. Iyer, T. Kurten, Z. Zhang, et al. Efficient isoprene secondary organic aerosol formation from a non-iepox pathway. *Environmental science & technology*, 50(18):9872–9880, 2016.

U. Lohmann and C. Hoose. Sensitivity studies of different aerosol indirect effects in mixed-phase clouds. *Atmospheric Chemistry and Physics*, 9(22):8917–8934, 2009.

U. Lohmann and E. Roeckner. Design and performance of a new cloud microphysics scheme developed for the echam general circulation model. *Climate Dynamics*, 12(8):557–572, 1996.

U. Lohmann, P. Stier, C. Hoose, S. Ferrachat, S. Kloster, E. Roeckner, and J. Zhang. Cloud microphysics and aerosol indirect effects in the global climate model echam5-ham. *Atmospheric Chemistry and Physics*, 7(13):3425–3446, 2007.

F. Lopez-Hilfiker, C. Mohr, E. L. DAmbro, A. Lutz, T. P. Riedel, C. J. Gaston, S. Iyer, Z. Zhang, A. Gold, J. D. Surratt, et al. Molecular composition and volatility of organic aerosol in the southeastern us: implications for iepox derived soa. *Environmental science & technology*, 50 (5):2200–2209, 2016.

B. Machenhauer and E. Rasmussen. On the integration of the spectral hydrodynamical equations by a transform method. Technical Report 3. 44 pp, Kobenhavns Universitet, Institut for Teoretisk Meteorologi, Copenhagen, 1972.

H. Macintyre and M. Evans. Sensitivity of a global model to the uptake of n_2o_5 by tropospheric aerosol. *Atmospheric Chemistry and Physics*, 10(15):7409–7414, 2010.

S. Madronich. The atmosphere and uv-b radiation at ground level, environmental uv photobiology ar young, lo bjorn, j. moan, w. nultsch, 1–38, 1993.

S. Madronich and J. G. Calvert. Permutation reactions of organic peroxy radicals in the troposphere. *Journal of Geophysical Research: Atmospheres*, 95(D5):5697–5715, 1990.

K. T. Malecha and S. A. Nizkorodov. Photodegradation of secondary organic aerosol particles as a source of small, oxygenated volatile organic compounds. *Environmental science & technology*, 50(18):9990–9997, 2016.

E. Manzini, M. Giorgetta, M. Esch, L. Kornblueh, and E. Roeckner. The influence of sea surface temperatures on the northern winter stratosphere: Ensemble simulations with the maecham5 model. *Journal of climate*, 19(16):3863–3881, 2006.

S. Martin, M. Andreae, D. Althausen, P. Artaxo, H. Baars, S. Borrmann, Q. Chen, D. Farmer, A. Guenther, S. Gunthe, et al. An overview of the amazonian aerosol characterization experiment 2008 (amaze-08). *Atmospheric Chemistry and Physics*, 10(23), 2010.

M. Martinez, H. Harder, T. Kovacs, J. Simpas, J. Bassis, R. Lesher, W. Brune, G. Frost, E. Williams, C. Stroud, et al. Oh and ho2 concentrations, sources, and loss rates during the southern oxidants study in nashville, tennessee, summer 1999. *Journal of Geophysical Research: Atmospheres*, 108(D19), 2003.

G. McFiggans, D. Topping, and M. Barley. The sensitivity of secondary organic aerosol component partitioning to the predictions of component properties–part 1: A systematic evaluation of some available estimation techniques. *Atmospheric Chemistry and Physics*, 10(21):10255–10272, 2010.

V. F. McNeill, J. L. Woo, D. D. Kim, A. N. Schwier, N. J. Wannell, A. J. Sumner, and J. M. Barakat. Aqueous-phase secondary organic aerosol and organosulfate formation in atmospheric aerosols: a modeling study. *Environmental science & technology*, 46(15):8075–8081, 2012.

B. Möbis and B. Stevens. Factors controlling the position of the intertropical convergence zone on an aquaplanet. *Journal of Advances in Modeling Earth Systems*, 4(4), 2012.

E. C. Monahan, D. E. Spiel, and K. L. Davidson. A model of marine aerosol generation via whitecaps and wave disruption. In *Oceanic whitecaps*, pages 167–174. Springer, 1986.

L. A. Morio, K. A. Hooper, J. Brittingham, T.-H. Li, R. E. Gordon, B. J. Turpin, and D. L. Laskin. Tissue injury following inhalation of fine particulate matter and hydrogen peroxide is associated with altered production of inflammatory mediators and antioxidants by alveolar macrophages. *Toxicology and applied pharmacology*, 177(3):188–199, 2001.

B. Murphy, N. M. Donahue, C. Fountoukis, M. Dall'Osto, C. O'Dowd, A. Kiendler-Scharr, and S. N. Pandis. Functionalization and fragmentation during ambient organic aerosol aging: application of the 2-d volatility basis set to field studies. *Atmospheric Chemistry and Physics*, 12(22):10797–10816, 2012.

D. Murphy, D. Cziczo, K. Froyd, P. Hudson, B. Matthew, A. Middlebrook, R. Peltier, A. Sullivan, D. Thomson, and R. Weber. Single-particle mass spectrometry of tropospheric aerosol particles. *Journal of Geophysical Research: Atmospheres*, 111(D23), 2006.

Y. Nannoolal, J. Rarey, D. Ramjugernath, and W. Cordes. Estimation of pure component properties: Part 1. estimation of the normal boiling point of non-electrolyte organic compounds via group contributions and group interactions. *Fluid Phase Equilibria*, 226:45–63, 2004.

Y. Nannoolal, J. Rarey, and D. Ramjugernath. Estimation of pure component properties: Part 3. estimation of the vapor pressure of non-electrolyte organic compounds via group contributions and group interactions. *Fluid Phase Equilibria*, 269(1):117–133, 2008.

P. D. Nightingale, G. Malin, C. S. Law, A. J. Watson, P. S. Liss, M. I. Liddicoat, J. Boutin, and R. C. Upstill-Goddard. In situ evaluation of air-sea gas exchange parameterizations using novel conservative and volatile tracers. *Global Biogeochemical Cycles*, 14(1):373–387, 2000.

A. Nölscher, T. Butler, J. Auld, P. Veres, A. Muñoz, D. Taraborrelli, L. Vereecken, J. Lelieveld, and J. Williams. Using total oh reactivity to assess isoprene photooxidation via measurement and model. *Atmospheric Environment*, 89:453–463, 2014.

T. E. Nordeng. *Extended versions of the convective parametrization scheme at ECMWF and their impact on the mean and transient activity of the model in the tropics*. European Centre for Medium-Range Weather Forecasts, 1994.

J. R. Odum, T. Hoffmann, F. Bowman, D. Collins, R. C. Flagan, and J. H. Seinfeld. Gas/particle partitioning and secondary organic aerosol yields. *Environmental Science & Technology*, 30(8):2580–2585, 1996.

S. O'Meara, A. M. Booth, M. H. Barley, D. Topping, and G. McFiggans. An assessment of vapour pressure estimation methods. *Physical Chemistry Chemical Physics*, 16(36):19453–19469, 2014.

J. J. Orlando and G. S. Tyndall. Laboratory studies of organic peroxy radical chemistry: an overview with emphasis on recent issues of atmospheric significance. *Chemical Society Reviews*, 41(19):6294–6317, 2012.

S. N. Pandis and J. H. Seinfeld. *Atmospheric chemistry and physics: From air pollution to climate change*. Wiley, 2006.

J. F. Pankow. Review and comparative analysis of the theories on partitioning between the gas and aerosol particulate phases in the atmosphere. *Atmospheric Environment (1967)*, 21(11): 2275–2283, 1987.

J. F. Pankow. An absorption model of gas/particle partitioning of organic compounds in the atmosphere. *Atmospheric Environment*, 28(2):185–188, 1994.

F. Paulot, J. D. Crounse, H. G. Kjaergaard, A. Kürten, J. M. S. Clair, J. H. Seinfeld, and P. O. Wennberg. Unexpected epoxide formation in the gas-phase photooxidation of isoprene. *Science*, 325(5941):730–733, 2009.

J. Peeters, T. L. Nguyen, and L. Vereecken. Ho x radical regeneration in the oxidation of isoprene. *Physical Chemistry Chemical Physics*, 11(28):5935–5939, 2009.

T. M. Peters, H. Chein, D. A. Lundgren, and P. B. Keady. Comparison and combination of aerosol size distributions measured with a low pressure impactor, differential mobility particle sizer, electrical aerosol analyzer, and aerodynamic particle sizer. *Aerosol Science and Technology*, 19(3):396–405, 1993.

N. A. Phillips. A coordinate system having some special advantages for numerical forecasting. *J. Meteor.*, 14:184–185, 1957.

S. D. Piccot, J. J. Watson, and J. W. Jones. A global inventory of volatile organic compound emissions from anthropogenic sources. *Journal of Geophysical Research: Atmospheres*, 97 (D9):9897–9912, 1992.

U. Pöschl. Atmospheric aerosols: composition, transformation, climate and health effects. *Angewandte Chemie International Edition*, 44(46):7520–7540, 2005.

U. Pöschl, S. Martin, B. Sinha, Q. Chen, S. Gunthe, J. Huffman, S. Borrmann, D. Farmer, R. Garland, G. Helas, et al. Rainforest aerosols as biogenic nuclei of clouds and precipitation in the amazon. *science*, 329(5998):1513–1516, 2010.

J.-P. Putaud, F. Raes, R. Van Dingenen, E. Brüggemann, M.-C. Facchini, S. Decesari, S. Fuzzi, R. Gehrig, C. Hüglin, P. Laj, et al. A european aerosol phenomenology2: chemical characteristics of particulate matter at kerbside, urban, rural and background sites in europe. *Atmospheric environment*, 38(16):2579–2595, 2004.

H. O. Pye, R. W. Pinder, I. R. Piletic, Y. Xie, S. L. Capps, Y.-H. Lin, J. D. Surratt, Z. Zhang, A. Gold, D. J. Luecken, et al. Epoxide pathways improve model predictions of isoprene markers and reveal key role of acidity in aerosol formation. *Environmental science & technology*, 47(19):11056–11064, 2013.

S. Rast, M. Schultz, I. Bey, T. van Noije, A. M. Aghedo, G. Brasseur, T. Diehl, M. Esch, L. Ganzeveld, I. Kirchner, et al. Evaluation of the tropospheric chemistry general circulation model echam5-moz and its application to the analysis of the chemical composition of the troposphere with an emphasis on the late retro period 1990-2000. 2014.

C. Reick, T. Raddatz, V. Brovkin, and V. Gayler. Representation of natural and anthropogenic land cover change in mpi-esm. *Journal of Advances in Modeling Earth Systems*, 5(3):459–482, 2013.

X. Ren, J. R. Olson, J. H. Crawford, W. H. Brune, J. Mao, R. B. Long, Z. Chen, G. Chen, M. A. Avery, G. W. Sachse, et al. Hox chemistry during intex-a 2004: Observation, model calculation, and comparison with previous studies. *Journal of Geophysical Research: Atmospheres*, 113(D5), 2008.

T. P. Riedel, Y.-H. Lin, S. H. Budisulistiorini, C. J. Gaston, J. A. Thornton, Z. Zhang, W. Vizuete, A. Gold, and J. D. Surratt. Heterogeneous reactions of isoprene-derived epoxides: reaction probabilities and molar secondary organic aerosol yield estimates. *Environmental Science & Technology Letters*, 2(2):38–42, 2015.

M. Riva, S. H. Budisulistiorini, Y. Chen, Z. Zhang, E. L. DAmbro, X. Zhang, A. Gold, B. J. Turpin, J. A. Thornton, M. R. Canagaratna, et al. Chemical characterization of secondary organic aerosol from oxidation of isoprene hydroxyhydroperoxides. *Environmental science & technology*, 50(18):9889–9899, 2016.

J. Rivera-Rios, T. Nguyen, J. Crounse, W. Jud, J. St Clair, T. Mikoviny, J. Gilman, B. Lerner, J. Kaiser, J. d. Gouw, et al. Conversion of hydroperoxides to carbonyls in field and laboratory instrumentation: Observational bias in diagnosing pristine versus anthropogenically controlled atmospheric chemistry. *Geophysical Research Letters*, 41(23):8645–8651, 2014.

G. C. Roberts, M. O. Andreae, J. Zhou, and P. Artaxo. Cloud condensation nuclei in the amazon basin:marine conditions over a continent? *Geophysical research letters*, 28(14):2807–2810, 2001.

E. Roeckner, L. , Arpe, M. Bengtsson, M. Christoph, L. Claussen, M. Dümenil, M. Esch, U. Giorgetta, and U. Schlese. The atmospheric general circulation model echam-4: Model description and simulation of present-day climate. Technical Report 218. 90 pp., Max-Planck Institute for Meteorology Hamburg Germany., 1996.

S. S. d. Sá, B. B. Palm, P. Campuzano-Jost, D. A. Day, M. K. Newburn, W. Hu, G. Isaacman-VanWertz, L. D. Yee, R. Thalman, J. Brito, et al. Influence of urban pollution on the

production of organic particulate matter from isoprene epoxydiols in central amazonia. *Atmospheric Chemistry and Physics*, 17(11):6611–6629, 2017.

S. Saarikoski, S. Carbone, S. Decesari, L. Giulianelli, F. Angelini, M. Canagaratna, N. Ng, A. Trimborn, M. Facchini, S. Fuzzi, et al. Chemical characterization of springtime submicrometer aerosol in po valley, italy. *Atmospheric Chemistry and Physics*, 12(18):8401–8421, 2012.

J. M. Samet, F. Dominici, F. C. Curriero, I. Coursac, and S. L. Zeger. Fine particulate air pollution and mortality in 20 us cities, 1987–1994. *New England journal of medicine*, 343 (24):1742–1749, 2000.

P. Saxena and L. M. Hildemann. Water-soluble organics in atmospheric particles: A critical review of the literature and application of thermodynamics to identify candidate compounds. *Journal of atmospheric chemistry*, 24(1):57–109, 1996.

M. G. Schultz, H. Akimoto, J. Bottenheim, B. Buchmann, I. E. Galbally, S. Gilge, D. Helmig, H. Koide, A. C. Lewis, P. C. Novelli, et al. The global atmosphere watch reactive gases measurement network. *Elementa: Science of the Anthropocene*, 3(1):000067, 2015.

M. G. Schultz, S. Stadtler, S. Schröder, D. Taraborrelli, B. Franco, J. Krefting, A. Henrot, S. Ferrachat, U. Lohmann, D. Neubauer, C. Siegenthaler-Le Drian, S. Wahl, H. Kokkola, T. Kühn, S. Rast, H. Schmidt, P. Stier, D. Kinnison, G. S. Tyndall, J. J. Orlando, and C. Wespes. The chemistry climate model echam6.3-ham2.3-moz1.0. *Geoscientific Model Development Discussions*, 2017:1–43, 2017. doi: 10.5194/gmd-2017-191. URL `https://www.geosci-model-dev-discuss.net/gmd-2017-191/`.

S. E. Schwartz. Mass-transport considerations pertinent to aqueous phase reactions of gases in liquid-water clouds. In *Chemistry of multiphase atmospheric systems*, pages 415–471. Springer, 1986.

J. Seinfeld and S. Pandis. Atmospheric chemistry and physics, 1326 pp, 1998.

J. H. Seinfeld and S. N. Pandis. *Atmospheric chemistry and physics: from air pollution to climate change*. John Wiley & Sons, 2012.

M. Shiraiwa, M. Ammann, T. Koop, and U. Pöschl. Gas uptake and chemical aging of semisolid organic aerosol particles. *Proceedings of the National Academy of Sciences*, 108(27):11003–11008, 2011.

S. Stadtler, T. Kühn, S. Schröder, D. Taraborrelli, M. G. Schultz, and H. Kokkola. Isoprene derived secondary organic aerosol in a global aerosol chemistry climate model. *Geoscientific Model Development*, 2017.

S. Stadtler, D. Simpson, S. Schröder, D. Taraborrelli, A. Bott, and M. Schultz. Ozone impacts of gas-aerosol uptake in global chemistry transport models. *Atmos. Chem. Phys.*, 2018. doi: https://doi.org/10.5194/acp-18-3147-2018.

H. Stark, R. L. Yatavelli, S. L. Thompson, H. Kang, J. E. Krechmer, J. R. Kimmel, B. B. Palm, W. Hu, P. L. Hayes, D. A. Day, et al. Impact of thermal decomposition on thermal desorption instruments: advantage of thermogram analysis for quantifying volatility distributions of organic species. *Environmental Science & Technology*, 51(15):8491–8500, 2017.

T. Stavrakou, J.-F. Müller, I. D. Smedt, M. V. Roozendael, M. Kanakidou, M. Vrekoussis, F. Wittrock, A. Richter, and J. Burrows. The continental source of glyoxal estimated by the synergistic use of spaceborne measurements and inverse modelling. *Atmospheric Chemistry and Physics*, 9(21):8431–8446, 2009.

O. Stein, J. Flemming, A. Inness, J. W. Kaiser, and M. G. Schultz. Global reactive gases forecasts and reanalysis in the macc project. *Journal of Integrative Environmental Sciences*, 9(sup1):57–70, 2012.

O. Stein, M. Schultz, I. Bouarar, H. Clark, V. Huijnen, A. Gaudel, M. George, and C. Clerbaux. On the wintertime low bias of northern hemisphere carbon monoxide found in global model simulations. *Atmospheric chemistry and physics*, 14(17):9295–9316, 2014. doi: https://doi.org/10.5194/acp-14-9295-2014.

R. Steinbrecher, G. Smiatek, R. Köble, G. Seufert, J. Theloke, K. Hauff, P. Ciccioli, R. Vautard, and G. Curci. Intra-and inter-annual variability of voc emissions from natural and semi-natural vegetation in europe and neighbouring countries. *Atmospheric Environment*, 43(7): 1380–1391, 2009.

B. Stevens, M. Giorgetta, M. Esch, T. Mauritsen, T. Crueger, S. Rast, M. Salzmann, H. Schmidt, J. Bader, K. Block, et al. Atmospheric component of the mpi-m earth system model: Echam6. *Journal of Advances in Modeling Earth Systems*, 5(2):146–172, 2013.

P. Stier, J. Feichter, S. Kinne, S. Kloster, E. Vignati, J. Wilson, L. Ganzeveld, I. Tegen, M. Werner, Y. Balkanski, et al. The aerosol-climate model echam5-ham. *Atmospheric Chemistry and Physics*, 5(4):1125–1156, 2005.

P. Stier, J. H. Seinfeld, S. Kinne, and O. Boucher. Aerosol absorption and radiative forcing. *Atmospheric Chemistry and Physics*, 7(19):5237–5261, 2007. doi: doi:10.5194/acp-7-5237-2007.

G. Stoffdatenbank. Gefahrstoffinformationssystem der gewerblichen berufsgenossenschaften. institut für arbeitschutz, 2006.

H. Sundqvist, E. Berge, and J. E. Kristjánsson. Condensation and cloud parameterization studies with a mesoscale numerical weather prediction model. *Monthly Weather Review*, 117 (8):1641–1657, 1989.

J. D. Surratt, S. M. Murphy, J. H. Kroll, N. L. Ng, L. Hildebrandt, A. Sorooshian, R. Szmigielski, R. Vermeylen, W. Maenhaut, M. Claeys, et al. Chemical composition of secondary organic aerosol formed from the photooxidation of isoprene. *The Journal of Physical Chemistry A*, 110(31):9665–9690, 2006.

J. D. Surratt, M. Lewandowski, J. H. Offenberg, M. Jaoui, T. E. Kleindienst, E. O. Edney, and J. H. Seinfeld. Effect of acidity on secondary organic aerosol formation from isoprene. *Environmental Science & Technology*, 41(15):5363–5369, 2007.

J. D. Surratt, A. W. Chan, N. C. Eddingsaas, M. Chan, C. L. Loza, A. J. Kwan, S. P. Hersey, R. C. Flagan, P. O. Wennberg, and J. H. Seinfeld. Reactive intermediates revealed in secondary organic aerosol formation from isoprene. *Proceedings of the National Academy of Sciences*, 107(15):6640–6645, 2010.

D. Tan, I. Faloona, J. Simpas, W. Brune, P. Shepson, T. Couch, A. Sumner, M. Carroll, T. Thornberry, E. Apel, et al. Ho x budgets in a deciduous forest: Results from the prophet summer 1998 campaign. *Journal of Geophysical Research: Atmospheres*, 106(D20):24407–24427, 2001.

D. Taraborrelli, M. Lawrence, T. Butler, R. Sander, and J. Lelieveld. Mainz isoprene mechanism 2 (mim2): an isoprene oxidation mechanism for regional and global atmospheric modelling. *Atmospheric Chemistry and Physics*, 9(8):2751–2777, 2009.

D. Taraborrelli, M. Lawrence, J. Crowley, T. Dillon, S. Gromov, C. Groß, L. Vereecken, and J. Lelieveld. Hydroxyl radical buffered by isoprene oxidation over tropical forests. *Nature Geoscience*, 5(3):190, 2012.

I. Tegen, S. P. Harrison, K. Kohfeld, I. C. Prentice, M. Coe, and M. Heimann. Impact of vegetation and preferential source areas on global dust aerosol: Results from a model study. *Journal of Geophysical Research: Atmospheres*, 107(D21), 2002.

J. A. Thornton, C. F. Braban, and J. P. Abbatt. N_2o_5 hydrolysis on sub-micron organic aerosols: the effect of relative humidity, particle phase, and particle size. *Physical Chemistry Chemical Physics*, 5(20):4593–4603, 2003.

X. Tie, G. Brasseur, L. Emmons, L. Horowitz, and D. Kinnison. Effects of aerosols on tropospheric oxidants: A global model study. *Journal of Geophysical Research: Atmospheres*, 106 (D19):22931–22964, 2001.

X. Tie, L. Emmons, L. Horowitz, G. Brasseur, B. Ridley, E. Atlas, C. Stround, P. Hess, A. Klonecki, S. Madronich, et al. Effect of sulfate aerosol on tropospheric nox and ozone budgets: Model simulations and topse evidence. *Journal of Geophysical Research: Atmospheres*, 108 (D4), 2003.

M. Tiedtke. A comprehensive mass flux scheme for cumulus parameterization in large-scale models. *Monthly Weather Review*, 117(8):1779–1800, 1989.

H. Timonen, M. Aurela, S. Carbone, K. Saarnio, S. Saarikoski, T. Mäkelä, M. Kulmala, V.-M. Kerminen, D. Worsnop, and R. Hillamo. High time-resolution chemical characterization of the water-soluble fraction of ambient aerosols with pils-toc-ic and ams. *Atmospheric Measurement Techniques*, 3(4):1063–1074, 2010.

A. Tokay, A. Kruger, and W. F. Krajewski. Comparison of drop size distribution measurements by impact and optical disdrometers. *Journal of Applied Meteorology*, 40(11):2083–2097, 2001.

C. Tomasi, S. Fuzzi, and A. Kokhanovsky. *Atmospheric Aerosols: Life Cycles and Effects on Air Quality and Climate*, volume 1. John Wiley & Sons, 2017.

J. Tonttila, Z. Maalick, T. Raatikainen, H. Kokkola, T. Kühn, and S. Romakkaniemi. Uclales-salsa v1. 0: a large-eddy model with interactive sectional microphysics for aerosol, clouds and precipitation. *Geoscientific Model Development*, 10(1):169, 2017.

D. Topping, M. Barley, M. Bane, N. J. Higham, B. Aumont, N. Dingle, and G. McFiggans. Umansysprop v1. 0: an online and open-source facility for molecular property prediction and atmospheric aerosol calculations. *Geosci. Model. Dev.*, 9:899–914, 2016. doi: https://doi.org/10.5194/gmd-9-899-2016.

K. Tsigaridis and M. Kanakidou. Global modelling of secondary organic aerosol in the troposphere: a sensitivity analysis. *Atmospheric Chemistry and Physics*, 3(5):1849–1869, 2003.

K. Tsigaridis, N. Daskalakis, M. Kanakidou, P. Adams, P. Artaxo, R. Bahadur, Y. Balkanski, S. Bauer, N. Bellouin, A. Benedetti, et al. The aerocom evaluation and intercomparison of organic aerosol in global models. *Atmospheric Chemistry and Physics*, 14(19):10845–10895, 2014.

A. van Donkelaar, R. V. Martin, M. Brauer, and B. L. Boys. Use of satellite observations for long-term exposure assessment of global concentrations of fine particulate matter. *Environmental health perspectives*, 123(2):135, 2015.

E. Vignati, J. Wilson, and P. Stier. M7: An efficient size-resolved aerosol microphysics module for large-scale aerosol transport models. *Journal of Geophysical Research: Atmospheres (1984–2012)*, 109(D22), 2004.

R. Volkamer, F. San Martini, L. T. Molina, D. Salcedo, J. L. Jimenez, and M. J. Molina. A missing sink for gas-phase glyoxal in mexico city: Formation of secondary organic aerosol. *Geophysical Research Letters*, 34(19), 2007.

A. Wahner, T. F. Mentel, M. Sohn, and J. Stier. Heterogeneous reaction of n_2o_5 on sodium nitrate aerosol. *Journal of Geophysical Research: Atmospheres (1984–2012)*, 103(D23):31103–31112, 1998.

R. Washenfelder, C. Young, S. Brown, W. Angevine, E. Atlas, D. Blake, D. Bon, M. Cubison, J. De Gouw, S. Dusanter, et al. The glyoxal budget and its contribution to organic aerosol for los angeles, california, during calnex 2010. *Journal of Geophysical Research: Atmospheres*, 116(D21), 2011.

M. Wild. Global dimming and brightening: A review. *Journal of Geophysical Research: Atmospheres*, 114(D10), 2009.

M. Wild. Decadal changes in radiative fluxes at land and ocean surfaces and their relevance for global warming. *Wiley Interdisciplinary Reviews: Climate Change*, 7(1):91–107, 2016.

M. Wild, H. Gilgen, A. Roesch, A. Ohmura, C. N. Long, E. G. Dutton, B. Forgan, A. Kallis, V. Russak, and A. Tsvetkov. From dimming to brightening: Decadal changes in solar radiation at earth's surface. *Science*, 308(5723):847–850, 2005.

W. E. Wilson and H. H. Suh. Fine particles and coarse particles: concentration relationships relevant to epidemiologic studies. *Journal of the Air & Waste Management Association*, 47 (12):1238–1249, 1997.

F. A. Winiberg, T. J. Dillon, S. C. Orr, C. B. Groß, I. Bejan, C. A. Brumby, M. J. Evans, S. C. Smith, D. E. Heard, and P. W. Seakins. Direct measurements of oh and other product yields from the ho 2+ ch 3 c (o) o 2 reaction. *Atmospheric Chemistry and Physics*, 16(6): 4023–4042, 2016.

G. M. Wolfe, J. D. Crounse, J. D. Parrish, J. M. S. Clair, M. R. Beaver, F. Paulot, T. P. Yoon, P. O. Wennberg, and F. N. Keutsch. Photolysis, oh reactivity and ozone reactivity of a proxy for isoprene-derived hydroperoxyenals (hpalds). *Physical Chemistry Chemical Physics*, 14 (20):7276–7286, 2012.

J. P. Wong, S. Zhou, and J. P. Abbatt. Changes in secondary organic aerosol composition and mass due to photolysis: relative humidity dependence. *The Journal of Physical Chemistry A*, 119(19):4309–4316, 2014.

J. Woo and V. McNeill. simplegamma v1. 0–a reduced model of secondary organic aerosol formation in the aqueous aerosol phase (aasoa). *Geoscientific Model Development*, 8(6): 1821–1829, 2015.

L. Xu, H. Guo, C. M. Boyd, M. Klein, A. Bougiatioti, K. M. Cerully, J. R. Hite, G. Isaacman-VanWertz, N. M. Kreisberg, C. Knote, et al. Effects of anthropogenic emissions on aerosol formation from isoprene and monoterpenes in the southeastern united states. *Proceedings of the National Academy of Sciences*, 112(1):37–42, 2015.

W. Yang and S. T. Omaye. Air pollutants, oxidative stress and human health. *Mutation Research/Genetic Toxicology and Environmental Mutagenesis*, 674(1):45 – 54, 2009. ISSN 1383-5718. doi: https://doi.org/10.1016/j.mrgentox.2008.10.005. URL `http://www.sciencedirect.com/science/article/pii/S1383571808003045`. Oxidative Stress and Mechanisms of Environmental Toxicity.

K. C. Young. A numerical simulation of wintertime, orographic precipitation: Part i. description of model microphysics and numerical techniques. *Journal of the Atmospheric Sciences*, 31 (7):1735–1748, 1974. doi: https://doi.org/10.1175/1520-0469(1974)031⟨1735:ANSOWO⟩2.0.CO;2.

J. Yu, H. E. Jeffries, and R. M. Le Lacheur. Identifying airborne carbonyl compounds in isoprene atmospheric photooxidation products by their pfbha oximes using gas chromatography/ion trap mass spectrometry. *Environmental science & technology*, 29(8):1923–1932, 1995.

D. Zhang, W. Lei, and R. Zhang. Mechanism of oh formation from ozonolysis of isoprene: kinetics and product yields. *Chemical Physics Letters*, 358(3):171–179, 2002.

Q. Zhang, J. Jimenez, M. Canagaratna, J. Allan, H. Coe, I. Ulbrich, M. Alfarra, A. Takami, A. Middlebrook, Y. Sun, et al. Ubiquity and dominance of oxygenated species in organic aerosols in anthropogenically-influenced northern hemisphere midlatitudes. *Geophysical Research Letters*, 34(13), 2007.

Q. Zhang, C. Parworth, M. Lechner, and J. Jimenez. Aerosol mass spectrometer global database, last accessed on 22.09.2017. URL `https://sites.google.com/site/amsglobaldatabase`.

J. Zimmermann and D. Poppe. A supplement for the radm2 chemical mechanism: the photooxidation of isoprene. *Atmospheric Environment*, 30(8):1255–1269, 1996.

A. Comparison of RefBase to RefM7JAM2

This section compares global surface area density, ozone, nitrogen oxides and the hydroxyl radical distributions from the ECHAM-HAMMOZ-SALSA RefBase run (year 2012) with the year 2012 of the reference run presented in Schultz et al. [2017]. Furthermore, carbon monoxide concentrations are evaluated against measurements in analogy to Schultz et al. [2017].

The reference run in Schultz et al. [2017] is called RefM7JAM2 in the following. The main differences between RefBase and RefM7JAM2 are the micro-physical model and the chemical mechanism. RefM7JAM2 uses M7 to simulate aerosol micro-physics, because it has been the standard aerosol micro-physics model in ECHAM-HAMMOZ for many years. Furthermore, the chemical mechanism JAM2 is used in RefM7JAM2, which is identical but does not contain the extensions of isoprene chemistry which have been developed for this study. Another difference between RefM7JAM2 and RefBase is a small bug-fix in the heterogeneous chemistry module. The effect of this fix results in slightly reduced reactive uptake of species undergoing heterogeneous chemistry (see section 3.4).

The development of the model version used in this study took place during almost three years. When SOA formation is turned off, JAM3 exchanged with JAM2, SALSA switched to M7, and a minor bug in the heterogeneous chemistry is re-introduced, results from this model are very similar to those of the released RefM7JAM2 model, but not bit-identical. Reasons for this are presently unclear, but might be discovered when the code is merged into the ECHAM-HAMMOZ master branch.

A.1. Aerosol surface area density

As shown in section 4.1.1, surface area density simulated by RefBase agrees well to the satellite based climatology by van Donkelaar et al. [2015]. Figure A.1 shows the differences between RefBase and RefM7JAM2. Overall, the negative values show that there is a higher surface area simulated in RefBase, especially over America, Central and South Africa, South Asia and North Australia. These can be explained by additional surface area related to iSOA. Moreover, RefM7JAM2 simulates a higher surface area density in East Asia.

Differences in surface area density are driven by different aerosol modules, plus the usage of a different sea-salt emission scheme, as can be seen point-wise in the southern ocean. Higher values in RefBase over tropical regions fit well to observations and resolve the low bias of ECHAM-HAMMOZ in terms of organic carbon described in Schultz et al. [2017].

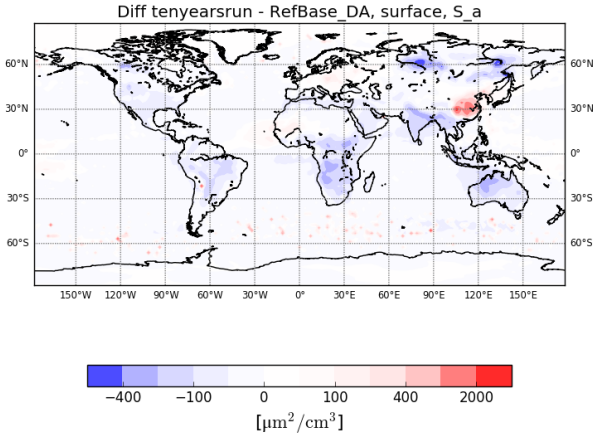

Figure A.1.: Difference between the annual mean surface area density calculated in RefM7JAM2 and RefBase. Blue means higher SAD in RefBase than in RefM7JAM2, accordingly for red colors RefM7JAM2 has higher values than RefBase. The global SAD distribution for RefBase is shown in figure 4.1.

A.2. Ozone, nitrogen oxides and hydroxyl radical

In figure A.2, surface ozone and nitrogen oxides in RefBase are shown. In both global fields higher mixing ratios of nitrogen oxides and ozone are found in the northern hemisphere due to emission patterns. RefBase uses the same emissions as the reference run RefM7JAM2, but still differences in mixing ratios can be found between these model versions. Figure A.3 shows resulting differences in annual mean surface mixing ratios.

The light red color in the difference between RefM7JAM2 and RefBase indicates that, globally, there are little differences up to 0.25 pptv in NO_x mixing ratios. Regionally, over South America, Central Africa and along the Himalaya, RefM7JAM2 has slightly higher (between 0.5 and 1 pptv) NO_x mixing ratios than RefBase. In contrast, RefBase has up to 3.5 ppbv more NO_x in East Asia. For ozone, RefBase simulates, globally, higher values than RefM7JAM2 except in the tropical regions of Central Africa, Indonesia and the equatorial pacific. Ozone is a compound, which is not emitted into the atmosphere, but exclusively formed by atmospheric chemistry. One controlling precursor is NOx. Nevertheless, from the small differences in NO_x, these large differences in annual ozone were unexpected. In North Australia, South Asia and western US, up to 10 ppbv higher ozone concentrations are simulated in RefBase compared to RefM7JAM2.

Figure A.4 shows zonal mean OH concentrations as annual mean for 2012 for RefBase (left) and RefM7JAM2 (right). Because of the annual mean, OH concentrations are symmetric around the equator. OH production depends on short wave radiation strength, so its concentration is highest around the equator. As can be seen from figure A.4, RefBase has slightly lower OH concentrations than RefM7JAM2. Especially in the southern hemisphere and in the upper troposphere, OH concentration is lower in RefBase.

These differences are unexpected, because previous runs with ECHAM-HAMMOZ JAM2 had shown that there is no difference larger than fluctuations in the third decimal point in gas-phase mixing ratios comparing SALSA to M7. Moreover, as shown in section 5.1, iSOA formation does not have major influences on atmospheric chemistry with exception of LC578OOH. Thus,

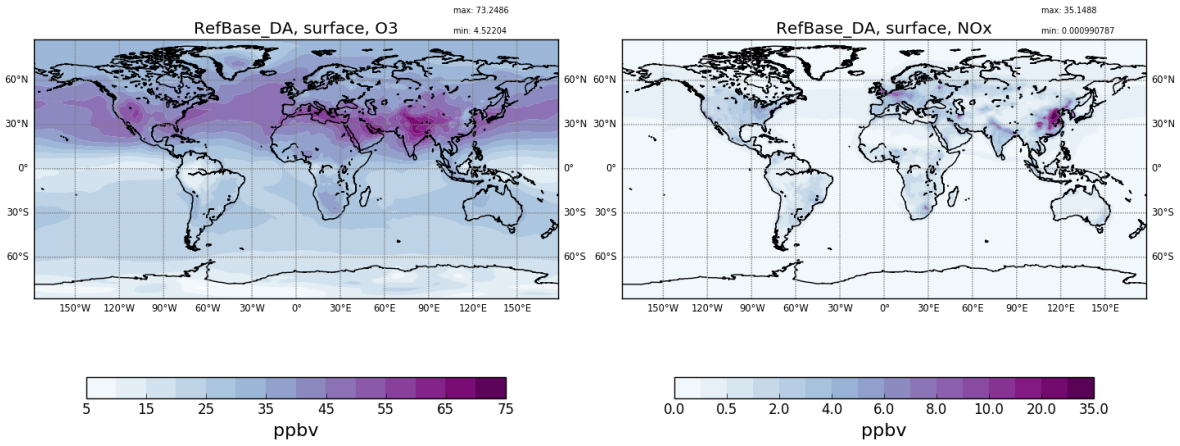

Figure A.2.: Surface ozone (left) and nitrogen oxide (right) distributions for 2012 (annual mean) in volume mixing ratio in ppbv from the reference run RefBase.

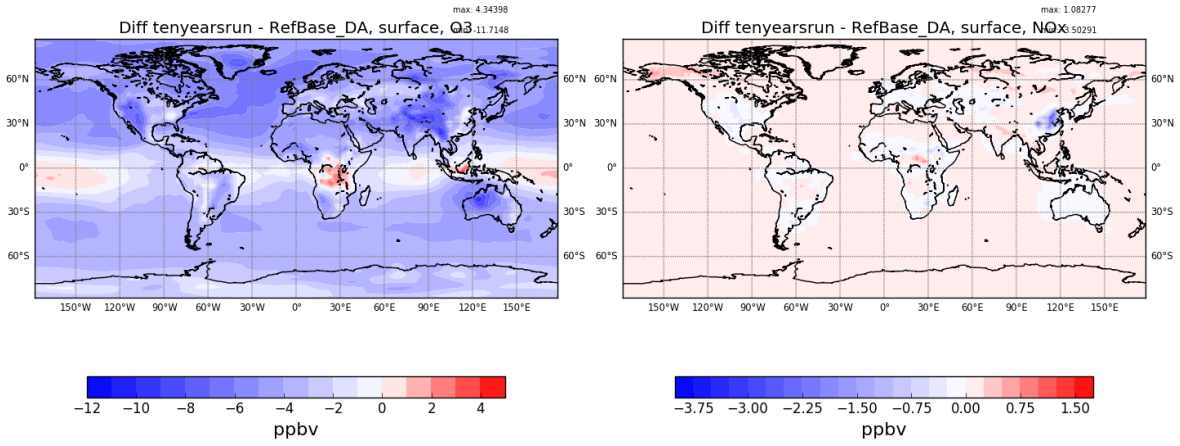

Figure A.3.: Differences between the reference run RefM7JAM2 and RefBase annual mean mixing ratios of ozone and nitrogen oxides. Blue means higher mixing ratios in RefBase than in RefM7JAM2, accordingly for red colors RefM7JAM2 has higher values than RefBase.

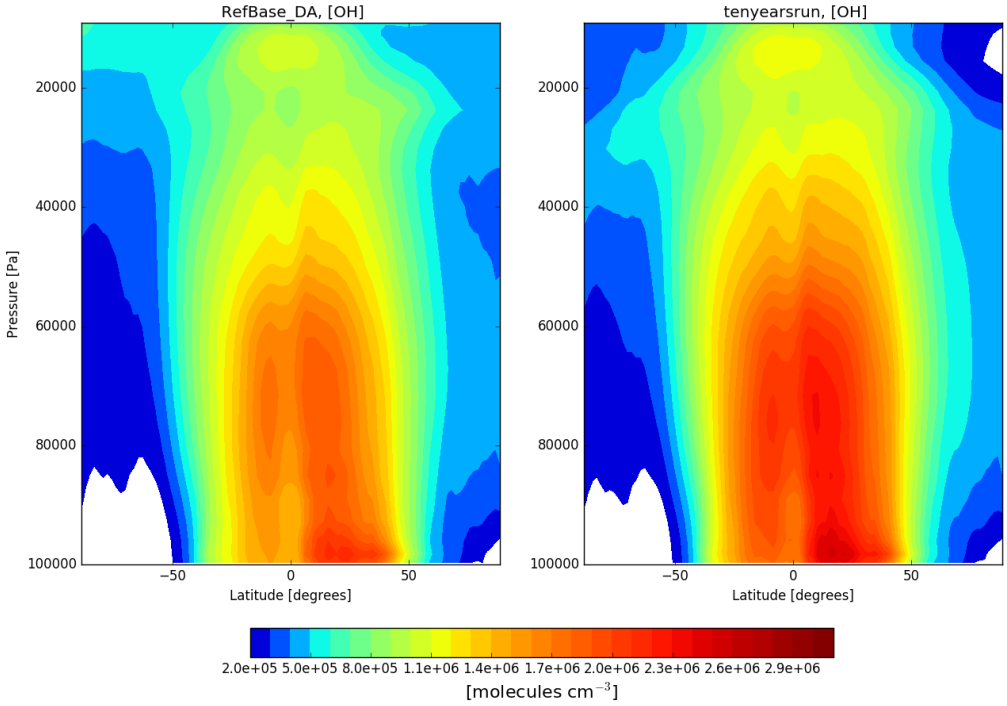

Figure A.4.: Annual and zonal mean OH concentrations in RefBase (left) and RefM7JAM2 (right) for the lower 20 km of the atmosphere.

reasons for these differences were explored by converting the RefBase code back to RefM7JAM2. This means, turning off iSOA formation, switching SALSA to M7, re-introducing the bug in heterogeneous chemistry and replacing JAM3 with JAM2. Major differences could only be reduced after switching back to JAM2, neither the aerosol micro-physical module nor the bug in heterogeneous chemistry could reduce difference patterns. Nevertheless, even after redoing RefM7JAM2 with the ECHAM-HAMMOZ code containing inactive iSOA formation, small differences remained. Concluding, the additions and changes made to HAM and MOZ which are required for iSOA formation influence gas-phase species.

A.3. Carbon monoxide

Figure A.5 shows surface CO concentrations in RefBase and from the data of the World Meteorological Organization Global Atmosphere Watch (GAW) network [Schultz et al., 2015] for January, April, July and October 2012. The latitudinal gradient is visible in this data representation. There are generally higher CO levels in the northern hemisphere, which decrease with decreasing latitude. ECHAM-HAMMOZ captures CO concentrations in the far south (south of 50° S) well, while it tends to underestimate CO concentrations north of 50° S. In all months a slight underestimation around 25° S is visible, but larger differences between the model and observations are found in the northern hemisphere. Especially in April and October the model does not capture higher values in observations north of the equator. Between 10° N and 50° N values of around 200 ppbv CO were observed in January, April, July and October. The model also simulates these higher values, but underestimates them to a greater extend than the lower

values south of 10° N. Observed peak values in April and July around 45° N are not captured by ECHAM-HAMMOZ.

The discrepancies between the model and the observations might result from inaccurate emissions, like around 25° S, this might be unknown biomass-burning emissions which vary with season. Around 45° N CO is influenced by anthropogenic emissions in North America, Europe and Asia. Also, these inventories still hold some uncertainties [Stein et al., 2014]. Moreover, ECHAM-HAMMOZ generates high OH concentrations [Schultz et al., 2017], which degrades CO too quickly compared to the real atmosphere. As seen in figure A.4, RefBase simulates less OH than RefM7JAM2, which is an improvement in this case. Compared to RefM7JAM2, CO observations and modeled values agree better (figure 10 Schultz et al. [2017], figure B.5). Note that RefM7JAM2 was compared to the year 2008, so it is probable that 2012, per se, compares better to CO observations.

Especially in connection with the chemical mechanism JAM3, OH concentrations are high. This can be seen in a reduced CH_4 lifetime of about one year in RefBase compared to RefM7JAM2.

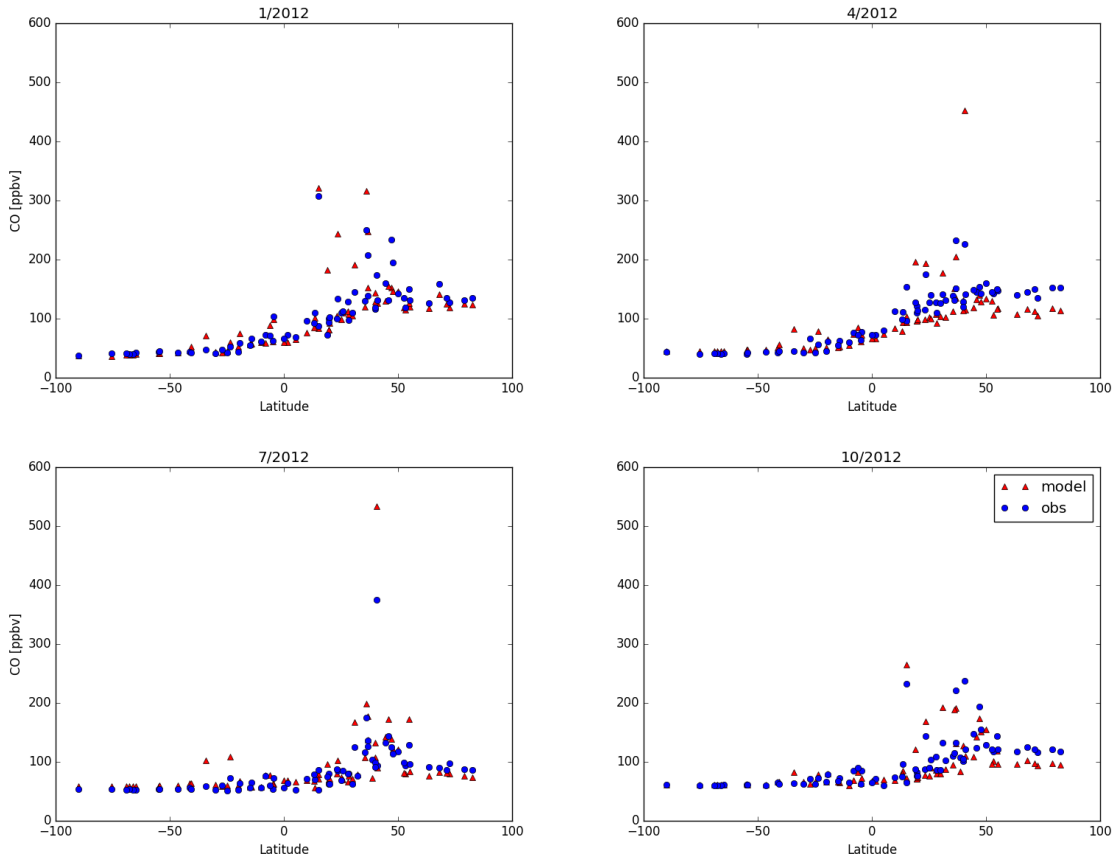

Figure A.5.: Comparison of monthly mean surface CO concentrations from RefBase with CO Global Atmospheric Watch (GAW) measurements. Results for January, April, July and October 2012 are shown. Each symbol represents data of one measurement location. This Figure is motivated by figure 11 in Schultz et al. [2017] for 2008.

B. Additional figures

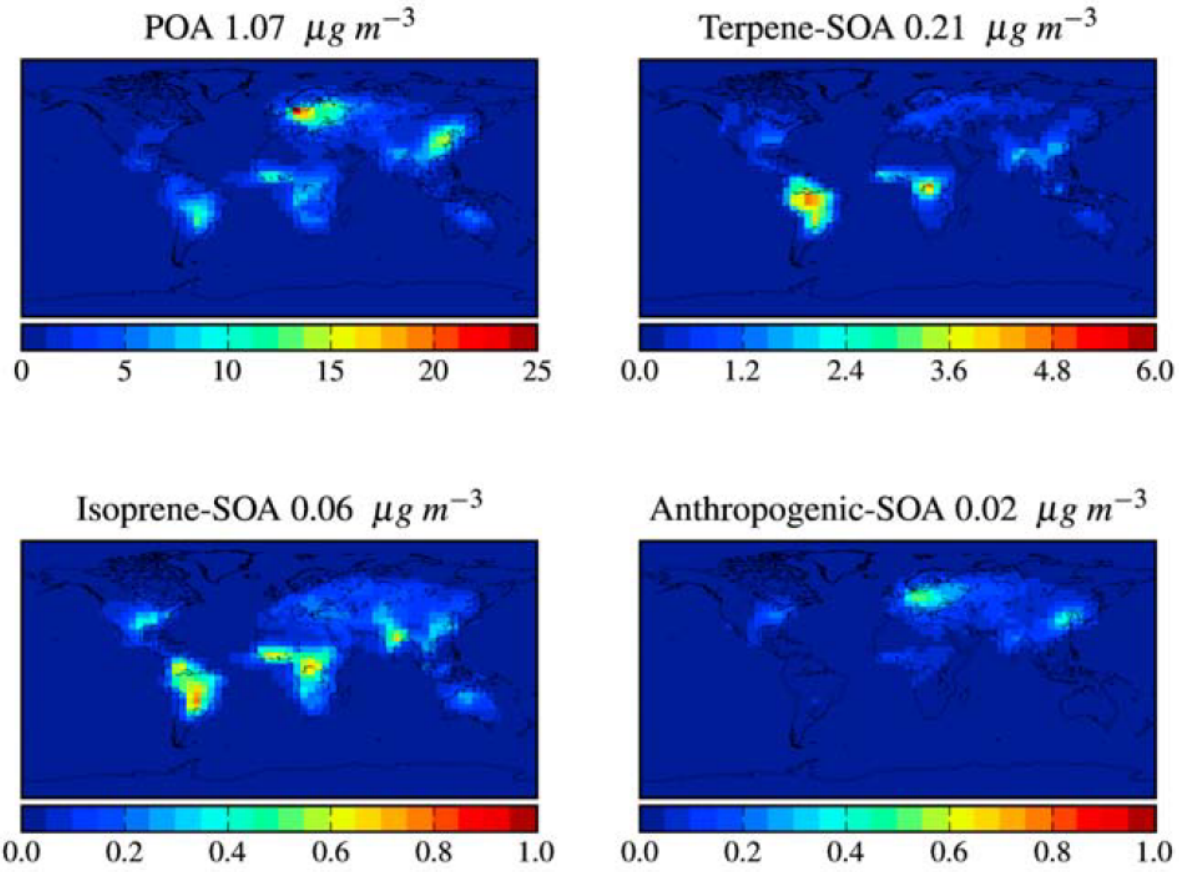

Figure B.1.: Surface POA and SOA concentrations for the reference run in Farina et al. [2010] (Goddard Institute for Space Studies General Circulation Model II (GISS II GCM)). The simulation period is July 1979 until July 1980, but the model represents a nonspecific, climatologically accurate twentieth century year.

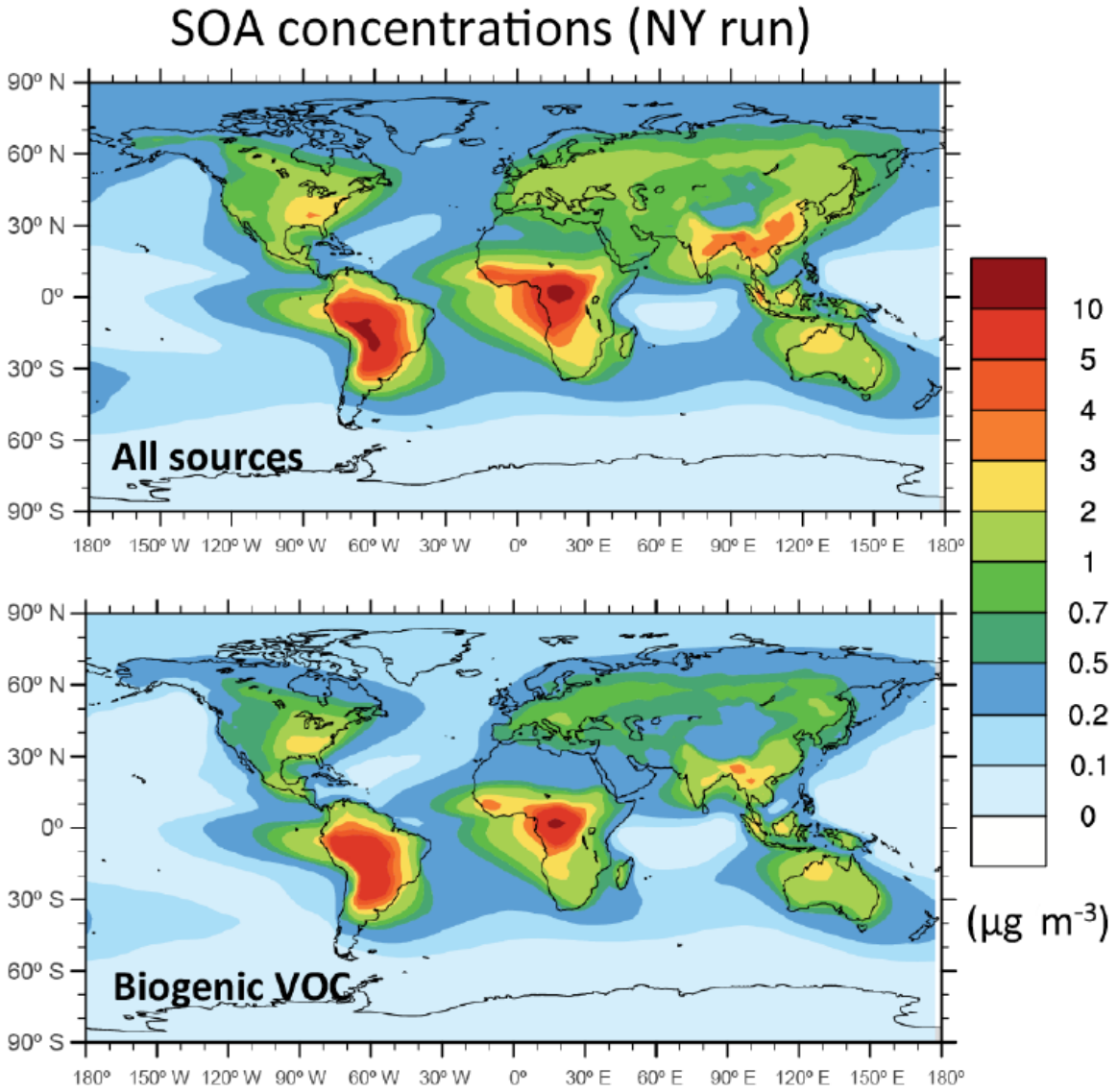

Figure B.2.: Average concentrations for SOA and its constituents in the lower troposphere (surface to 5 km) in the time period 2005 – 2008 as predicted by the GEOS-Chem with the new VBS approach presented in Hodzic et al. [2016].

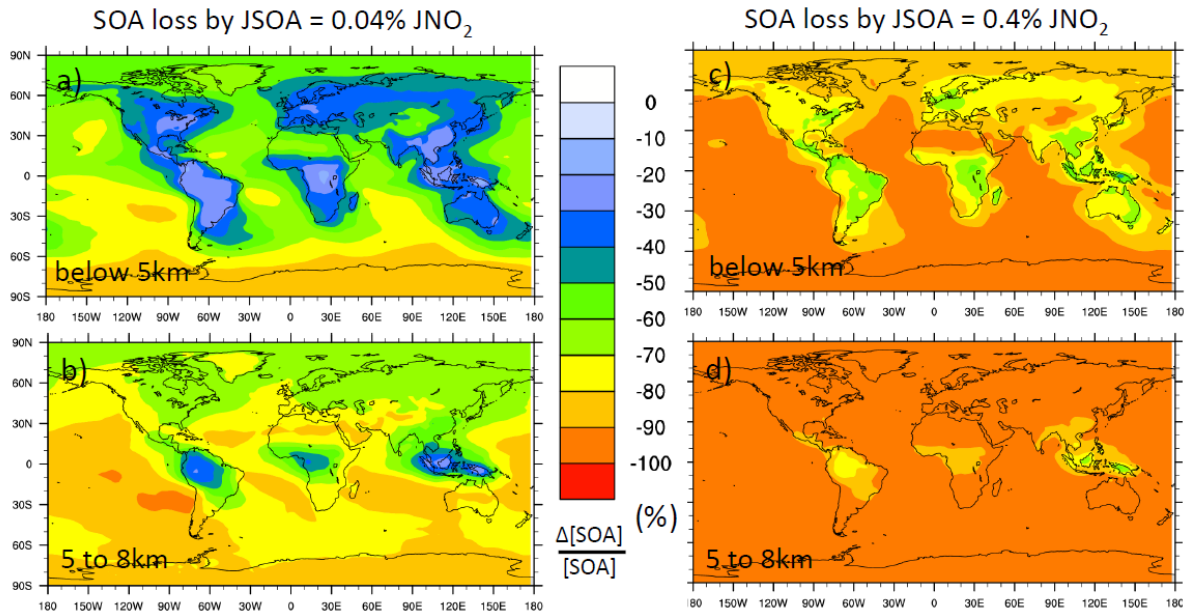

Figure B.3.: [Hodzic et al., 2015]: "Relative reductions (%) in SOA concentrations due to particle-phase photolysis in the lower (a, c) and upper (b, d) troposphere. Two in-particle photolysis rates are considered, i.e., J_{SOA} of 0.04 % J_{NO_2} (left side) and J_{SOA} of 0.4 % J_{NO_2} (right side)".

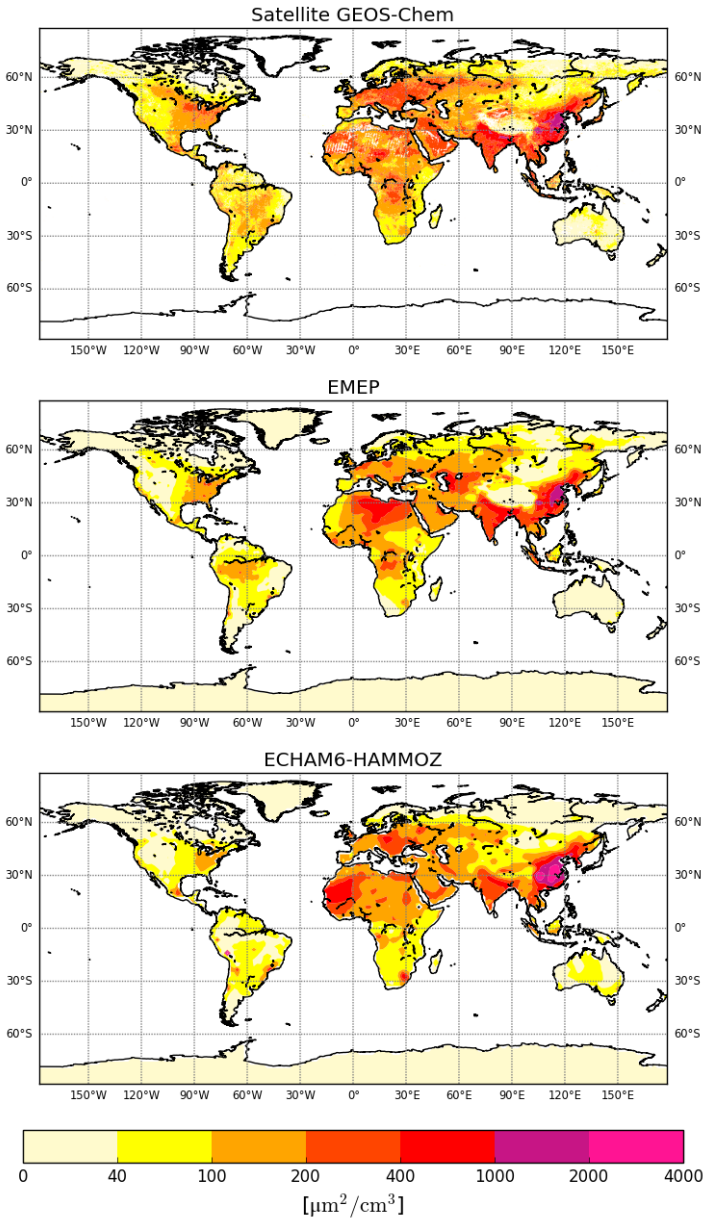

Figure B.4.: Comparison of surface area density in Stadtler et al. [2018] between the satellite based climatology by van Donkelaar et al. [2015] to the model ECHAM-HAMMOZ and EMEP MSC-W for the year 2012. Note that Stadtler et al. [2018] used JAM2 and M7 to explore the impacts of heterogeneous reactions.

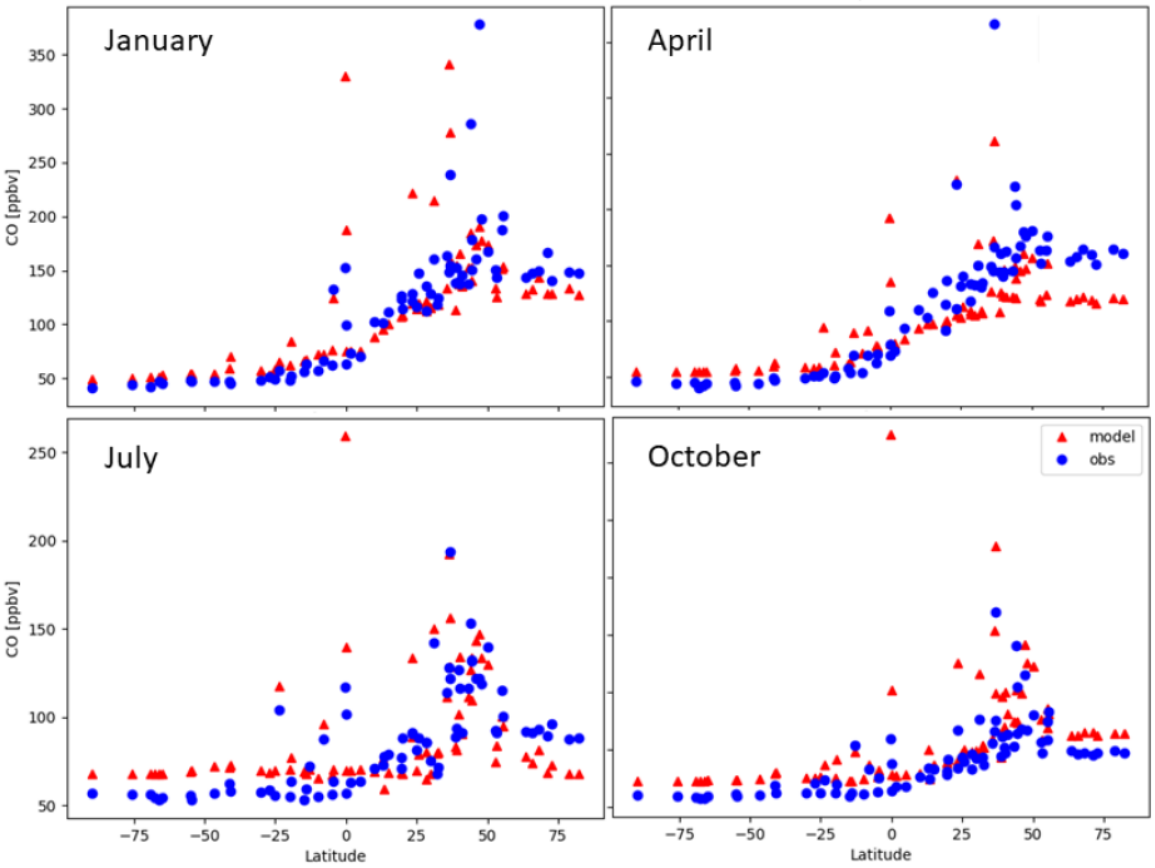

Figure B.5.: "Comparison of monthly mean surface CO measurements from GAW with ECHAM-HAMMOZ reference run (RefM7JAM2) results for January, April, July, and October 2008. Each symbol represents data of one measurement location" by Schultz et al. [2017].

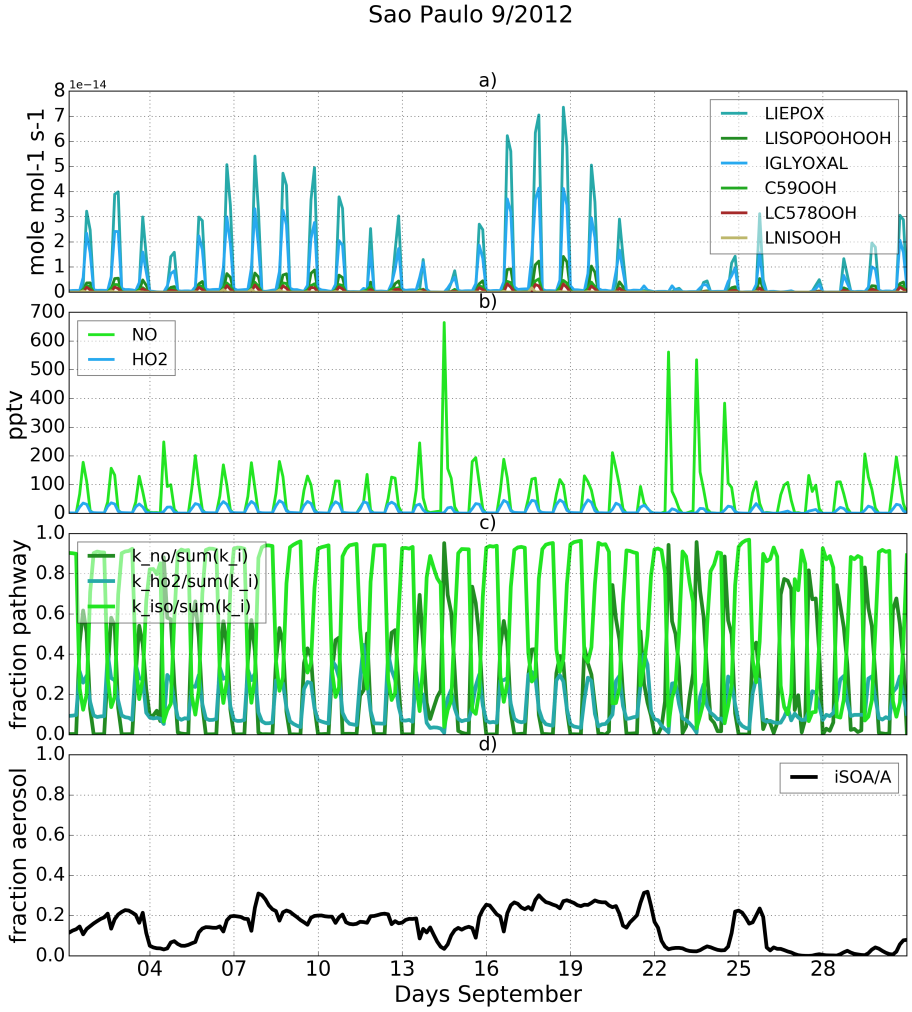

Figure B.6.: Similar to figure 4.11, but with total chemical precursor production rates. Note the complete suppression of iSOA precursor production for the peak values over 400 pptv.

C. Additional reactions in JAM3

Table C.1.: JAM3 mechanism additional isoprene oxidation reactions compared to the JAM2 mechanism described in Schultz et al. [2017].

$C_5H_8 + O_3 \longrightarrow 0.051 \cdot CH_3O_2 + 0.1575 \cdot CH_3CO + 0.054 \cdot LHMVKABO_2 + 0.522 \cdot CO + 0.068750 \cdot HCOOH + 0.11 \cdot H_2O_2 + 0.324750 \cdot MACR + 0.1275 \cdot C_3H_6 + 0.2625 \cdot HO_2 + 0.255 \cdot CO_2 + 0.749750 \cdot CH_2O + 0.041250 \cdot MACO_2H + 0.27 \cdot OH + 0.244 \cdot MVK$	$7.86 \cdot 10^{-15} \exp(-1913/T)$	·	
$LISOPACO_2 + CH_3O_2 \longrightarrow 0.75 \cdot CH_2O + 0.75 \cdot LHC_4ACCHO + 0.25 \cdot CH_3OH + 0.25 \cdot ISOPAOH + HO_2$	$2.4 \cdot 10^{-12}$		products: Tyndall (p.c.)
$LISOPACO_2 \longrightarrow HO_2 + HPALD$	$6.198 \cdot 10^8 \exp(-7700/T)$	·	Bulk isomerization (1,6-H-shift) rate constant for all ISOPO2 by Crounse et al. [2011] and adjusted by Fuchs et al. [2013] given as $1.5 * k(ISOPO2 + HO2) * 2 \cdot 10^{21} \cdot \exp(-9000/T) => k = 2.05 \cdot 10^{-13} \cdot \exp(1300/T) \cdot 210^{21} \cdot \exp(-9000/T) = 6.19810^8 \cdot \exp(-7700/T)$
$ISOPBO_2 \longrightarrow HO_2 + HPALD$	$6.198e + 08 \exp(-7700./T)$	·	see note of [LISOPACO2]
$ISOPDO_2 \longrightarrow HO_2 + HPALD$	$6.198e + 08 \exp(-7700./T)$	·	see note of [LISOPACO2]
$ISOPBO_2 \longrightarrow HCHO + MVK + OH$	$3.570e + 13 \exp(-10770./T)$	·	1,5-H-shift as in LIM-J by da Silva [2010] and adjusted by Fuchs et al. [2013]
$ISOPDO_2 \longrightarrow HCHO + MACR + OH$	$1.905e + 13 \exp(-10570./T)$	·	1,5-H-shift as in LIM-J by da Silva [2010] and adjusted by Fuchs et al. [2013]
$LIECO_3 + HO_2 \longrightarrow 0.6 \cdot LIECO_3H + 0.4 \cdot CO_2 + 0.4 \cdot OH + 0.25 \cdot LHMVKABO_2 + 0.15 \cdot MACRO_2$	$8.207 \cdot 10^{-13} \exp(980./T)$	·	k scaled to $2.2 \cdot 10^{-11}$ as recommended by Winiberg ($A = 5.2 \cdot 10^{-13} \cdot 1.578$); cacm products distribution unchanged (Winiberg et al. [2016] and Groß et al. [2014])
$LISOPACO_2 + LISOPACO_2 \longrightarrow 1.5 \cdot LHC_4ACCHO + HO_2 + 0.5 \cdot ISOPAOH$	$3.350 \cdot 10^{-12}$		k: avg. for primary isoprene RO2 MCM (Jenkin et al. [2003], Tab. 3); products: based on the HOCH2CH2O2 self-reaction (Orlando and Tyndall [2012], Tab.8)
$ISOPBO_2 + ISOPBO_2 \longrightarrow 2 \cdot MVK + 2 \cdot CH_2O + 2 \cdot HO_2$	$6.900 \cdot 10^{-14}$		k: for tertiary isoprene RO2 MCM (Jenkin et al. [2003], Tab. 3)

Table C.1.: JAM3 mechanism additional isoprene oxidation reactions (continued).

$ISOPDO_2 + ISOPDO_2 \longrightarrow 1.12 \cdot MACR + 1.12 \cdot CH_2O + 1.12 \cdot HO_2 + 0.44 \cdot HCOC_5 + 0.44 \cdot ISOPDOH$	$4.800 \cdot 10^{-12}$	k : for secondary isoprene RO2 MCM (Jenkin et al. [2003], Tab. 3); products: based on the i-C3H7O2 self-reaction (Orlando and Tyndall [2012], Tab.8)
$LISOPACO_2 + ISOPBO_2 \longrightarrow LHC_4ACCHO + 0.75 \cdot MVK + 0.75 \cdot CH_2O + 1.5 \cdot HO_2 + 0.25 \cdot ISOPBOH$	$4.808 \cdot 10^{-13}$	k : $(3.35 \cdot 10^{-12} \cdot 6.9 \cdot 10^{-14})^{0.5}$ geometric average of self-reaction ks (arbitrary estimate by Madronich and Calvert [1990])
$LISOPACO_2 + ISOPDO_2 \longrightarrow 0.75 \cdot LHC_4ACCHO + 0.5 \cdot MACR + 0.5 \cdot CH_2O + HO_2 + 0.25 \cdot ISOPAOH + 0.25 \cdot HCOC_5 + 0.25 \cdot ISOPDOH$	$4.010 \cdot 10^{-12}$	k : $(3.35 \cdot 10^{-12} * 4.8 \cdot 10^{-12})^{0.5}$ geometric average of self-reaction k (arbitrary estimate by Madronich and Calvert [1990])
$ISOPBO_2 + ISOPDO_2 \longrightarrow 0.75 \cdot MVK + 0.75 \cdot MACR + 1.5 \cdot CH_2O + 1.5 \cdot HO_2 + 0.25 \cdot ISOPBOH + 0.25 \cdot HCOC_5$	$5.755 \cdot 10^{-13}$	k : $(6.9 \cdot 10^{-14} \cdot 4.8 \cdot 10^{-12})^{0.5}$ geometric average of self-reaction k (arbitrary estimate by Madronich and Calvert [1990])
$LHC_4ACCO_3 \longrightarrow HO_2 + PACALD$	$1.230 \cdot 10^9 \cdot \exp(-6186/T)$	1,6-H-shift (not bulk!) rate constant for the Z41 isomer as in SI Taraborrelli et al. [2012] 2012
$LHC_4ACCO_3 + HO_2 \longrightarrow 0.37 \cdot LHC_4ACCO_3H + 0.12 \cdot LHC_4ACCO_2H + 0.12 \cdot O_3 + 0.51 \cdot CO_2 + 0.51 \cdot OH + 0.255 \cdot HYAC + 0.255 \cdot GLYALD + 0.255 \cdot CH_3CO + 0.255 \cdot CO + 0.255 \cdot HO_2$	$8.207 \cdot 10^{-13} \cdot \exp(980/T)$	k scaled to $2.2 \cdot 10^{-11}$ as recommended by Winiberg ($A = 5.2 \cdot 10^{-13} \cdot 1.578$) ; product distribution in analogy to $CH_3CO_3 + HO_2$ reactions (Winiberg et al. [2016] and Groß et al. [2014])

D. MOZ JAM3 chemical mechanism

Table D.1.: JAM3 chemical mechanism

Tropospheric photolysis reactions	
$O_3 + hv \longrightarrow O_1D + O_2$	
$O_3 + hv \longrightarrow O + O_2$	
$H_2O_2 + hv \longrightarrow 2 \cdot OH$	
$N_2O + hv \longrightarrow N_2 + O_1D$	
$NO + hv \longrightarrow N + O$	juser1
$NO_2 + hv \longrightarrow NO + O$	
$NO_3 + hv \longrightarrow NO_2 + O$	
$NO_3 + hv \longrightarrow NO + O_2$	
$HNO_3 + hv \longrightarrow NO_2 + OH$	
$HONO + hv \longrightarrow NO + OH$	
$HO_2NO_2 + hv \longrightarrow NO_3 + OH$	
$HO_2NO_2 + hv \longrightarrow HO_2 + NO_2$	
$N_2O_5 + hv \longrightarrow NO_2 + NO_3$	
$N_2O_5 + hv \longrightarrow NO + O + NO_3$	
$CO_2 + hv \longrightarrow CO + O$	
$CH_4 + hv \longrightarrow CH_3O_2 + H$	
$CH_4 + hv \longrightarrow 1.44 \cdot H_2 + 0.18 \cdot CH_2O + 0.18 \cdot O + 0.66 \cdot OH + 0.44 \cdot CO_2 + 0.38 \cdot CO + 0.05 \cdot H_2O$	
$CH_2O + hv \longrightarrow CO + 2 \cdot H$	
$CH_2O + hv \longrightarrow CO + H_2$	
$CH_3OOH + hv \longrightarrow CH_2O + H + OH$	
$CH_3O_2NO_2 + hv \longrightarrow HO_2 + NO_3 + HCHO$	
$CH_3O_2NO_2 + hv \longrightarrow CH_3O_2 + NO_2$	
$C_2H_5O_2NO_2 + hv \longrightarrow HO_2 + NO_3 + CH_3CHO$	
$C_2H_5O_2NO_2 + hv \longrightarrow C_2H_5O_2 + NO_2$	
$CH_3CHO + hv \longrightarrow CH_3O_2 + CO + HO_2$	
$CH_3COOOH + hv \longrightarrow CH_3O_2 + OH + CO_2$	
$C_2H_5OOH + hv \longrightarrow CH_3CHO + HO_2 + OH$	
$PAN + hv \longrightarrow 0.6 \cdot CH_3CO + 0.6 \cdot NO_2 + 0.4 \cdot CH_3O_2 + 0.4 \cdot NO_3 + 0.4 \cdot CO_2$	

Table D.1.: JAM3 chemical mechanism (... continued)

$EOOH + hv \longrightarrow EO + OH$	
$GLYOXAL + hv \longrightarrow 2 \cdot CO + 2 \cdot HO_2$	jglyoxal at 30 SZA and 300DU O3 1E-4 s-1
$GLYALD + hv \longrightarrow 2 \cdot HO_2 + CO + CH_2O$	
$HOCH_2CO_3H + hv \longrightarrow CH_2O + HO_2 + OH + CO_2$	
$HCOCO_2H + hv \longrightarrow 2 \cdot HO_2 + CO + CO_2$	
$HCOCO_3H + hv \longrightarrow CO + HO_2 + OH + CO_2$	
$CH_3COCH_3 + hv \longrightarrow CH_3CO + CH_3O_2$	
$C_3H_7OOH + hv \longrightarrow 0.82 \cdot CH_3COCH_3 + OH + HO_2 + 0.27 \cdot CH_3CHO$	
$POOH + hv \longrightarrow CH_2O + CH_3CHO + HO_2 + OH$	
$HYAC + hv \longrightarrow CH_3CO + HO_2 + CH_2O$	
$CH_3COCHO + hv \longrightarrow CH_3CO + CO + HO_2$	
$ROOH + hv \longrightarrow CH_2O + CH_3CO + OH$	
$PR_2O_2HNO_3 + hv \longrightarrow 0.83 \cdot HO_2 + 0.83 \cdot NOA + 0.17 \cdot CH_2O + 0.17 \cdot CH_3CHO + OH$	
$NOA + hv \longrightarrow CH_2O + CH_3CO + NO_2$	at 30 SZA and 300DU O3 J(NOA) = 3.5E-5 s-1 1/3 J(GLYOXAL) Mller et al. 2014
$MEK + hv \longrightarrow C_2H_5O_2 + CH_3CO$	
$MEKOOH + hv \longrightarrow CH_3CO + OH + CH_3CHO$	
$MEKNO_3 + hv \longrightarrow CH_3CHO + CH_3CO + NO_2$	at 30 SZA and 300DU O3 J(MEKNO3) J(NOA) = 3.5E-5 s-1 1/3 J(GLYOXAL) Mller et al. 2014
$MACR + hv \longrightarrow HO_2 + 0.5 \cdot MCO_3 + 0.5 \cdot CH_2O + 0.5 \cdot CH_3CO + 0.5 \cdot CO$	
$MACR + hv \longrightarrow HO_2 + 0.5 \cdot MCO_3 + 0.5 \cdot CH_2O + 0.5 \cdot CH_3CO + 0.5 \cdot CO$	
$MACROOH + hv \longrightarrow HO_2 + HYAC + OH + CO$	
$MACROH + hv \longrightarrow CO + HYAC + 2 \cdot HO_2 + H_2O$	
$MPAN + hv \longrightarrow MCO_3 + NO_2$	
$MACO_3H + hv \longrightarrow CH_2O + CH_3CO + OH + CO_2$	
$MVK + hv \longrightarrow 0.5 \cdot C_3H_6 + 0.5 \cdot CH_3CO + 0.5 \cdot CH_2O + CO + 0.5 \cdot HO_2$	

Table D.1.: JAM3 chemical mechanism (... continued)

$LHMVKABOOH + hv \longrightarrow 0.3 \cdot CH_3COCHO + OH + 0.3 \cdot CH_2O + 0.3 \cdot HO_2 + 0.7 \cdot CH_3CO + 0.7 \cdot GLYALD$	
$MVKN + hv \longrightarrow CH_3CO + GLYALD + NO_2$	at 30 SZA and 300DU O3 J(MVKN) = 5.6E-5 s-1 1/2 J(GLYOXAL) Mller et al. 2014
$MACRN + hv \longrightarrow CO + HYAC + HO_2 + NO_2$	at 30 SZA and 300DU O3 J(MACRN) = 3.5E-4 s-1 3.5 J(GLYOXAL) Mller et al. 2014
$CO_2H_3CHO + hv \longrightarrow CH_3COCHO + CO + 2 \cdot HO_2$	
$CO_2H_3CO_3H + hv \longrightarrow CH_3COCHO + HO_2 + OH + CO_2$	MIM2: 2 channels
$BIACETOH + hv \longrightarrow CH_3CO + HOCH_2CO$	
$ALKOOH + hv \longrightarrow 0.4 \cdot CH_3CHO + 0.25 \cdot CH_2O + 0.25 \cdot CH_3COCH_3 + HO_2 + 0.8 \cdot MEK + OH$	
$ALKNO_3 + hv \longrightarrow 0.4 \cdot CH_3CHO + 0.25 \cdot CH_2O + 0.25 \cdot CH_3COCH_3 + HO_2 + 0.8 \cdot MEK + NO_2$	
$LISOPACOOH + hv \longrightarrow HO_2 + LHC_4ACCHO + OH$	
$LISOPACNO_3 + hv \longrightarrow HO_2 + LHC_4ACCHO + NO_2$	
$HPALD + hv \longrightarrow LHC_4ACCO_3 + OH$	D. Taraborrelli: J(MACR)/phi(MACR) = 2.*jmacr_a/0.004 = 500.*jmacr_a
$PACALD + hv \longrightarrow OH + 0.5 \cdot HO_2 + 0.5 \cdot CO + 0.5 \cdot CH_3COCHO + 0.5 \cdot GLYOX + 0.5 \cdot CH_3CO$	D. Taraborrelli: average of product yields of C5PACALD 1 and 2 in MCMv3.3.1, 2*J(MACR)/phi(MACR)=2.*jhpald = 1000.*jmacr_a
$LIECHO + hv \longrightarrow CO + HO_2 + 0.6 \cdot LHMVKABO_2 + 0.4 \cdot MACRO_2$	
$LIECO_3H + hv \longrightarrow 0.6 \cdot LHMVKABO_2 + 0.4 \cdot MACRO_2 + CO_2 + OH$	
$ISOPBOOH + hv \longrightarrow CH_2O + MVK + HO_2 + OH$	
$ISOPBNO_3 + hv \longrightarrow CH_2O + MVK + HO_2 + NO_2$	
$ISOPDOOH + hv \longrightarrow CH_2O + MACR + HO_2 + OH$	
$ISOPDNO_3 + hv \longrightarrow CH_2O + MACR + HO_2 + NO_2$	
$NISOPOOH + hv \longrightarrow HO_2 + NC_4CHO + OH$	
$NC_4CHO + hv \longrightarrow LHC_4ACCO_3 + NO_2$	at 30 SZA and 300DU O3 J(NC4CHO) = 5.6E-4 s-1 5.6 J(GLYOXAL) Mller et al. 2014

Table D.1.: JAM3 chemical mechanism (... continued)

$LNISOOH + hv \longrightarrow NOA + OH + 0.5 \cdot GLYOXAL + 0.5 \cdot CO + HO_2 + 0.5 \cdot CO_2$	
$LHC_4ACCHO + hv \longrightarrow 0.5 \cdot LHC_4ACCO_3 + 0.25 \cdot HYAC + 0.25 \cdot GLYALD + 0.25 \cdot CH_3CO + 0.75 \cdot CO + 1.25 \cdot HO_2$	
$LC_{578}OOH + hv \longrightarrow 0.5 \cdot HYAC + 0.5 \cdot CH_3COCHO + 0.5 \cdot GLYOXAL + 0.5 \cdot GLYALD + HO_2 + OH$	
$LHC_4ACCO_3H + hv \longrightarrow 0.5 \cdot HYAC + 0.5 \cdot GLYALD + 0.5 \cdot CH_3CO + 0.5 \cdot CO + 0.5 \cdot HO_2 + OH + CO_2$	
$HCOC_5 + hv \longrightarrow CH_2O + CH_3CO + HOCH_2CO$	
$C_{59}OOH + hv \longrightarrow HOCH_2CO + HYAC + NO_2 + OH$	NO2 added
$LISOPOOHOOH + hv \longrightarrow 0.25 \cdot CH_3COCHO + 0.25 \cdot GLYALD + 0.25 \cdot GLYOXAL + 0.25 \cdot HYAC + 0.25 \cdot CO + 0.25 \cdot MACROH + 0.25 \cdot CH_2O + 0.25 \cdot CO_2H_3CHO + HO_2$	products of LC578O2 + NO
$LISOPNO_3OOH + hv \longrightarrow HOCH_2CO + HYAC + NO_2 + OH$	like for C59OOH
$LISOPNO_3NO_3 + hv \longrightarrow HOCH_2CO + HYAC + NO_2 + NO_2$	like for C59OOH but with NO2 instead of OH
$MBOOOH + hv \longrightarrow HO_2 + OH + 0.67 \cdot GLYALD + 0.67 \cdot CH_3COCH_3 + 0.33 \cdot IBUTALOH + 0.33 \cdot CH_2O$	
$IBUTALOH + hv \longrightarrow 2 \cdot HO_2 + CO + CH_3COCH_3$	
$IBUTALOHOOH + hv \longrightarrow CH_3COCH_3 + OH + CO_2 + HO_2$	Tyndall (p.c.)
$BEPOMUC + hv \longrightarrow BIGALD_1 + 1.5 \cdot HO_2 + 1.5 \cdot CO$	
$BIGALD_1 + hv \longrightarrow 0.6 \cdot MALO_2 + HO_2$	
$TOLOOH + hv \longrightarrow OH + 0.6 \cdot GLYOXAL + 0.4 \cdot CH_3COCHO + HO_2 + 0.2 \cdot BIGALD_1 + 0.2 \cdot BIGALD_2 + 0.2 \cdot BIGALD_3$	
$TEPOMUC + hv \longrightarrow 0.5 \cdot CH_3CO + HO_2 + 1.5 \cdot CO$	MCM also has reactions with OH, O3, NO3
$CATEC_1OOH + hv \longrightarrow CATEC_1O + OH$	
$BIGALD_2 + hv \longrightarrow 0.6 \cdot DICARBO_2 + 0.6 \cdot HO_2$	
$BIGALD_3 + hv \longrightarrow 0.6 \cdot CO + 0.6 \cdot HO_2 + 0.6 \cdot MDIALO_2$	
$BIGALD_4 + hv \longrightarrow CO + HO_2 + CH_3COCHO + CH_3CO$	
$TERPOOH + hv \longrightarrow 0.4 \cdot CH_2O + 0.05 \cdot CH_3COCH_3 + 0.945 \cdot TERPROD_1 + HO_2 + OH$	
$TERPROD_1 + hv \longrightarrow CO + HO_2 + TERPROD_2$	

Table D.1.: JAM3 chemical mechanism (... continued)

$TERP_2OOH + hv \longrightarrow OH + 0.372 \cdot CH_2O + 0.3 \cdot CH_3COCH_3 + 0.25 \cdot CO + CO_2 + TERPROD_2 + HO_2 + 0.25 \cdot GLYALD$	
$TERPROD_2 + hv \longrightarrow 0.15 \cdot CH_3COCH_2O_2 + 0.68 \cdot CH_2O + 0.8 \cdot CO_2 + 0.5 \cdot CH_3COCH_3 + 1.2 \cdot HO_2 + 1.7 \cdot CO$	
$ISOPBNO_3 + hv \longrightarrow HO_2 + NO_2 + TERPROD_1$	
$NTERPNO_3 + hv \longrightarrow NO_2 + OH + TERPROD_1$	
$MTHOM + hv \longrightarrow HO_2 + OH + TERPROD_2$	
Stratospheric photolysis reactions	
$O_2 + hv \longrightarrow O + O_1D$	juser1
$O_2 + hv \longrightarrow 2 \cdot O$	juser1
$H_2O + hv \longrightarrow H + OH$	
$H_2O + hv \longrightarrow H_2 + O_1D$	
$H_2O + hv \longrightarrow 2 \cdot H + O$	
$CL_2 + hv \longrightarrow 2 \cdot CL$	
$CL_2O_2 + hv \longrightarrow 2 \cdot CL$	
$CLO + hv \longrightarrow CL + O$	
$HCL + hv \longrightarrow CL + H$	
$HOCL + hv \longrightarrow CL + OH$	
$CLONO_2 + hv \longrightarrow CL + NO_3$	
$CLONO_2 + hv \longrightarrow CLO + NO_2$	
$OCLO + hv \longrightarrow CLO + O$	
$BRO + hv \longrightarrow BR + O$	
$HBR + hv \longrightarrow BR + H$	
$HOBR + hv \longrightarrow BR + OH$	
$BRONO + hv \longrightarrow BR + NO_2$	50% branching ratio assigned to both possible channels. Cross-sections consistent with Burkholder and Orlando, Chem. Phys. lett. (2000)

Table D.1.: JAM3 chemical mechanism (... continued)

$BRONO + hv \longrightarrow BRO + NO$	50% branching ratio assigned to both possible channels. Cross-sections consistent with Burkholder and Orlando, Chem. Phys. lett. (2000)
$BRNO_2 + hv \longrightarrow BR + NO_2$	after having compared JPL cross-sections and jval max calculated by Parrella et al. ACP (2012)
$BRONO_2 + hv \longrightarrow BR + NO_3$	
$BRONO_2 + hv \longrightarrow BRO + NO_2$	
$BR_2 + hv \longrightarrow 2 \cdot BR$	
$BRCL + hv \longrightarrow BR + CL$	
$HF + hv \longrightarrow F + H$	
$SF_6 + hv \longrightarrow$	
$CH_3BR + hv \longrightarrow BR + CH_3O_2$	
$CH_2BR_2 + hv \longrightarrow 2 \cdot BR$	
$CHBR_3 + hv \longrightarrow 3 \cdot BR$	
$CH_3CL + hv \longrightarrow CH_3O_2 + CL$	
$CH_3CCL_3 + hv \longrightarrow 3 \cdot CL$	
$CF_3BR + hv \longrightarrow BR + F + COF_2$	
$CF_2CLBR + hv \longrightarrow BR + CL + COF_2$	
$CCL_4 + hv \longrightarrow 4 \cdot CL + CO_2$	mgs: added CO_2
$CFC_{11} + hv \longrightarrow 2 \cdot CL + COFCL$	
$CFC_{12} + hv \longrightarrow 2 \cdot CL + COF_2$	
$CFC_{113} + hv \longrightarrow 2 \cdot CL + COFCL + COF_2$	
$CFC_{114} + hv \longrightarrow 2 \cdot CL + 2 \cdot COF_2$	
$CFC_{115} + hv \longrightarrow CL + F + 2 \cdot COF_2$	
$HCFC_{22} + hv \longrightarrow CL + COF_2$	
$HCFC_{141}B + hv \longrightarrow CL + COFCL$	
$HCFC_{142}B + hv \longrightarrow CL + COF_2$	
$H_{1202} + hv \longrightarrow 2 \cdot BR + COF_2$	
$H_{2402} + hv \longrightarrow 2 \cdot BR + 2 \cdot COF_2$	

Table D.1.: JAM3 chemical mechanism (... continued)

$COF_2 + hv \longrightarrow 2 \cdot F$		
$COFCL + hv \longrightarrow CL + F$		
(Tropospheric) O_x Reactions		
reaction	rate coefficient	reference
$O + O_2 + M \longrightarrow M + O_3$	kO_O2	
$O + O_3 \longrightarrow 2 \cdot O_2$	$8.000e-12 * exp(-2060./T)$	JPL(2011)
$O + O + M \longrightarrow M + O_2$	kO_O	not in JPL(2011)
$O_1D + N_2 \longrightarrow N_2 + O$	$2.150e-11 * exp(110./T)$	
$O_1D + O_2 \longrightarrow O + O_2$	$3.135e-11 * exp(55./T)$	
$O_1D + O_2 \longrightarrow O + O_2$	$1.650e-12 * exp(55./T)$	
$O_1D + H_2O \longrightarrow 2 \cdot OH$	$1.630e-10 * exp(60./T)$	JPL(2011)
(Tropospheric) HO_x Reactions		
reaction	rate coefficient	reference
$H + O_2 + M \longrightarrow HO_2 + M$	$ktroe(4.400e-32, 1.3, 7.500e-11, -0.2, 0.6)$	JPL(2011)
$H + O_3 \longrightarrow O_2 + OH$	$1.400e-10 * exp(-470./T)$	JPL(2011)
$H + HO_2 \longrightarrow 2 \cdot OH$	$7.200e-11$	JPL(2011)
$H + HO_2 \longrightarrow H_2O + O$	$1.600e-12$	JPL(2011)
$H + HO_2 \longrightarrow H_2 + O_2$	$6.900e-12$	JPL(2011)
$H_2 + O \longrightarrow H + OH$	$1.600e-11 * exp(-4570./T)$	
$H_2 + OH \longrightarrow H + H_2O$	$2.800e-12 * exp(-1800./T)$	JPL(2011)
$OH + O \longrightarrow H + O_2$	$1.800e-11 * exp(180./T)$	JPL(2011)
$OH + OH \longrightarrow H_2O + O$	$1.800e-12$	JPL(2011)
$OH + OH + M \longrightarrow H_2O_2 + M$	$ktroe(6.900e-31, 1., 2.600e-11, 0., 0.6)$	JPL(2011)

Table D.1.: JAM3 chemical mechanism (... continued)

$OH + O_3 \longrightarrow HO_2 + O_2$	$1.700e-12 * exp(-940./T)$	JPL(2011)
$HO_2 + O \longrightarrow O_2 + OH$	$3.000e{-}11 * exp(200./T)$	JPL(2011)
$HO_2 + OH \longrightarrow H_2O + O_2$	$4.800e{-}11 * exp(250./T)$	JPL(2011)
$HO_2 + O_3 \longrightarrow OH + 2 \cdot O_2$	$1.000e-14 * exp(-490./T)$	JPL(2011)
$HO_2 + HO_2 \longrightarrow H_2O_2 + O_2$	$kHO2_HO2$	
$H_2O_2 + O \longrightarrow HO_2 + OH$	$1.400e-12 * exp(-2000./T)$	JPL(2011)
$H_2O_2 + OH \longrightarrow H_2O + HO_2$	$1.800e-12$	JPL(2011)
NO_x Reactions		
reaction	rate coefficient	reference
$N + OH \longrightarrow H + NO$	$5.000e-11$	
$N + O_2 \longrightarrow NO + O$	$1.500e-11 * exp(-3600./T)$	JPL(2011)
$N + NO \longrightarrow N_2 + O$	$2.100e{-}11 * exp(100./T)$	JPL(2011)
$N + NO_2 \longrightarrow 0.5 \cdot N_2O + 0.5 \cdot O + 0.5 \cdot NO + 0.25 \cdot N_2 + 0.25 \cdot O_2$	$5.800e{-}12 * exp(220./T)$	JPL(2011), products: Kinnison (p.c.)
$NO + O + M \longrightarrow M + NO_2$	$ktroe(9.000e-32, 1.5, 3.000e-11, 0., 0.6)$	JPL(2011)
$NO + O_3 \longrightarrow NO_2 + O_2$	$3.000e-12 * exp(-1500./T)$	JPL(2011)
$NO + HO_2 \longrightarrow NO_2 + OH$	$3.300e{-}12 * exp(270./T)$	JPL(2011)
$NO_2 + O \longrightarrow NO + O_2$	$5.100e{-}12 * exp(210./T)$	ref?
$NO_2 + O + M \longrightarrow M + NO_3$	$ktroe(2.500e-31, 1.8, 2.200e-11, 0.7, 0.6)$	JPL(2011)
$NO_2 + O_3 \longrightarrow NO_3 + O_2$	$1.200e-13 * exp(-2450./T)$	JPL(2011)
$NO_2 + H \longrightarrow NO + OH$	$4.000e-10 * exp(-340./T)$	JPL(2011)

Table D.1.: JAM3 chemical mechanism (... continued)

$NO_2 + OH + M \longrightarrow HNO_3 + M$	$ktroe(1.800e-30, 3., 2.800e-11, 0., 0.6)$	JPL(2011); there is a second channel -¿HOONO
$NO_3 + O \longrightarrow NO_2 + O_2$	$1.000e-11$	JPL(2011)
$NO_3 + OH \longrightarrow HO_2 + NO_2$	$2.200e-11$	JPL(2011)
$NO_3 + HO_2 \longrightarrow NO_2 + OH + O_2$	$3.500e-12$	JPL(2011)
$NO_3 + NO \longrightarrow 2 \cdot NO_2$	$1.500e-11*exp(170./T)$	JPL(2011)
$HNO_3 + OH \longrightarrow H_2O + NO_3$	$kHNO3_OH$	usrrxt: X=M6.5e-34*exp(1335/T); X/(1+X/(2.7e-17*exp(2199/T)))+2.4e-14*exp(460/T) - JPL(2011)
$NO + OH \longrightarrow HONO$	$ktroe(7.000e-31, 2.6, 3.600e-11, 0.1, 0.6)$	JPL(2011)
$HONO + OH \longrightarrow H_2O + NO_2$	$1.800e-11 * exp(-390./T)$	JPL(2011)
$NO_2 + HO_2 + M \longrightarrow HO_2NO_2 + M$	$kNO2_HO2$	user defined NO2 reaction with bare HO2
$NO_2 + HO_2 + M \longrightarrow HO_2NO_2 + M$	$kNO2_HO2$	user defined NO2 reaction with HO2 water complex
$HO_2NO_2 + OH \longrightarrow H_2O + NO_2 + O_2$	$1.300e-12*exp(380./T)$	JPL(2011)
$HO_2NO_2 + M \longrightarrow HO_2 + NO_2 + M$	$kHO2NO2$	user defined; usrrxt: [NO2_NO3]*exp(-10900./T)/2.1e-27 JPL (2011)
$NO_2 + NO_3 + M \longrightarrow M + N_2O_5$	$ktroe(2.000e-30, 4.4, 1.400e-12, 0.7, 0.6)$	JPL(2011)
$N_2O_5 + M \longrightarrow NO_2 + NO_3 + M$	$kN2O5$	user defined; usrrxt: [NO2_NO3]$*\exp(-11000/T)/2.7e-27$ JPL (2011)
$NH_3 + OH \longrightarrow$	$1.700e-12 * \exp(-710./T)$	JPL (2011)

C1 oxidation reaction	rate coefficient	reference

Table D.1.: JAM3 chemical mechanism (... continued)

$CO + OH \longrightarrow CO_2 + H$	kCO_OH	usrrxt: JPL(2011), Table 2-1
$CO + OH + M \longrightarrow CO_2 + HO_2 + M$	$ktroe(5.900e-33, 1.4, 1.100e-12, -1.3, 0.6)$	
$CH_4 + OH \longrightarrow CH_3O_2 + H_2O$	$2.450e-12 * exp(-1775./T)$	JPL(2011)
$CH_3OH + OH \longrightarrow CH_2O + HO_2 + H_2O$	$2.900e-12 * exp(-345./T)$	JPL(2011)
$CH_3O_2 + NO \longrightarrow CH_2O + NO_2 + HO_2$	$1.960e{-}12 * exp(403./T)$	Orlando&Tyndall (2012)
$CH_3O_2 + HO_2 \longrightarrow CH_3OOH + O_2$	$3.800e{-}13 * exp(730./T)$	Orlando&Tyndall (2012)
$CH_3O_2 + CH_3O_2 \longrightarrow 2 \cdot CH_2O + 2 \cdot HO_2$	$7.400e-13 * exp(-520./T)$	Atkinson et al.(2006)
$CH_3O_2 + CH_3O_2 \longrightarrow CH_2O + CH_3OH$	$2.330e{-}14 * exp(678./T)$	own fit for T=240-300K
$CH_2O + O \longrightarrow HO_2 + OH + CO$	$3.400e-11 * exp(-1600./T)$	JPL(2011)
$CH_2O + OH \longrightarrow CO + H_2O + H$	$5.500e{-}12 * exp(125./T)$	JPL(2011)
$CH_2O + HO_2 \longrightarrow HOCH_2OO$	$9.700e{-}15 * exp(625./T)$	IUPAC(2012), JPL(2011) is 30% lower
$CH_2O + NO_3 \longrightarrow CO + HO_2 + HNO_3$	$6.000e-13 * exp(-2058./T)$	ref?
$CH_3OOH + OH \longrightarrow 0.7 \cdot CH_3O_2 + 0.3 \cdot OH + 0.3 \cdot CH_2O + H_2O$	$3.800e{-}12 * exp(200./T)$	JPL(2011)
$HCOOH + OH \longrightarrow CO_2 + HO_2 + H_2O$	$4.000e-13$	JPL(2011)
$HOCH_2OO \longrightarrow CH_2O + HO_2$	$2.400e+12 * exp(-7000./T)$	CAM-CHEM (ref?)
$HOCH_2OO + NO \longrightarrow HCOOH + NO_2 + HO_2$	$2.600e{-}12 * exp(265./T)$	CAM-CHEM (ref?)
$HOCH_2OO + HO_2 \longrightarrow H_2O + HCOOH$	$7.500e{-}13 * exp(700./T)$	CAM-CHEM (ref?)
$HCN + OH \longrightarrow CO + NO + H_2O$	$1.200e-13 * exp(-400./T)$	JPL(2011), products: Tyndall
$CH_3O_2 + NO_2 + M \longrightarrow CH_3O_2NO_2 + M$	$ktroe(1.000e-30, 4.8, 7.200e-12, 2.1, 0.6)$	JPL(2011)
$CH_3O_2NO_2 + M \longrightarrow CH_3O_2 + NO_2 + M$	$kCH3O2NO2$	user defined

Table D.1.: JAM3 chemical mechanism (... continued)

C2 oxidation reaction	rate coefficient	reference
$C_2H_2 + OH + M \longrightarrow 0.65 \cdot GLYOXAL + 0.65 \cdot OH + 0.35 \cdot HCOOH + 0.35 \cdot HO_2 + 0.35 \cdot CO + M$	$ktroe(5.500e-30, 0., 8.300e-13, -2., 0.6)$	JPL(2011)
$C_2H_4 + OH + M \longrightarrow EO_2 + M$	$ktroe(1.000e-28, 4.5, 7.500e-12, 0.85, 0.6)$	JPL(2011)
$C_2H_4 + O_3 \longrightarrow CH_2O + 0.65 \cdot CO + 0.15 \cdot OH + 0.15 \cdot HO_2 + 0.5 \cdot H_2O + 0.35 \cdot HCOOH$	$9.100e-15 * exp(-2580./T)$	IUPAC(2012)
$C_2H_6 + OH \longrightarrow C_2H_5O_2 + H_2O$	$7.660e-12 * exp(-1020./T)$	JPL(2011)
$C_2H_5OH + OH \longrightarrow CH_3CHO + HO_2 + H_2O$	$3.350e-12 * exp(0./T)$	JPL(2011)
$CH_3CHO + OH \longrightarrow CH_3CO + H_2O$	$4.630e-12 * exp(350./T)$	JPL(2011)
$CH_3CHO + NO_3 \longrightarrow CH_3CO + HNO_3$	$1.400e-12 * exp(-1900./T)$	JPL(2011)
$CH_3COOOH + OH \longrightarrow 0.5 \cdot CH_3CO_3 + H_2O + 0.5 \cdot CH_2O + 0.5 \cdot CO_2 + 0.5 \cdot OH$	$1.000e-12$	Orlando (p.c.) cacm: added OH in second channel 20140613
$C_2H_5O_2 + NO \longrightarrow CH_3CHO + HO_2 + NO_2$	$2.620e-12 * exp(373./T)$	Orlando&Tyndall (2012)
$C_2H_5O_2 + HO_2 \longrightarrow C_2H_5OOH + O_2$	$7.400e-13 * exp(700./T)$	Orlando&Tyndall (2012)
$C_2H_5O_2 + CH_3O_2 \longrightarrow 0.7 \cdot CH_2O + 0.8 \cdot CH_3CHO + HO_2 + 0.3 \cdot CH_3OH + 0.2 \cdot C_2H_5OH$	$2.000e-13$	Orlando (p.c.), products: Tyndall (p.c.)
$C_2H_5O_2 + CH_3CO_3 \longrightarrow CH_3CHO + HO_2 + CH_3O_2 + CO_2$	$1.800e-12 * exp(500./T)$	10% lower than CH3O2 + CH3CO3; Orlando&Tyndall (2012) only give k@298K
$C_2H_5O_2 + C_2H_5O_2 \longrightarrow 1.6 \cdot CH_3CHO + 1.2 \cdot HO_2 + 0.4 \cdot C_2H_5OH$	$7.600e-14$	Orlando&Tyndall (2012)
$C_2H_5O_2 + NO_2 + M \longrightarrow C_2H_5O_2NO_2 + M$	$ktroe(1.200e-29, 4., 9.000e-12, 0., 0.6)$	JPL(2011)
$C_2H_5O_2NO_2 + M \longrightarrow C_2H_5O_2 + NO_2 + M$	$kC2H5O2NO2$	user defined being 5 times the one for CH3O2NO2 as estimated by Zabel et al(1989) at the tropopause

Table D.1.: JAM3 chemical mechanism (... continued)

$C_2H_5OOH + OH \longrightarrow 0.5 \cdot C_2H_5O_2 + 0.5 \cdot CH_3CHO + 0.5 \cdot OH + H_2O$	$3.800e{-}12{*}exp(200./T)$	no data, analog to CH3OOH+OH
$CH_3CO + O_2 \longrightarrow CH_3CO_3$	$kCH3CO_O2$	user defined: k=5.1E-12*(1. - 1./(1.+9.4E-18*cair)) IUPAC and Gro et al. 2014. Rate constant is the high-pressure limit as recommended by IUPAC.
$CH_3CO + O_2 \longrightarrow HCHO + OH + CO$	$kCH3CO_O2$	user defined: k=5.1E-12*1./(1.+9.4E-18*cair) IUPAC and Gro et al. 2014. Rate constant is the high-pressure limit as recommended by IUPAC; the co-product of OH should be lactone
$CH_3CO_3 + NO \longrightarrow CH_3O_2 + CO_2 + NO_2$	$7.500e{-}12{*}exp(290./T)$	Orlando&Tyndall (2012)
$CH_3CO_3 + NO_2 + M \longrightarrow M + PAN$	$ktroe(2.700e-28, 7.1, 1.200e-11, 0.9, 0.6)$	
$CH_3CO_3{+}HO_2 \longrightarrow 0.37 \cdot CH_3COOOH{+}0.12 \cdot CH_3COOH{+}0.12 \cdot O_3{+}0.51 \cdot CH_3O_2 + 0.51 \cdot OH + 0.51 \cdot CO_2$	$8.207e{-}13{*}exp(980./T)$	k scaled to 2.2e-11 as recommeded by Winiberg (A = 5.2e-13 * 1.578) (Winiberg et al. 2016 and Gro et al. 2014)
$CH_3CO_3 + CH_3O_2 \longrightarrow CH_2O + 0.9 \cdot CH_3O_2 + 0.9 \cdot HO_2 + 0.9 \cdot CO_2 + 0.1 \cdot CH_3COOH$	$2.000e{-}12{*}exp(500./T)$	Orlando&Tyndall (2012)
$CH_3CO_3 + CH_3CO_3 \longrightarrow 2 \cdot CH_3O_2 + 2 \cdot CO_2$	$2.900e{-}12{*}exp(500./T)$	Orlando&Tyndall (2012)
$CH_3COOH + OH \longrightarrow CH_3O_2 + CO_2 + H_2O$	$3.150e{-}14{*}exp(920./T)$	JPL(2011)
$PAN + M \longrightarrow CH_3CO_3 + NO_2 + M$	$kPAN$	user defined
$PAN + OH \longrightarrow CH_2O + CO_2 + NO_3$	$4.000e-14$	JPL(2011), includes implicit NO-¿NO2 conversion
$EO_2 + NO \longrightarrow 0.75 \cdot EO + NO_2 + 0.5 \cdot CH_2O + 0.25 \cdot HO_2$	$4.200e{-}12{*}exp(180./T)$	CAM-CHEM cacm: changed 20140613
$EO_2 + HO_2 \longrightarrow EOOH$	$7.500e{-}13{*}exp(700./T)$	
$EO_2 + CH_3O_2 \longrightarrow 0.5 \cdot EO + 0.5 \cdot O_2 + 0.5 \cdot CH_2O + 0.5 \cdot HO_2 + 0.5 \cdot CH_3OH + 0.5 \cdot GLYALD$	$4.000e-12*exp(1000./T)$	Tyndall (p.c.) cacm: There is a 2nd molecular channel in the EO2+CH3O2 reaction, giving HOCH2-CH2OH + CH2O, but I am happy to ignore (JO).
$EO_2 + CH_3CO_3 \longrightarrow CH_3O_2 + EO + CO_2$	$1.000e-11$	
$EO + O_2 \longrightarrow GLYALD + HO_2$	$1.000e-14$	CAM-CHEM

Table D.1.: JAM3 chemical mechanism (... continued)

$EO \longrightarrow 2 \cdot CH_2O + HO_2$	$1.600e + 11 * exp(-4150./T)$	CAM-CHEM
$GLYOXAL + OH \longrightarrow 0.6 \cdot HO_2 + 1.2 \cdot CO + H_2O + 0.4 \cdot HCOCO_3$	$3.100e{-}12{*}exp(340./T)$	MCM
$GLYOXAL + NO_3 \longrightarrow 0.6 \cdot HO_2 + 1.2 \cdot CO + 0.4 \cdot HCOCO_3 + HNO_3$	$2.500e - 12$	MIM2
$GLYALD + OH \longrightarrow 0.2 \cdot GLYOXAL + 0.2 \cdot HO_2 + 0.8 \cdot HOCH_2CO + H_2O$	$1.000e - 11$	MIM2
$GLYALD + NO_3 \longrightarrow HNO_3 + HOCH_2CO$	$1.440e - 12 * exp(-1862./T)$	MIM2
$HOCH_2CO + O_2 \longrightarrow HOCH_2CO$	$kHOCH2CO_O2$	user defined: k=5.1E-12*(1. - 1./(1.+1.85E-18*cair)) IUPAC and Gro et al. 2014. Rate constant is the high-pressure limit as recommended by IUPAC.
$HOCH_2CO + O_2 \longrightarrow HCHO + OH + CO_2$	$kHOCH2CO_O2$	user defined: k=5.1E-12*1./(1.+1.85E-18*cair) IUPAC and Gro et al. 2014. Rate constant is the high-pressure limit as recommended by IUPAC; the co-product of OH should be lactone
$HOCH_2CO_3 + NO_2 + M \longrightarrow CH_2O + CO_2 + HNO_3 + M$	$ktroe(2.700e - 28, 7.1, 1.200e - 11, 0.9, 0.6)$	Orlando&Tyndall (2012)
$HOCH_2CO_3 + HO_2 \longrightarrow 0.37 \cdot HOCH_2CO_3H + 0.12 \cdot HOCH_2CO_2H + 0.12 \cdot O_3 + 0.51 \cdot CO_2 + 0.51 \cdot OH + 0.51 \cdot HO_2 + 0.51 \cdot CH_2O$	$8.207e{-}13{*}exp(980./T)$	k scaled to 2.2e-11 as recommeded by Winiberg (A = 5.2e-13 * 1.578) ; product distribution in analogy to CH3CO3 + HO2 reactions (Winiberg et al. 2016 and Gro et al. 2014)
$HOCH_2CO_3 + CH_3O_2 \longrightarrow 2 \cdot CH_2O + CO_2 + 2 \cdot HO_2$	$1.000e - 11$	MIM2
$HOCH_2CO_3 + CH_3CO_3 \longrightarrow CH_3O_2 + 2 \cdot CO_2 + HO_2 + CH_2O$	$1.000e - 11$	MIM2
$HOCH_2CO_3 + NO \longrightarrow HO_2 + NO_2 + CH_2O + CO_2$	$8.100e{-}12{*}exp(270./T)$	MIM2
$HOCH_2CO_3 + NO_3 \longrightarrow HO_2 + NO_2 + CH_2O + CO_2$	$4.000e - 12$	MIM2
$HOCH_2CO_2H + OH \longrightarrow CH_2O + HO_2 + CO_2 + H_2O$	$2.730e - 12$	MIM2
$HOCH_2CO_3H + OH \longrightarrow H_2O + HOCH_2CO_3$	$6.190e - 12$	MIM2
$HCOCO_3 + CH_3O_2 \longrightarrow CO + 2 \cdot HO_2 + CO_2 + CH_2O$	$1.000e - 11$	MIM2
$HCOCO_3 + CH_3CO_3 \longrightarrow CO + HO_2 + CH_3O_2 + 2 \cdot CO_2$	$1.000e - 11$	MIM2

Table D.1.: JAM3 chemical mechanism (... continued)

$HCOCO_3 + HO_2 \longrightarrow CO + HO_2 + CO_2 + OH$	$8.207e{-}13 * exp(980./T)$	k scaled to 2.2e-11 as recommeded by Winiberg (A = 5.2e-13 * 1.578) (Winiberg et al. 2016 and Gro et al. 2014) ; only products from OH-channel that is considered dominant
$HCOCO_3 + NO \longrightarrow CO + HO_2 + NO_2 + CO_2$	$8.100e{-}12 * exp(270./T)$	MIM2
$HCOCO_3 + NO_3 \longrightarrow CO + HO_2 + NO_2 + CO_2$	$4.000e-12$	MIM2
$HCOCO_2H + OH \longrightarrow CO + HO_2 + CO_2 + H_2O$	$1.230e-11$	MIM2
$HCOCO_3H + OH \longrightarrow H_2O + HCOCO_3$	$1.580e-11$	MIM2
$CH_3CN + OH \longrightarrow CH_2O + H_2O + CO + NO_2$	$7.800e-13 * exp(-1050./T)$	products: Tyndall

C3 oxidation reaction	rate coefficient	reference
$C_3H_6 + OH + M \longrightarrow M + PO_2$	$ktroe(8.000e-27, 3.5, 3.000e-11, 0., 0.5)$	IUPAC 2006
$C_3H_6 + O_3 \longrightarrow 0.28 \cdot CH_3O_2 + 0.1 \cdot CH_4 + 0.075 \cdot CH_3COOH + 0.56 \cdot CO + 0.075 \cdot HCOOH + 0.09 \cdot H_2O_2 + 0.28 \cdot HO_2 + 0.2 \cdot CO_2 + 0.545 \cdot CH_3CHO + 0.545 \cdot CH_2O + 0.36 \cdot OH$	$5.500e-15 * exp(-1880./T)$	IUPAC 2006
$C_3H_6 + NO_3 \longrightarrow PRONO_3BO_2$	$4.600e-13 * exp(-1156./T)$	IUPAC 2006
$C_3H_8 + OH \longrightarrow C_3H_7O_2 + H_2O$	$7.600e-12 * exp(-585./T)$	IUPAC 2006
$CH_3COCH_3 + OH \longrightarrow CH_3COCH_2O_2 + H_2O$	$kCH3COCH3_OH$	
$C_3H_7O_2 + NO \longrightarrow 0.82 \cdot CH_3COCH_3 + NO_2 + HO_2 + 0.27 \cdot CH_3CHO$	$2.900e{-}12 * exp(350./T)$	Orlando&Tyndall, 2012, 0.27*CH3CHO for 0.18*CH3CH2CHO
$C_3H_7O_2 + HO_2 \longrightarrow C_3H_7OOH + O_2$	$7.500e{-}13 * exp(700./T)$	CAM-CHEM
$C_3H_7O_2 + CH_3O_2 \longrightarrow CH_2O + 2 \cdot HO_2 + 0.82 \cdot CH_3COCH_3 + 0.27 \cdot CH_3CHO$	$3.750e-13 * exp(-40./T)$	CAM-CHEM
$C_3H_7O_2 + CH_3CO_3 \longrightarrow 0.82 \cdot CH_3COCH_3 + HO_2 + 0.27 \cdot CH_3CHO + CO_2 + CH_3O_2$	$1.000e-11$	0.27*CH3CHO for 0.18*CH3CH2CHO

Table D.1.: JAM3 chemical mechanism (... continued)

$C_3H_7OOH + OH \longrightarrow 0.41 \cdot CH_3COCH_3 + 0.5 \cdot OH + 0.5 \cdot C_3H_7O_2 + 0.5 \cdot H_2O + 0.135 \cdot CH_3CHO$	$3.800e{-}12{*}exp(200./T)$	CAM-CHEM; J.O.: 1.5*CH3CHO as surrogate for propanal
$PO_2 + NO \longrightarrow CH_2O + CH_3CHO + HO_2 + NO_2$	$4.200e{-}12{*}exp(180./T)$	CAM-CHEM
$PO_2 + NO_3 \longrightarrow CH_2O + CH_3CHO + HO_2 + NO_2$	$2.500e-12$	MIM2
$PO_2 + HO_2 \longrightarrow O_2 + POOH$	$7.500e{-}13{*}exp(700./T)$	CAM-CHEM
$PO_2 + CH_3O_2 \longrightarrow 0.5 \cdot CH_3CHO + 1.25 \cdot CH_2O + HO_2 + 0.5 \cdot HYAC + 0.25 \cdot CH_3OH$	$8.300e-13$	products: Tyndall (p.c.), CH3CH(OH)CH2OH goes to HYAC cacm: added CH2O 20140613
$PO_2 + CH_3CO_3 \longrightarrow CH_2O + CH_3CHO + HO_2 + CH_3O_2 + CO_2$	$1.000e-11$	
$POOH + OH \longrightarrow 0.5 \cdot PO_2 + 0.5 \cdot HYAC + 0.5 \cdot OH + H_2O$	$3.800e{-}12{*}exp(200./T)$	CAM-CHEM
$HYAC + OH \longrightarrow CH_3COCHO + HO_2 + H_2O$	$3.000e-12$	IUPAC 2006
$CH_3COCHO + OH \longrightarrow CH_3CO + CO + H_2O$	$8.400e{-}13{*}exp(830./T)$	CAM-CHEM
$CH_3COCHO + NO_3 \longrightarrow CO + HNO_3 + CH_3CO$	$1.400e-12*exp(-1860./T)$	CAM-CHEM
$CH_3COCH_2O_2 + NO \longrightarrow CH_2O + CH_3CO + NO_2$	$2.900e{-}12{*}exp(300./T)$	CAM-CHEM
$CH_3COCH_2O_2 + HO_2 \longrightarrow 0.85 \cdot O_2 + 0.85 \cdot ROOH + 0.15 \cdot CH_2O + 0.15 \cdot CH_3CO + 0.15 \cdot OH + 0.15 \cdot H_2O$	$8.600e{-}13{*}exp(700./T)$	CAM-CHEM + MCM
$CH_3COCH_2O_2 + CH_3O_2 \longrightarrow 0.3 \cdot CH_3CO + 0.8 \cdot CH_2O + 0.3 \cdot HO_2 + 0.2 \cdot HYAC + 0.5 \cdot CH_3COCHO + 0.5 \cdot CH_3OH$	$7.100e{-}13{*}exp(500./T)$	CAM-CHEM
$CH_3COCH_2O_2 + CH_3CO_3 \longrightarrow CH_2O + CH_3CO + CH_3O_2 + CO_2$	$1.000e-11$	
$ROOH + OH \longrightarrow CH_3COCH_2O_2 + H_2O$	$3.800e{-}12{*}exp(200./T)$	CAM-CHEM
$PRONO_3BO_2 + NO \longrightarrow 0.83 \cdot HO_2 + 0.83 \cdot NOA + 0.17 \cdot CH_2O + 0.17 \cdot CH_3CHO + 1.17 \cdot NO_2$	$2.540e{-}12{*}exp(360./T)$	MIM2 + MCM3.2
$PRONO_3BO_2 + NO_3 \longrightarrow 0.83 \cdot HO_2 + 0.83 \cdot NOA + 0.17 \cdot CH_2O + 0.17 \cdot CH_3CHO + 1.17 \cdot NO_2$	$2.500e-12$	MIM2 + MCM3.2
$PRONO_3BO_2 + HO_2 \longrightarrow PR_2O_2HNO_3$	$1.320e{-}12{*}exp(360./T)$	MIM2
$PRONO_3BO_2 + CH_3O_2 \longrightarrow 0.915 \cdot HO_2 + 0.915 \cdot NOA + 0.835 \cdot CH_2O + 0.085 \cdot CH_3CHO + 0.25 \cdot CH_3OH$	$1.000e-12$	
$PRONO_3BO_2 + CH_3CO_3 \longrightarrow 0.83 \cdot HO_2 + 0.83 \cdot NOA + 0.17 \cdot CH_2O + 0.17 \cdot CH_3CHO + CH_3O_2 + CO_2$	$1.000e-11$	
$PR_2O_2HNO_3 + OH \longrightarrow 0.5 \cdot PRONO_3BO_2 + 0.5 \cdot NOA + 0.5 \cdot OH + H_2O$	$7.000e-12$	MIM2 (combined)
$NOA + OH \longrightarrow CH_3COCHO + NO_2 + H_2O$	$1.300e-13$	MIM2

Table D.1.: JAM3 chemical mechanism (... continued)

C4 oxidation reaction	rate coefficient	reference
$BIGENE + OH \longrightarrow ENEO_2$	$5.400e-11$	CAM-CHEM
$MEK + OH \longrightarrow H_2O + MEKO_2$	$2.300e-12 * exp(-170./T)$	CAM-CHEM
$MEKO_2 + NO \longrightarrow CH_3CHO + CH_3CO + NO_2$	$4.032e-12*exp(180./T)$	treated like MEKBO2 from MCM; A=4.200e-12*0.96 ¡- 4% nitrate yield as for MVKN
$MEKO_2 + NO \longrightarrow MEKNO_3$	$1.680e-13*exp(180./T)$	A=4.200e-12*0.04 ¡- 4% nitrate yield as for MVKN
$MEKO_2 + HO_2 \longrightarrow MEKOOH$	$7.500e-13*exp(700./T)$	CAM-CHEM
$MEKO_2 + CH_3O_2 \longrightarrow 0.3 \cdot CH_3CHO + 0.3 \cdot CH_3CO + CH_2O + 0.3 \cdot HO_2 + 0.3 \cdot O_2 + 0.5 \cdot BIACETOH + 0.5 \cdot CH_3OH + 0.266 \cdot HYAC$	$1.000e-12$	Tyndall (p.c.) cacm: added CH2O to first and third channel 20140613
$MEKO_2 + CH_3CO_3 \longrightarrow CH_3CHO + CH_3CO + CH_3O_2 + CO_2$	$1.000e-11$	
$MEKOOH + OH \longrightarrow H_2O + MEKO_2$	$3.800e-12*exp(200./T)$	CAM-CHEM
$ENEO_2 + NO \longrightarrow CH_3CHO + 0.5 \cdot CH_2O + 0.5 \cdot CH_3COCH_3 + HO_2 + NO_2$	$4.200e-12*exp(180./T)$	CAM-CHEM
$ENEO_2 + HO_2 \longrightarrow 1.333 \cdot POOH + O_2$	$7.500e-13*exp(700./T)$	factor 4/3 to preserve carbon
$ENEO_2 + CH_3O_2 \longrightarrow 0.665 \cdot HYAC + 0.5 \cdot CH_3OH + 0.5 \cdot CH_3CHO + 0.25 \cdot CH_3COCH_3 + 0.75 \cdot CH_2O + HO_2$	$1.000e-12$	products: Tyndall (p.c.)
$ENEO_2 + CH_3CO_3 \longrightarrow CH_3CHO + 0.5 \cdot CH_2O + 0.5 \cdot CH_3COCH_3 + HO_2 + CH_3O_2 + CO_2$	$1.000e-11$	
$MACR + OH \longrightarrow 0.45 \cdot MCO_3 + 0.55 \cdot MACRO_2$	$1.860e-11*exp(175./T)$	Tnydall (p.c.)
$MACR + O_3 \longrightarrow 0.59 \cdot CH_3COCHO + 0.41 \cdot CH_3CO + 0.82 \cdot CO + 0.41 \cdot HO_2 + 0.82 \cdot OH + 0.033750 \cdot HCOOH + 0.556250 \cdot CH_2O + 0.123750 \cdot H_2O_2$	$1.360e-15 * exp(-2112./T)$	
$MACR + NO_3 \longrightarrow HNO_3 + MCO_3$	$2.880e-12 * exp(-1862./T)$	
$MCO_3 + CH_3O_2 \longrightarrow 0.315 \cdot CH_3CO + 0.585 \cdot CH_3O_2 + 0.585 \cdot CO + 1.9 \cdot CH_2O + 0.9 \cdot CO_2 + 0.9 \cdot HO_2 + 0.1 \cdot MACO_2H$	$1.000e-11$	MCO3 is an acyl radical, therefore kRO2_CH3CO3
$MCO_3 + CH_3CO_3 \longrightarrow CH_2O + 0.35 \cdot CH_3CO + 1.65 \cdot CH_3O_2 + 0.65 \cdot CO + 2 \cdot CO_2$	$1.000e-11$	

Table D.1.: JAM3 chemical mechanism (... continued)

$MCO_3 + HO_2 \longrightarrow 0.51 \cdot OH + 0.178 \cdot CH_3CO + 0.332 \cdot CH_3O_2 + 0.332 \cdot CO + 0.51 \cdot CH_2O + 0.51 \cdot CO_2 + 0.12 \cdot MACO_2H + 0.12 \cdot O_3 + 0.37 \cdot MACO_3H + 0.37 \cdot O_2$	$8.207e{-}13{*}exp(980./T)$	k scaled to 2.2e-11 as recommeded by Winiberg (A = 5.2e-13 * 1.578) ; product distribution in analogy to CH3CO3 + HO2 reactions (Winiberg et al. 2016 and Gro et al. 2014)
$MCO_3 + NO \longrightarrow CH_2O + 0.35 \cdot CH_3CO + 0.65 \cdot CH_3O_2 + 0.65 \cdot CO + NO_2 + CO_2$	$8.700e{-}12{*}exp(290./T)$	
$MCO_3 + NO_3 \longrightarrow CH_2O + 0.35 \cdot CH_3CO + 0.65 \cdot CH_3O_2 + 0.65 \cdot CO + NO_2 + CO_2$	$4.000e-12$	
$MCO_3 + NO_2 + M \longrightarrow M + MPAN$	$ktroe(2.700e-28, 7.1, 1.200e-11, 0.9, 0.3)$	
$MACRO_2 + CH_3O_2 \longrightarrow 0.75 \cdot CO + 0.75 \cdot HYAC + CH_2O + 1.5 \cdot HO_2 + 0.25 \cdot MACROH + 0.25 \cdot O_2$	$9.200e-14$	products: Tyndall (p.c.)
$MACRO_2 + CH_3CO_3 \longrightarrow 0.85 \cdot CO + 0.85 \cdot HYAC + 0.15 \cdot CH_2O + 0.15 \cdot CH_3COCHO + HO_2 + CH_3O_2 + CO_2$	$1.000e-11$	
$MACRO_2 + NO \longrightarrow NO_2 + 0.85 \cdot CO + 0.85 \cdot HYAC + HO_2 + 0.15 \cdot CH_2O + 0.15 \cdot CH_3COCHO$	$2.464e{-}12{*}exp(360./T)$	A=2.54e-12*0.97 ¡- 3% MACRN-yield inferred from HYAC 42% yield at high-NO from Crounse et al. 2011 Tyndall (p.c.)
$MACRO_2 + NO \longrightarrow MACRN$	$7.620e{-}14{*}exp(360./T)$	A=2.54e-12*0.03 ¡- 3% MACRN-yield inferred from HYAC 42% yield at high-NO from Crounse et al. 2011 Tyndall (p.c.)
$MACRO_2 + NO_3 \longrightarrow 0.85 \cdot CO + 0.85 \cdot HYAC + 0.15 \cdot CH_2O + 0.15 \cdot CH_3COCHO + HO_2 + NO_2$	$2.500e-12$	
$MACRO_2 + HO_2 \longrightarrow 0.6 \cdot MACROOH + 0.4 \cdot CO + 0.4 \cdot HYAC + 0.4 \cdot HO_2 + 0.4 \cdot OH$	$1.820e-13 * exp(1300./T)$	
$MACRO_2 \longrightarrow CO + HYAC + OH$	$2.900e+07 * exp(-5297./T)$	Isomerisation according to Crounse et al., 2012
$MACROOH + OH \longrightarrow CO + HYAC + OH + H_2O$	$1.800e-11$	
$MACROH + OH \longrightarrow CO_2 + HYAC + HO_2 + H_2O$	$1.800e-11$	
$MPAN + M \longrightarrow MCO_3 + NO_2 + M$	$kMPAN$	usrrxt as in MOZ
$MPAN + OH \longrightarrow CO + HYAC + NO_2$	$3.200e-11$	rate: Orlando et al.(2002)

Table D.1.: JAM3 chemical mechanism (... continued)

$MACO_2H + OH \longrightarrow CH_2O + CH_3CO + CO_2 + H_2O$	$1.510e-11$	products should be pyruvic acid+CH2O+HO2
$MACO_3H + OH \longrightarrow H_2O + MCO_3$	$1.870e-11$	
$MVK + OH \longrightarrow LHMVKABO_2$	$4.130e{-}12{*}exp(452./T)$	
$MVK + O_3 \longrightarrow 0.85 \cdot CH_3COCHO + 0.85 \cdot HCOOH + 0.15 \cdot CH_3CO + 0.15 \cdot OH + 0.15 \cdot CO + 0.15 \cdot CH_2O$	$7.510e-16*exp(-1521./T)$	products according to IUPAC(2012)
$LHMVKABO_2 + CH_3O_2 \longrightarrow 0.9 \cdot CH_2O + 0.35 \cdot GLYALD + 0.65 \cdot HO_2 + 0.35 \cdot CH_3CO + 0.175 \cdot BIACETOH + 0.25 \cdot CH_3OH + 0.25 \cdot MACROH + 0.15 \cdot CH_3COCHO + 0.075 \cdot CO_2H_3CHO$	$1.000e-12$	products: Tyndall (p.c.)
$LHMVKABO_2 + CH_3CO_3 \longrightarrow 0.3 \cdot CH_3COCHO + 0.7 \cdot GLYALD + 0.7 \cdot CH_3CO + 0.3 \cdot CH_2O + 0.3 \cdot HO_2 + CH_3O_2 + CO_2$	$1.000e-11$	
$LHMVKABO_2 + HO_2 \longrightarrow 0.34 \cdot LHMVKABOOH + 0.66 \cdot CH_3CO + 0.66 \cdot OH + 0.66 \cdot GLYALD$	$1.820e-13*exp(1300./T)$	Praske et al. J. Phys. Chem. A 2015
$LHMVKABO_2 + NO \longrightarrow NO_2 + 0.3 \cdot CH_2O + 0.3 \cdot CH_3COCHO + 0.3 \cdot HO_2 + 0.7 \cdot CH_3CO + 0.7 \cdot GLYALD$	$2.438e{-}12{*}exp(360./T)$	A=2.54e-12*0.96 ¡- 4% nitrate yield Praske et al. J. Phys. Chem. A 2015
$LHMVKABO_2 + NO \longrightarrow MVKN$	$1.020e{-}13{*}exp(360./T)$	A=2.54e-12*0.04 ¡- 4% nitrate yield Praske et al. J. Phys. Chem. A 2015
$LHMVKABO_2 + NO_3 \longrightarrow 0.3 \cdot CH_3COCHO + 0.7 \cdot GLYALD + 0.7 \cdot CH_3CO + 0.3 \cdot CH_2O + 0.3 \cdot HO_2 + NO_2$	$2.500e-12$	
$MVKN + OH \longrightarrow CH_3COCHO + HO_2 + CO_2 + NO_2 + H_2O$	$5.600e-12$	k from Paulot et al.2009; simplified products
$MACRN + OH \longrightarrow CO_2 + HYAC + NO_2 + H_2O$	$5.000e-11$	k from Paulot et al.2009; simplified products
$LHMVKABOOH + OH \longrightarrow 0.3 \cdot CO_2H_3CHO + OH + H_2O + 0.7 \cdot BIACETOH$	$4.500e-12$	
$CO_2H_3CHO + OH \longrightarrow CO_2H_3CO_3 + H_2O$	$2.450e-11$	
$CO_2H_3CHO + NO_3 \longrightarrow CO_2H_3CO_3 + HNO_3$	$5.760e-12*exp(-1862./T)$	
$CO_2H_3CO_3 + CH_3O_2 \longrightarrow CH_3COCHO + 2 \cdot HO_2 + CO_2 + CH_2O$	$1.000e-11$	products: Tyndall (p.c.)
$CO_2H_3CO_3 + CH_3CO_3 \longrightarrow CH_3COCHO + HO_2 + CH_3O_2 + 2 \cdot CO_2$	$1.000e-11$	
$CO_2H_3CO_3 + HO_2 \longrightarrow 0.49 \cdot CO_2H_3CO_3H + 0.51 \cdot CO_2 + 0.51 \cdot OH + 0.51 \cdot HO_2 + 0.51 \cdot CH_3COCHO$	$8.207e{-}13{*}exp(980./T)$	k scaled to 2.2e-11 as recommeded by Winiberg (A = 5.2e-13 * 1.578) ; product distribution in analogy to CH3CO3 + HO2 reactions (Winiberg et al. 2016 and Gro et al. 2014)

Table D.1.: JAM3 chemical mechanism (... continued)

$CO_2H_3CO_3 + NO \longrightarrow CH_3COCHO + HO_2 + NO_2 + CO_2$	$8.100e{-}12{*}exp(270./T)$	
$CO_2H_3CO_3 + NO_3 \longrightarrow CH_3COCHO + HO_2 + NO_2 + CO_2$	$4.000e-12$	
$CO_2H_3CO_3H + OH \longrightarrow CO_2H_3CO_3 + H_2O$	$1.000e-12$	Orlando (p.c.)
$MALO_2 + NO_2 + M \longrightarrow 0.8 \cdot LC_5PAN_{1719} + M$	$ktroe(2.700e-28, 7.1, 1.200e-11, 0.9, 0.6)$	Orlando&Tyndall (2012) - Same as k(CH3CO3 + NO2); LC5PAN as a surrogate
$MALO_2 + NO \longrightarrow 0.4 \cdot GLYOXAL + HO_2 + 0.4 \cdot CO + 0.4 \cdot CO_2 + NO_2 + 0.6 \cdot CO_2H_3CHO$	$7.500e{-}12{*}exp(290./T)$	products: Tyndall (p.c.), use CO2H3CHO in lieu of GUNK
$MALO_2 + HO_2 \longrightarrow 0.16 \cdot GLYOXAL + HO_2 + 0.16 \cdot CO + 0.16 \cdot CO_2 + 0.16 \cdot OH + 0.84 \cdot CO_2H_3CHO$	$4.300e-13 * exp(1040./T)$	
$MALO_2 + CH_3O_2 \longrightarrow 0.4 \cdot GLYOXAL + 2 \cdot HO_2 + 0.4 \cdot CO + 0.4 \cdot CO_2 + 0.6 \cdot CO_2H_3CHO + CH_2O$	$1.000e-12$	products: Tyndall (p.c.)
$MALO_2 + CH_3CO_3 \longrightarrow 0.4 \cdot GLYOXAL + HO_2 + 0.4 \cdot CO + 1.4 \cdot CO_2 + 0.6 \cdot CO_2H_3CHO + CH_3O_2$	$1.000e-11$	
$MDIALO_2 + HO_2 \longrightarrow 0.4 \cdot OH + 0.332 \cdot HO_2 + 0.068 \cdot CH_3COCHO + 0.136 \cdot CO + 0.068 \cdot CH_3O_2 + 0.068 \cdot GLYOXAL$	$4.300e-13 * exp(1040./T)$	
$MDIALO_2 + NO \longrightarrow NO_2 + 0.83 \cdot HO_2 + 0.17 \cdot CH_3COCHO + 0.34 \cdot CO + 0.17 \cdot CH_3O_2 + 0.17 \cdot GLYOXAL$	$7.500e{-}12{*}exp(290./T)$	
$MDIALO_2 + NO_2 + M \longrightarrow M$	$ktroe(2.700e-28, 7.1, 1.200e-11, 0.9, 0.6)$	Orlando&Tyndall (2012) - Same as k(CH3CO3 + NO2)
$MDIALO_2 + CH_3O_2 \longrightarrow 1.83 \cdot HO_2 + 0.17 \cdot CH_3COCHO + 0.34 \cdot CO + 0.17 \cdot CH_3O_2 + 0.17 \cdot GLYOXAL + CH_2O$	$1.000e-12$	
$MDIALO_2 + CH_3CO_3 \longrightarrow 0.83 \cdot HO_2 + 0.17 \cdot CH_3COCHO + 0.34 \cdot CO + 1.17 \cdot CH_3O_2 + 0.17 \cdot GLYOXAL + CO_2$	$1.000e-11$	

C5 oxidation reaction	rate coefficient	reference
$BIGALKANE + OH \longrightarrow ALKO_2 + H_2O$	$3.500e-12$	
$C_5H_8 + OH \longrightarrow 0.4 \cdot LISOPACO_2 + 0.35 \cdot ISOPBO_2 + 0.25 \cdot ISOPDO_2$	$2.700e{-}11{*}exp(390./T)$	Tyndall (p.c.); MCM3.2 has yields .25, .5, .25

Table D.1.: JAM3 chemical mechanism (... continued)

$C_5H_8 + O_3 \longrightarrow 0.051 \cdot CH_3O_2 + 0.1575 \cdot CH_3CO + 0.054 \cdot LHMVKABO_2 + 0.522 \cdot CO + 0.068750 \cdot HCOOH + 0.11 \cdot H_2O_2 + 0.324750 \cdot MACR + 0.1275 \cdot C_3H_6 + 0.2625 \cdot HO_2 + 0.255 \cdot CO_2 + 0.749750 \cdot CH_2O + 0.041250 \cdot MACO_2H + 0.27 \cdot OH + 0.244 \cdot MVK$	$7.860e-15 * exp(-1913./T)$	
$C_5H_8 + NO_3 \longrightarrow NISOPO_2$	$3.030e-12 * exp(-446./T)$	
$MBO + OH \longrightarrow MBOO_2$	$8.100e{-}12 * exp(610./T)$	
$MBO + O_3 \longrightarrow 0.35 \cdot CO + 0.5 \cdot CH_2O + 0.1 \cdot CH_3COCH_3 + 0.9 \cdot IBUTALOH + 0.25 \cdot HCOOH + 0.06 \cdot HO_2 + 0.06 \cdot OH$	$1.000e-17$	
$MBO + NO_3 \longrightarrow MBONO_3O_2$	$4.600e-14 * exp(-400./T)$	
$ALKO_2 + NO \longrightarrow 0.4 \cdot CH_3CHO + 0.25 \cdot CH_2O + 0.25 \cdot CH_3COCH_3 + HO_2 + 0.8 \cdot MEK + NO_2$	$3.780e{-}12 * exp(180./T)$	A=4.200e-12*0.9 ¡- 10% ALKNO3-yield, products ???
$ALKO_2 + NO \longrightarrow ALKNO_3$	$4.200e{-}13 * exp(180./T)$	10% ALKNO3-yield, products ???
$ALKO_2 + HO_2 \longrightarrow ALKOOH$	$7.500e{-}13 * exp(700./T)$	
$ALKO_2 + CH_3O_2 \longrightarrow 0.3 \cdot CH_3CHO + 1.1875 \cdot CH_2O + 0.1875 \cdot CH_3COCH_3 + 0.75 \cdot HO_2 + 0.6 \cdot MEK + 0.25 \cdot ALKOH$	$1.000e-12$	products ???
$ALKO_2 + CH_3CO_3 \longrightarrow 0.4 \cdot CH_3CHO + 0.25 \cdot CH_2O + 0.25 \cdot CH_3COCH_3 + HO_2 + 0.8 \cdot MEK + CH_3O_2 + CO_2$	$1.000e-11$	
$ALKOOH + OH \longrightarrow ALKO_2 + H_2O$	$3.800e{-}12 * exp(200./T)$	
$ALKOH + OH \longrightarrow 1.25 \cdot MEK + HO_2 + H_2O$	$5.000e-12$	Tyndall (p.c.), MEK yield to account for C
$ALKNO_3 + OH \longrightarrow 0.4 \cdot CH_3CHO + 0.25 \cdot CH_2O + 0.25 \cdot CH_3COCH_3 + HO_2 + 0.8 \cdot MEK + NO_2$	$2.000e-12$	
$LISOPACO_2 + HO_2 \longrightarrow LISOPACOOH$	$2.050e-13 * exp(1300./T)$	add OH channel
$LISOPACO_2 + NO \longrightarrow HO_2 + 0.977 \cdot LHC_4ACCHO + NO_2 + 0.0277 \cdot CH_3COCHO + 0.0277 \cdot GLYOXAL + 0.0277 \cdot HYAC + 0.0277 \cdot GLYALD$	$2.235e{-}12 * exp(360./T)$	A=2.54e-12*0.88 ¡- average 12% nitrate yield from Paulot et al. 2009; Tyndall (p.c.); direct GLYOXAL channel from lab meas. 2% over total -¿ 0.02/0.88 = 0.0227
$LISOPACO_2 + NO \longrightarrow LISOPACNO_3$	$3.050e{-}13 * exp(360./T)$	A=2.54e-12*0.12 ¡- average 12% nitrate yield from Paulot et al. 2009;

Table D.1.: JAM3 chemical mechanism (... continued)

$LISOPACO_2 + NO_3 \longrightarrow HO_2 + LHC_4ACCHO + NO_2$	$2.500e-12$		
$LISOPACO_2 + CH_3O_2 \longrightarrow 0.75 \cdot CH_2O + 0.75 \cdot LHC_4ACCHO + 0.25 \cdot CH_3OH + 0.25 \cdot ISOPAOH + HO_2$	$2.400e-12$		products: Tyndall (p.c.)
$LISOPACO_2 + CH_3CO_3 \longrightarrow HO_2 + LHC_4ACCHO + CH_3O_2 + CO_2$	$1.000e-11$		
$LISOPACO_2 \longrightarrow HO_2 + HPALD$	$6.198e+08 \cdot exp(-7700./T)$	*	Bulk isomerization (1,6-H-shift) rate constant for all ISOPO2 by Crounse et al. (2011) and adjusted by Fuchs et al. 2013 given as 1.5*k(ISOPO2 + HO2)*2E21*exp(-9000/temp) =¿ k = 2.05e-13*exp(1300./temp)*2E21*exp(-9000/temp) = 6.198e8*exp(-7700./temp)
$ISOPBO_2 \longrightarrow HO_2 + HPALD$	$6.198e+08 \cdot exp(-7700./T)$	*	see note of [LISOPACO2]
$ISOPDO_2 \longrightarrow HO_2 + HPALD$	$6.198e+08 \cdot exp(-7700./T)$	*	see note of [LISOPACO2]
$ISOPBO_2 \longrightarrow HCHO + MVK + OH$	$3.570e+13 \cdot exp(-10770./T)$	*	1,5-H-shift as in LIM-J by da Silva et al. 2010 and adjusted by Fuchs et al. 2013
$ISOPDO_2 \longrightarrow HCHO + MACR + OH$	$1.905e+13 \cdot exp(-10570./T)$	*	1,5-H-shift as in LIM-J by da Silva et al. 2010 and adjusted by Fuchs et al. 2013
$LISOPACOOH + OH \longrightarrow 0.415 \cdot LIEPOX + 0.415 \cdot OH + 0.415 \cdot LISOPOOHO_2 + 0.14 \cdot LHC_4ACCHO + 0.03 \cdot H_2O + 0.03 \cdot LISOPACO_2$	$1.540e-10$		k from MCMv3.3.1 and OH-addition branching ratios estimated with site-specific SAR by Peeters et al. J. Phys. Chem. A (2007) and H-abstraction channel assumed to be like the one for CH3OOH + OH reaction and abstraction from the alpha-hydroperoxyl allyl hydrogen estimated by SAR of MOM (Taraborrelli in prep.) being 2.12E-11
$ISOPAOH + OH \longrightarrow LISOPOOHO_2$	$9.300e-11$		OH-addition to double bond and products approximated with the one from ISOPOOH + OH reaction leading to similar SOA precursors.
$LISOPACNO_3 + OH \longrightarrow LISOPNO_3O_2$	$6.000e-11$		
$LIEPOX + OH \longrightarrow 0.29 \cdot IEC_1O_2 + 0.71 \cdot LIECHO + 0.71 \cdot HO_2 + H_2O$	$1.500e-11$		MCM3.2

Table D.1.: JAM3 chemical mechanism (... continued)

$LIECHO + OH \longrightarrow H_2O + LIECO_3$	$1.760e-11$	MCM3.2
$LIECHO + NO_3 \longrightarrow HNO_3 + LIECO_3$	$1.050e-11 * exp(-1860./T)$	MCM3.2
$LIECO_3 + HO_2 \longrightarrow 0.6 \cdot LIECO_3H + 0.4 \cdot CO_2 + 0.4 \cdot OH + 0.25 \cdot LHMVKABO_2 + 0.15 \cdot MACRO_2$	$8.207e-13*exp(980./T)$	k scaled to 2.2e-11 as recommeded by Winiberg (A = 5.2e-13 * 1.578) ; cacm products distribution unchanged (Winiberg et al. 2016 and Gro et al. 2014)
$LIECO_3 + NO \longrightarrow 0.6 \cdot LHMVKABO_2 + 0.4 \cdot MACRO_2 + NO_2 + CO_2$	$7.500e-12*exp(290./T)$	MCM3.2
$LIECO_3 + NO_3 \longrightarrow 0.6 \cdot LHMVKABO_2 + 0.4 \cdot MACRO_2 + NO_2 + CO_2$	$4.000e-12$	MCM3.2
$LIECO_3H + OH \longrightarrow H_2O + LIECO_3$	$1.040e-11$	MCM3.2
$IEC_1O_2 + HO_2 \longrightarrow LIECO_3H$	$2.050e-13 * exp(1300./T)$	MCM3.2 plus shortcut
$IEC_1O_2 + NO \longrightarrow BIACETOH + NO_2 + CH_2O + HO_2$	$2.700e-12*exp(360./T)$	MCM3.2
$IEC_1O_2 + NO_3 \longrightarrow BIACETOH + NO_2 + CH_2O + HO_2$	$2.300e-12$	MCM3.2
$ISOPBO_2 + HO_2 \longrightarrow ISOPBOOH$	$2.050e-13 * exp(1300./T)$	
$ISOPBO_2 + NO \longrightarrow CH_2O + MVK + HO_2 + NO_2$	$2.235e-12*exp(360./T)$	A=2.54e-12*0.88 ¡- average 12% nitrate yield from Paulot et al. 2009;
$ISOPBO_2 + NO \longrightarrow ISOPBNO_3$	$3.050e-13*exp(360./T)$	A=2.54e-12*0.12 ¡- average 12% nitrate yield from Paulot et al. 2009;
$ISOPBO_2 + NO_3 \longrightarrow CH_2O + MVK + HO_2 + NO_2$	$2.500e-12$	
$ISOPBO_2 + CH_3O_2 \longrightarrow 0.75 \cdot MVK + 1.75 \cdot CH_2O + 1.5 \cdot HO_2 + 0.25 \cdot ISOPBOH$	$8.000e-13$	products: Tyndall (p.c.)
$ISOPBO_2 + CH_3CO_3 \longrightarrow CH_2O + MVK + HO_2 + CH_3O_2 + CO_2$	$1.000e-11$	
$ISOPBOOH + OH \longrightarrow 0.63 \cdot LIEPOX + 0.63 \cdot OH + 0.12 \cdot LISOPOOHO_2 + 0.15 \cdot H_2O + 0.15 \cdot ISOPBO_2$	$7.500e-11$	St. Clair et al. 2015
$ISOPBOH + OH \longrightarrow LISOPOOHO_2$	$3.850e-11$	OH-addition to double bond and products approximated with the one from ISOPOOH + OH reaction leading to similar SOA precursors.
$ISOPBNO_3 + OH \longrightarrow LISOPNO_3O_2$	$1.360e-11$	products changed 20140617

Table D.1.: JAM3 chemical mechanism (... continued)

$ISOPDO_2 + HO_2 \longrightarrow ISOPDOOH$	$2.050e-13 * exp(1300./T)$	
$ISOPDO_2 + NO \longrightarrow CH_2O + MACR + HO_2 + NO_2$	$2.235e{-}12{*}exp(360./T)$	A=2.54e-12*0.88 ¡- average 12% nitrate yield from Paulot et al. 2009;
$ISOPDO_2 + NO \longrightarrow ISOPDNO_3$	$3.050e{-}13{*}exp(360./T)$	A=2.54e-12*0.12 ¡- average 12% nitrate yield from Paulot et al. 2009;
$ISOPDO_2 + NO_3 \longrightarrow CH_2O + MACR + HO_2 + NO_2$	$2.500e-12$	
$ISOPDO_2 + CH_3O_2 \longrightarrow 0.5 \cdot MACR + 1.25 \cdot CH_2O + HO_2 + 0.25 \cdot CH_3OH + 0.25 \cdot HCOC_5 + 0.25 \cdot ISOPDOH$	$2.900e-12$	products: Tyndall (p.c.)
$ISOPDO_2 + CH_3CO_3 \longrightarrow CH_2O + MACR + HO_2 + CH_3O_2 + CO_2$	$1.000e-11$	
$LISOPACO_2 + LISOPACO_2 \longrightarrow 1.5 \cdot LHC_4ACCHO + HO_2 + 0.5 \cdot ISOPAOH$	$3.350e-12$	k: avg. for primary isoprene RO2 MCM (Saunders et al.2003, Tab. 3); products: based on the HOCH2CH2O2 self-reaction (Orlando&Tyndall2012, Tab.8)
$ISOPBO_2 + ISOPBO_2 \longrightarrow 2 \cdot MVK + 2 \cdot CH_2O + 2 \cdot HO_2$	$6.900e-14$	k: for tertiary isoprene RO2 MCM (Saunders et al.2003, Tab. 3)
$ISOPDO_2 + ISOPDO_2 \longrightarrow 1.12 \cdot MACR + 1.12 \cdot CH_2O + 1.12 \cdot HO_2 + 0.44 \cdot HCOC_5 + 0.44 \cdot ISOPDOH$	$4.800e-12$	k: for secondary isoprene RO2 MCM (Saunders et al.2003, Tab. 3); products: based on the i-C3H7O2 self-reaction (Orlando&Tyndall2012, Tab.8)
$LISOPACO_2 + ISOPBO_2 \longrightarrow LHC_4ACCHO + 0.75 \cdot MVK + 0.75 \cdot CH_2O + 1.5 \cdot HO_2 + 0.25 \cdot ISOPBOH$	$4.808e-13$	k: $(3.35e\text{-}12{*}6.9e\text{-}14)^{0.5}$ geometric average of self-reaction ks (arbitrary estimate by Madronich and Calvert 1990)
$LISOPACO_2 + ISOPDO_2 \longrightarrow 0.75 \cdot LHC_4ACCHO + 0.5 \cdot MACR + 0.5 \cdot CH_2O + HO_2 + 0.25 \cdot ISOPAOH + 0.25 \cdot HCOC_5 + 0.25 \cdot ISOPDOH$	$4.010e-12$	k: $(3.35e\text{-}12{*}4.8e\text{-}12)^{0.5}$ geometric average of self-reaction ks (arbitrary estimate by Madronich and Calvert 1990)
$ISOPBO_2 + ISOPDO_2 \longrightarrow 0.75 \cdot MVK + 0.75 \cdot MACR + 1.5 \cdot CH_2O + 1.5 \cdot HO_2 + 0.25 \cdot ISOPBOH + 0.25 \cdot HCOC_5$	$5.755e-13$	k: $(6.9e\text{-}14{*}4.8e\text{-}12)^{0.5}$ geometric average of self-reaction ks (arbitrary estimate by Madronich and Calvert 1990)
$ISOPDOOH + OH \longrightarrow 0.79 \cdot LIEPOX + 0.79 \cdot OH + 0.14 \cdot LISOPOOHO_2 + 0.07 \cdot H_2O + 0.07 \cdot ISOPDO_2$	$1.180e-10$	St. Clair et al. (2015)

Table D.1.: JAM3 chemical mechanism (... continued)

$ISOPDOH + OH \longrightarrow LISOPOOHO_2$	$7.380e-11$	OH-addition to double bond and products approximated with the one from ISOPOOH + OH reaction leading to similar SOA precursors.
$ISOPDNO_3 + OH \longrightarrow LISOPNO_3O_2$	$6.100e-11$	OH-addition to double bond
$NISOPO_2 + HO_2 \longrightarrow NISOPOOH$	$2.050e-13 * exp(1300./T)$	
$NISOPO_2 + NO \longrightarrow HO_2 + NC_4CHO + NO_2$	$2.540e{-}12 * exp(360./T)$	
$NISOPO_2 + NO_3 \longrightarrow HO_2 + NC_4CHO + NO_2$	$2.500e-12$	
$NISOPO_2 + CH_3O_2 \longrightarrow 0.75 \cdot CH_2O + 0.75 \cdot NC_4CHO + HO_2 + 0.25 \cdot CH_3OH + 0.25 \cdot LISOPACNO_3$	$1.300e-12$	products: Tyndall (p.c.)
$NISOPO_2 + CH_3CO_3 \longrightarrow HO_2 + NC_4CHO + CH_3O_2 + CO_2$	$1.000e-11$	
$NISOPOOH + OH \longrightarrow NC_4CHO + OH + H_2O$	$1.030e-10$	
$NC_4CHO + OH \longrightarrow H_2O + LNISO_3$	$4.160e-11$	
$NC_4CHO + O_3 \longrightarrow 0.445 \cdot NO_2 + 0.89 \cdot CO + 0.075625 \cdot H_2O_2 + 0.034375 \cdot HCOCO_2H + 0.555 \cdot NOA + 0.445 \cdot HO_2 + 0.520625 \cdot GLYOXAL + 0.89 \cdot OH + 0.445 \cdot CH_3COCHO$	$2.400e-17$	
$NC_4CHO + NO_3 \longrightarrow HNO_3 + LNISO_3$	$6.120e-12 * exp(-1862./T)$	
$LNISO_3 + HO_2 \longrightarrow 0.8 \cdot LNISOOH + 0.2 \cdot NOA + 0.2 \cdot OH + 0.2 \cdot CO_2 + 0.2 \cdot CO + 0.2 \cdot HO_2$	$1.930e-13 * exp(1300./T)$	products: Tyndall (p.c.)
$LNISO_3 + NO \longrightarrow NOA + 0.5 \cdot GLYOXAL + 0.5 \cdot CO + HO_2 + NO_2 + 0.5 \cdot CO_2$	$4.270e{-}12 * exp(360./T)$	
$LNISO_3 + NO_3 \longrightarrow NOA + 0.5 \cdot GLYOXAL + 0.5 \cdot CO + HO_2 + NO_2 + 0.5 \cdot CO_2$	$3.302e{-}12 * exp(360./T)$	
$LNISO_3 + CH_3O_2 \longrightarrow 0.375 \cdot GLYOXAL + 0.875 \cdot NOA + CH_2O + 1.75 \cdot HO_2 + 0.625 \cdot CO_2 + 0.0625 \cdot MACRN + 0.0625 \cdot MVKN + 0.5 \cdot CO$	$1.000e-12$	products: Tyndall (p.c.); previous RONO2 split into 50% MACRN + 50% MVKN
$LNISO_3 + CH_3CO_3 \longrightarrow NOA + 0.5 \cdot GLYOXAL + 0.5 \cdot CO + HO_2 + CH_3O_2 + 1.5 \cdot CO_2$	$1.000e-11$	
$LNISOOH + OH \longrightarrow H_2O + LNISO_3$	$2.650e-11$	
$LHC_4ACCHO + OH \longrightarrow 0.52 \cdot LC_{578}O_2 + 0.48 \cdot LHC_4ACCO_3 + H_2O$	$4.520e-11$	

Table D.1.: JAM3 chemical mechanism (... continued)

$LHC_4ACCHO + O_3 \longrightarrow 0.2225 \cdot CH_3CO + 0.89 \cdot CO + 0.017188 \cdot HOCH_2CO_2H + 0.075625 \cdot H_2O_2 + 0.017188 \cdot HCOCO_2H + 0.2775 \cdot HYAC + 0.6675 \cdot HO_2 + 0.260313 \cdot GLYOXAL + 0.2225 \cdot CH_2O + 0.89 \cdot OH + 0.260313 \cdot GLYALD + 0.5 \cdot CH_3COCHO$	$2.400e-17$	
$LHC_4ACCHO + NO_3 \longrightarrow HNO_3 + LHC_4ACCO_3$	$6.120e-12 * exp(-1862./T)$	
$LC_{578}O_2 + NO \longrightarrow 0.25 \cdot CH_3COCHO + 0.25 \cdot GLYALD + 0.25 \cdot GLYOXAL + 0.25 \cdot HYAC + 0.25 \cdot CO + 0.25 \cdot MACROH + 0.25 \cdot CH_2O + 0.25 \cdot CO_2H_3CHO + HO_2 + NO_2$	$2.540e{-}12{*}exp(360./T)$	products: Tyndall (p.c.)
$LC_{578}O_2 + NO_3 \longrightarrow 0.25 \cdot CH_3COCHO + 0.25 \cdot GLYALD + 0.25 \cdot GLYOXAL + 0.25 \cdot HYAC + 0.25 \cdot CO + 0.25 \cdot MACROH + 0.25 \cdot CH_2O + 0.25 \cdot CO_2H_3CHO + HO_2 + NO_2$	$2.500e-12$	products: Tyndall (p.c.)
$LC_{578}O_2 + HO_2 \longrightarrow LC_{578}OOH$	$2.050e-13 * exp(1300./T)$	add OH channel
$LC_{578}O_2 + CH_3O_2 \longrightarrow 0.156250 \cdot CH_3COCHO + 0.156250 \cdot GLYALD + 0.156250 \cdot GLYOXAL + 0.156250 \cdot HYAC + 0.156250 \cdot CO + 0.468750 \cdot MACROH + 1.031250 \cdot CH_2O + 0.3125 \cdot CO_2H_3CHO + 1.25 \cdot HO_2 + 0.125 \cdot CH_3OH$	$1.000e-12$	products: Tyndall (p.c.)
$LC_{578}O_2 + CH_3CO_3 \longrightarrow 0.25 \cdot CH_3COCHO + 0.25 \cdot GLYALD + 0.25 \cdot GLYOXAL + 0.25 \cdot HYAC + 0.25 \cdot CO + 0.25 \cdot MACROH + 0.25 \cdot CH_2O + 0.25 \cdot CO_2H_3CHO + CH_3O_2 + CO_2$	$1.000e-11$	
$LC_{578}O_2 \longrightarrow BIACETOH + CO + OH$	$1.450e+07 * exp(-5297./T)$	Isomerisation according to Crounse et al., 2012 but k/2 because only C57O2 undergoes 1,4-H-shift; the main product should be HO12CO3C4 here approximated with BIACETOH + HO2 assuming a reaction with OH.
$LC_{578}OOH + OH \longrightarrow H_2O + LC_{578}O_2$	$3.160e-11$	
$LHC_4ACCO_3 \longrightarrow HO_2 + PACALD$	$1.230e+09 * exp(-6186./T)$	1,6-H-shift (not bulk!) rate constant for the Z41 isomer as in SI Taraborrelli et al., Nat. Geosc. 2012

Table D.1.: JAM3 chemical mechanism (... continued)

$LHC_4ACCO_3 + CH_3O_2 \longrightarrow CH_2O + 0.1 \cdot LHC_4ACCO_2H + 0.45 \cdot GLYALD + 0.45 \cdot HYAC + 0.45 \cdot CH_3CO + 0.45 \cdot CO + 0.45 \cdot HO_2 + 0.9 \cdot CO_2$	$1.000e-11$	products: Tyndall (p.c.)
$LHC_4ACCO_3 + CH_3CO_3 \longrightarrow 0.5 \cdot HYAC + 0.5 \cdot GLYALD + 0.5 \cdot CH_3CO + 0.5 \cdot CO + 0.5 \cdot HO_2 + CH_3O_2 + 2 \cdot CO_2$	$1.000e-11$	
$LHC_4ACCO_3 + HO_2 \longrightarrow 0.37 \cdot LHC_4ACCO_3H + 0.12 \cdot LHC_4ACCO_2H + 0.12 \cdot O_3 + 0.51 \cdot CO_2 + 0.51 \cdot OH + 0.255 \cdot HYAC + 0.255 \cdot GLYALD + 0.255 \cdot CH_3CO + 0.255 \cdot CO + 0.255 \cdot HO_2$	$8.207e-13*exp(980./T)$	k scaled to 2.2e-11 as recommeded by Winiberg (A = 5.2e-13 * 1.578) ; product distribution in analogy to CH3CO3 + HO2 reactions (Winiberg et al. 2016 and Gro et al. 2014)
$LHC_4ACCO_3 + NO \longrightarrow 0.5 \cdot HYAC + 0.5 \cdot GLYALD + 0.5 \cdot CH_3CO + 0.5 \cdot CO + 0.5 \cdot HO_2 + NO_2 + CO_2$	$8.100e-12*exp(270./T)$	
$LHC_4ACCO_3 + NO_3 \longrightarrow 0.5 \cdot HYAC + 0.5 \cdot GLYALD + 0.5 \cdot CH_3CO + 0.5 \cdot CO + 0.5 \cdot HO_2 + NO_2 + CO_2$	$4.000e-12$	
$LHC_4ACCO_3 + NO_2 + M \longrightarrow LC_5PAN_{1719} + M$	$ktroe(2.700e-28, 7.1, 1.200e-11, 0.9, 0.3)$	
$LHC_4ACCO_2H + OH \longrightarrow 0.5 \cdot HYAC + 0.5 \cdot GLYALD + 0.5 \cdot CH_3CO + 0.5 \cdot CO + 0.5 \cdot HO_2 + CO_2 + H_2O$	$2.520e-11$	
$LHC_4ACCO_3H + OH \longrightarrow H_2O + LHC_4ACCO_3$	$2.880e-11$	
$LC_5PAN_{1719} + M \longrightarrow LHC_4ACCO_3 + NO_2 + M$	$kLC5PAN1719$	user defined; must add to usrrxt: k0=4.9e-3*exp(-12100./T)*M, kinf=5.4e16*exp(-13830./T), fc=0.3
$LC_5PAN_{1719} + OH \longrightarrow CO + MACROH + NO_2$	$2.520e-11$	
$HCOC_5 + OH \longrightarrow C_{59}O_2$	$3.810e-11$	
$C_{59}O_2 + CH_3O_2 \longrightarrow 0.75 \cdot HOCH_2CO + 0.75 \cdot HYAC + CH_2O + 0.75 \cdot HO_2 + 0.3125 \cdot MACROH$	$1.000e-12$	Tyndall (p.c.)
$C_{59}O_2 + CH_3CO_3 \longrightarrow HOCH_2CO + HYAC + CH_3O_2 + CO_2$	$1.000e-11$	
$C_{59}O_2 + NO \longrightarrow HOCH_2CO + HYAC + NO_2$	$2.540e-12*exp(360./T)$	
$C_{59}O_2 + NO_3 \longrightarrow HOCH_2CO + HYAC + NO_2$	$2.500e-12$	
$C_{59}O_2 + HO_2 \longrightarrow C_{59}OOH$	$2.050e-13*exp(1300./T)$	

Table D.1.: JAM3 chemical mechanism (... continued)

$C_{59}OOH + OH \longrightarrow C_{59}O_2 + H_2O$	$9.700e-12$	
$MBOO_2 + NO \longrightarrow HO_2 + 0.67 \cdot CH_3COCH_3 + 0.67 \cdot GLYALD + 0.33 \cdot CH_2O + 0.33 \cdot IBUTALOH + NO_2$	$2.600e{-}12 * exp(365./T)$	
$MBOO_2 + CH_3O_2 \longrightarrow 0.9165 \cdot CH_2O + 0.625 \cdot MACROH + 0.25 \cdot CH_3OH + HO_2 + 0.3335 \cdot CH_3COCH_3 + 0.3335 \cdot GLYALD + 0.1665 \cdot IBUTALOH$	$3.750e-13 * exp(-40./T)$	
$MBOO_2 + CH_3CO_3 \longrightarrow 0.67 \cdot CH_3COCH_3 + 0.67 \cdot GLYALD + 0.33 \cdot CH_2O + 0.33 \cdot IBUTALOH + HO_2 + CH_3O_2 + CO_2$	$1.000e-11$	
$MBOO_2 + HO_2 \longrightarrow MBOOOH$	$7.500e{-}13 * exp(700./T)$	
$MBOOOH + OH \longrightarrow 0.5 \cdot MBOO_2 + 0.625 \cdot MACROH + 0.5 \cdot OH + H_2O$	$3.800e{-}12 * exp(200./T)$	other products are very sticky
$IBUTALOH + OH \longrightarrow H_2O + IBUTALOHO_2$	$1.400e-11$	
$IBUTALOHO_2 + NO \longrightarrow CO_2 + NO_2 + HO_2 + CH_3COCH_3$	$2.600e{-}12 * exp(365./T)$	
$IBUTALOHO_2 + HO_2 \longrightarrow 0.6 \cdot IBUTALOHOOH + 0.4 \cdot HO_2 + 0.4 \cdot OH + 0.4 \cdot CH_3COCH_3 + 0.4 \cdot CO_2$	$4.300e-13 * exp(1040./T)$	
$IBUTALOHO_2 + CH_3O_2 \longrightarrow CH_3COCH_3 + 2 \cdot HO_2 + CO_2 + CH_2O$	$1.000e-12$	products: Tyndall (p.c.)
$IBUTALOHO_2 + CH_3CO_3 \longrightarrow CH_3COCH_3 + HO_2 + CH_3O_2 + 2 \cdot CO_2$	$1.000e-11$	
$IBUTALOHOOH + OH \longrightarrow H_2O + IBUTALOHO_2$	$1.000e-12$	Tyndall (p.c.)
$MBONO_3O_2 + HO_2 \longrightarrow$	$4.300e-13 * exp(1040./T)$	products extremely sticky
$MBONO_3O_2 + NO \longrightarrow 0.25 \cdot CH_2O + 0.25 \cdot IBUTALOH + 1.25 \cdot NO_2 + 0.500250 \cdot NOA + 0.75 \cdot CH_3COCH_3 + 0.75 \cdot HO_2$	$2.600e{-}12 * exp(365./T)$	
$MBONO_3O_2 + NO_3 \longrightarrow 0.25 \cdot CH_2O + 0.25 \cdot IBUTALOH + 1.25 \cdot NO_2 + 0.500250 \cdot NOA + 0.75 \cdot CH_3COCH_3 + 0.75 \cdot HO_2$	$2.400e-12$	
$MBONO_3O_2 + CH_3O_2 \longrightarrow 0.875 \cdot CH_2O + 0.125 \cdot IBUTALOH + 0.125 \cdot NO_2 + 0.250125 \cdot NOA + 0.375 \cdot CH_3COCH_3 + 0.875 \cdot HO_2 + 0.25 \cdot CH_3OH + 0.625 \cdot MACROH$	$1.000e-12$	Tyndall (p.c.), molecular products extremely sticky(?)
$MBONO_3O_2 + CH_3CO_3 \longrightarrow 0.25 \cdot CH_2O + 0.25 \cdot IBUTALOH + 0.25 \cdot NO_2 + 0.500250 \cdot NOA + 0.75 \cdot CH_3COCH_3 + 0.75 \cdot HO_2 + CH_3O_2 + CO_2$	$1.000e-11$	
$DICARBO_2 + HO_2 \longrightarrow 0.4 \cdot OH + 0.068 \cdot CH_3COCHO + 0.068 \cdot HO_2 + 0.068 \cdot CO + 0.4 \cdot CO_2 + 0.332 \cdot CH_3CO + 0.332 \cdot GLYOXAL$	$4.300e-13 * exp(1040./T)$	60% sticky products

Table D.1.: JAM3 chemical mechanism (... continued)

$DICARBO_2 + NO \longrightarrow 0.17 \cdot CH_3COCHO + 0.17 \cdot HO_2 + 0.17 \cdot CO + CO_2 + 0.83 \cdot CH_3CO + 0.83 \cdot GLYOXAL + NO_2$	$7.500e{-}12{*}exp(290./T)$	
$DICARBO_2 + NO_2 + M \longrightarrow M$	$ktroe(2.700e - 28, 7.1, 1.200e - 11, 0.9, 0.6)$	Orlando&Tyndall (2012), Same as k(CH3CO3 + NO2), sticky nitrate
$DICARBO_2 + CH_3O_2 \longrightarrow 0.17 \cdot CH_3COCHO + 1.17 \cdot HO_2 + 0.17 \cdot CO + CO_2 + 0.83 \cdot CH_3CO + 0.83 \cdot GLYOXAL + CH_2O$	$1.000e - 12$	
$DICARBO_2 + CH_3CO_3 \longrightarrow 0.17 \cdot CH_3COCHO + 0.17 \cdot HO_2 + 0.17 \cdot CO + 2 \cdot CO_2 + 0.83 \cdot CH_3CO + 0.83 \cdot GLYOXAL + CH_3O_2$	$1.000e - 11$	
$HPALD + OH \longrightarrow 0.641 \cdot OH + 0.385 \cdot PACALD + 0.256 \cdot BIGALD_3 + 0.359 \cdot CH_3COCHO + 0.359 \cdot GLYOX + 0.359 \cdot HO_2$	$5.200e - 11$	simplification of chemistry in MCMv3.3.1
$PACALD + OH \longrightarrow CH_3COCHO + HCOCO_3H + HO_2$	$4.720e - 11$	k and products for C5PACALD2 from MCMv3.3.1 assuming an implict RO2-¿RO conversion
$LISOPOOHO_2 + HO_2 \longrightarrow LISOPOOHOOH$	$2.050e - 13 * exp(1300./T)$	
$LISOPOOHO_2 + NO \longrightarrow CH_2O + HO_2 + 0.5 \cdot MACROOH + 0.5 \cdot LHMVKABOOH + NO_2$	$2.540e{-}12{*}exp(360./T)$	A=2.54e-12*0.12 ¡- average 12% nitrate yield from Paulot et al. 2009; nitrate yield left for the moment equal to the one of the simple ISOPO2 (it should be higher)
$LISOPOOHO_2 + NO \longrightarrow LISOPNO_3OOH$	$3.050e{-}13{*}exp(360./T)$	A=2.54e-12*0.12 ¡- average 12% nitrate yield from Paulot et al. 2009; nitrate yield left for the moment equal to the one of the simple ISOPO2 (it should be higher)
$LISOPOOHO_2 + NO_3 \longrightarrow CH_2O + HO_2 + 0.5 \cdot MACROOH + 0.5 \cdot LHMVKABOOH + NO_2$	$2.500e - 12$	
$LISOPOOHO_2 + CH_3O_2 \longrightarrow 1.5 \cdot CH_2O + 0.75 \cdot HO_2 + 0.375 \cdot MACROOH + 0.375 \cdot LHMVKABOOH + 0.25 \cdot LISOPOOHOOH$	$8.000e - 13$	
$LISOPOOHO_2 + CH_3CO_3 \longrightarrow CH_2O + HO_2 + 0.5 \cdot MACROOH + 0.5 \cdot LHMVKABOOH + CH_3O_2 + CO_2$	$1.000e - 11$	

Table D.1.: JAM3 chemical mechanism (... continued)

$LISOPNO_3O_2 + HO_2 \longrightarrow LISOPNO_3OOH$	$2.050e - 13 * exp(1300./T)$	
$LISOPNO_3O_2 + NO \longrightarrow CH_2O + 0.5 \cdot MACRN + 0.5 \cdot MVKN + HO_2 + NO_2$	$2.235e{-}12 * exp(360./T)$	A=2.54e-12*0.88 ¡- average 12% nitrate yield from Paulot et al. 2009; nitrate yield left for the moment equal to the one of the simple ISOPO2 (it should be higher); previous RONO2 split into 50% MACRN + 50% MVKN
$LISOPNO_3O_2 + NO \longrightarrow LISOPNO_3NO_3$	$3.050e{-}13 * exp(360./T)$	A=2.54e-12*0.12 ¡- average 12% nitrate yield from Paulot et al. 2009; nitrate yield left for the moment equal to the one of the simple ISOPO2 (it should be higher)
$LISOPNO_3O_2 + NO_3 \longrightarrow CH_2O + 0.5 \cdot MACRN + 0.5 \cdot MVKN + HO_2 + NO_2$	$2.500e - 12$	previous RONO2 split into 50% MACRN + 50% MVKN
$LISOPNO_3O_2 + CH_3O_2 \longrightarrow 0.3525 \cdot MACRN + 0.3525 \cdot MVKN + 1.75 \cdot CH_2O + 1.5 \cdot HO_2 + 0.25 \cdot LISOPNO_3OOH$	$8.000e - 13$	previous RONO2 split into 50% MACRN + 50% MVKN
$LISOPNO_3O_2 + CH_3CO_3 \longrightarrow CH_2O + 0.5 \cdot MACRN + 0.5 \cdot MVKN + HO_2 + CH_3O_2 + CO_2$	$1.000e - 11$	previous RONO2 split into 50% MACRN + 50% MVKN
$LISOPOOHOOH + OH \longrightarrow H_2O + LISOPOOHO_2$	$7.600e{-}12 * exp(200./T)$	twice the k (CH3OOH + OH -¿ CH3O2)
$LISOPOOHOOH + OH \longrightarrow LC_{578}OOH + OH$	$2.104e - 11$	k for H-abstractions from SAR in MOM by a secondary carbon bearing a -OH group and a secondary and a tertiary carbon atoms bearing an -OOH group: 8.42E-13*3.44+(8.42E-13+1.75E-12)*7
$LISOPNO_3OOH + OH \longrightarrow H_2O + LISOPNO_3O_2$	$3.800e{-}12 * exp(200./T)$	
$LISOPNO_3OOH + OH \longrightarrow C_{59}OOH + OH$	$1.515e - 11$	k for H-abstractions from SAR in MOM by a secondary carbon bearing a -OH group and a tertiary carbon atom bearing an -OOH group: 8.42E-13*3.44+1.75E-12*7

Table D.1.: JAM3 chemical mechanism (... continued)

$LISOPNO_3NO_3 + OH \longrightarrow 0.5 \cdot MACRN + 0.5 \cdot MVKN + NO_2 + CH_2O + HO_2$	$8.916e-12$	k for H-abstractions from SAR in MOM by a secondary and a tertiary carbon bearing a -OH group: (8.42E-13+1.75E-12)*3.44 ; previous RONO2 split into 50% MACRN + 50% MVKN
C6 oxidation		
reaction	rate coefficient	reference
$BENZ + OH \longrightarrow 0.53 \cdot PHENOL + 0.12 \cdot BEPOMUC + 0.65 \cdot HO_2 + 0.35 \cdot BENZO_2$	$2.300e-12 * exp(-193./T)$	
$PHENOL + OH \longrightarrow 0.14 \cdot PHENO_2 + 0.8 \cdot HO_2 + 0.8 \cdot CATECHOL + 0.06 \cdot C_6H_5O$	$4.700e-13 * exp(1220./T)$	
$PHENOL + NO_3 \longrightarrow 0.26 \cdot PHENO_2 + 0.74 \cdot C_6H_5O + 0.74 \cdot HNO_3$	$3.800e-12$	NPHENO2 approximated with PHENO2
$PHENO_2 + NO \longrightarrow HO_2 + 0.7 \cdot GLYOXAL + NO_2$	$2.600e-12 * exp(365./T)$	
$PHENO_2 + HO_2 \longrightarrow PHENOOH$	$7.500e-13 * exp(700./T)$	
$PHENO_2 + CH_3O_2 \longrightarrow 2 \cdot HO_2 + 0.7 \cdot GLYOXAL + CH_2O$	$1.000e-12$	
$PHENO_2 + CH_3CO_3 \longrightarrow HO_2 + 0.7 \cdot GLYOXAL + CH_3O_2 + CO_2$	$1.000e-11$	
$PHENOOH + OH \longrightarrow H_2O + PHENO_2$	$3.800e-12 * exp(200./T)$	
$C_6H_5O + NO_2 \longrightarrow$	$2.100e-12$	yields sticky nitrate
$C_6H_5O + O_3 \longrightarrow C_6H_5O_2$	$2.800e-13$	
$C_6H_5O_2 + NO \longrightarrow C_6H_5O + NO_2$	$2.600e-12 * exp(365./T)$	
$C_6H_5O_2 + NO_3 \longrightarrow C_6H_5O + NO_2$	$2.300e-12$	MCM3.2
$C_6H_5O_2 + HO_2 \longrightarrow C_6H_5OOH$	$7.500e-13 * exp(700./T)$	
$C_6H_5O_2 + CH_3O_2 \longrightarrow C_6H_5O + CH_2O + HO_2$	$1.000e-12$	
$C_6H_5O_2 + CH_3CO_3 \longrightarrow C_6H_5O + CH_3O_2 + CO_2$	$1.000e-11$	
$C_6H_5OOH + OH \longrightarrow C_6H_5O_2$	$3.800e-12 * exp(200./T)$	
$BENZO_2 + NO \longrightarrow GLYOXAL + NO_2 + 0.5 \cdot BIGALD_1 + HO_2$	$2.600e-12 * exp(365./T)$	according to MCM, 8% sticky nitrate yield and 0.5*BZFUONE
$BENZO_2 + HO_2 \longrightarrow BENZOOH$	$7.500e-13 * exp(700./T)$	
$BENZO_2 + CH_3O_2 \longrightarrow GLYOXAL + 0.5 \cdot BIGALD_1 + 2 \cdot HO_2 + CH_2O$	$1.000e-12$	
$BENZO_2 + CH_3CO_3 \longrightarrow GLYOXAL + 0.5 \cdot BIGALD_1 + HO_2 + CH_3O_2 + CO_2$	$1.000e-11$	
$BENZOOH + OH \longrightarrow BENZO_2$	$3.800e-12 * exp(200./T)$	

Table D.1.: JAM3 chemical mechanism (... continued)

$CATECHOL + OH \longrightarrow CATEC_1O$	$1.000e-10$	
$CATECHOL + NO_3 \longrightarrow CATEC_1O + HNO_3$	$9.900e-11$	
$CATEC_1O + NO_2 \longrightarrow$	$2.100e-12$	yields sticky nitrate
$CATEC_1O + O_3 \longrightarrow CATEC_1O_2$	$2.800e-13$	
$CATEC_1O_2 + HO_2 \longrightarrow CATEC_1OOH$	$7.500e{-}13{*}exp(700./T)$	
$CATEC_1O_2 + NO \longrightarrow CATEC_1O + NO_2$	$2.600e{-}12{*}exp(365./T)$	
$CATEC_1O_2 + NO_3 \longrightarrow CATEC_1O + NO_2$	$2.300e-12$	MCM3.2
$CATEC_1O_2 + CH_3O_2 \longrightarrow CATEC_1O + CH_2O + HO_2$	$1.000e-12$	
$CATEC_1O_2 + CH_3CO_3 \longrightarrow CATEC_1OCH_3O_2 + CO_2$	$1.000e-11$	
$CATEC_1OOH + OH \longrightarrow CATEC_1O_2$	$1.900e{-}12{*}exp(190./T)$	
C7 oxidation		
reaction	rate coefficient	reference
$TOL + OH \longrightarrow 0.18 \cdot CRESOL + 0.1 \cdot TEPOMUC + 0.07 \cdot BZOO + 0.65 \cdot TOLO_2 + 0.28 \cdot HO_2$	$1.700e{-}12{*}exp(352./T)$	
$CRESOL + OH \longrightarrow 0.2 \cdot PHENO_2 + 0.73 \cdot HO_2 + 0.73 \cdot CATECHOL + 0.07 \cdot C_6H_5O$	$4.700e-11$	CATECHOL and PHENO2 omits one CH3 group of MCATECHOL and CRESO2
$CRESOL + NO_3 \longrightarrow 0.61 \cdot PHENO_2 + 0.39 \cdot C_6H_5O + 0.49 \cdot HNO_3$	$1.400e-11$	CRESO2 and NCRESO2 approximated with PHENO2; TOL1O with C6H5O (see MCM for details)
$TOLO_2 + HO_2 \longrightarrow TOLOOH$	$7.500e{-}13{*}exp(700./T)$	
$TOLO_2 + NO \longrightarrow NO_2 + 0.6 \cdot GLYOXAL + 0.4 \cdot CH_3COCHO + HO_2 + 0.2 \cdot BIGALD_1 + 0.2 \cdot BIGALD_2 + 0.2 \cdot BIGALD_3$	$2.600e{-}12{*}exp(365./T)$	
$TOLO_2 + CH_3O_2 \longrightarrow 0.6 \cdot GLYOXAL + 0.4 \cdot CH_3COCHO + 2 \cdot HO_2 + CH_2O$	$1.000e-12$	
$TOLO_2 + CH_3CO_3 \longrightarrow 0.6 \cdot GLYOXAL + 0.4 \cdot CH_3COCHO + HO_2 + CH_3O_2 + CO_2 + 0.2 \cdot BIGALD_1 + 0.2 \cdot BIGALD_2 + 0.2 \cdot BIGALD_3$	$1.000e-11$	
$TOLOOH + OH \longrightarrow TOLO_2$	$3.800e{-}12{*}exp(200./T)$	
$BZOO + HO_2 \longrightarrow BZOOH$	$7.500e{-}13{*}exp(700./T)$	
$BZOO + NO \longrightarrow BZALD + NO_2 + HO_2$	$2.600e{-}12{*}exp(365./T)$	MCM forms 10% nitrate
$BZOO + CH_3O_2 \longrightarrow BZALD + 2 \cdot HO_2 + CH_2O$	$1.000e-12$	
$BZOO + CH_3CO_3 \longrightarrow BZALD + HO_2 + CH_3O_2 + CO_2$	$1.000e-11$	

Table D.1.: JAM3 chemical mechanism (... continued)

$BZOOH + OH \longrightarrow BZOO$	$3.800e{-}12{*}exp(200./T)$	
$BZALD + OH \longrightarrow ACBZO_2$	$5.900e{-}12{*}exp(225./T)$	
$ACBZO_2 + NO_2 + M \longrightarrow M + PBZNIT$	$ktroe(2.700e-28, 7.1, 1.200e-11, 0.9, 0.6)$	Orlando & Tyndall (2012) - Same as k(CH3CO3 + NO2)
$PBZNIT + M \longrightarrow ACBZO_2 + NO_2 + M$	$kPBZNIT$	user defined; usrrxt: CH3CO3_NO2 * exp(-14000/T) / 9.0e-29 JPL (2011)
$ACBZO_2 + NO \longrightarrow C_6H_5O_2 + NO_2$	$7.500e{-}12{*}exp(290./T)$	
$ACBZO_2 + HO_2 \longrightarrow 0.51 \cdot C_6H_5O_2 + 0.51 \cdot OH + 0.51 \cdot CO_2$	$8.207e{-}13{*}exp(980./T)$	k scaled to 2.2e-11 as recommeded by Winiberg (A = 5.2e-13 * 1.578) ; product distribution in analogy to CH3CO3 + HO2 reactions; two channels neglected (Winiberg et al. 2016 and Gro et al. 2014)
$ACBZO_2 + CH_3O_2 \longrightarrow C_6H_5O_2 + CH_2O + HO_2$	$1.000e-12$	
$ACBZO_2 + CH_3CO_3 \longrightarrow C_6H_5O_2 + CH_3O_2 + CO_2$	$1.000e-11$	
C8 oxidation		
reaction	rate coefficient	reference
$XYL + OH \longrightarrow 0.15 \cdot XYLOL + 0.23 \cdot TEPOMUC + 0.06 \cdot BZOO + 0.56 \cdot XYLENO_2 + 0.38 \cdot HO_2$	$1.700e-11$	
$XYLOL + OH \longrightarrow 0.3 \cdot XYLOLO_2 + 0.63 \cdot HO_2 + 0.63 \cdot CATECHOL + 0.07 \cdot C_6H_5O$	$8.400e-11$	CATECHOL omits two CH3 groups of O-, M- and P-XYCATECH
$XYLOL + NO_3 \longrightarrow 0.61 \cdot PHENO_2 + 0.39 \cdot C_6H_5O + 0.49 \cdot HNO_3$	$3.200e-11$	XYLOLO2 and NXYLOLO2 approximated with PHENO2; XY1O with C6H5O (see MCM for details)
$XYLOLO_2 + NO \longrightarrow HO_2 + NO_2 + 0.17 \cdot GLYOXAL + 0.51 \cdot CH_3COCHO$	$2.600e{-}12{*}exp(365./T)$	
$XYLOLO_2 + HO_2 \longrightarrow XYLOLOOH$	$7.500e{-}13{*}exp(700./T)$	
$XYLOLO_2 + CH_3O_2 \longrightarrow 0.17 \cdot GLYOXAL + 0.51 \cdot CH_3COCHO + 2 \cdot HO_2 + CH_2O$	$1.000e-12$	
$XYLOLO_2 + CH_3CO_3 \longrightarrow HO_2 + 0.17 \cdot GLYOXAL + 0.51 \cdot CH_3COCHO + CH_3O_2 + CO_2$	$1.000e-11$	

Table D.1.: JAM3 chemical mechanism (... continued)

$XYLOLOOH + OH \longrightarrow XYLOLO_2$	$3.800e{-}12{*}exp(200./T)$	
$XYLENO_2 + HO_2 \longrightarrow XYLENOOH$	$7.500e{-}13{*}exp(700./T)$	
$XYLENO_2 + NO \longrightarrow HO_2 + NO_2 + 0.34 \cdot GLYOXAL + 0.54 \cdot CH_3COCHO + 0.06 \cdot BIGALD_1 + 0.2 \cdot BIGALD_2 + 0.15 \cdot BIGALD_3 + 0.21 \cdot BIGALD_4$	$2.600e{-}12{*}exp(365./T)$	
$XYLENO_2 + CH_3O_2 \longrightarrow 0.34 \cdot GLYOXAL + 0.54 \cdot CH_3COCHO + 2 \cdot HO_2 + CH_2O + 0.06 \cdot BIGALD_1 + 0.2 \cdot BIGALD_2 + 0.15 \cdot BIGALD_3 + 0.21 \cdot BIGALD_4$	$1.000e-12$	cacm: added BIGALDs 20140617
$XYLENO_2 + CH_3CO_3 \longrightarrow HO_2 + 0.34 \cdot GLYOXAL + 0.54 \cdot CH_3COCHO + 0.06 \cdot BIGALD_1 + 0.2 \cdot BIGALD_2 + 0.15 \cdot BIGALD_3 + 0.21 \cdot BIGALD_4 + CH_3O_2 + CO_2$	$1.000e-11$	
$XYLENOOH + OH \longrightarrow XYLENO_2$	$3.800e{-}12{*}exp(200./T)$	
C10/C15 oxidation (terpenes, sesqui-terpenes)		
reaction	rate coefficient	reference
$APIN + OH \longrightarrow TERPO_2$	$1.200e{-}11{*}exp(440./T)$	
$BPIN + OH \longrightarrow TERPO_2$	$1.600e{-}11{*}exp(470./T)$	
$LIMON + OH \longrightarrow TERPO_2$	$4.200e{-}11{*}exp(400./T)$	
$MYRC + OH \longrightarrow TERPO_2$	$2.100e-10$	
$CARENE_3 + OH \longrightarrow TERPO_2$	$8.800e-11$	Atkinson and Arey 2003
$TBETAOCI + OH \longrightarrow TERPO_2$	$2.520e-10$	Atkinson and Arey 2003
$SABIN + OH \longrightarrow TERPO_2$	$1.170e-10$	
$BCARY + OH \longrightarrow TERPO_2$	$2.000e-10$	
$AFARN + OH \longrightarrow TERPO_2$	$2.190e-10$	Kim et al. J. Phys. Chem. A (2011)
$BFARN + OH \longrightarrow TERPO_2$	$2.880e-10$	Kim et al. J. Phys. Chem. A (2011)
$APIN + O_3 \longrightarrow 0.07 \cdot MTHOM + 0.39 \cdot TERPROD_1 + 0.27 \cdot TERPROD_2 + 0.63 \cdot OH + 0.57 \cdot HO_2 + 0.23 \cdot CO + 0.27 \cdot CO_2 + 0.52 \cdot CH_3COCH_3 + 0.34 \cdot CH_2O + 0.05 \cdot HCOOH + 0.05 \cdot BIGALKANE + 0.06 \cdot CH_3CO + 0.06 \cdot CH_3COCH_2O_2$	$6.300e-16 * exp(-580./T)$	7% ELVOC-yield according to Ehn et al. 2014 for endocyclic alkenes

Table D.1.: JAM3 chemical mechanism (... continued)

$BPIN + O_3 \longrightarrow 0.43 \cdot TERPROD_1 + 0.3 \cdot TERPROD_2 + 0.63 \cdot OH + 0.57 \cdot HO_2 + 0.23 \cdot CO + 0.27 \cdot CO_2 + 0.52 \cdot CH_3COCH_3 + 0.34 \cdot CH_2O + 0.05 \cdot HCOOH + 0.05 \cdot BIGALKANE + 0.06 \cdot CH_3CO + 0.06 \cdot CH_3COCH_2O_2$	$1.700e-15 * exp(-1300./T)$		
$LIMON + O_3 \longrightarrow 0.07 \cdot MTHOM + 0.39 \cdot TERPROD_1 + 0.27 \cdot TERPROD_2 + 0.63 \cdot OH + 0.57 \cdot HO_2 + 0.23 \cdot CO + 0.27 \cdot CO_2 + 0.52 \cdot CH_3COCH_3 + 0.34 \cdot CH_2O + 0.05 \cdot HCOOH + 0.05 \cdot BIGALKANE + 0.06 \cdot CH_3CO + 0.06 \cdot CH_3COCH_2O_2$	$3.000e-15 * exp(-780./T)$		7% ELVOC-yield according to Ehn et al. 2014 for endocyclic alkenes
$MYRC + O_3 \longrightarrow 0.43 \cdot TERPROD_1 + 0.3 \cdot TERPROD_2 + 0.63 \cdot OH + 0.57 \cdot HO_2 + 0.23 \cdot CO + 0.27 \cdot CO_2 + 0.52 \cdot CH_3COCH_3 + 0.34 \cdot CH_2O + 0.05 \cdot HCOOH + 0.05 \cdot BIGALKANE + 0.06 \cdot CH_3CO + 0.06 \cdot CH_3COCH_2O_2$	$4.700e-16$		
$CARENE_3 + O_3 \longrightarrow 0.07 \cdot MTHOM + 0.39 \cdot TERPROD_1 + 0.27 \cdot TERPROD_2 + 0.63 \cdot OH + 0.57 \cdot HO_2 + 0.23 \cdot CO + 0.27 \cdot CO_2 + 0.52 \cdot CH_3COCH_3 + 0.34 \cdot CH_2O + 0.05 \cdot HCOOH + 0.05 \cdot BIGALKANE + 0.06 \cdot CH_3CO + 0.06 \cdot CH_3COCH_2O_2$	$3.700e-17$		7% ELVOC-yield according to Ehn et al. 2014 for endocyclic alkenes; Atkinson and Arey 2003
$TBETAOCI + O_3 \longrightarrow 0.43 \cdot TERPROD_1 + 0.3 \cdot TERPROD_2 + 0.63 \cdot OH + 0.57 \cdot HO_2 + 0.23 \cdot CO + 0.27 \cdot CO_2 + 0.52 \cdot CH_3COCH_3 + 0.34 \cdot CH_2O + 0.05 \cdot HCOOH + 0.05 \cdot BIGALKANE + 0.06 \cdot CH_3CO + 0.06 \cdot CH_3COCH_2O_2$	$5.400e-16$		Atkinson and Arey 2003 for cis-ocimene
$SABIN + O_3 \longrightarrow 0.43 \cdot TERPROD_1 + 0.3 \cdot TERPROD_2 + 0.63 \cdot OH + 0.57 \cdot HO_2 + 0.23 \cdot CO + 0.27 \cdot CO_2 + 0.52 \cdot CH_3COCH_3 + 0.34 \cdot CH_2O + 0.05 \cdot HCOOH + 0.05 \cdot BIGALKANE + 0.06 \cdot CH_3CO + 0.06 \cdot CH_3COCH_2O_2$	$8.300e-17$		Atkinson and Arey 2003
$BCARY + O_3 \longrightarrow 0.645 \cdot TERPROD_1 + 0.45 \cdot TERPROD_2 + 0.63 \cdot OH + 0.57 \cdot HO_2 + 0.23 \cdot CO + 0.27 \cdot CO_2 + 0.52 \cdot CH_3COCH_3 + 0.34 \cdot CH_2O + 0.05 \cdot HCOOH + 0.05 \cdot BIGALKANE + 0.06 \cdot CH_3CO + 0.06 \cdot CH_3COCH_2O_2$	$1.200e-14$		

Table D.1.: JAM3 chemical mechanism (... continued)

$AFARN + O_3 \longrightarrow 0.645 \cdot TERPROD_1 + 0.45 \cdot TERPROD_2 + 0.63 \cdot OH + 0.57 \cdot HO_2 + 0.23 \cdot CO + 0.27 \cdot CO_2 + 0.52 \cdot CH_3COCH_3 + 0.34 \cdot CH_2O + 0.05 \cdot HCOOH + 0.05 \cdot BIGALKANE + 0.06 \cdot CH_3CO + 0.06 \cdot CH_3COCH_2O_2$	$3.520e-12 * exp(-2589./T)$		Kim et al. J. Phys. Chem. A (2011)
$BFARN + O_3 \longrightarrow 0.645 \cdot TERPROD_1 + 0.45 \cdot TERPROD_2 + 0.63 \cdot OH + 0.57 \cdot HO_2 + 0.23 \cdot CO + 0.27 \cdot CO_2 + 0.52 \cdot CH_3COCH_3 + 0.34 \cdot CH_2O + 0.05 \cdot HCOOH + 0.05 \cdot BIGALKANE + 0.06 \cdot CH_3CO + 0.06 \cdot CH_3COCH_2O_2$	$1.810e-12 * exp(-2347./T)$		Kim et al. J. Phys. Chem. A (2011)
$APIN + NO_3 \longrightarrow NTERPO_2$	$1.200e-12 * exp(490./T)$		
$BPIN + NO_3 \longrightarrow NTERPO_2$	$2.500e-12$		
$LIMON + NO_3 \longrightarrow NTERPO_2$	$1.100e-11$		
$MYRC + NO_3 \longrightarrow NTERPO_2$	$1.200e-11$		
$CARENE_3 + NO_3 \longrightarrow NTERPO_2$	$9.100e-12$		Atkinson and Arey 2003
$TBETAOCI + NO_3 \longrightarrow NTERPO_2$	$2.200e-11$		Atkinson and Arey 2003
$SABIN + NO_3 \longrightarrow NTERPO_2$	$1.000e-11$		Atkinson and Arey 2003
$BCARY + NO_3 \longrightarrow NTERPO_2 + 0.5 \cdot TERPROD_1$	$1.900e-11$		
$AFARN + NO_3 \longrightarrow NTERPO_2 + 0.5 \cdot TERPROD_1$	$1.900e-11$		like for BCARY
$BFARN + NO_3 \longrightarrow NTERPO_2 + 0.5 \cdot TERPROD_1$	$1.900e-11$		like for BCARY
$TERPO_2 + NO \longrightarrow NO_2 + 0.486 \cdot CH_2O + 0.0608 \cdot CH_3COCH_3 + 0.939 \cdot TERPROD_1 + HO_2$	$3.108e-12 * exp(180./T)$		26% alkyl nitrate yield according to Rindelaub et al. Atmos. Environ. 2015 for alpha-pinene
$TERPO_2 + NO \longrightarrow TERPNO_3$	$1.092e-12 * exp(180./T)$		26% alkyl nitrate yield according to Rindelaub et al. Atmos. Environ. 2015 for alpha-pinene
$TERPO_2 + HO_2 \longrightarrow TERPOOH$	$7.500e-13 * exp(700./T)$		
$TERPO_2 + CH_3O_2 \longrightarrow 1.15 \cdot CH_2O + 0.05 \cdot CH_3COCH_3 + 0.945 \cdot TERPROD_1 + HO_2 + 0.25 \cdot CH_3OH$	$2.000e-12 * exp(500./T)$		
$TERPO_2 + CH_3CO_3 \longrightarrow 0.4 \cdot CH_2O + 0.05 \cdot CH_3COCH_3 + 0.945 \cdot TERPROD_1 + HO_2 + CH_3O_2 + CO_2$	$1.000e-11$		
$TERPOOH + OH \longrightarrow H_2O + TERPO_2$	$3.300e-11$		
$TERPROD_1 + OH \longrightarrow TERP_2O_2$	$5.700e-11$		
$TERPROD_1 + NO_3 \longrightarrow 0.5 \cdot TERP_2O_2 + 0.5 \cdot NTERPO_2 + 0.5 \cdot NO_2$	$1.000e-12$		
$TERPNO_3 + OH \longrightarrow NO_2 + TERPROD_1 + H_2O$	$3.500e-12$		

Table D.1.: JAM3 chemical mechanism (... continued)

$TERP_2O_2 + NO \longrightarrow NO_2 + 0.459 \cdot CH_2O + 0.365 \cdot CH_3COCH_3 + 0.304 \cdot CO + CO_2 + TERPROD_2 + HO_2 + 0.365 \cdot GLYALD$	$3.108e{-}12{*}exp(180./T)$	26% alkyl nitrate yield according to Rindelaub et al. Atmos. Environ. 2015 for alpha-pinene
$TERP_2O_2 + NO \longrightarrow TERPNO_3$	$1.092e{-}12{*}exp(180./T)$	26% alkyl nitrate yield according to Rindelaub et al. Atmos. Environ. 2015 for alpha-pinene
$TERP_2O_2 + HO_2 \longrightarrow TERP_2OOH$	$7.500e{-}13{*}exp(700./T)$	
$TERP_2O_2 + CH_3O_2 \longrightarrow TERPROD_2 + 0.93 \cdot CH_2O + 0.25 \cdot CH_3OH + HO_2 + 0.5 \cdot CO_2 + 0.125 \cdot CO + 0.125 \cdot GLYALD + 0.15 \cdot CH_3COCH_3$	$2.000e{-}12{*}exp(500./T)$	
$TERP_2O_2 + CH_3CO_3 \longrightarrow 0.34 \cdot CH_2O + 0.27 \cdot CH_3COCH_3 + 0.225 \cdot CO + 2 \cdot CO_2 + TERPROD_2 + HO_2 + 0.225 \cdot GLYALD + CH_3O_2$	$1.000e-11$	
$TERP_2OOH + OH \longrightarrow H_2O + TERP_2O_2$	$2.300e-11$	
$TERPROD_2 + OH \longrightarrow 0.15 \cdot CH_3COCH_2O_2 + 0.68 \cdot CH_2O + 1.8 \cdot CO_2 + 0.5 \cdot CH_3COCH_3 + 0.65 \cdot CH_3CO + 0.2 \cdot HO_2 + 0.7 \cdot CO$	$3.400e-11$	
$NTERPO_2 + NO \longrightarrow 2 \cdot NO_2 + TERPROD_1$	$3.108e{-}12{*}exp(180./T)$	26% alkyl nitrate yield according to Rindelaub et al. Atmos. Environ. 2015 for alpha-pinene
$NTERPO_2 + NO \longrightarrow NTERPNO_3$	$1.092e{-}12{*}exp(180./T)$	26% alkyl nitrate yield according to Rindelaub et al. Atmos. Environ. 2015 for alpha-pinene
$NTERPO_2 + HO_2 \longrightarrow NTERPNO_3$	$7.500e{-}13{*}exp(700./T)$	
$NTERPO_2 + CH_3O_2 \longrightarrow 0.5 \cdot NTERPNO_3 + 0.75 \cdot CH_2O + 0.25 \cdot CH_3OH + 0.5 \cdot HO_2 + 0.5 \cdot TERPROD_1 + 0.5 \cdot NO_2$	$2.000e{-}12{*}exp(500./T)$	
$NTERPO_2 + CH_3CO_3 \longrightarrow CH_3O_2 + TERPROD_1 + CO_2 + NO_2$	$1.000e-11$	
$NTERPO_2 + NO_3 \longrightarrow 2 \cdot NO_2 + TERPROD_1$	$2.400e-12$	
$NTERPNO_3 + OH \longrightarrow NO_2 + TERPROD_1 + H_2O$	$3.500e-12$	
$MTHOM + OH \longrightarrow HO_2 + TERPROD_1$	$1.000e-11$	a general rate coefficient for oxygenated VOC

Tropospheric halogen + organics reactions reaction	rate coefficient	reference
$CL + CH_2O \longrightarrow HCL + HO_2 + CO$	$8.100e-11 * exp(-30./T)$	
$CL + CH_4 \longrightarrow CH_3O_2 + HCL$	$7.300e-12 * exp(-1280./T)$	
$CL + CH_3CN \longrightarrow CH_2O + HCL + CO + NO$	$1.600e-11 * exp(-2140./T)$	JPL(2011), products: Tyndall

Table D.1.: JAM3 chemical mechanism (... continued)

$CL+C_2H_2+M \longrightarrow 0.1 \cdot CL+0.1 \cdot GLYOXAL+0.9 \cdot HCL+0.9 \cdot HO_2+ 1.8 \cdot CO + M$	$ktroe(5.200e 30, 2.4, 2.200e 10, 0.7, 0.6)$	– – –		
$CL + C_2H_4 + M \longrightarrow HO_2 + 2 \cdot CO + HCL + M$	$ktroe(1.600e 29, 3.3, 3.100e 10, 1., 0.6)$	– – –		
$CL + C_2H_6 \longrightarrow C_2H_5O_2 + HCL$	$7.200e - exp(-70./T)$	11	*	
$CL + CH_3O_2 \longrightarrow 0.5 \cdot CLO + 0.5 \cdot CH_2O + 0.5 \cdot HCL + 0.5 \cdot OH + 0.5 \cdot CO + HO_2$	$1.600e - 10$			50% CH2OO is produced and assumed to be produced mostly in dry environments and thus decomposing
$CL + CH_3OH \longrightarrow CH_2O + HO_2 + HCL$	$7.100e - exp(-75./T)$	11	*	IUPAC
$CL + CH_3OOH \longrightarrow CH_2O + OH + HCL$	$5.900e - 11$			IUPAC
$CL + CH_3CHO \longrightarrow CH_3CO + HCL$	$8.000e - 11$			IUPAC
$CL+GLYALD \longrightarrow 0.35 \cdot GLYOXAL+0.35 \cdot HO_2+0.65 \cdot HOCH_2CO+ HCL$	$7.600e - 11$			k by Bacher et al., J. Atmos. Chem. (2001); products by Niki et al., J. Phys. Chem. (1987)
$CL + GLYOXAL \longrightarrow HCL + HCOCO_3$	$3.441e - 11$			k(298K) from Niki et al. 1985 k(CH2O + Cl) has been adjusted for the k(CH2O + Cl) by JPL used here
$CL + C_3H_8 \longrightarrow C_3H_7O_2 + HCL$	$1.400e - 10$			IUPAC
$CL + CH_3COCH_3 \longrightarrow CH_3COCH_2O_2 + HCL$	$1.500e - exp(-590./T)$	11	*	IUPAC
$CL + HYAC \longrightarrow CH_3COCHO + HO_2 + HCL$	$5.400e - 11$			Calvert et al.(2008)
$CL + BIGALKANE \longrightarrow ALKO_2 + HCL$	$1.935e - 10$			from the reaction with OH, BIGALKANE seems to be methyl-butane whose k is an average of k given by Qian et al. Int. J. Chem. Kin. (2002) and Anderson et al., J. Phys. Chem. A (2007)
$CL + MEK \longrightarrow HCL + MEKO_2$	$3.800e-11 * exp(16./T)$			Calvert et al. (2011)
$CLO + CH_3O_2 \longrightarrow CL + HO_2 + CH_2O$	$3.300e - exp(-115./T)$	12	*	

Table D.1.: JAM3 chemical mechanism (... continued)

$BR + CH_2O \longrightarrow HBR + HO_2 + CO$	$1.700e-11 * exp(-800./T)$	
$BR + CH_3CHO \longrightarrow CH_3CO + HBR$	$1.800e-11 * exp(-460./T)$	IUPAC
$BRO + CH_3O_2 \longrightarrow HOBR + OH + HO_2 + CO$	$2.420e-14 * exp(1617./T)$	Shallcross et al. 2015 DOI: 10.1021/jp5108203, CH2OO assumed to be produced mostly in dry environments and thus decomposing
Sulfur reactions		
reaction	rate coefficient	reference
$SO_2 + OH + M \longrightarrow H_2SO_4 + HO_2$	$ktroe(3.300e-31, 4.3, 1.600e-12, 0., 0.6)$	JPL(2011)
$DMS + OH \longrightarrow CH_3SO_2 + HCHO$	$1.130e-11 * exp(-253./T)$	
$DMS + OH \longrightarrow DMSO + HO_2$	$1.e-9 * exp(5820./T) * [O_2]/(1.e30 + 5. * exp(6280./T) * [O_2])$	
$DMS + NO_3 \longrightarrow CH_3SO_2 + HNO_3 + HCHO$	$1.900e-13 * exp(520./T)$	
$DMS + CL \longrightarrow CH_3SO_2 + HCL + HCHO$	$3.300e-10$	
$DMS + BR \longrightarrow CH_3SO_2 + HBR + HCHO$	$9.000e-11 * exp(-2386./T)$	
$DMS + BRO \longrightarrow BR + DMSO$	$4.400e-13$	
$DMSO + OH \longrightarrow 0.6 \cdot SO_2 + HCHO + 0.6 \cdot CH_3O_2 + 0.4 \cdot HO_2 + 0.4 \cdot CH_3SO_3H$	$1.000e-10$	
$CH_3SO_2 \longrightarrow CH_3O_2 + SO_2$	$1.800e+13 * exp(-8661./T)$	
$CH_3SO_2 + O_3 \longrightarrow CH_3SO_3$	$3.000e-13$	
$CH_3SO_3 + HO_2 \longrightarrow CH_3SO_3H$	$5.000e-11$	
Stratospheric O1D reactions		
reaction	rate coefficient	reference
$O_1D + N_2O \longrightarrow 2 \cdot NO$	$7.250e-11 * exp(20./T)$	

Table D.1.: JAM3 chemical mechanism (... continued)

$O_1D + N_2O \longrightarrow N_2 + O_2$	$4.630e-11 * exp(20./T)$	
$O_1D + O_3 \longrightarrow 2 \cdot O_2$	$1.200e-10$	
$O_1D + CFC_{11} \longrightarrow 2 \cdot CL + COFCL$	$2.020e-10$	
$O_1D + CFC_{12} \longrightarrow 2 \cdot CL + COF_2$	$1.204e-10$	
$O_1D + CFC_{113} \longrightarrow 2 \cdot CL + COFCL + COF_2$	$1.500e-10$	
$O_1D + CFC_{114} \longrightarrow 2 \cdot CL + 2 \cdot COF_2$	$9.750e-11$	
$O_1D + CFC_{115} \longrightarrow CL + F + 2 \cdot COF_2$	$1.500e-11$	
$O_1D + HCFC_{22} \longrightarrow CL + COF_2$	$7.200e-11$	
$O_1D + HCFC_{141}B \longrightarrow CL + COFCL$	$1.794e-10$	
$O_1D + HCFC_{142}B \longrightarrow CL + COF_2$	$1.628e-10$	
$O_1D + CCL_4 \longrightarrow 4 \cdot CL$	$2.840e-10$	
$O_1D + CH_3BR \longrightarrow BR$	$1.674e-10$	
$O_1D + CF_2CLBR \longrightarrow BR + CL + COF_2$	$9.600e-11$	
$O_1D + CF_3BR \longrightarrow BR + F + COF_2$	$4.100e-11$	
$O_1D + H_{1202} \longrightarrow 2 \cdot BR + COF_2$	$1.012e-10$	
$O_1D + H_{2402} \longrightarrow 2 \cdot BR + 2 \cdot COF_2$	$1.200e-10$	
$O_1D + CHBR_3 \longrightarrow 3 \cdot BR$	$4.490e-10$	
$O_1D + CH_2BR_2 \longrightarrow 2 \cdot BR$	$2.570e-10$	
$O_1D + COF_2 \longrightarrow 2 \cdot F$	$2.140e-11$	
$O_1D + COFCL \longrightarrow CL + F$	$1.900e-10$	
$O_1D + CH_4 \longrightarrow CH_3O_2 + OH$	$1.310e-10$	
$O_1D + CH_4 \longrightarrow CH_2O + H + HO_2$	$3.500e-11$	
$O_1D + CH_4 \longrightarrow CH_2O + H_2$	$9.000e-12$	
$O_1D + H_2 \longrightarrow H + OH$	$1.200e-10$	
$O_1D + HCL \longrightarrow CL + OH$	$1.500e-10$	
$O_1D + HBR \longrightarrow BR + OH$	$1.200e-10$	
$O_1D + HCN \longrightarrow CO + OH + NO$	$7.700e-11 * exp(100./T)$	Strekowski, 2001, products: Tyndall
Stratospheric inorganic halogen reactions		
reaction	rate coefficient	reference
$CL + O_3 \longrightarrow CLO + O_2$	$2.300e-11 * exp(-200./T)$	

Table D.1.: JAM3 chemical mechanism (... continued)

$CL + H_2 \longrightarrow H + HCL$	$3.050e - 11 * exp(-2270./T)$
$CL + H_2O_2 \longrightarrow HCL + HO_2$	$1.100e - 11 * exp(-980./T)$
$CL + HO_2 \longrightarrow HCL + O_2$	$1.400e-11*exp(270./T)$
$CL + HO_2 \longrightarrow CLO + OH$	$3.600e - 11 * exp(-375./T)$
$CL_2O_2 + M \longrightarrow 2 \cdot CLO + M$	$kCL2O2$
$CLO + O \longrightarrow CL + O_2$	$2.800e-11*exp(85./T)$
$CLO + OH \longrightarrow CL + HO_2$	$7.400e-12*exp(270./T)$
$CLO + OH \longrightarrow HCL + O_2$	$6.000e-13*exp(230./T)$
$CLO + HO_2 \longrightarrow HOCL + O_2$	$2.600e-12*exp(290./T)$
$CLO + NO \longrightarrow CL + NO_2$	$6.400e-12*exp(290./T)$
$CLO + NO_2 + M \longrightarrow CLONO_2 + M$	$ktroe(1.800e - 31, 3.4, 1.500e - 11, 1.9, 0.6)$
$CLO + CLO \longrightarrow 2 \cdot CL + O_2$	$3.000e - 11 * exp(-2450./T)$
$CLO + CLO \longrightarrow CL_2 + O_2$	$1.000e - 12 * exp(-1590./T)$
$CLO + CLO \longrightarrow CL + OCLO$	$3.500e - 13 * exp(-1370./T)$
$CLO + CLO + M \longrightarrow CL_2O_2 + M$	$ktroe(1.600e - 32, 4.5, 3.000e - 12, 2., 0.6)$
$HCL + OH \longrightarrow CL + H_2O$	$1.800e - 12 * exp(-250./T)$
$HCL + O \longrightarrow CL + OH$	$1.000e - 11 * exp(-3300./T)$
$HOCL + O \longrightarrow CLO + OH$	$1.700e - 13$

Table D.1.: JAM3 chemical mechanism (... continued)

$HOCL + CL \longrightarrow CLO + HCL$	$3.400e-12 * exp(-130./T)$	
$HOCL + OH \longrightarrow CLO + H_2O$	$3.000e-12 * exp(-500./T)$	
$CLONO_2 + O \longrightarrow CLO + NO_3$	$3.600e-12 * exp(-840./T)$	
$CLONO_2 + OH \longrightarrow HOCL + NO_3$	$1.200e-12 * exp(-330./T)$	
$CLONO_2 + CL \longrightarrow CL_2 + NO_3$	$6.500e{-}12 * exp(135./T)$	
$BR + O_3 \longrightarrow BRO + O_2$	$1.600e-11 * exp(-780./T)$	
$BR + HO_2 \longrightarrow HBR + O_2$	$4.800e-12 * exp(-310./T)$	
$BR + NO_2 + M \longrightarrow 0.85 \cdot BRONO + 0.15 \cdot BRNO_2 + M$	$ktroe(4.200e-31, 2.4, 2.700e-11, 0., 0.6)$	
$BRONO + M \longrightarrow BR + NO_2 + M$	$1.648e+11 * exp(-7399./T)$	fit to upper limit by Wine et al. NATO ASI series 1993 and scaled 1.5 factor to match data by Orlando and Burkholder (2000)
$BRO + O \longrightarrow BR + O_2$	$1.900e{-}11 * exp(230./T)$	
$BRO + OH \longrightarrow BR + HO_2$	$1.700e{-}11 * exp(250./T)$	
$BRO + HO_2 \longrightarrow HOBR + O_2$	$4.500e{-}12 * exp(460./T)$	
$BRO + NO \longrightarrow BR + NO_2$	$8.800e{-}12 * exp(260./T)$	
$BRO + NO_2 + M \longrightarrow BRONO_2 + M$	$ktroe(5.200e-31, 3.2, 6.900e-12, 2.9, 0.6)$	
$BRO + CLO \longrightarrow BR + OCLO$	$9.500e{-}13 * exp(550./T)$	
$BRO + CLO \longrightarrow BR + CL + O_2$	$2.300e{-}12 * exp(260./T)$	
$BRO + CLO \longrightarrow BRCL + O_2$	$4.100e{-}13 * exp(290./T)$	
$BRO + BRO \longrightarrow 2 \cdot BR + O_2$	$2.400e-12 * exp(40./T)$	
$BRO + BRO \longrightarrow BR_2 + O_2$	$2.800e{-}14 * exp(860./T)$	

Table D.1.: JAM3 chemical mechanism (... continued)

$HBR + OH \longrightarrow BR + H_2O$	$5.500e{-}12{*}exp(200./T)$	
$HBR + O \longrightarrow BR + OH$	$5.800e - 12 * exp(-1500./T)$	
$HOBR + O \longrightarrow BRO + OH$	$1.200e - 10 * exp(-430./T)$	
$BRONO_2 + O \longrightarrow BRO + NO_3$	$1.900e{-}11{*}exp(215./T)$	
$BRONO_2 + BR \longrightarrow BR_2 + NO_3$	$5.805e - 11$	Average of k at 298K by Orlando and Tyndall (1996) and Harwood et al. (1998)
$BR_2 + OH \longrightarrow BR + HOBR$	$2.100e{-}11{*}exp(240./T)$	
$F + H_2O \longrightarrow HF + OH$	$1.400e - 11$	
$F + H_2 \longrightarrow H + HF$	$1.400e - 10 * exp(-500./T)$	
$F + CH_4 \longrightarrow CH_3O_2 + HF$	$1.600e - 10 * exp(-260./T)$	
$F + HNO_3 \longrightarrow HF + NO_3$	$6.000e{-}12{*}exp(400./T)$	
Stratospheric organic halogen reactions		
reaction	rate coefficient	reference
$CH_3BR + OH \longrightarrow BR + H_2O + HO_2$	$2.350e - 12 * exp(-1300./T)$	
$CH_3BR + CL \longrightarrow HCL + HO_2 + BR$	$1.400e - 11 * exp(-1030./T)$	
$CH_2BR_2 + OH \longrightarrow 2 \cdot BR + H_2O$	$2.000e - 12 * exp(-840./T)$	
$CHBR_3 + OH \longrightarrow 3 \cdot BR$	$1.350e - 12 * exp(-600./T)$	
$CH_2BR_2 + CL \longrightarrow 2 \cdot BR + HCL$	$6.300e - 12 * exp(-800./T)$	
$CHBR_3 + CL \longrightarrow 3 \cdot BR + HCL$	$4.850e - 12 * exp(-850./T)$	
$CH_3CL + CL \longrightarrow CO + HO_2 + 2 \cdot HCL$	$2.170e - 11 * exp(-1130./T)$	

Table D.1.: JAM3 chemical mechanism (... continued)

$CH_3CL + OH \longrightarrow CO + HO_2 + HCL + H_2O$	$2.400e - 12 * exp(-1250./T)$			products: Tyndall(p.c.), implicitly includes NO-¿NO2 conversion with CH2ClO2
$CH_3CCL_3 + OH \longrightarrow H_2O + 3 \cdot CL$	$1.640e - 12 * exp(-1520./T)$			
$HCFC_{22} + OH \longrightarrow CL + H_2O + COF_2$	$1.050e - 12 * exp(-1600./T)$			
$HCFC_{141}B + OH \longrightarrow CL + COFCL$	$1.250e - 12 * exp(-1600./T)$			
$HCFC_{142}B + OH \longrightarrow CL + COF_2$	$1.300e - 12 * exp(-1770./T)$			

(Tropospheric) heterogeneous reactions		
reaction	reaction probability	reference
$O_3 \longrightarrow HO_2$	$\gamma = 10^{-6}$	Stadtler et al., 2018
$HO_2 \longrightarrow 0.5 \cdot H_2O_2$	$\gamma = 0.2$	Stadtler et al., 2018
$NO_3 \longrightarrow$	$\gamma = 0.001$	Stadtler et al., 2018
$NO_2 \longrightarrow 0.5 \cdot HONO$	$\gamma = 10^{-4}$	Stadtler et al., 2018
$HNO_3 \longrightarrow$	$\gamma_{SS} = 0.01$, $\gamma_{DU} = 0.1$	Stadtler et al., 2017
$N_2O_5 \longrightarrow$	$\gamma = f(T, RH)$	Stadtler et al., 2018

Stratospheric heterogeneous reactions		
reaction	reaction probability	reference
$N_2O_5 \longrightarrow 2 \cdot HNO_3$	$hetN2O5$	het1
$CLONO_2 \longrightarrow HNO_3 + HOCL$	$hetCLONO2$	het2
$BRONO_2 \longrightarrow HNO_3 + HOBR$	$hetBRONO2$	het3
$CLONO_2 + HCL \longrightarrow CL_2 + HNO_3$	$hetCLONO2_HCL$	het4
$HOCL + HCL \longrightarrow CL_2 + H_2O$	$hetHOCL_HCL$	het5
$HOBR + HCL \longrightarrow BRCL + H_2O$	$hetHOBR_HCL$	het6
$N_2O_5 \longrightarrow 2 \cdot HNO_3$	$hetN2O5$	het7
$CLONO_2 \longrightarrow HNO_3 + HOCL$	$hetCLONO2$	het8
$CLONO_2 + HCL \longrightarrow CL_2 + HNO_3$	$hetCLONO2_HCL$	het9
$HOCL + HCL \longrightarrow CL_2 + H_2O$	$hetHOCL_HCL$	het10
$BRONO_2 \longrightarrow HNO_3 + HOBR$	$hetBRONO2$	het11

Table D.1.: JAM3 chemical mechanism (... continued)

$N_2O_5 \longrightarrow 2 \cdot HNO_3$	$hetN2O5$	het12
$CLONO_2 \longrightarrow HNO_3 + HOCL$	$hetCLONO2$	het13
$BRONO_2 \longrightarrow HNO_3 + HOBR$	$hetBRONO2$	het14
$CLONO_2 + HCL \longrightarrow CL_2 + HNO_3$	$hetCLONO2_HCL$	het15
$HOCL + HCL \longrightarrow CL_2 + H_2O$	$hetHOCL_HCL$	het16
$HOBR + HCL \longrightarrow BRCL + H_2O$	$hetHOBR_HCL$	het17
Sulfate aerosol reactions	reaction probability	from Lamarque et al., 2012
$N_2O_5 \longrightarrow 2 \cdot HNO_3$	$\gamma = 0.04$	
$CLONO_2 \longrightarrow HOCL + HNO_3$	$f(sulfuricacidwt\%)$	
$BRONO_2 \longrightarrow HOBR + HNO_3$	$f(T, P, HCl, H2O, r)$	
$CLONO_2 + HCL \longrightarrow CL_2 + HNO_3$	$f(T, P, H2O, r)$	
$HOCL + HCL \longrightarrow CL_2 + H_2O$	$f(T, P, HCl, H2O, r)$	
$HOBR + HCL \longrightarrow BRCL + H_2O$	$f(T, P, HCl, HOBr, H2O, r)$	
Nitric acid dihydrate reactions	reaction probability	from Lamarque et al., 2012
$N_2O_5 \longrightarrow 2 \cdot HNO_3$	$\gamma = 0.0004$	
$CLONO_2 \longrightarrow HOCL + HNO_3$	$\gamma = 0.004$	
$CLONO_2 + HCL \longrightarrow CL_2 + HNO_3$	$\gamma = 0.2$	
$HOCL + HCL \longrightarrow CL_2 + H_2O$	$\gamma = 0.1$	
$BRONO_2 \longrightarrow HOBR + HNO_3$	$\gamma = 0.3$	
Ice aerosol reactions	reaction probability	from Lamarque et al., 2012
$N_2O_5 \longrightarrow 2 \cdot HNO_3$	$\gamma = 0.02$	
$CLONO_2 \longrightarrow HOCL + HNO_3$	$\gamma = 0.3$	
$BRONO_2 \longrightarrow HOBR + HNO_3$	$\gamma = 0.3$	
$CLONO_2 + HCL \longrightarrow CL_2 + HNO_3$	$\gamma = 0.3$	
$HOCL + HCL \longrightarrow CL_2 + H_2O$	$\gamma = 0.2$	
$HOBR + HCL \longrightarrow BRCL + H_2O$	$\gamma = 0.3$	

List of Figures

List of Tables

Acknowledgments

Dicebat Bernardus Carnotensis nos esse quasi nanos gigantum umeris insidentes, ut possimus plura eis et remotiora videre, non utique proprii visus acumine, aut eminentia corporis, sed quia in altum subvehimur et extollimur magnitudine gigantea.

As the quote above says, this thesis could not have been accomplished without great minds, guiding me. I gratefully acknowledge Martin Schultz and Andreas Bott for their great supervision, the fruitful discussions and navigation through the life as a doctoral researcher at the Institute for Energy and Climate – Troposphere (IEK-8). The IEK-8 and the Forschungszentrum Jülich created an inspiring atmosphere with the possibility of scientific exchange through ought the different disciplines. I could quickly learn and develop myself in this interdisciplinary environment.

This thesis was created in close collaboration with Harri Kokkola and Thomas Kühn. I had the possibility to visit them in Kuopio, to develop the coupling between MOZ and SALSA. For me, this was a great time, which enabled a solid communication with Harri and Thomas. On a daily basis, we chatted and coded. In my impression, Thomas and I worked together even closer than me and Sabine. I am thankful for Harri and Thomas for being part of my group.

My special thanks to David Simpson for teaching me how to publish a paper, reply to reviews, throw away all results and redo everything again and again. I enjoyed the visit in Gothenburg, because I got to know Dave and "his" EMEP model, which is so incredibly quick.

The global modeling group at IEK-8 changed with time, but always gave me feedback to find bugs and understand if the model is simulating what is happening in the atmosphere. I thank Sabine Schröder, Domenico Taraborelli, Olaf Stein, Najmeh Kaffashzadeh and Olga Lyapina for the motivational feedback. Especially, Sabine not only helped me with the model code, but also keeping up my motivation and good mood in office.

I thank my dear scientific colleagues from various universities and research institutions Thomas Mentel, Martin Kaminski, Kostas Tsigaridis, Dennis Booge, Zhujun Yu, Sebastian Schmitt, Georgios Gkatzelis, Defeng Zhao, Sungah Kang, Anna Novelli, Aaron van Donkelaar, Colombe Siegenthaler-Le Drian and Sylvaine Ferrachat for the endless support and motivation. While discussing we find open questions, mistakes, bugs and more work, but also unlimited curiosity.

My family and friends were so patient, supporting me emotionally and with feedback on my posters, presentations, videos, papers and my thesis. With their help, I improved my scientific communication to non-scientists and scientists of different fields. My thanks to Josephin Beer, Staicy Stadtler, Till Renger, Arnold Stadtler and Alessandra Gniezinski.

ECHAM-HAMMOZ simulations were supported by the Forschungszentrum Jülich and performed at the Jülich Supercomputing Centre [2016]. The ECHAM-HAMMOZ model is developed by a consortium composed of ETH Zurich, Max Planck Institut für Meteorologie, Forschungszentrum Jülich, University of Oxford, the Finnish Meteorological Institute and the Leibniz Institute for Tropospheric Research, and managed by the Center for Climate Systems Modeling (C2SM) at ETH Zurich.

Curriculum Vitae

JOURNAL PUBLICATIONS

S. Stadtler, D. Simpson, S. Schröder, D. Taraborrelli, A. Bott, and M. Schultz. **Ozone impacts of gas-aerosol uptake in global chemistry transport models**. *Atmospheric Chemistry and Physics*,
https://doi.org/10.5194/acp-18-3147-2018, 2018.

S. Stadtler, T. Kühn, S. Schröder, D. Taraborrelli, M. G. Schultz, and H. Kokkola. **Isoprene derived secondary organic aerosol in the global aerosol chemistry climate model ECHAM6.3-HAM2.3MOZ1.0**. *Geoscientific Model Development*,
https://doi.org/10.5194/gmd-2017-244, in Discussion, 2017.

M. G. Schultz, S. Stadtler, S. Schröder, D. Taraborrelli, A. Henrot, N. Kaffashzadeh, B. Franco, S. Ferrachat, C. Siegenthaler-Le Drian, U. Lohmann, D. Neubauer, S. Wahl, H. Kokkola, T. Kuehn, P. Stier, D. Kinnison, G. Tyndall, and J. Orlando. **The chemistry climate model ECHAM6.3-HAM2.3MOZ1.0**. *Geoscientific Model Development*,
https://doi.org/10.5194/gmd-2017-191, in Discussion, 2017.

H. Kokkola, T. Kühn, A. Laakso, T. Bergman, K. Lehtinen, T. Mielonen, A. Arola, S. Stadtler, H. Korhonen, S. Ferrachat, U. Lohmann, D. Neubauer, I. Tegen, C. Siegenthaler-Le Drian, M. G. Schultz, I. Bey, P. Stier, and S. Romakkaniemi **SALSA2.0: The sectional aerosol module of the aerosol-chemistry-climate model ECHAM6.3.0-HAM2.1-MOZ1.0**. *Geoscientific Model Development*, https://doi.org/10.5194/gmd-2018-47, in Discussion, 2018.

S. Stadtler, S. Schröder, D. Taraborrelli, and M. Schultz. **The impact of heterogeneous reactions on tropospheric ozone**. Oral presentation at the ECHAM-HAMMOZ Workshop, March 2016, Zürich, Switzerland.

S. Stadtler, D. Simpson, S. Schröder, D. Taraborrelli, A. Bott, and M. Schultz. **Heterogeneous Chemistry in Global Chemistry Transport Models**. Oral presentation at the EGU, April 2016, Vienna, Austria.

S. Stadtler, T. Kühn, S. Schröder, D. Taraborrelli, M. G. Schultz, and H. Kokkola. **Isoprene derived secondary organic aerosol in ECHAM6-HAMMOZ**. Oral presentation at the ECHAM-HAMMOZ Workshop, March 2017, Zürich, Switzerland.

S. Stadtler, T. Kühn, S. Schröder, D. Taraborrelli, M. G. Schultz, and H. Kokkola. **Isoprene derived secondary organic aerosol in a global aerosol chemistry climate model**. Poster presentation at the EGU, April 2017, Vienna, Austria.

S. Stadtler, T. Kühn, S. Schröder, D. Taraborrelli, M. G. Schultz, and H. Kokkola. **Isoprene derived secondary organic aerosol in a global chemistry climate model (ECHAM6-HAMMOZ)**. Poster presentation at the AeroCom Workshop, October 2017, Helsinki, Finland.